ÉCOLE
POLYTECHNIQUE
DE BRUXELLES
UNIVERSITÉ LIBRE DE BRUXELLES

Study of the eikonal approximation to model exotic reactions

Thesis presented by Chloë HEBBORN
in fulfilment of the requirements of the PhD Degree in Engineering Science and Technology (“Docteur en Sciences de l’ingénieur et technologies”)
Année académique 2019-2020

Supervisor : Professor Pierre CAPEL
Physique Nucléaire et Physique Quantique
Co-supervisor Nathalie VAECK
Service de Chimie Quantique et Photophysique

Thesis jury :

Jean-Marc SPARENBERG (Université libre de Bruxelles, Chair)
Pierre CAPEL (Université libre de Bruxelles, Secretary)
Daniel BAYE (Université libre de Bruxelles)
Filomena NUNES (Michigan State University)
Jan RYCKEBUSCH (Universiteit Gent)
Nathalie VAECK (Université libre de Bruxelles)

fnrs
FREEDOM TO RESEARCH

Abstract

In the mid-eighties, the development of radioactive-ion beams enabled the exploration of regions of the nuclear landscape away from the valley of stability. Close to the neutron dripline, in the light neutron-rich region, halo nuclei were observed. These nuclei exhibit a surprisingly large matter radius and a strongly clusterized structure. These two features can be explained by the weak binding of one or two neutrons which allows them to tunnel far from the rest of the nucleons, surrounding the nucleus by a diffuse halo. These nuclear structures have challenged the usual description of the nucleus, described as a compact many-body object with nucleons piling up into well defined orbitals. Because they are short-lived, these nuclei are often studied through reaction processes, such as elastic scattering, breakup and knockout. To infer precise information from the experimental data, an accurate reaction model coupled with a realistic description of the nucleus is needed.

Compared to other state-of-the-art methods, the eikonal approximation is very cheap from a computational viewpoint. This model assumes that the projectile-target relative motion does not differ much from the initial plane wave. It also makes the adiabatic approximation, which sees the internal coordinates of the projectile as frozen during the collision. These two assumptions hold for reactions occurring at high energy, i.e., above 60 MeV/nucleon, in which the deflection of the projectile by the target is small and the collision time is brief.

In this thesis, I focus on improvements of the eikonal approximation. First, I study the extension of the validity of the eikonal model down to 10 MeV/nucleon, in the energy range of the facilities HIE-ISOLDE at CERN and ReA12 at the upcoming FRIB. To this end, I analyse different corrections to the eikonal approximation, which account for the deflection of the projectile by the target. I assess their accuracy for the elastic-scattering and breakup observables of one-neutron halo nuclei at 10 MeV/nucleon. Next, I develop a dynamical correction to the eikonal approximation, which applies to both nuclear and Coulomb interactions while conserving the eikonal numerical cost. I study this correction in the cases of breakup reactions of one-neutron halo nuclei on light and heavy targets. Then, I investigate which nuclear-structure information can be inferred from knockout reactions of one-neutron halo nuclei. To do so, I conduct a sensitivity analysis of their observables to the nuclear structure of the projectile, described within a halo effective field theory. In particular, I study the influence onto the cross sections of the ground-state wave function, the presence of subthreshold bound states and resonances.

Keywords: halo nuclei, nuclear reactions, eikonal approximation, breakup, knockout, low-energy corrections, reaction dynamics.

Résumé

Le développement de faisceaux radioactifs dans le courant des années 80 a rendu possible l'exploration des régions de la charte des noyaux situées loin de la vallée de la stabilité. Près de la limite de la stabilité, dans la région des noyaux légers riches en neutrons, les noyaux à halo ont été observés. Ces noyaux présentent un rayon de matière étonnament grand et une structure en amas très prononcée. Ces deux caractéristiques sont expliquées par la faible énergie de liaison d'un ou deux neutrons, qui leur permet de se trouver par effet tunnel loin des autres nucléons, entourant le noyau d'un halo diffus. Ces structures nucléaires ont remis en question la description habituelle du noyau, décrit comme un object compact composé de nucléons qui s'empilent dans des orbitales bien définies. À cause de leurs très courtes durées de vie, ces noyaux sont souvent étudiés par le biais de réactions, telles que la diffusion élastique, les réactions de dissociation et de knockout. Afin de déduire des informations fiables à partir des données expérimentales, un modèle précis de réaction incluant une description réaliste des noyaux est nécessaire.

Comparée aux autres méthodes, l'approximation eikonale présente un coût numérique réduit. Ce modèle suppose que le mouvement relatif projectile-cible diffère peu de l'onde plane incidente. Il repose également sur l'approximation adiabatique, qui considère que les coordonnées internes du projectile sont figées pendant la collision. Ces deux hypothèses sont valables pour les réactions se produisant à haute énergie, au-dessus de 60 MeV/nucléon, dans lesquelles la déflexion du projectile par la cible est faible et la durée de la collision est courte.

Dans cette thèse, je me concentre sur plusieurs corrections à l'approximation eikonale. Dans un premier temps, j'étudie l'extension de la validité de ce modèle jusqu'à 10 MeV/nucléon, dans la gamme d'énergie de HIE-ISOLDE au CERN et de ReA12 au futur FRIB. Pour ce faire, j'analyse différentes corrections à l'approximation eikonale améliorant la déflexion du projectile par la cible. J'évalue leur précision pour les observables de diffusion élastique et de dissociation de noyaux à halo d'un neutron à 10 MeV/nucléon. Ensuite, je développe une correction dynamique à l'approximation eikonale, qui s'applique aux interactions nucléaire et Coulombienne tout en conservant son faible coût numérique. Je l'étudie pour des réactions de dissociation de noyaux à halo d'un neutron incident sur des cibles légères et lourdes. Après, je détermine quelles informations de la structure nucléaire peuvent être déduites à partir des réactions de knockout de noyaux à halo d'un neutron. Pour ce faire, j'effectue une analyse de sensibilité de leurs observables à la structure nucléaire du projectile, décrit dans une théorie effective des champs. En particulier, j'étudie l'influence sur les sections efficaces de la fonction d'onde de l'état fondamental, la présence d'états liés sous le seuil et de résonances.

Mots-clés: noyaux à halo, collisions nucléaires, approximation eikonale, réaction de dissociation, réaction de knockout, corrections à basses énergies, dynamique de réaction.

Acknowledgements

Conducting a PhD has been a challenging and exciting experience, which would not have been possible without the help of many people along the way.

Undoubtedly, my supervisor, Pierre Capel, is the person who has supported me from the very beginning until the very end. During my master's thesis, he transmitted his passion for research in nuclear physics and since then, for the last five years, he has always taken the time to guide and encourage me. I am also grateful for his patience and availability, even when he had a busy schedule. For all of these reasons, my biggest thanks go to him and I really hope that many more PhD students will have the chance to have him as a supervisor. I also very much appreciate the non-physics related discussions we had through the years and I hope we will have many more chances to see each other and talk at conferences.

I also had the great pleasure of working with Daniel Baye. I have learned a great deal from our discussions about both physics and his method of working. I have appreciated his precision, pedagogical qualities and availability. I also gratefully acknowledge him for his time and support.

This PhD thesis would not have been possible without the friendship of Frederic Colomer. First, as a student, on the benches at the Ecole polytechnique de Bruxelles and then as a colleague. I am really happy we could share this PhD experience together and I do not know where to start to thank you. I wish you all the best for your next adventures!

I have conducted this PhD in two different universities, in Brussels and Mainz, where I have met a lot of great colleagues. I would like to thank them all for the physics and non-physics exchanges we had for the last years and for the nice atmosphere of both departments. A warm thank you goes to Jean-Marc, Pierre D., Jérémy, Laura, Nam, Charlie, Javier, Sonia, Bijay, Johannes, Victoria, Simone and Asia. I have also enjoyed the lunches (or kebab when Fred was insisting) I have shared with Jean, Jean-Philippe and Gilles during the years in Brussels. I hope the ones I forgot in the list here will forgive me.

I would like to express my gratitude to my family and friends for their constant support and for listening attentively to me talking about nuclear collisions even if they have no knowledge on quantum mechanics. Though, most of them are still struggling to describe what is my research subject, they have never wavered in their support. Special thanks to my partner Rafa for every little attentions and for being always optimistic even during the hard period of writing a thesis coupled with a corona lockdown.

Finally, I would like to thank the jury members of this thesis, I hope you will enjoy reading it. I am also grateful to Professors Filomena Nunes, Antonio Moro, Andrea Vitturi, Kazuyuki Ogata, Jeffrey Tostevin, Daniel Phillips, Charlotte Elster and Sofia Quaglioni with who I have discussed some of the work of this thesis and/or learned about nuclear theory. I would particularly like to thank Filomena for her support and interesting comments on my work.

This work was supported by the Fund for Research Training in Industry and Agriculture (FRIA). I thank the Fonds de la Recherche Scientifique (F.R.S.-FNRS) for his funding. I also gratefully acknowledge the Institut für Kernphysik at Johannes Gutenberg-Universität Mainz for welcoming me for almost two years.

To my grandmother who has always encouraged me during my studies and during the PhD, but who unfortunately passed away before seeing the end of it.

To my nephew and two nieces born during the completion of this thesis and whose arrivals in this world have brought me a lot of joy.

Contents

Introduction

All the chemical elements on Earth and in the Universe were created in Stars billions of years ago by means of reactions between atomic nuclei [1, 2]. Nuclei being the fuel of Stars and the core of matter, studying their structure and how they interact is therefore essential to understand where we come from and how the Universe is evolving. Before the eighties, the study of very radioactive nuclei was difficult, because they are not observed in Nature as they decay too quickly. In the mid-eighties, the acceleration of short-lived nuclei became possible, allowing experimentalists to access parts of the nuclear landscape still unexplored. In most cases, these exotic nuclei are probed by making them collide with a target before they have the time to decay [3]. Several facilities have been built to this end, such as CYCLONE at Louvain-la-Neuve in Belgium, ISOLDE at CERN in Switzerland, GANIL in France, GSI in Germany, NSCL and the upcoming FRIB in the USA and RIKEN in Japan [4, 5]. To extract reliable information from these collisions, an accurate reaction model coupled with a realistic description of the nucleus is needed.

It is well known from quantum mechanics that the neutrons and protons inside the nucleus tend to rearrange to minimize their energy. Consequently, the formation of tightly-bound clusters of nucleons arises in both stable and unstable nuclei [6]. Close to the dripline, the nuclear binding is weak and this clustering effect is enhanced. In particular, in the light exotic sector of the nuclear chart, halo nuclei present a strongly clusterized structure, in which one or two loosely-bound nucleons have a high probability of presence far from the rest of the nucleons [7, 8]. Accordingly, they exhibit a surprisingly large matter radius. They are usually seen as a compact core to which one or two nucleons are loosely bound, surrounding the core by a diffuse halo. Haloes have challenged the usual description of a nucleus, seeing the nucleons as piling up in well defined orbitals and forming compact object.

Due to its low-binding energy, the halo dissociates easily from the core when the nucleus is colliding with a target. These reactions—called breakup—hence reveal the cluster structure inside the nucleus. They are often used to probe halo nuclei since they exhibit high statistics [9, 10]. Because the computing power is limited, the description of each nucleon involved in the collision is feasible only for very light systems. It is therefore common in reaction theory to describe the nucleus as a bound state of nucleon clusters [11]. The collision of a halo nucleus with a target is thus modelled as a few-body problem. State-of-the-art methods, such as the Faddeev formalism [12, 13] and the Continuum-Discretized Coupled Channels method [14, 15, 16, 17], solve the few-body problem in a fully-quantal approach and are accurate. Nevertheless, these methods are computationally-challenging and thus often restricted to a simple description of the projectile, e.g., to a small number of clusters. This motivates the use of approximations, such as the eikonal model [18], that are less time consuming.

The eikonal approximation assumes that the projectile is only slightly deflected by the target during the collision[1] . In its most usual implementation, it also includes the adiabatic approximation which sees the internal coordinates of the projectile as frozen during the collision. These two assumptions hold only at high enough energy, i.e., above $60A$ MeV[2], where the deflection of the projectile by the target is small and the collision time is shorter than the excitation time of the projectile. Additionally to its small numerical cost, the eikonal model provides a simple semiclassical interpretation of the collision. The projectile is seen as following a straight-line trajectory at constant impact parameter and velocity, along which its wave function accumulates a phase resulting from its interaction with the target.

Nowadays, facilities such as HIE-ISOLDE at CERN and the future ReA12 at FRIB, are or will be able to deliver radioactive-ion beams at energies around $10A$ MeV. Extending the validity of the eikonal model to such energies would therefore be of great interest. This is the first goal of my thesis. To improve the eikonal description at low energies, I study corrections that account for the deflection of the projectile by the target. Since the adiabatic approximation might no longer hold at these energies, I also assess the significance of the dynamical effects, associated with the excitation of the projectile during the reaction. I evaluate the accuracy of these corrections for elastic-scattering and breakup observables of one-neutron halo nuclei [20, 21, 22].

Because it relies on the adiabatic approximation, the eikonal model does not correctly treat the Coulomb interaction [23, 24]. Indeed, an adiabatic approach is not suited for infinite-range interactions, because the collision time can no longer be considered small. The second objective of my thesis is to correct for this adiabatic treatment by including dynamical effects at first order induced by both the Coulomb and nuclear interactions. In collaboration with Daniel Baye, we have developed a model that is compatible with the Coulomb interaction, while keeping the small numerical cost of the eikonal approximation. We have studied the accuracy of such a model to describe the breakup of one-neutron halo nuclei on light and heavy targets, i.e., with a small and large Coulomb repulsion between the nuclei [25].

Knockout reactions correspond also to the dissociation of the nucleus into its more fundamental clusters but they refer to an inclusive measurement, in which only the charged core is detected. These reactions exhibit therefore even higher statistics than exclusive breakup, where all fragments are measured in coincidence after the dissociation. Hence these reactions are often favoured for the low intensities available at radioactive-ion beam facilities and have been one of the first probes of exotic nuclei [9]. In the last thirty years, various exotic nuclei have been studied with these reactions. It has been noted by Gade and collaborators that the ratio between experimental data and theoretical predictions of one-nucleon knockout decreases when the binding energy of the removed nucleon increases [26, 27]. Surprisingly, this trend is not observed in the analysis of other reactions performed on the same nuclei, such as transfer [28, 29]. Several groups have attempted to explain this trend, but none of them has managed to explain why only the information inferred from these reactions are binding-energy dependent. In this thesis, my goal is to make a first step in that direction by understanding why theory and experiments agree well for loosely-bound nuclei and to pin down what structure information can be

---

[1] The eikonal approximation was first developed in ray optics to describe the reflection and refraction of light by an object. It assumes that the lights travels in a straight line, which is valid if the size of the object is large compared to the wavelength of the light. The etymology of the word eikonal also echoes with the ray optics: eikonal comes from the greek word *εἰκών* which means image [19].

[2] This notation A MeV refers to MeV per nucleon and is used in the rest of this thesis.

safely inferred from these data [30, 31].

The first Chapter of this thesis introduces the notion of halo nuclei, their discovery and main features. I will also discuss the different reactions that are studied in this thesis, and how the halo structure manifests itself in their observables. In Chapter 2, I will present two- and three-body models of reaction and the different formalisms used in this thesis to solve the corresponding Schrödinger equation. The different corrections aiming at extending the eikonal model down to $10A$ MeV are studied in Chapter 3. The inclusion of dynamical effects at first order within the eikonal model and an analysis of their impact on breakup cross sections are presented in Chapter 4. In the last Chapter, I will evaluate the sensitivity of knockout reactions to the description of the projectile's structure. Finally, I will conclude and discuss the prospects of this thesis.

Chapter 1

Probing halo nuclei with reactions

1.1 Halo nuclei

1.1.1 Discovery of halo nuclei

In the mid-eighties, the development of radioactive-ion beams (RIBs) has opened the door to regions of the nuclear landscape still unexplored. This technological breakthrough has enabled the discovery of unexpected nuclear structures. In particular, in the lower left corner of the nuclear chart, halo nuclei have been observed [8, 32, 33]. These nuclei exhibit a much larger radius compared to their isobars. Their large size challenges the usual vision of nuclei as compact objects but can be understood with the quantum tunnel effect. Being located close to the neutron dripline, the binding energies of the last one or two neutrons are very low. This weak binding allows them to tunnel out into the classically-forbidden region far from the rest of the nucleons. These neutrons thus form a diffuse halo around a tight core composed of the other nucleons [7].

^{6}He and ^{11}Li were the first halo nuclei discovered by Tanihata *et al.* [32, 33]. These two nuclei exhibit two neutrons in their halo and can thus be seen as composed of three clusters, a compact core with two halo neutrons. Besides their halo structure, these nuclei are Borromean [34], meaning that the three-cluster system is bound but both binary subsystems are unbound. For example, ^{11}Li is bound but ^{10}Li and the dineutron are unbound. Since the experiment of Tanihata *et al.*, other halo nuclei have been discovered. Among these, one-neutron halo nuclei, such as ^{11}Be and ^{15}C, exhibit one neutron in their halo.

Table 1.1 displays the separation energies of one neutron S_n or two neutrons S_{2n}, the root mean square distance $r_n^{\rm rms}$ between the halo neutron and the core of ^{11}Be and ^{15}C, as well as the root mean square distance $r_{2n}^{\rm rms}$ between the two halo neutrons of ^{6}He and ^{11}Li. We can see that these root mean square distances are of the order of 5 to 7 fm. These distances are more than twice the size of the core of the halo nucleus which is about 1.4-2.6 fm [35, 36, 37, 38], suggesting that the halo neutrons have a high probability to be located far from the core.

Close to the proton dripline, proton-halo nuclei, such as ^{8}B, have also been observed. However, due the additional Coulomb repulsion between the proton halo and the core, the formation of a proton halo is less probable than neutron halo and is favoured for nuclei with charge $Z < 10$ [39]. Fig. 1.1.1 displays the light region of the nuclear chart up to fluorine where most of the halo nuclei have been observed.

	S_n or S_{2n} [MeV]	r_n^{rms} or r_{2n}^{rms} [fm]	Refs.
$^{11}\text{Be} \equiv {}^{10}\text{Be} + n$	0.5016	5.77 ± 0.16	[35, 40]
$^{15}\text{C} \equiv {}^{14}\text{C} + n$	1.218	5.82 ± 0.6	[36, 41]
$^{6}\text{He} \equiv {}^{4}\text{He} + n + n$	0.973	5.9 ± 1.2	[37, 42]
$^{11}\text{Li} \equiv {}^{9}\text{Li} + n + n$	0.3691	6.6 ± 1.5	[37, 40]

Table 1.1: Neutron separation energies S_n or S_{2n}, the rms distances between the halo neutron with the core r_n^{rms} and between both halo neutrons r_{2n}^{rms} for archetypical one- and two-neutron halo nuclei, respectively.

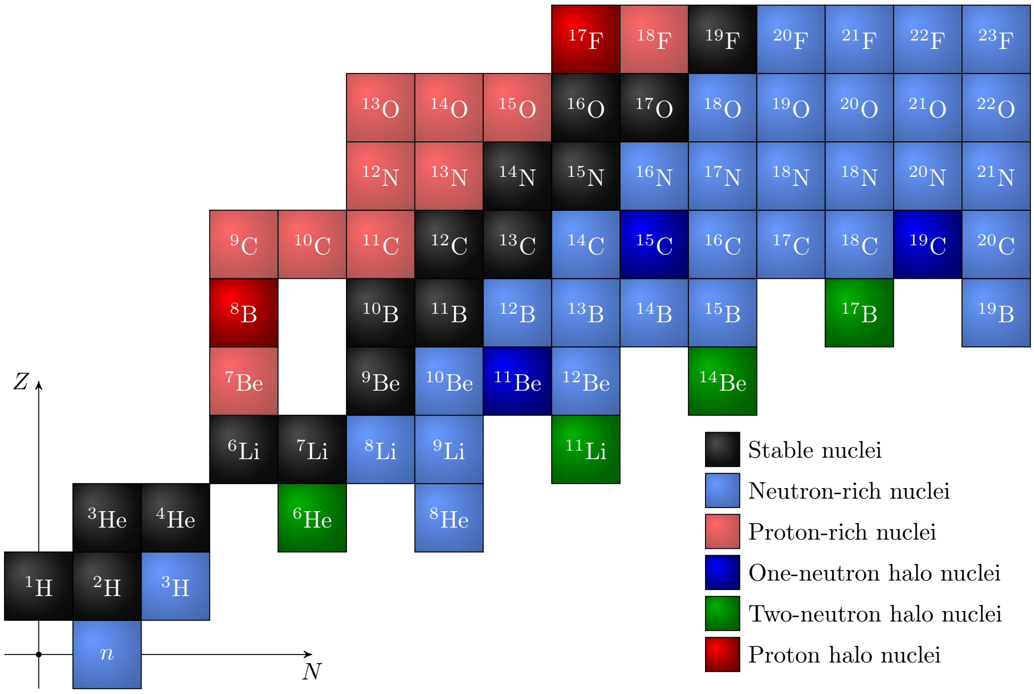

Figure 1.1.1: Light region of the nuclear chart where most halo nuclei are observed. Figure courtesy of Frederic Colomer.

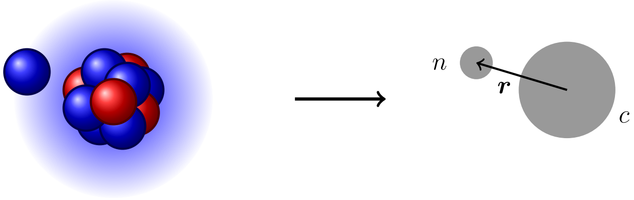

Figure 1.1.2: Simple two-body model of one-neutron halo nuclei.

1.1.2 Simple model of one-neutron halo nuclei

There is no clear definition of halo nuclei. However, it is common knowledge that halo nuclei are loosely bound, display a large spatial extension due to the fact that the halo neutrons have a high probability of presence outside the range of the nuclear potential, and exhibit a clear cluster structure [43]. I illustrate this definition in this section by modelling a one-neutron halo nucleus of mass number A with a simple two-body model.

Because the halo neutron has a high probability of presence far from the rest of the nucleons, the A-body problem can be seen as a two-cluster system, composed of a core c assumed in its ground state[1] and a valence neutron n. The wave function of the A-body system is therefore approximated by a two-body wave function describing the core-neutron relative motion. This simplification is represented in Fig. 1.1.2 and is called the single-particle approximation. The orbital angular momentum of the neutron in the ground state of the halo nucleus is denoted l, its spin s and its total angular momentum j, obtained from the coupling of l and s.

In this single-particle approximation, the core and the neutron are assumed structureless and their interaction is simulated through an effective central potential V_{lj} in the partial wave lj, which is adjusted to reproduce the one-neutron separation energy S_n of the ground state. In this simple model, the radial wave function u_{nlj} describing the core-neutron relative motion in the ground state is solution of the radial Schrödinger equation [44]

$$\left[-\frac{d^2}{dr^2}+\frac{l(l+1)}{r^2}+\frac{2\mu_{cn}}{\hbar^2}V_{lj}(r)\right]u_{nlj}(r)=-\kappa^2 u_{nlj}(r), \tag{1.1.1}$$

with $\boldsymbol{r}$ the core-neutron relative coordinate, $\kappa=\sqrt{2\mu_{cn}S_n/\hbar^2}$ and μ_{cn} the core-neutron reduced mass. The radial wave functions u_{nlj} are characterized by an additional quantum number n, which corresponds to their number of nodes. In this equation, we can note the presence of a repulsive term proportional to $l(l+1)$. The attractive effective potential combined with this repulsive term form the *centrifugal barrier*. This barriers tends to push the valence neutron close to the core and thus prevents the formation of a halo. Therefore, to ensure that the centrifugal barrier is not too large, the orbital angular momentum l of the ground state of a one-neutron halo nucleus is mostly 0 or 1 [39, 45, 46].

Since the valence neutron has a large probability of presence far from the core, the main properties of halo nuclei are influenced by the asymptotic part of the radial wave function. For a short-range interaction, such as the nuclear force, the radial wave function of the ground state behaves asymptotically [44]

$$u_{nlj}(r)\underset{r\to\infty}{\longrightarrow} b_{nlj}\,e^{-\kappa r}, \tag{1.1.2}$$

---

[1] As it will be explained in the next section, in an actual nucleus, different states of the core contribute to the halo-nucleus ground-state wave function.

where b_{nlj} is the single-particle asymptotic normalization constant (SPANC). This constant is linked to the probability of the valence neutron to be located far from the core. By approximating the wave function by its asymptotic behaviour, the root mean square core-neutron distance can be approached by [7]

$$\begin{aligned} r_n^{\mathrm{rms}} &\approx \sqrt{\frac{\int_0^{+\infty} dr\, r^2 \left|b_{nlj}\, e^{-\kappa r}\right|^2}{\int_0^{+\infty} dr\, \left|b_{nlj}\, e^{-\kappa r}\right|^2}} \qquad (1.1.3)\\ &= \sqrt{\frac{\hbar^2}{4\mu_{cn} S_n}}. \qquad (1.1.4) \end{aligned}$$

This simple model illustrates that the neutron is tunnelling into the classically-forbidden region, outside the potential range. Both the probability of finding a neutron outside this range and the root mean square core-neutron distance increase when the binding energy of the ground state decreases. Therefore, one-neutron halo nuclei are characterized by binding energies smaller than a few MeVs [39, 45, 46].

A similar picture can be used to describe two-neutrons halo nuclei, in which a three-cluster description of the nucleus is used, i.e., two valence neutrons and a core. Two criteria favouring the appearance of the halo can also be determined: the centrifugal repulsive term has to be small and the two-neutrons separation energy S_{2n} has to be lower than a few MeVs [39, 45, 46].

1.1.3 Single-particle approximation

In the previous section, I have considered an extreme version of the single-particle approximation, which assumes that the core of the one-neutron halo nucleus is in its ground state. In an actual nucleus, the configurations in which the core is in an excited state also contribute to the halo-nucleus ground state. To express these different configurations, I denote here the spins characterizing the states of the halo nucleus J and the core I_c with M, π and M_c, π_c the corresponding projections and parities. In general, a state $J^\pi M$ of a one-neutron halo nucleus can be described as a combination of configurations, in which the neutron is bound to the core, which is itself in a state $I_c^{\pi_c} M_c$. The A-body wave function $\psi_A^{J^\pi M}$ describing the state $J^\pi M$ can thus be expressed [47]

$$\psi_A^{J^\pi M}(\boldsymbol{r_1}, \cdots, \boldsymbol{r_{A-1}}, \boldsymbol{r}) = \sum_{I_c^{\pi_c}} \left[\chi_{A-1}^{I_c^{\pi_c} M_c}(\boldsymbol{r_1}, \cdots, \boldsymbol{r_{A-1}}) \otimes \Theta_{I_c^{\pi_c} M_c}^{J^\pi M}(\boldsymbol{r})\right]^{J^\pi M}, \qquad (1.1.5)$$

where $\boldsymbol{r_1}, \cdots \boldsymbol{r_{A-1}}$ are the coordinates of the $A-1$ nucleons composing the core, $\chi_{A-1}^{I_c^{\pi_c} M_c}$ is the core wave function in the state $I_c^{\pi_c} M_c$ and $\Theta_{I_c^{\pi_c} M_c}^{J^\pi M}$ is the c-n overlap wave function. These overlap functions are defined as [47]

$$\Theta_{I_c^{\pi_c} M_c}^{J^\pi M}(\boldsymbol{r}) = \int d\boldsymbol{r_1} \cdots d\boldsymbol{r_{A-1}} \left[\psi_A^{J^\pi M}(\boldsymbol{r_1}, \cdots, \boldsymbol{r_{A-1}}, \boldsymbol{r})\right]^* \chi_{A-1}^{I_c^{\pi_c} M_c}(\boldsymbol{r_1}, \cdots, \boldsymbol{r_{A-1}}), \qquad (1.1.6)$$

and are usually decomposed into their radial $\mathcal{U}_{lj}$ and angular parts [48]

$$\Theta_{I_c^{\pi_c} M_c}^{J^\pi M}(\boldsymbol{r}) = \sum_{ljm} \frac{1}{r} \mathcal{U}_{lj}(r) \left\langle \Omega_r | ljm \right\rangle, \qquad (1.1.7)$$

where Ω_r is the angular part of $\boldsymbol{r}$, l and j are respectively the orbital and total angular momenta of the neutron bound to the $I_c^{\pi_c} M_c$ core forming a $J^\pi M$ state of the halo nucleus and m is the projection of j. Similarly to the single-particle wave function (1.1.2), the radial overlap function is also characterized by an asymptotic normalization constant (ANC) [48]

$$\mathcal{U}_{lj}(r) \underset{r\to\infty}{\longrightarrow} \mathcal{C}_{lj}\, e^{-\kappa r}. \tag{1.1.8}$$

It is common in reaction theory to approximate the overlap wave function by a normalized single-particle wave function obtained from an effective potential V_{lj}, i.e., $\mathcal{U}_{lj} \approx u_{nlj}$ [see Eq. (1.1.1)]. In this single-particle view, the A-body wave function is approximated by [49]

$$\psi_A^{J^\pi M}(\boldsymbol{r_1},\cdots,\boldsymbol{r_{A-1}},\boldsymbol{r}) \approx \sum_{I_c^{\pi_c} lj} \sqrt{S_{lj}^{J^\pi I_c^{\pi_c}}} \left[\chi_{A-1}^{I_c^{\pi_c} M_c}(\boldsymbol{r_1},\cdots,\boldsymbol{r_{A-1}}) \otimes \frac{1}{r} u_{nlj}(r)\, \langle \Omega_r | ljm\rangle \right]^{J^\pi M}, \tag{1.1.9}$$

where $S_{lj}^{J^\pi I_c^{\pi_c}}$ are the so-called spectroscopic factors. These factors can be interpreted as the probability of finding the halo neutron bound to the $I_c^{\pi_c}$ core in a lj orbital. They are obtained from structure calculations through [47]

$$S_{lj}^{J^\pi I_c^{\pi_c}} = \int dr\, |\mathcal{U}_{lj}(r)|^2 \,. \tag{1.1.10}$$

Within this approximation, one can relate the SPANC b_{nlj} (1.1.2) to the projectile ANC $\mathcal{C}_{lj}$ (1.1.8) through [48]

$$\mathcal{C}_{lj} = \sqrt{S_{lj}^{J^\pi I_c^{\pi_c}}}\, b_{nlj}. \tag{1.1.11}$$

When $S_{lj}^{J^\pi I_c^{\pi_c}} = 1$, the projectile is described by only one single-particle state and the asymptotic normalization constants are equal.

As it will be explained in the following of this Chapter, the spectroscopic factors are often inferred from experimental data using the single-particle approximation (1.1.9) and compared to theoretical predictions from nuclear-structure models. However, one should keep in mind that these factors are model-dependent [50]. Indeed, the probability of an orbital occupancy depends on the effective nucleon-nucleon potential used to solve the A-body Schrödinger equation.

1.1.4 Description of ^{11}Be

Because all the calculations in this thesis are made for ^{11}Be, I discuss here in more details its structure. Being a one-neutron halo nucleus, ^{11}Be is often seen as a ^{10}Be compact core to which a halo neutron is loosely bound. Besides its halo structure, this nucleus also exhibits an anomalous order of states compared to the one predicted by a simple shell model reasoning. In an extreme shell model view, ^{10}Be has a 0^+ ground state since its neutrons fill the shells up to $p3/2$, the halo neutron occupies the $p1/2$ shell and ^{11}Be has a $1/2^-$ ground state. This prediction is not verified by experiments which find a $1/2^+$ ground state, indicating that an s halo neutron is coupled to the 0^+ ground state of ^{10}Be. As we can see on the spectrum of ^{11}Be in the column "Exp." in Fig. 1.1.3, the $1/2^-$ state exists but is at slightly higher energy than the $1/2^+$. The unexpected order of these two states is called the *parity inversion* [38].

Interestingly, recent *ab initio* calculations [51] have been able to reproduce the parity inversion of ^{11}Be. This structure model is called *ab initio* referring to the fact that its

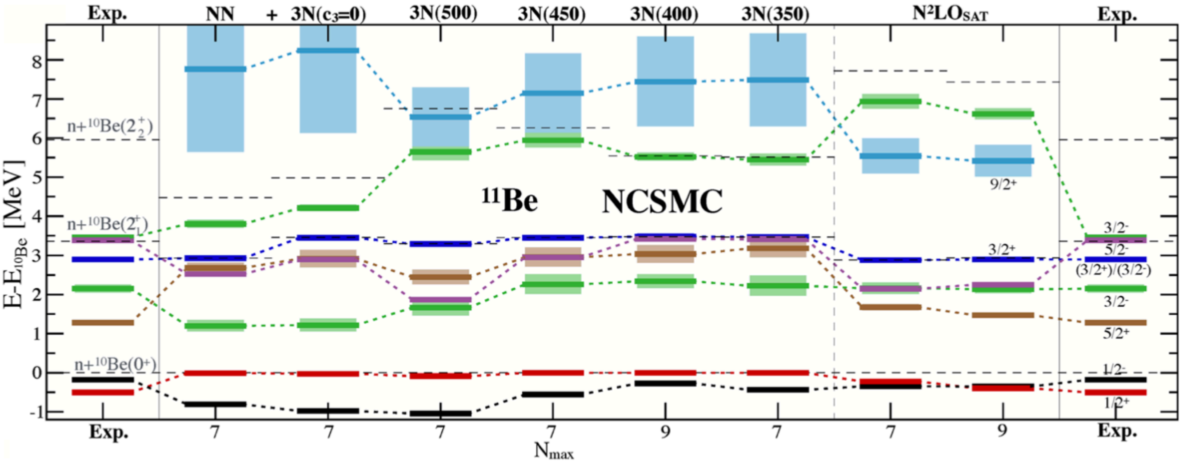

Figure 1.1.3: Spectrum of ^{11}Be relatively to the ^{10}Be-n separation threshold, obtained with the no-core shell model with continuum and various chiral nuclear forces. The light boxes correspond to the resonance widths. The extreme left and right columns are the experimental values. This figure is taken from Ref. [51].

building blocks are each individual nucleon and its only input is a realistic nucleon-nucleon interaction. Calci *et al.* have shown in Ref. [51] that the parity inversion can be obtained with the no-core shell model with continuum [52] (NCSMC) for the chiral nuclear force denoted N2LO$_{\rm SAT}$ (see Fig. 1.1.3). They have found that the $1/2^+$ ground state of ^{11}Be is dominated by the single-particle component $0^+ \otimes s1/2$ with a spectroscopic factor $S^{1/2^+0^+}_{s1/2} = 0.9$ and has a small $2^+ \otimes d5/2$ admixture characterized by $S^{1/2^+2^+}_{d5/2} = 0.16$. They have also estimated the ANC of the $0^+ \otimes s1/2$ halo configuration to be $\mathcal{C}_{s1/2} = 0.786$ fm^{-1}.

Their analysis emphasizes that the ^{10}Be-n continuum of states, describing the states where the halo neutron is unbound to the core, influences greatly the properties of the bound states. Moreover, the order of these states is highly sensitive to the choice of the nucleon-nucleon force (see the results for different nuclear forces in the columns of Fig. 1.1.3). They also note that the parity inversion can be obtained only when the three-nucleons force is included in their model. This confirms that the parity inversion results from a many-body effect, as already proven in previous works (see the discussion in Sec. 13.6 of Ref. [38]).

Fig. 1.1.3 also shows the ^{10}Be-n resonant states, located above the ^{10}Be-n separation threshold. Interestingly, the NCSMC calculation with N2LO$_{\rm SAT}$ also reproduces fairly well the resonant part of the ^{11}Be spectrum. In particular, Calci *et al.* predict that the $5/2^+$ and $3/2^+$ resonant states have strong single-particle components [51]. These resonances therefore influence the ^{10}Be-n relative motion and impact the breakup cross sections, as it will be discussed further in this Chapter. These states are respectively located at 1.28 MeV and at 2.86 MeV and characterized by the widths $\Gamma_{5/2^+} = 100$ keV and $\Gamma_{3/2^+} = 122$ keV [40].

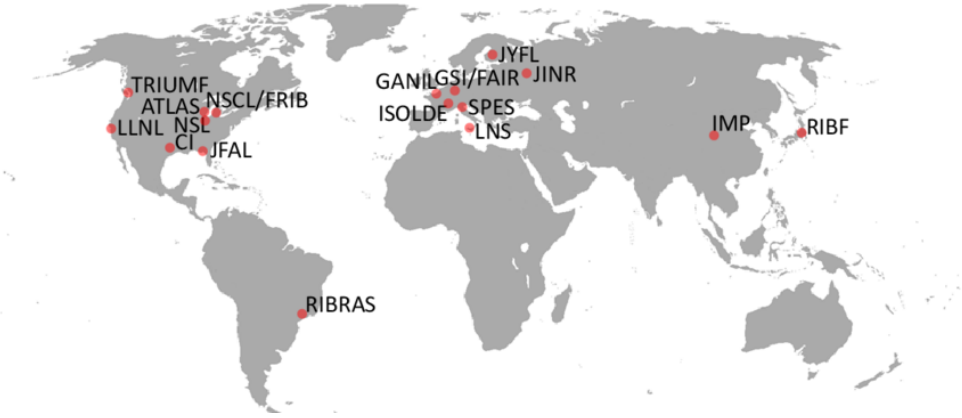

Figure 1.2.1: Radioactive-ion beam facilities in the world. This figure is taken from Ref. [54].

1.2 Experimental probes

1.2.1 Experimental facilities

Because halo nuclei are located far from the valley of stability, they are very short lived. For example the half-lifetime of ^{11}Be is about 13.8 s and the one of ^{11}Li about 8.7 ms. Their direct study through usual spectroscopic techniques, where they would constitute a fixed target, is therefore not possible. They are thus often probed through indirect techniques, such as reactions in which the exotic nuclei are the projectiles.

There are two main methods used to generate these exotic beams. The in-flight separation technique [53] relies on a heavy-ion primary beam at high energy impinging on a light target. The isotopes of the secondary beam is produced through the fission and the fragmentation of the primary beam and are selected with magnetic rigidity. Because the secondary beam retains 90% or more of the kinetic energy of the primary beam, this method is well suited to provide exotic beams at high energies (between $50A$ and $1500A$ MeV) [53]. Different facilities such as NSCL and the future FRIB in the USA, RIKEN in Japan, GSI in Germany and GANIL in France apply this technique (see map in Fig. 1.2.1).

The second method is the isotope separation on-line [55] (ISOL) which uses light-ion or neutron beams impinging on a thick target often composed of heavy elements. Two reactions, the fission and spallation, occur in the target. The reaction products are thermalized inside the target and diffuse out to an ion source. After being ionized, the isotopes are selected with magnetic rigidity and reaccelerated at energies up to around $10A$ MeV [55]. The ISOL method is applied in different facilities such as CERN in Switzerland and at TRIUMF in Canada (see map in Fig. 1.2.1).

I present in the next sections different observables that are used to study the halo structure. After briefly reviewing the interaction cross sections, the magnetic dipole and electric quadrupole moments, I discuss the elastic and inelastic scatterings, the diffractive-breakup and knockout cross sections, since these are the reaction channels I study in this thesis.

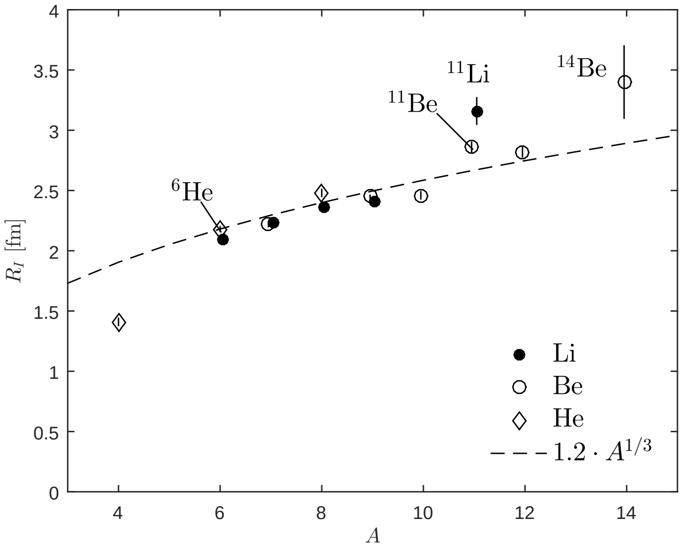

Figure 1.2.2: Interaction radii for He, Li and Be isotopes as a function of their mass numbers. The data are taken from Refs. [32, 56]. Figure courtesy of Frederic Colomer.

1.2.2 Interaction cross sections

Historically, the first experimental probe of halo nuclei is the interaction cross section. Tanihata *et al.* [32, 33] measured these observables for various He, Li and Be isotopes. This cross section is defined as the total cross section in which the projectile number of nucleons changes. Using a simple geometrical model where both the projectile and the target are seen as hard spheres, the interaction cross section σ_I can be written as [33]

$$\sigma_I = \pi(R_{I,P} + R_{I,T})^2, \tag{1.2.1}$$

where $R_{I,P}$ and $R_{I,T}$ are respectively the projectile and the target interaction radii. Since the interaction radius of the projectile does not vary much for different targets [32, 33], it can be extracted from measurements using various targets.

The interaction radii are somehow related to the size of the nucleus since a larger spatial extension would lead to a larger interaction cross section. In stable nuclei, the nuclear density inside the nucleus is rather constant for different number of mass A, suggesting that each nucleon occupies the same volume in the nucleus. This leads to the semiclassical liquid-drop model which sees the nucleus as a quantum droplet of radius [57]

$$R = r_0 A^{1/3} \tag{1.2.2}$$

where $r_0 \sim 1.2 - 1.4$ fm describes the space that the nucleon takes inside the nucleus.

Fig. 1.2.2 displays the interaction radii of He, Li and Be isotopes as a function of their mass number. We can see that most of the stable nuclei follow roughly the law in $1.2A^{1/3}$ fm, and therefore are well described by the semiclassical liquid-drop model. However, ^{11}Be, ^{11}Li and ^{14}Be deviate from this law and exhibit larger interaction radii. This enhancement can be caused by a large size and/or a strong deformation of the nucleus. Further analyses [56] have shown that these large interaction radii are due to long tail of the nuclear density, which is now understood as the halo structure [7]. Note that even if the interaction radius of ^{6}He does not deviate strongly from the $1.2A^{1/3}$ law, it is surprisingly large compared to the one of ^{4}He.

	μ [μ_N]	Q [mb]
^{9}Li	3.4391 ± 0.00006	-27.4 ± 1.0
^{11}Li	3.6678 ± 0.0025	-31.2 ± 4.5

Table 1.2: Magnetic dipole (μ) and electric quadrupole (Q) moments of ^{9}Li and ^{11}Li. The values are taken from Refs. [58, 59, 60] and are respectively expressed in nuclear magneton μ_N and in mb.

1.2.3 Magnetic dipole and electric quadrupole moments

We have just seen that the large interaction radii of halo nuclei are caused by a long tail of the density. To study separately the distribution of protons inside the nucleus, it is useful to analyse the magnetic dipole (μ) and electric quadrupole (Q) moments. These observables are mainly sensitive to the distribution of protons inside the nucleus.

A series of experiments [58, 59, 60] have shown that both moments are rather constant for ^{9}Li and ^{11}Li isotopes. Their results are summarized in Table 1.2. This indicates that the distribution of protons is similar in both nuclei, which is consistent with the picture of ^{11}Li seen as a ^{9}Li core to which two neutrons are loosely bound.

1.2.4 Elastic- and inelastic-scattering cross sections

The elastic-scattering process corresponds to the deflection of a projectile by a target, in which both nuclei stay in their ground states. Because all the results in this thesis are obtained with ^{11}Be, I illustrate the effect of the halo on elastic-scattering cross sections of ^{11}Be. Fig. 1.2.3 displays the experimental elastic-scattering cross sections of ^{9}Be (red triangles), ^{10}Be (blue diamonds), and ^{11}Be (black squares) off a ^{64}Zn target at 24.5 MeV as a function of the deflection angle θ [61]. The ^{9}Be cross section has been measured in Catania, and the experiments on ^{10}Be and ^{11}Be have been conducted at REX-ISOLDE at CERN.

While the elastic-scattering cross sections of ^{9}Be and ^{10}Be are similar, the one of ^{11}Be strongly differs from them. Indeed, the angular distribution does not exhibit a peak at $\theta \sim 40°$ as in the cases of ^{9}Be and ^{10}Be and the total cross section is smaller. Di Pietro *et al.* have shown that this reduction is caused by an enhancement of the transfer and the breakup channels of ^{11}Be [62]. Because these two reactions are peripheral, i.e., they are mostly sensitive to the tail of the ground-state wave function of the projectile, this indicates that ^{11}Be has an anomalous large spatial extension compared to ^{9}Be and ^{10}Be. This is consistent with the halo structure of ^{11}Be.

In the inelastic scattering, the projectile or/and the target are in their excited states. For example, the inelastic-scattering reaction

$$^{11}\mathrm{Be} + {}^{208}\mathrm{Pb} \rightarrow {}^{11}\mathrm{Be}^{*} + {}^{208}\mathrm{Pb} \quad \text{at } 64A \text{ MeV}, \tag{1.2.3}$$

was measured at RIKEN [63]. In this reaction, ^{11}Be is first in its $1/2^+$ ground state and is excited to $1/2^-$ bound state. From this measurement, they could extract the E1 strength for the Coulomb excitation from the $1/2^+$ ground state to the $1/2^-$ excited state of ^{11}Be.

In this thesis, I analyse elastic-scattering observables of ^{11}Be in the study of the extension of the range of validity of the eikonal model down to low energies in Chapter 3. The accuracy of each correction is evaluated by comparing these cross sections. I also examine the impact of the inelastic-scattering strength onto the diffractive-breakup channel of ^{11}Be in Chapter 5.

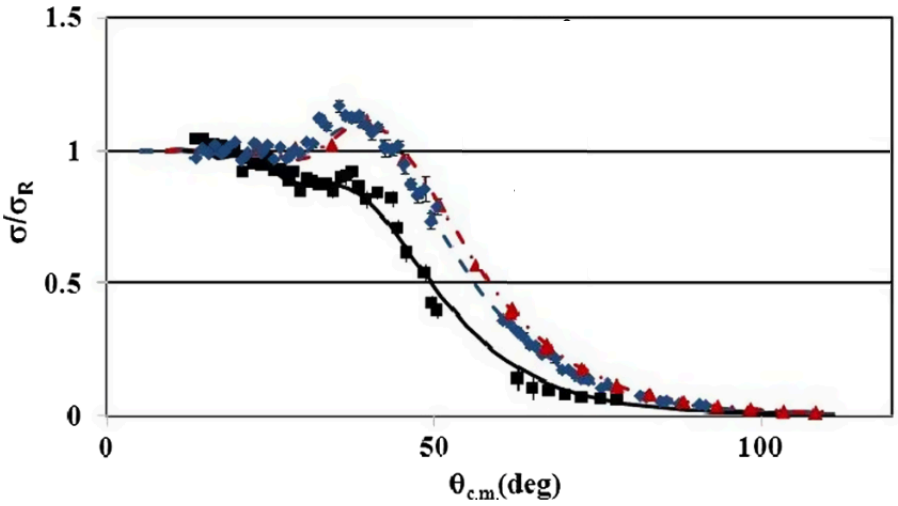

Figure 1.2.3: Elastic-scattering cross sections of ^{9}Be (red triangles), ^{10}Be (blue diamonds), and ^{11}Be (black squares) off ^{64}Zn target at 24.5 MeV. This figure is taken from Ref. [61].

1.2.5 Diffractive breakup

Breakup reactions of halo nuclei correspond to the dissociation of the halo from the core, and hence reveal the cluster structure inside the nucleus. Because halo nuclei are loosely bound, the probability that the halo neutron dissociates from the core is large. Accordingly, breakup cross sections have high statistics. In diffractive-breakup—also referred as exclusive breakup—reactions, both the halo neutron and the core are detected in coincidence after the dissociation [35, 64]. Their observables usually depend on the core-neutron relative physical quantity. In particular, an interesting observable is the breakup distribution as a function of the core-neutron relative energy after dissociation. Fig. 1.2.4 shows the experimental diffractive-breakup cross section of ^{11}Be with (a) ^{208}Pb at 69A MeV and (b) ^{12}C at 67A MeV as a function of the relative ^{10}Be-n energy after dissociation. These reactions have been measured at RIKEN [35, 65]. The collision on a lead target is dominated by the Coulomb interaction, and thus by electric transitions. This implies that the cross section is particularly large because the strengths of the electric transitions Eλ depend on r^{λ} and are thus enhanced by the halo structure. Moreover, the breakup cross section of ^{11}Be with lead is strongly related to the energy distribution of the E1 strength from the ground state to the ^{10}Be-n continuum [10, 35, 66, 67]. This is particularly true for the very forward angles since they exclude most of the higher-order Coulomb and nuclear-induced transitions [35, 66, 68, 69]. This can be understood in a semiclassical view by the fact that forward angles correspond to large impact parameters and are therefore mainly influenced by the Coulomb interaction.

At forward angles, the breakup distribution after the collision on a carbon target has a similar shape as the one after the breakup on lead. As just seen, this is explained by the fact that the Coulomb interaction dominates in this angular range. Nevertheless, the statistics are smaller since the Coulomb interaction is minor on a light nucleus. On the contrary, for a larger angular cutoff, the shape of the breakup distribution obtained with a carbon target strongly differs from the one with a lead target, suggesting that other reaction mechanisms take place in this nuclear-dominated reaction. In particular, there are two peaks at $E_{\text{rel}} = 1.28$ MeV and 2.86 MeV. These peaks are located at the

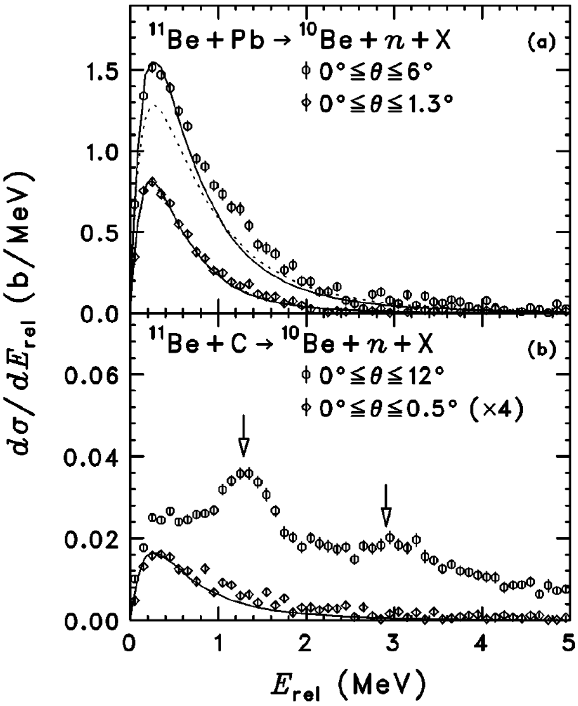

Figure 1.2.4: Relative ^{10}Be-n energy distribution after the diffractive breakup of ^{11}Be with (a) ^{208}Pb at 69A MeV and (b) ^{12}C at 67A MeV. The open circles correspond to data for the whole acceptance region [up to (a) 6° and (b) 12°] and the open diamonds to data for the selected forward angles [up to (a) 1.3° and (b) 0.5°]. This figure is taken from Ref. [35].

energy of the resonant states $5/2^+$ and $3/2^+$ (see the spectrum of ^{11}Be in Fig 1.1.3). The widths of the peaks are of the order of the widths of the resonances $\Gamma_{5/2^+} = 100$ keV and $\Gamma_{3/2^+} = 122$ keV [40]. These two peaks are less visible in the Coulomb-dominated breakup distribution, because the $5/2^+$ and $3/2^+$ states cannot be reached by direct E1 transitions from the initial s ground state. In the collision with a carbon target, nuclear-induced transitions populate these resonant states because they have a large single-particle component.

Besides carrying information on the cluster structure inside the nucleus and the E1 strength function, Coulomb-dominated energy distributions are also used to infer radiative capture rates that are of astrophysical interest [70, 71]. Indeed, if the Coulomb breakup of two- or three-cluster nuclei is seen as resulting from an exchange of virtual photons between the projectile and the target, it can be seen as the time-reversed reaction of the radiative capture. Further studies [66, 67, 68, 69, 72, 73, 74] have shown that to extract accurate capture rates and E1 strength functions, the interferences between the Coulomb and nuclear interactions should be well accounted for.

These diffractive-breakup energy distributions are analysed in Chapters 3, 4 and 5. In Chapter 3, I assess the accuracy of the corrections to the eikonal approximation by studying the energy distribution after the diffractive breakup of ^{11}Be on a carbon target at 20A and 10A MeV. I also analyse how the dynamical correction to the eikonal approximation developed in Chapter 4 reproduces the diffractive-breakup energy distributions of ^{11}Be measured at RIKEN. In the last Chapter, I study the influence of a resonance $5/2^+$ on the energy distribution following the diffractive breakup of ^{11}Be with ^{9}Be at 60A MeV.

1.2.6 Knockout cross sections

Knockout reactions of one-neutron halo nuclei correspond also to the dissociation of the halo from the core but contrary to the diffractive breakup only the remaining core of the halo nucleus is detected after the dissociation [9, 75, 76, 77, 78]. These so-called inclusive reactions exhibit much higher statistics since the neutron is not measured. Hence they are often favoured for the low intensities available at radioactive-ion beam facilities. Knockout reactions are usually performed at high energy (between $50A$ MeV and $100A$ MeV) on light targets. Typical observables are the parallel- and transverse-momentum distributions of the remaining core [79].

If the reaction occurs at high-enough energy, the adiabatic approximation, which sees the internal coordinates of the projectile as frozen during the collision, can safely be made. Indeed, at high energy, the collision time is brief and the nucleons inside the projectile do not have the time to rearrange. In this view, the momentum distribution of the remaining core after the reaction is the same as the one that the core had inside the projectile prior to the collision. According to the Heisenberg principle, a larger spatial extension of the nucleus is associated with a narrow momentum distribution. These observables therefore provide information on the core-neutron spatial distribution within the projectile and should be surprisingly narrow for spatially-extended nuclei, such as halo nuclei.

The first measurement of momentum distribution of ^{9}Li after the dissociation of ^{11}Li was made by Kobayashi *et al.* [80]. The authors have noted that both the transverse- and parallel-momentum distributions of the core were particularly narrow, confirming that ^{11}Li has a large root mean square radius and exhibits a halo structure. A few years later, it was shown in Ref. [81] that the transverse-momentum distribution is more sensitive to the reaction mechanisms than the parallel-momentum distribution. The authors of Ref. [81] have also emphasized that the shape of the parallel-momentum distribution is rather insensitive to the projectile-target interaction, confirming that this observable is a reasonable probe of the projectile ground-state wave function.

Following the experiment of Kobayashi *et al.*, a series of measurements have been done on various exotic nuclei. Fig. 1.2.5 displays the parallel-momentum distribution of the remaining core after the one-neutron knockout on a carbon target of isotopes in the light sector of the nuclear chart. These measurements have been performed at GANIL [75]. We can directly note that the distributions are narrower, when $N = 8$ and $N = 14$ are crossed. These neutron numbers are associated with the filling of the p shell and the $d5/2$ sub-shell. Such distributions bare therefore signs of shell structure. Moreover, ^{14}B and ^{15}C have an enhanced one-neutron knockout cross sections, suggesting that these two isotopes are particularly loosely bound and may exhibit a halo structure.

Because these distributions are sensitive to the ground-state wave function, these observables can also be used as spectroscopic tool. This is illustrated in Fig. 1.2.6, which displays the parallel-momentum distribution of ^{10}Be in its 0^{+} ground state after the one-neutron knockout of ^{11}Be with ^{12}C at $60A$ MeV. This experiment was measured at the NSCL [76]. The curves are obtained within the eikonal model of reaction assuming different orbital angular momenta l of the neutron. The theoretical calculations assuming that the halo neutron is in an s wave are in good agreement with the experimental data. This confirms the parity inversion of ^{11}Be discussed previously.

As explained in Sec. 1.1.3, in an actual nucleus, several configurations contribute to each state. In the analysis of knockout reactions, it is common to use the spectator core model which approximates the theoretical cross sections $\sigma_{\rm th}^{J^\pi I_c^{\pi_c}}$ for a one-neutron removal

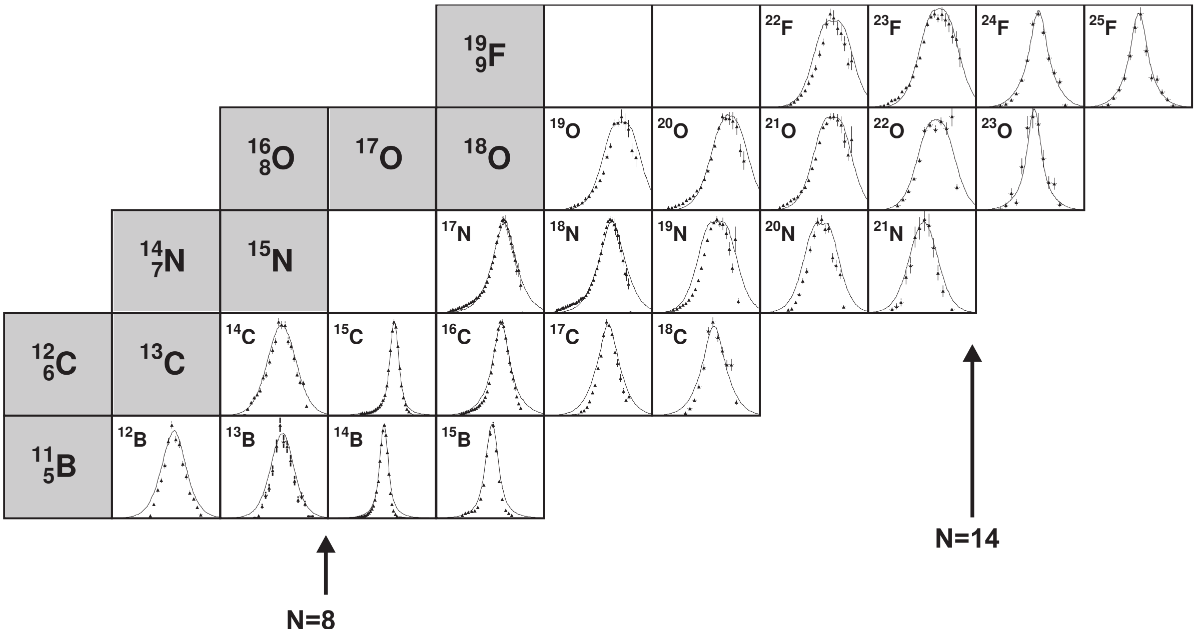

Figure 1.2.5: Parallel-momentum distribution of the remaining core after the one-neutron knockout of various isotopes on a carbon target. This figure is taken from Ref. [75].

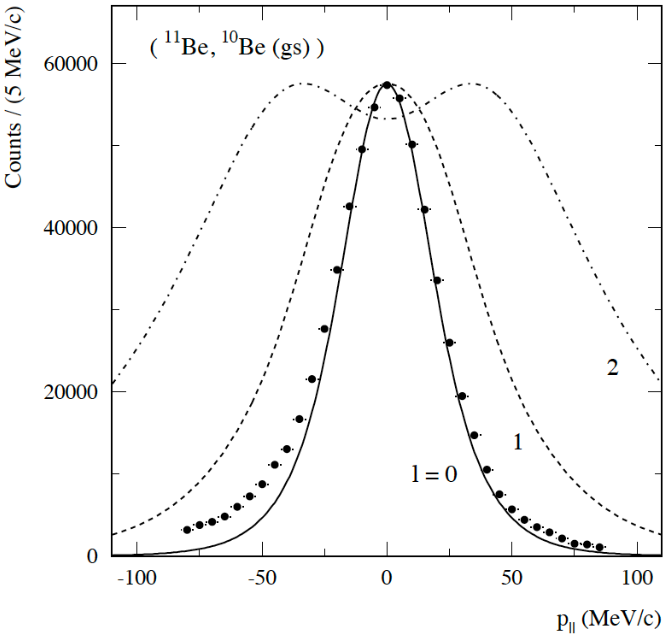

Figure 1.2.6: Parallel-momentum distribution of ^{10}Be after the one-neutron knockout of ^{11}Be with ^{12}C at 60A MeV. Only the cross section leading to the ground state of ^{10}Be is shown. The curves are calculations assuming that the halo neutron in a s, p or d orbital. This figure is taken from Ref. [76].

from the initial state J^π of the halo nucleus to a final state $I_c^{\pi_c}$ of the core by [9, 82]

$$\sigma_{\text{th}}^{J^\pi I_c^{\pi_c}} = \sum_{lj} S_{lj}^{J^\pi I_c^{\pi_c}} \sigma_{sp}(lj), \tag{1.2.4}$$

where σ_{sp} are the cross sections calculated assuming a normalized single-particle wave function describing the neutron bound to the core in the lj orbital. Al-Khalili has studied in Ref. [83] the deviations from such an approximation by allowing couplings between different single-particle states. He has shown that these couplings enhances the knockout cross sections of ^{11}Be by less than 9% and decreases ^{15}C cross sections by less than 6%. Because these deviations are relatively small, the spectator model (1.2.4) seems to be reliable, at least for loosely-bound nuclei.

Using this spectator view, Aumann *et al.* have conducted an analysis of the distribution of ^{10}Be in its 0^+ and 2^+ states after the neutron is knocked out. They deduce that the $1/2^+$ ground state of ^{11}Be is dominated by the single-particle component $0^+ \otimes s1/2$ with a small $2^+ \otimes d5/2$ admixture [76]. They have also evaluated the total theoretical cross section σ_{th} with [9, 82]

$$\sigma_{\text{th}} = \sum_{I_c^{\pi_c}} \sigma_{\text{th}}^{J^\pi I_c^{\pi_c}}, \tag{1.2.5}$$

where $\sigma_{\text{th}}^{J^\pi I_c^{\pi_c}}$ (1.2.4) are obtained with the eikonal model of reaction and the spectroscopic factors are predicted by shell model calculations. They have shown that this value is in good agreement with the experimental data.

In Refs. [26, 27], Gade *et al.* have analysed for various nuclei the agreement between knockout experimental data and the theoretical predictions obtained with the eikonal model of reaction and the shell-model spectroscopic factors. Their systematic study is made for both neutron- and proton-removal of loosely- and deeply-bound nucleons. They have studied the ratio $R_s = \sigma_{\text{exp}}/\sigma_{\text{th}}$, called the *quenching factor*, between the experimental cross section σ_{exp} summed over all final states of the core $I_c^{\pi_c}$ and the corresponding theoretical prediction σ_{th} (1.2.5). Assuming that the reaction model used for the analysis is accurate, this factor should therefore indicate deviations from shell-model predictions of the spectroscopic factor. In Fig. 1.2.7, Gade *et al.* plot the quenching factor inferred from a one-neutron (red) [resp. one-proton (blue)] knockout as a function of the difference ΔS of the neutron [resp. proton] and proton [resp. neutron] separation energies, i.e, $\Delta S = S_n - S_p$ for one-neutron knockout experiments and $\Delta S = S_p - S_n$ for one-proton knockout experiments. Because the asymmetry of the number of protons and neutrons inside the nucleus is closely related to the separation energies, the nuclei located further from $\Delta S = 0$ are more asymmetric. As illustrated in Fig. 1.2.7 and noted by Gade *et al.*, the quenching factor is strongly dependent on the asymmetry of the studied nucleus [26, 27].

The fact that the quenching factor is smaller than 1 is not surprising. Analyses of other reactions, such as quasi-elastic electron scattering $(e,e'p)$ [84, 85], $(p,2p)$ and (p,pn) reactions at $350A$-$400A$ MeV [86] and transfer reactions around $10A$-$30A$ MeV [28, 29, 87], also predict a quenching factor around 0.6. The reduction of the quenching factor is associated to the lack of nucleon-nucleon correlations within the shell model, which thus tends to overestimate the single-particle orbital occupancy. However, the strong dependence of the quenching factor on the asymmetry of the nucleus inferred from knockout data has not been observed in the analyses of the other experiments [28, 86]. Part of this asymmetry dependence might also be explained by the lack of nucleon-nucleon correlations within the shell model. Indeed, if the shell model misses more correlations for deeply-bound than loosely-bound nucleons, the deviations from the shell model should be greater for

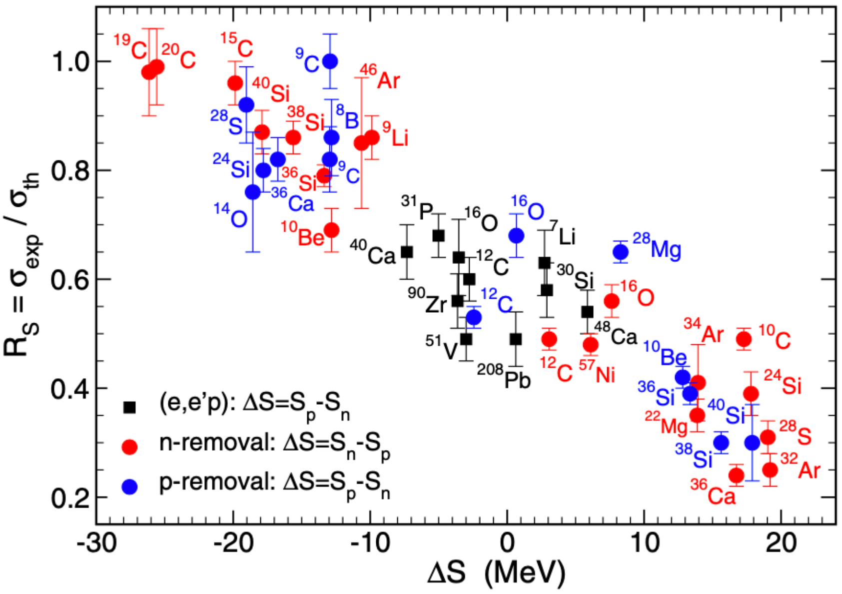

Figure 1.2.7: Quenching factors obtained from various knockout reactions as a function of the parameter ΔS, used as a measure of the asymmetry of the number of neutron and proton. The red data points are inferred from one-neutron knockout reaction and the blue points from the one-proton knockout. The black squares are deduced from quasi-elastic electron scattering $(e,e'p)$ [84, 85]. This figure is taken from Ref. [26]

the knockout of a deeply-bound than a loosely-bound nucleon. A recent study [88] on neutron-rich oxygen isotopes goes in that direction: it shows that when nucleon-nucleon correlations are included, the spectroscopic strengths decrease for a larger separation energy of the nucleon. However, it is not clear why such a reduction is not observed in other reaction observables. Another recent study [89] also points out that the model of reaction might also be at stake. In particular, the adiabatic treatment of the reaction would not be appropriate for reactions involving deeply-bound nuclei with beam energies smaller than 80A MeV.

Knockout cross sections are powerful probes of nuclei, since they carry information about the size of the nucleus and can be used as a spectroscopic tool. Unfortunately, the discrepancy with shell model predictions is still not well understood. The slope in Fig. 1.2.7 is still the object of numerous theoretical studies nowadays. In this thesis, I will try to understand the upper left corner of the Fig. 1.2.7, i.e, why theoretical predictions and experimental data agree well for loosely-bound nuclei. To do so, I analyse the sensitivity of knockout cross sections of one-neutron halo nuclei to the description of the projectile nuclear structure in Chapter 5. I also analyse the influence of dynamical effects on parallel-momentum observables in Chapter 4.

Chapter 2

Nuclear reaction theory

This thesis focuses on collisions involving a one-neutron halo nucleus with a target, and more particularly on the elastic-scattering, breakup and knockout channels. Since one-neutron halo nuclei exhibit a clear clusterized structure (see Chapter 1), they are often modelled as two-body objects and their collision as a three-body problem [11]. Because solving this system exactly can be heavy from a computational viewpoint, many approximations have been developed [11]. The aim of this Chapter is to summarize the models used in this thesis and their ranges of validity. To understand the three-body problem, notions of reaction theory are needed. The first section thus focuses on simpler two-body collisions [44]. By describing the collision of two nuclei as two- or three-body problems, some reaction channels are neglected. The optical model accounts for these channels through the use of complex potentials and is exposed in the second section. Finally, in the third section, the exact solutions of the three-body problem and some approximations are presented.

2.1 Two-body scattering

I consider a projectile P, of mass m_P and charge Z_Pe, impinging on a target T, of mass m_T and charge Z_Te. I assume both nuclei to be structureless and spinless, and their interaction to be modelled by a central potential V. In the center-of-mass rest frame[1], their relative motion is described by the solution Ψ of the following stationary Schrödinger equation [44]

$$\left[\frac{\boldsymbol{p}^2}{2\mu} + V(r)\right] \Psi(\boldsymbol{r}) = E\ \Psi(\boldsymbol{r}), \tag{2.1.1}$$

where $\boldsymbol{r}$ is the P-T relative coordinate, $\boldsymbol{p}$ the corresponding momentum, E the total energy in this rest frame and

$$\mu = \frac{m_P m_T}{m_P + m_T} \tag{2.1.2}$$

is the P-T reduced mass.

I consider first[2] only the nuclear interaction simulated by a nuclear potential V_N, i.e, $V = V_N$ in Eq. (2.1.1), which respects [44]

$$\lim_{r\to\infty} r^2 V_N(r) = 0. \tag{2.1.3}$$

---

[1] See the removal of the center-of-mass motion in Appendix 10A of Ref. [90].

[2] The treatment of the Coulomb interaction will be introduced further in the Chapter.

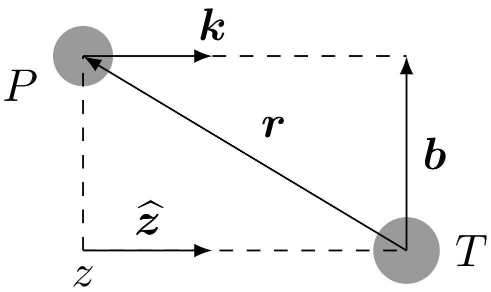

Figure 2.1.1: Coordinate system: the projectile-target relative coordinate $\boldsymbol{r}$ is expanded in its transverse $\boldsymbol{b}$ and longitudinal z components.

I am interested in the stationary scattering states, associated with positive-energy solutions $E = \hbar^2k^2/(2\mu)$ of Eq. (2.1.1). These solutions are characterized by the initial wave vector $\boldsymbol{k}$ and behave asymptotically as [44]

$$\Psi_{\boldsymbol{k}}(\boldsymbol{r}) \underset{r\to\infty}{\longrightarrow} e^{i\boldsymbol{kr}} + f_{\boldsymbol{k}}(\Omega)\frac{e^{ikr}}{r} \tag{2.1.4}$$

where Ω is the angle between the initial $\boldsymbol{k}$ and final $\boldsymbol{k}'$ momenta. The equation (2.1.4) can be seen as the superposition of a free "incoming" plane wave and a "outgoing" scattered wave. The amplitude of the scattered wave deflected to an angle Ω is given by the function $f_{\boldsymbol{k}}$, called the *scattering amplitude*. All the dependency on the potential is contained into this scattering amplitude: if there is no potential, the solutions are plane waves and the scattering amplitude is nil [44]. We can also note that the scattered wave has the same wave number as the incident wave, i.e., $|\boldsymbol{k}'| = |\boldsymbol{k}| = k$. It results from the fact that I study here elastic scattering and thus the total kinetic energy is conserved.

I consider in the following developments that the projectile propagates towards the target with the momentum $\hbar\boldsymbol{k} = \hbar k\hat{\boldsymbol{z}}$ and velocity $v = \hbar k/\mu$, where I choose the z-axis along the incoming beam (see the coordinate system in Fig. 2.1.1). Moreover, since the potential is assumed to be central, the dependency of the scattering amplitude on the azimuthal angle can be removed. Accordingly, the solutions (2.1.4) become

$$\Psi_{\boldsymbol{k}}(\boldsymbol{r}) \underset{r\to\infty}{\longrightarrow} e^{ikz} + f_{\boldsymbol{k}}(\theta)\frac{e^{ikr}}{r}, \tag{2.1.5}$$

where θ is the angle between $\hat{\boldsymbol{z}}$ and the direction of propagation of the scattered wave $\hat{\boldsymbol{k}}'$.

The scattering amplitude $f_{\boldsymbol{k}}$ can be computed as [90, 91]

$$\begin{aligned} f_{\boldsymbol{k}}(\theta) &= \frac{1}{2\pi}\frac{\mu}{\hbar^2}\left\langle e^{i\boldsymbol{k}'\boldsymbol{r}}\middle| V_N \middle| \Psi_{\boldsymbol{k}}\right\rangle & (2.1.6)\\ &= \frac{1}{2\pi}\frac{\mu}{\hbar^2}T_{fi}(\theta), & (2.1.7)\end{aligned}$$

where the T-matrix elements T_{fi} are defined.

The elastic scattering cross section is directly obtained from the square modulus of this amplitude [44]

$$\frac{d\sigma}{d\theta} = |f_{\boldsymbol{k}}(\theta)|^2. \tag{2.1.8}$$

In the following, I present an exact method to compute this scattering amplitude—called the partial-wave expansion—and the eikonal approximation.

2.1.1 Partial-wave expansion

The Schrödinger equation (2.1.1) can be rewritten as a function of the orbital momentum operator $\boldsymbol{L}$ [44]

$$\left[-\frac{\hbar^2}{2\mu}\left(\frac{1}{r}\frac{\partial^2}{\partial r^2}r-\frac{\boldsymbol{L^2}}{\hbar^2 r^2}\right)+V_N(r)\right]\Psi(\boldsymbol{r})=E\Psi(\boldsymbol{r}), \tag{2.1.9}$$

where only the nuclear interaction is considered. In this method, the solutions of Eq. (2.1.9) are expanded onto the eigenstates of $\boldsymbol{L}^2$ and $\boldsymbol{L_z}$, called the *spherical harmonics* $Y_l^{m_l}$. The partial waves hence read [44]

$$\phi_{lm_l}(\boldsymbol{r})=\frac{1}{r}u_l(r)Y_l^{m_l}(\Omega), \tag{2.1.10}$$

where l is the orbital angular momentum and m_l is its projection.

The scattering states ϕ_{klm_l}, associated with positive-energy solutions, are characterized by the wave number k and their radial component u_{kl} are solutions of the radial Schrödinger equation [44]

$$\left[\frac{d^2}{dr^2}-\frac{l(l+1)}{r^2}-\frac{2\mu}{\hbar^2}V_N(r)+k^2\right]u_{kl}(r)=0. \tag{2.1.11}$$

These functions u_{kl} tend asymptotically to [44]

$$u_{kl}(r)\underset{r\to\infty}{\longrightarrow}\cos[\delta_l(k)]kr\,j_l(kr)+\sin[\delta_l(k)]kr\,n_l(kr), \tag{2.1.12}$$

where δ_l are the nuclear phase shifts, j_l and n_l are the spherical Bessel functions of the first and the second kind, respectively [92]. From these solutions, the scattering amplitude can be determined [44]

$$f_{\boldsymbol{k}}(\theta)=\frac{1}{2ik}\sum_{l=0}^{+\infty}(2l+1)\left[e^{2i\delta_l(k)}-1\right]P_l(\cos\theta), \tag{2.1.13}$$

where P_l are Legendre polynomials [92].

Eq. (2.1.13) can also be written as a function of the nuclear S-matrix S_l, which relates the initial and final state of the collision. It reads [44]

$$f_{\boldsymbol{k}}(\theta)=\frac{1}{2ik}\sum_{l=0}^{+\infty}(2l+1)\left[S_l(k)-1\right]P_l(\cos\theta), \tag{2.1.14}$$

with [44]

$$S_l(k)=e^{2i\delta_l(k)}. \tag{2.1.15}$$

Since the projectile and the target are charged, the Coulomb potential should also be accounted for, which for pointlike particles reads

$$V_C(r)=\frac{Z_T Z_P e^2}{4\pi\epsilon_0 r}, \tag{2.1.16}$$

with ϵ_0 the vacuum electric permittivity. Since this long-range potential deforms the initial plane wave at large distance [first term of (2.1.5)], the scattering amplitude cannot be computed with Eq. (2.1.14).

For a pure Coulomb potential, i.e., $V = V_C$ in Eq. (2.1.1), the stationary scattering states behave asymptotically as [90]

$$\Psi^C_{\boldsymbol{k}}(\boldsymbol{r}) \underset{|r-z|\to\infty}{\longrightarrow} e^{i[kz+\eta\ln k(r-z)]} + f^C_{\boldsymbol{k}}(\theta)\frac{e^{i(kr-\eta\ln 2kr)}}{r}, \tag{2.1.17}$$

where

$$\eta = \frac{Z_T Z_P e^2}{4\pi\epsilon_0\hbar v} \tag{2.1.18}$$

is the Sommerfeld parameter. The Coulomb interaction distorts both the incoming and the scattered waves through a logarithm function, varying slowly with the distance. The factor $f^C_{\boldsymbol{k}}$ is called the Coulomb scattering amplitude and is given by [90]

$$f^C_{\boldsymbol{k}}(\theta) = -\frac{\eta}{2k\sin^2\frac{\theta}{2}}e^{2i\left(\sigma_0-\eta\ln\sin\frac{\theta}{2}\right)} \tag{2.1.19}$$

$$\text{with} \quad \sigma_0 = \arg\Gamma(1+i\eta). \tag{2.1.20}$$

When both the Coulomb and nuclear interactions are considered, i.e., $V = V_N + V_C$ in Eq. (2.1.1), the stationary scattering states behave asymptotically as [90]

$$\Psi_{\boldsymbol{k}}(\boldsymbol{r}) \underset{r\to\infty}{\longrightarrow} \Psi^C_{\boldsymbol{k}}(\boldsymbol{r}) + f^{\text{add}}_{\boldsymbol{k}}(\theta)\frac{e^{i(kr-\eta\ln 2kr)}}{r}, \tag{2.1.21}$$

where the additional scattering amplitude $f^{\text{add}}_{\boldsymbol{k}}$ is given by [90]

$$f^{\text{add}}_{\boldsymbol{k}}(\theta) = \frac{1}{2ik}\sum_{l=0}^{\infty}(2l+1)e^{2i\sigma_l}\left[S_l(k)-1\right]P_l(\cos\theta). \tag{2.1.22}$$

The Coulomb phase shifts σ_l are defined as [90]

$$\sigma_l = \arg\Gamma(l+1+i\eta) \tag{2.1.23}$$

$$= \sigma_0 + \sum_{n=1}^{l}\arctan\frac{\eta}{n}. \tag{2.1.24}$$

As in Eq. (2.1.8), the differential cross section is computed from the total scattering amplitude [44, 90]

$$\frac{d\sigma}{d\theta} = |f^C_{\boldsymbol{k}}(\theta) + f^{\text{add}}_{\boldsymbol{k}}(\theta)|^2. \tag{2.1.25}$$

Therefore, the calculation of the cross sections requires only the knowledge of the nuclear phase shifts δ_l, which can be computed numerically, e.g. with a Numerov algorithm or with the R-matrix method [93]. In practice, the resolution of all radial equations associated with each l is not feasible, the scattering amplitude (2.1.22) is approached by a finite sum. Truncating this sum is valid thanks to the presence of the centrifugal term $l(l+1)/r^2$ in Eq. (2.1.11). This term strongly suppresses the radial wave function when [90]

$$\frac{\hbar^2}{2\mu a^2}l(l+1) \gg E, \tag{2.1.26}$$

where a is the range of the nuclear potential. The nuclear phase shifts are therefore negligible for large l. Since the number of radial equations to solve and thus the computational time increase with the energy, the partial-wave expansion is mostly used at low energies.

2.1.2 Eikonal approximation

The eikonal approximation [18] is based on the fact that, at sufficiently high energy, the projectile is only slightly deflected by the target and the wave function does not differ much from the initial plane wave [first term of (2.1.5)]. The eikonal model factorizes this plane wave out of the wave function [91]

$$\Psi_{\boldsymbol{k}}(\boldsymbol{r}) = e^{ikz}\widehat{\Psi}(\boldsymbol{r}) \tag{2.1.27}$$

which modifies Eq. (2.1.1) into [91]

$$2ik\frac{\partial\widehat{\Psi}}{\partial z}(\boldsymbol{r}) + \Delta_{\boldsymbol{r}}\widehat{\Psi}(\boldsymbol{r}) - \frac{2\mu}{\hbar^2}V_N(r)\widehat{\Psi}(\boldsymbol{r}) \quad = \quad 0, \tag{2.1.28}$$

where only the nuclear interaction is considered.

The eikonal approximation assumes that the function $\widehat{\Psi}$ varies smoothly with $\boldsymbol{r}$ and neglects its second derivatives in front of its first derivative [91]

$$|\Delta_{\boldsymbol{r}}\widehat{\Psi}(\boldsymbol{r})| \ll k\left|\frac{\partial}{\partial z}\widehat{\Psi}(\boldsymbol{r})\right|. \tag{2.1.29}$$

It simplifies the Schrödinger equation (2.1.1) into [91]

$$\frac{\partial\widehat{\Psi}(\boldsymbol{r})}{\partial z} = -\frac{i}{\hbar v}V_N(r)\widehat{\Psi}(\boldsymbol{r}). \tag{2.1.30}$$

Note that by neglecting the derivatives of the wave function along the transverse coordinate $\boldsymbol{b}$ (see Fig. 2.1.1), part of the interference between the neighbouring $\boldsymbol{b}$s is missing in the eikonal approximation.

Eq. (2.1.30) can be solved analytically and the eikonal solutions read [91]

$$\Psi^{\text{eik}}_{\boldsymbol{k}}(\boldsymbol{b}, z) = e^{ikz}e^{-\frac{i}{\hbar v}\int_{-\infty}^{z} dz'\, V_N(r')}, \tag{2.1.31}$$

where r' depends on z'. They can be interpreted semiclassically as the projectile following a straight-line trajectory at constant impact parameter b and accumulating a phase through its interaction with the target during the collision. Asymptotically, these solutions behave as [91]

$$\Psi^{\text{eik}}_{\boldsymbol{k}}(\boldsymbol{b}, z) \quad \underset{z\to+\infty}{\longrightarrow} \quad e^{ikz}e^{i\chi^N(b)} \tag{2.1.32}$$

$$\text{with} \quad \chi^N(b) \quad = \quad -\frac{1}{\hbar v}\int_{-\infty}^{+\infty} dz\, V_N(r) \tag{2.1.33}$$

the nuclear eikonal phase.

The eikonal scattering amplitude is obtained with Eqs. (2.1.6) and (2.1.31)

$$f_{\boldsymbol{k}}(\theta) = \frac{\mu}{2\pi\hbar^2}\int d\boldsymbol{r}\, e^{-i\boldsymbol{q}_\perp \boldsymbol{b}}\int_{-\infty}^{\infty} dz\, e^{-iq_z z}V_N(r)e^{\frac{i}{\hbar v}\int_{-\infty}^{z} dz'\, V_N(r')}, \tag{2.1.34}$$

where $\boldsymbol{q}_\perp$ and $\boldsymbol{q}_{\boldsymbol{z}}$ are respectively the transverse and longitudinal components of the transferred momentum $\hbar\boldsymbol{q} = \hbar(\boldsymbol{k}' - k\hat{\boldsymbol{z}})$. Its norm is given by $\hbar q = 2\hbar k \sin\frac{\theta}{2}$ (see coordinate system in Fig. 2.1.1). Since the eikonal model assumes that the wave function does not differ much from a plane wave, the transferred momentum is approximated to be purely transverse $\boldsymbol{q} \approx \boldsymbol{q}_\perp$ and the exponential depending on $q_z z$ is neglected. This corresponds to a small-angles approximation. Thereby, the scattering amplitude becomes [91]

$$f_{\boldsymbol{k}}(\theta) \approx -ik \int_0^\infty b\, db\, J_0(qb) \left[e^{i\chi^N(b)} - 1 \right], \tag{2.1.35}$$

where J_0 is a Bessel function [92] and the relation (9.1.21) of Ref. [92] is used. The main advantage of this model is that the whole information about the collision is contained within the eikonal phases, which are easily computed from the nuclear potential.

Similarly to the partial-wave expansion S-matrix (2.1.15), the nuclear eikonal S-matrix S^{eik} can be defined and the scattering amplitude (2.1.35) is written as [91]

$$f_{\boldsymbol{k}}(\theta) = -ik \int_0^\infty b\, db\, J_0(qb) \left[S^{\text{eik}}(b) - 1 \right], \tag{2.1.36}$$

with

$$S^{\text{eik}}(b) = e^{i\chi^N(b)}. \tag{2.1.37}$$

When the Coulomb potential (2.1.16) is considered, the eikonal phase (2.1.33) diverges logarithmically. To cope with this issue, the Coulomb interaction is accounted for by adding to the nuclear eikonal phase χ^N (2.1.33) [91]

$$\chi^C_{PT}(b) = 2\eta \ln{(kb)} \tag{2.1.38}$$

which leads to the exact Coulomb scattering amplitude.

The eikonal scattering amplitude considering both the Coulomb and a short-range interactions reads [91]

$$f_{\boldsymbol{k}}(\theta) = f^C_{\boldsymbol{k}}(\theta) - ik \int_0^\infty b\, db\, J_0(qb) e^{i\chi^C_{PT}(b)} \left[S^{\text{eik}}(b) - 1 \right], \tag{2.1.39}$$

where $f^C_{\boldsymbol{k}}$ is the Coulomb scattering amplitude (2.1.19). The eikonal scattering amplitude is thus simply obtained by an integral over all impact parameters which depends on the eikonal S-matrix. Note that both the scattering amplitudes of the partial-wave expansion (2.1.25) and of the eikonal model (2.1.39), are given by the sum of a Coulomb term and an additional term which depends on both the short-range nuclear interaction and the Coulomb potential.

This high-energy model holds only when the projectile is slightly deflected by the target, and the deviations from the incoming plane wave are small. In Chapter 3, different corrections aiming to extend the range of validity of the eikonal approximation towards lower energies are studied. They are all based on the idea of improving the P-T nuclear and Coulomb deflections within the eikonal model.

2.2 The optical model

So far, the elastic-scattering process is assumed to be the only possible outcome of the collision. However, other channels such as breakup or rearrangement reactions are open, especially between composite projectiles and targets such as nuclei. The optical model simulates these inelastic reactions as absorption from the elastic channel and its use implies a simple modification of the nuclear potential. It is based on the same idea as the complex refractive index in optics, which simulates the absorption of photons in transparent media.

Thus, the optical model simulates the other channels by a complex scattering potential, called *optical potential*.

These optical potentials are formally derived in Ref. [94], where it is shown that they are non-local and energy-dependent. This non-locality arises from the antisymmetrization of the nuclei many-body wave functions and from the couplings between the different channels [94]. Because non-locality is difficult to treat, optical potentials are often parametrized as local interactions[3]. The energy dependency is usually not explicitly taken into account within the reaction model. In this thesis, the optical potentials are assumed local and their energy dependency is not treated explicitly in the reaction model.

These potentials are given by the sum of a nuclear V_N and Coulomb V_C potentials

$$V(r) = V_N(r) + V_C(r). \tag{2.2.1}$$

The nuclear part is often parametrized by a Woods-Saxon form

$$V_N(r) = -V_R\, f_{WS}(r, R_R, a_R) - i\, W_I\, f_{\mathrm{WS}}(r, R_I, a_I) + i\, 4a_D W_D\, \frac{d}{dr} f_{\mathrm{WS}}(r, R_D, a_D), \tag{2.2.2}$$

where

$$f_{\mathrm{WS}}(r, R_X, a_X) = \frac{1}{1 + e^{\frac{r-R_X}{a_X}}}. \tag{2.2.3}$$

This Wood-Saxon shape is chosen for phenomenological potentials since it reproduces roughly the densities of nuclear matter [57]. The radii R_R, R_I and R_D depend thus on the size of both interacting nuclei. The parameters a_R, a_I and a_D are the diffusenesses of the distributions and V_R, W_I and W_D are the depths. The Coulomb interaction V_C is often described by the potential of a uniformly charged sphere of radius R_C, which reads

$$V_C(r) = Z_P Z_T \frac{e^2}{4\pi\epsilon_0} \times \begin{cases} \left(\frac{3}{2} - \frac{r^2}{2R_C^2}\right) \frac{1}{R_C} & \text{for } r \leq R_C \\ \frac{1}{r} & \text{for } r \geq R_C \end{cases} \tag{2.2.4}$$

Usually, all parameters of the nuclear and Coulomb potentials are fit to reproduce elastic-scattering data.

The effect of such complex potentials can be understood with the continuity equation. With a complex interaction, the probability current [90]

$$\boldsymbol{J} = \frac{1}{2\mu} \left[\Psi_{\boldsymbol{k}}^* \left(\boldsymbol{p} \Psi_{\boldsymbol{k}} \right) + \Psi_{\boldsymbol{k}} \left(\boldsymbol{p} \Psi_{\boldsymbol{k}} \right)^* \right] \tag{2.2.5}$$

does not verify the equation of continuity. Indeed, since the Hamiltonian is no longer Hermitian, its divergence is non-zero and is given by [90]

$$\operatorname{div} \boldsymbol{J}(\boldsymbol{r}) = \frac{2}{\hbar} \mathrm{Im}\{V(r)\} |\Psi_{\boldsymbol{k}}(\boldsymbol{r})|^2, \tag{2.2.6}$$

where $\Psi_{\boldsymbol{k}}$ is a stationary scattering state, solution of the Schrödinger equation (2.1.1) using an optical potential. Because we want to model absorption from the elastic-scattering

---

[3] Recent studies have shown that the non-locality of the nuclear force affects significantly transfer reactions [95, 96].

channel, the divergence should be negative: the number of scattered particles should be inferior to the number of incident particles. Therefore, the imaginary part of the potential $\text{Im}\{V\}$ should be negative.

With a complex scattering potential, the nuclear phase shifts δ_l (2.1.12) and the nuclear eikonal phases χ^N (2.1.33) are complex. In both models, it is clear that the S-matrices, respectively (2.1.15) and (2.1.37), are no longer unitary. The contributions of each l in the partial-wave expansion or b in the eikonal model to the respective scattering amplitudes (2.1.22) and (2.1.39) are diminished. This supports the interpretation that a complex potential models absorption from the elastic channel.

2.3 Three-body reactions

2.3.1 Three-body model of the reaction

I now consider the collision of a one-neutron halo nucleus projectile P with a target T. As mentioned in Chapter 1, one-neutron halo nuclei have a very clusterized structure and they can be modelled as two-body objects [7], composed of a core c of mass m_c and charge Z_c and a loosely-bound neutron n of mass m_n. The number of mass, the mass and the charge of the projectile are denoted respectively A, $m_P = m_c + m_n$ and $Z_P = Z_c$. I assume here all particles to be structureless and the spins of the target and the core to be nil. The spin of the neutron is considered and denoted I.

In this simplified view, the structure of the halo nucleus is thus described by the internal single-particle Hamiltonian [11, 15, 38]

$$h_{cn} = \frac{\boldsymbol{p}^2}{2\mu_{cn}} + V_{cn}(r), \tag{2.3.1}$$

where $\boldsymbol{p}$ and $\boldsymbol{r}$ are respectively the c-n relative momentum and coordinate (see coordinate system in Fig. 2.3.1), $\mu_{cn} = m_c m_n/(m_c + m_n)$ is the c-n reduced mass and V_{cn} is a real effective potential simulating the c-n interaction. In this thesis (except in Chapter 5), the c-n potential is composed of a central term V_0 and a spin-orbit potential

$$V_{cn}(r) = V_0(r) + \frac{\boldsymbol{L}\cdot\boldsymbol{I}}{\hbar^2} V_{LI}(r), \tag{2.3.2}$$

where $\boldsymbol{L}$ and $\boldsymbol{I}$ are respectively the orbital and spin angular momentum operators. The central term is parametrized as a purely real Woods-Saxon potential (2.2.2)–(2.2.3) and the spin-orbit term as

$$V_{LI}(r) = V_{LS}\frac{1}{r}\frac{d}{dr} f_{\text{WS}}(r, R_R, a_R) \tag{2.3.3}$$

with the Woods-Saxon function f_{WS} (2.2.3).

The internal Hamiltonian is diagonalized in the basis coupling the orbital angular momentum $\boldsymbol{L}$ and the spin of the neutron $\boldsymbol{I}$. The basis states are the common eigenstates of the set of operators $\boldsymbol{L}^2$, $\boldsymbol{I}^2$ $\boldsymbol{J}^2$ and $\boldsymbol{J}_z$, with the total angular momentum defined as [90]

$$\boldsymbol{J} = \boldsymbol{L} + \boldsymbol{I}. \tag{2.3.4}$$

In the coupled basis, the eigenstates ϕ_{ljm} are associated with the quantum numbers of the orbital angular momentum l, the total angular momentum j and its projection m. Since

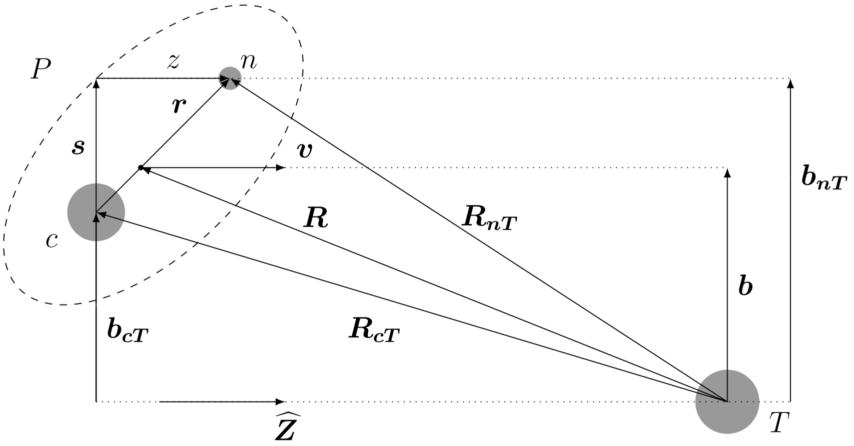

Figure 2.3.1: Coordinates of the three-body system: the internal coordinate of the projectile $\boldsymbol{r} \equiv (\boldsymbol{s}, z)$, the projectile-target relative coordinate $\boldsymbol{R} \equiv (\boldsymbol{b}, Z)$, the core-target relative coordinate $\boldsymbol{R_{cT}}$, the fragment-target relative coordinate $\boldsymbol{R_{nT}}$ and their transverse components $\boldsymbol{b_{cT}}$ and $\boldsymbol{b_{nT}}$.

the internal Hamiltonian is invariant under rotation, the eigenstates can be expressed as the product of a radial function and a spin-angular part [90]

$$\phi_{ljm}(\boldsymbol{r}) = \frac{1}{r} u_{lj}(r) \left\langle \Omega_r | ljm \right\rangle , \tag{2.3.5}$$

with Ω_r the angular part of $\boldsymbol{r}$. The spin-angular part is related to the eigenstates of the operator sets $\{\boldsymbol{L}^2, \boldsymbol{L}_z\}$ and $\{\boldsymbol{I}^2, \boldsymbol{I}_z\}$ through [90]

$$\left\langle \Omega_r | ljm \right\rangle = \sum_{m_l=-l}^{+l} \sum_{\nu=-I}^{+I} (l I m_l \nu | jm) Y_l^{m_l}(\Omega_r) \left| I \nu \right\rangle \tag{2.3.6}$$

where m_l and ν are respectively the projection of l and I.

As mentioned in Secs. 1.1.2 and 2.1.1, the eigenvalues can be positive or negative. The negative energies E_{nlj} are discrete and correspond to bound states, which are characterized by the number of nodes n of their radial wave function. Their radial part is normalized and behaves asymptotically as [15]

$$u_{nlj}(r) \underset{r\to\infty}{\longrightarrow} b_{nlj}\, i\, \kappa_{nlj}\, h_l^{(1)}(i\kappa_{nlj} r) \tag{2.3.7}$$

where b_{nlj} is the single-particle asymptotic normalization coefficient (SPANC), $\kappa_{nlj} = \sqrt{2\mu_{cn}|E_{nlj}|/\hbar^2}$ and $h_l^{(1)}$ is a modified spherical Bessel function of the third kind [92]. As seen in Chapter 1, the SPANC b_{nlj} is related to the ANC $\mathcal{C}_{lj}$ (1.1.8) of the c-n overlap function through Eq. (1.1.11).

The positive-energy part of the spectrum is continuous and describes the states in which the neutron is not bound to the core. These states ϕ_{kljm} are associated with the c-n wave number k and the energy $E = \hbar^2 k^2/(2\mu_{cn})$. Their radial parts u_{kl} behave asymptotically as [44]

$$u_{klj}(r) \underset{r\to\infty}{\longrightarrow} \cos[\delta_{lj}(k)] kr\, j_l(kr) + \sin[\delta_{lj}(k)] kr\, n_l(kr), \tag{2.3.8}$$

with δ_{lj} the phase shifts, j_l and n_l the spherical Bessel functions of the first and the second kind, respectively [92].

As usual in reaction theory, I neglect the structure of the target and simulate its interaction with the projectile constituents c and n by local optical potentials V_{cT} and V_{nT} (2.2.1), respectively [11, 15, 38]. After removing the center-of-mass contribution (see Refs. [97, 98]), the P-T relative motion is described by the three-body wave function Ψ, solution of the Schrödinger equation [11, 15, 38]

$$\left[\frac{\boldsymbol{P}^2}{2\mu} + h_{cn} + V_{cT}(R_{cT}) + V_{nT}(R_{nT})\right] \Psi(\boldsymbol{R},\boldsymbol{r}) = E_{\rm tot}\Psi(\boldsymbol{R},\boldsymbol{r}), \tag{2.3.9}$$

where $\boldsymbol{P}$ and $\boldsymbol{R}$ are respectively the P-T relative momentum and coordinate (see Fig. 2.3.1) and μ is the P-T reduced mass (2.1.2). The c-T and n-T coordinates, respectively $\boldsymbol{R_{cT}}$ and $\boldsymbol{R_{nT}}$ are related to $\boldsymbol{R}$ and $\boldsymbol{r}$ through

$$\boldsymbol{R} = \frac{m_c}{m_P}\boldsymbol{R_{cT}} + \frac{m_n}{m_P}\boldsymbol{R_{nT}} \tag{2.3.10}$$

$$\text{and} \quad \boldsymbol{r} = \boldsymbol{R_{nT}} - \boldsymbol{R_{cT}}. \tag{2.3.11}$$

Eq. (2.3.9) is solved with the initial condition that the projectile is in its ground state $\phi_{n_0 l_0 j_0 m_0}$ and is impinging on the target with a momentum $\boldsymbol{K} = K\hat{\boldsymbol{Z}}$ and velocity $\boldsymbol{v} = \hbar K\hat{\boldsymbol{Z}}/\mu$ along the beam direction, that I choose to be the Z axis (see Fig. 2.3.1), i.e., [11, 15, 38]

$$\Psi^{(m_0)}(\boldsymbol{R},\boldsymbol{r}) \underset{Z\to-\infty}{\longrightarrow} \exp(iKZ + \cdots)\, \phi_{n_0 l_0 j_0 m_0}(\boldsymbol{r}). \tag{2.3.12}$$

where the "$\cdots$" reflects the fact that long-range interactions distort the incoming plane wave even at large distance. Accordingly, the total energy $E_{\rm tot}$ in Eq. (2.3.9) is related to the energy of the projectile ground state $E_{n_0 l_0 j_0}$ and the initial P-T momentum $\hbar K$ through

$$E_{\rm tot} = E_{n_0 l_0 j_0} + \frac{\hbar^2 K^2}{2\mu}. \tag{2.3.13}$$

2.3.2 Cross sections

The cross sections can be calculated with the T-matrix formalism [97, 99], which requires the knowledge of the three-body wave function Ψ, solutions of the Schrödinger equation (2.3.9) with (2.3.12) as initial condition. As explained in Chapter 1, I focus in this thesis on three channels: the elastic scattering, the diffractive breakup and the knockout.

The elastic scattering corresponds to the deflection of the projectile to a certain angle Ω. The T-matrix element for the elastic scattering of a one-neutron halo nucleus in the direction $\boldsymbol{K'} \equiv (K', \Omega)$ reads [97, 99]

$$T_{fi}(\Omega) = \left\langle e^{i\boldsymbol{K'R}}\phi_{n_0 l_0 j_0 m'_0} \middle| V_{cT} + V_{nT} \middle| \Psi^{(m_0)} \right\rangle. \tag{2.3.14}$$

where m'_0 is the final projection of the total angular momentum of the ground state. Since the projectile stays in its initial state, the energy conservation imposes $K' = K$. The elastic-scattering cross section from an initial state with a projection m_0 to a final state with m'_0 can be obtained through Eqs. (2.1.7)–(2.1.8).

The diffractive breakup of one-neutron halo nuclei corresponds to the dissociation of the halo neutron from the core. In this exclusive process, both fragments survive the collision and typical observables depend on a c-n relative quantity, e.g., c-n relative energy or c-n relative momentum. The T-matrix element for the diffractive breakup is given by [97, 99]

$$T_{fi}(\boldsymbol{K'},\boldsymbol{k}) = \left\langle e^{i\boldsymbol{K'R}}\phi^{(-)}_{\boldsymbol{k}\nu}\middle|V_{cT}+V_{nT}\middle|\Psi^{(m_0)}\right\rangle, \tag{2.3.15}$$

where $\boldsymbol{K'} \equiv (K',\Omega)$ is the final wave vector between the target and center-of-mass of P, and $\phi^{(-)}_{\boldsymbol{k}\nu}$ is an incoming stationary scattering state characterized by the final c-n wave vector $\boldsymbol{k} = (k,\Omega_k)$ and the spin projection ν. The partial-wave expansion of these stationary scattering states $\phi^{(-)}_{\boldsymbol{k}\nu}$ depend directly on the wave functions of the c-n continuum ϕ_{kljm} (2.3.5), i.e., the eigenfunctions of the Hamiltonian (2.3.1) with positive eigenvalues. They read [97]

$$\phi^{(-)}_{\boldsymbol{k}\nu} = \frac{4\pi}{k}\sum_{l=0}^{+\infty}\sum_{j=|l-I|}^{l+I}\sum_{m=-j}^{+j}(lIm-\nu\nu|jm)Y_l^{m-\nu*}(\Omega_k)e^{-i[\delta_{lj}(k)+l\pi/2]}\phi_{kljm}(\boldsymbol{r}). \tag{2.3.16}$$

The diffractive breakup cross section as a function of Ω, the deflection angle of the center-of-mass of P, and $\boldsymbol{k}$ can be obtained as [97, 99]

$$\frac{d\sigma_{bu}}{d\boldsymbol{k}d\Omega} = \frac{1}{(2\pi)^5}\frac{\mu K'}{\hbar^3 v}|T_{fi}(\boldsymbol{K'},\boldsymbol{k})|^2. \tag{2.3.17}$$

There are two possible processes that contribute to the knockout reaction: the diffractive breakup, where the neutron survives the collision, and the stripping, where the neutron is absorbed by the target. Consequently, the stripping cross section has to account for all possible absorption channels of the neutron with the target. In Ref. [100], Hussein and McVoy derive this cross section assuming that the core acts as a spectator during the reaction, i.e., it can only scatter with the target. With this approximation and the use of a closure relation, they show that the stripping cross section as a function of the deflection angle of the core, Ω_{cT}, and its energy E_{cT} reads [100]

$$\frac{d\sigma_{str}}{d\Omega_{cT}dE_{cT}} = \frac{2}{\hbar v}\frac{\mu_{cT}K_{cT}}{(2\pi)^3\hbar^2}\left\langle\rho_n^{(+)}\middle|-\mathrm{Im}\{V_{nT}\}\middle|\rho_n^{(+)}\right\rangle \tag{2.3.18}$$

where

$$\rho_n^{(+)}(\boldsymbol{R_{nT}}) = \int d\boldsymbol{R_{cT}}\,\zeta^{(-)*}_{\boldsymbol{K'_{cT}}}(\boldsymbol{R_{cT}})\Psi^{(m_0)}(\boldsymbol{R},\boldsymbol{r}), \tag{2.3.19}$$

$\boldsymbol{K'_{cT}} \equiv (K_{cT},\Omega_{cT})$ is the final c-T momentum, $K_{cT} = \sqrt{2\mu_{cT}E_{cT}/\hbar^2}$ and $\mu_{cT} = m_c m_T/(m_c+m_T)$ is the c-T reduced mass. The wave function $\zeta^{(-)}_{\boldsymbol{K'_{cT}}}$ is an incoming scattering state of the c-T system. This distorted wave function is solution to Eq. (2.1.1) applied to the c-T system, i.e., with the potential V_{cT} and energy E_{cT}.

2.3.3 Solving the three-body Schrödinger equation

2.3.3.1 Exact solution

As just seen, the collision of a one-neutron halo nucleus with a target is modelled as a three-body problem, composed of the core c, the halo neutron n and the target T. Within this framework, the reaction observables depend directly on the three-body wave function, describing the relative motion between the fragments. The exact solution of the three-body

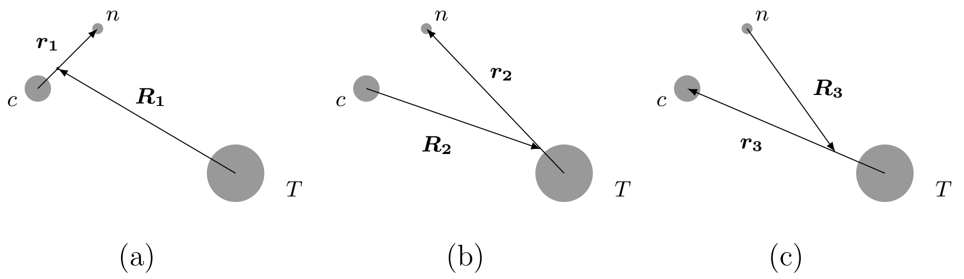

Figure 2.3.2: Three different Jacobi sets and their coordinates $(\boldsymbol{R_i}, \boldsymbol{r_i})$ with $i = 1, 2, 3$. The first Jacobi set corresponds to the coordinates that are used in the rest of this Chapter, $(\boldsymbol{R_1}, \boldsymbol{r_1}) = (\boldsymbol{R}, \boldsymbol{r})$ (see Fig. 2.3.1).

problem has to consider all possible reaction channels between these three objects. The coordinates defined previously (see Fig. 2.3.1) are only convenient for the elastic scattering and the breakup of the projectile. Indeed, describing the asymptotic condition of a c-T or a n-T bound state in this set of coordinates is numerically challenging, when not impossible.

To decouple these reactions channels and to express properly their asymptotic behaviour, the Jacobi sets $(\boldsymbol{R_i}, \boldsymbol{r_i})$ with $i = 1, 2, 3$ (see Fig. 2.3.2) can be used. The first Jacobi set is the same as the one used so far $(\boldsymbol{R_1}, \boldsymbol{r_1}) = (\boldsymbol{R}, \boldsymbol{r})$ (see Fig. 2.3.1). The second and third Jacobi sets are convenient to describe n-T and c-T bound states, respectively. Faddeev [12] has suggested to write the three-body wave function as a linear combination of three functions $\psi^{(i)}$ expressed in each Jacobi set

$$\Psi^{\text{exact}} = \sum_{i=1}^{3} \psi^{(i)}(\boldsymbol{r_i}, \boldsymbol{R_i}). \tag{2.3.20}$$

Using this definition, the Schrödinger equation (2.3.9) transforms into a set of three coupled equations [12, 15]

$$\begin{cases} \left(E_{\text{tot}} - \frac{\boldsymbol{P_1}^2}{2\mu} - \frac{\boldsymbol{p_1}^2}{2\mu_{cn}} - V_{cn}\right)\psi^{(1)} = V_{cn}\left(\psi^{(2)} + \psi^{(3)}\right) \\ \left(E_{\text{tot}} - \frac{\boldsymbol{P_2}^2}{2\mu_2} - \frac{\boldsymbol{p_2}^2}{2\mu_{nT}} - V_{nT}\right)\psi^{(2)} = V_{nT}\left(\psi^{(1)} + \psi^{(3)}\right) \\ \left(E_{\text{tot}} - \frac{\boldsymbol{P_3}^2}{2\mu_3} - \frac{\boldsymbol{p_3}^2}{2\mu_{cT}} - V_{cT}\right)\psi^{(3)} = V_{cT}\left(\psi^{(1)} + \psi^{(2)}\right) \end{cases} \tag{2.3.21}$$

where $\boldsymbol{P_i}$ and $\boldsymbol{p_i}$ are the momentum corresponding to the coordinates $\boldsymbol{R_i}$ and $\boldsymbol{r_i}$, respectively. The reduced masses appearing in Eq. (2.3.21) are defined as $\mu_2 = (m_n + m_T)m_c/(m_P + m_T)$, $\mu_{nT} = m_n m_T/(m_n + m_T)$ and $\mu_3 = (m_c + m_T)m_n/(m_P + m_T)$. Because the three functions $\psi^{(i)}$ are coupled, they are all influenced by the different channels. Therefore, the description of one channel requires the knowledge of all three functions [15].

Nowadays, different groups solve this system of equations for problems describing up to five bodies (e.g. see Refs. [13, 101]). The main drawbacks are the numerical cost and the limitation to nuclei with low charges. Indeed, the infinite range of the Coulomb potentials makes the decoupling of the asymptotics of $\psi^{(i)}$ challenging.

2.3.3.2 Continuum-Discretized Coupled Channels

The Continuum-Discretized Coupled Channels (CDCC) method [17] approaches the solution of the three-body system within the first Jacobi set $(\boldsymbol{R_1}, \boldsymbol{r_1}) = (\boldsymbol{R}, \boldsymbol{r})$. This approximation holds if there are no c-T and n-T bound states or resonances in the low-energy part of the c-T or n-T continuum [102]. Consequently, the Faddeev equations (2.3.21) are reduced to Eq. (2.3.9).

Since the effective potential V_{cn} is real, the internal Hamiltonian (2.3.1) is Hermitian and its eigenstates ϕ_{nljm} and ϕ_{kljm} form a complete basis of the vectorial space of the projectile internal coordinate $\boldsymbol{r}$. This basis is particularly well suited to describe the elastic-scattering and breakup channels of the projectile. The idea of CDCC is to expand the three-body wave function onto these eigenstates, composed of a finite number of bound states ϕ_{nljm} and a continuum of unbound states ϕ_{kljm} [11, 15, 102]

$$\Psi(\boldsymbol{R},\boldsymbol{r}) = \sum_{nljm} \phi_{nljm}(\boldsymbol{r})\psi_{nljm}(\boldsymbol{R}) + \sum_{ljm}\int_0^\infty dE\, \phi_{kljm}(\boldsymbol{r})\psi_{kljm}(\boldsymbol{R}). \tag{2.3.22}$$

Asymptotically, the coefficients of this expansion ψ_{nljm} and ψ_{kljm} describe the projectile-target relative motion. In particular, the first sum of Eq. (2.3.22) corresponds to the elastic and inelastic outcomes of the collision while the second represents the breakup channel.

The main difficulty of this basis is due to the continuum in energy, i.e., the integral on E in Eq. (2.3.22), which is not practical when inserted into the three-body Schrödinger equation (2.3.9). The idea of the CDCC method is to discretize this continuum in small intervals, called *bins*, and to truncate the corresponding sum. There are several ways to achieve this (see Refs. [14, 15]), but the most common one is the average method. In this method, the radial wave functions $\tilde{u}_{ilj}$ of each bin i defined by $[k_{i-1}, k_i]$ form a square-integrable basis. These functions are constructed through a superposition of stationary scattering states [11, 15, 102]

$$\tilde{u}_{ilj}(r) = \sqrt{\frac{2}{\pi N_i}}\int_{k_{i-1}}^{k_i} dk\, w_i(k) u_{klj}(r) \tag{2.3.23}$$

where w_i is a weight function, $N_i = \int_{k_{i-1}}^{k_i} dk\, |w_i(k)|^2$ is a normalization constant and u_{klj} is the radial part of a c-n scattering state (2.3.8). The discrete energies $\tilde{E}_{ilj}$ associated to the bin wave functions $\tilde{\phi}_{iljm}$ are given by

$$\tilde{E}_{ilj} = \left\langle \tilde{\phi}_{iljm} \middle| h_{cn} \middle| \tilde{\phi}_{iljm} \right\rangle. \tag{2.3.24}$$

With this discretization, the three-body wave function (2.3.22) becomes [11, 15, 102]

$$\Psi^{\mathrm{CDCC}}(\boldsymbol{R},\boldsymbol{r}) = \sum_p \phi_p(\boldsymbol{r})\psi_p(\boldsymbol{R}) \tag{2.3.25}$$

where ϕ_p represent either bound states $p = nljm$ (ϕ_{nljm} with $E_{nlj} < 0$) or a bin state $p = iljm$ ($\tilde{\phi}_{iljm}$ with $\tilde{E}_{ilj} > 0$). Using the expansion (2.3.25), the Schrödinger equation (2.3.9) transforms into a set of coupled equations [11, 15, 102]

$$\left[-\frac{\boldsymbol{P}^2}{2\mu} + V_{pp}(\boldsymbol{R}) - (E_{\mathrm{tot}} - E_p)\right]\psi_p(\boldsymbol{R}) + \sum_{p\neq p'} V_{pp'}(\boldsymbol{R})\psi_{p'}(\boldsymbol{R}) = 0, \tag{2.3.26}$$

where $E_p = E_{nlj}$ for bound states and $E_p = \tilde{E}_{ilj}$ for bin states. The potentials $V_{pp'}(\boldsymbol{R}) = \langle\phi_p|V_{nT} + V_{cT}|\phi_{p'}\rangle$ couple bound and continuum states.

The coefficients ψ_p are also expanded onto the spherical harmonics $Y_L^{M_L}$ [11, 15, 102]

$$\psi_p(\boldsymbol{R}) = \sum_{LM_L} i^L \chi_{pL}(R) Y_L^{M_L}(\Omega_R), \tag{2.3.27}$$

where L is the orbital angular momentum associated with the P-T motion and M_L is its projection. The three-body wave function is thus described by the total angular momentum $J_{\rm tot}$ resulting from the coupling of L and j. By inserting the expansion (2.3.27) into Eq. (2.3.26), the CDCC partial-wave coupled equations for each $J_{\rm tot}$ become [11, 15, 102]

$$\left\{-\frac{\hbar^2}{2\mu}\left[\frac{d}{dR^2}-\frac{L(L+1)}{R^2}\right]+V^{J_{\rm tot}}_{\alpha\alpha}(R)-(E_{\rm tot}-E_p)\right\}\chi^{J_{\rm tot}}_{\alpha}(R) \\ +\sum_{\alpha\neq\alpha'} i^{L'-L}V^{J_{\rm tot}}_{\alpha\alpha'}(R)\chi^{J_{\rm tot}}_{\alpha'}(R)=0 \quad (2.3.28)$$

where α represents the channel characterized by the quantum numbers $\{p,L\}$ and $V^{J_{\rm tot}}_{\alpha\alpha'}(R) = \left\langle[\phi_p Y_L]^{J_{\rm tot}}\middle|V_{nT}+V_{cT}\middle|[\phi_{p'} Y_{L'}]^{J_{\rm tot}}\right\rangle$ are the coupling potentials. The equations (2.3.28) are solved with the boundary conditions [11, 15, 102]

$$\chi^{J_{\rm tot}}_{\alpha}(R) \underset{R\to\infty}{\longrightarrow} \frac{1}{\sqrt{v_\alpha}}\left[I_\alpha(K_\alpha R)\delta_{\alpha\alpha_0}-O_\alpha(K_\alpha R)S^{J_{\rm tot}}_{\alpha\alpha_0}\right] \quad (2.3.29)$$

where $I_\alpha = G_\alpha - i\,F_\alpha$ and $O_\alpha = I^*_\alpha$ are respectively an incoming and outgoing Coulomb function [92], $K_\alpha = \sqrt{2\mu(E_{\rm tot}-E_p)/\hbar^2}$ and $v_\alpha = \hbar K_\alpha/\mu$ are the asymptotic momentum and velocity in the channel α and α_0 is the initial channel, i.e., at $Z\to-\infty$ [15]. The S-matrix elements $S^{J_{\rm tot}}_{\alpha\alpha_0}$, defined in this boundary condition, represent the amplitude of populating the channel α from the initial channel α_0. The elastic-scattering and breakup cross sections are computed from these S-matrix elements and their expressions can be found in Ref. [15].

This method is fully quantal and is thus very accurate [103, 104, 105]. Contrary to the Faddeev formalism, it does not have a restriction on the charge of the nuclei involved in the reaction. The main drawback of CDCC is that the numerical cost scales with the energy since higher partial waves L of ψ_p (2.3.27) have to be considered and thus more coupled equations (2.3.28) have to be solved. It also has convergence issues at energies below 10A MeV due to the discretization of the continuum [103].

2.3.3.3 Dynamical Eikonal Approximation

Similarly to the two-body case (see Sec. 2.1.2), the eikonal model [18] reflects the fact that at high-energy the projectile is only slightly deflected by the target and thus their relative wave function does not differ much from the initial plane wave (2.3.12). By factorizing this plane wave out of the wave function

$$\Psi(\boldsymbol{R},\boldsymbol{r}) = e^{iKZ}\ \widehat{\Psi}(\boldsymbol{R},\boldsymbol{r}), \quad (2.3.30)$$

and neglecting the second derivative of $\widehat{\Psi}$ in front of its first derivative, the Schrödinger equation (2.3.9) modifies into [97, 106]

$$i\hbar v\frac{\partial}{\partial Z}\widehat{\Psi}^{\rm DEA}(\boldsymbol{R},\boldsymbol{r}) =[h_{cn}-E_{n_0l_0j_0}+V_{cT}(R_{cT})+V_{nT}(R_{nT})]\widehat{\Psi}^{\rm DEA}(\boldsymbol{R},\boldsymbol{r}). \quad (2.3.31)$$

This equation corresponds to the Dynamical Eikonal Approximation (DEA) [97, 106]. It is equivalent to a time-dependent Schrödinger equation which considers straight-line trajectories, i.e, at constant impact parameter with a constant velocity v and with $t = Z/v$. However, it is important to emphasize that no semiclassical approximation has been made and therefore $\boldsymbol{b}$ and Z are quantum variables. The main difference between the DEA and a time-dependent model is that some interferences between the neighbouring bs are taken into account within the DEA. Note that it still misses part of these interferences since the second derivatives along the coordinate $\boldsymbol{b}$ is neglected.

Because this partial-derivative equation (2.3.31) has a similar form as a time-dependent Schrödinger equation, it can be computed with similar numerical methods. In this work, it is solved through a numerical evolution calculation as a function of the transverse coordinate $\boldsymbol{b}$ [107, 108]. The observables are computed from the asymptotic behaviour of the wave function, i.e., at $Z \to +\infty$. The derivation of the DEA cross sections can be found in Refs. [97, 109]; I present the main steps in Appendix A. This model reproduces well breakup data above $40A$ MeV, where the P-T deflection is small [107, 109]. It also provides energy distribution of breakup on a heavy target at $68A$ MeV close to CDCC calculations [110]. Compared to CDCC, the DEA has a reduced numerical cost.

2.3.3.4 Usual eikonal approximation

The usual eikonal model [18] makes a subsequent approximation: the adiabatic or sudden approximation, which sees the internal coordinates of the projectile as frozen during the collision. This approximation only holds at high energy, where the collision occurs in a brief time, and the nucleons inside the projectile do not have the time to rearrange. The internal Hamiltonian is therefore replaced by the energy of the initial state of the projectile (2.3.12), i.e., $h_{cn} \approx E_{n_0 l_0 j_0}$ in Eq. (2.3.31). The eikonal equation reads [18]

$$i\hbar v \frac{\partial}{\partial Z} \widehat{\Psi}^{\mathrm{eik}}(\boldsymbol{R},\boldsymbol{r}) = [V_{cT}(R_{cT}) + V_{nT}(R_{nT})]\widehat{\Psi}^{\mathrm{eik}}(\boldsymbol{R},\boldsymbol{r}). \tag{2.3.32}$$

The solutions satisfying Eq. (2.3.32) can be derived analytically as in the two-body case (2.1.31), they read [11]

$$\Psi^{\mathrm{eik}(m_0)}(\boldsymbol{R},\boldsymbol{r}) = e^{iKZ} e^{-\frac{i}{\hbar v}\int_{-\infty}^{Z} dZ'\, V_{cT}(R'_{cT})+V_{nT}(R'_{nT})} \phi_{n_0 l_0 j_0 m_0}(\boldsymbol{r}) \tag{2.3.33}$$

where $R'_{(c,n)T} = \sqrt{b^2_{(c,n)T} + Z'^2}$. Both elastic-scattering and breakup cross sections, derived in Appendix A, are computed from the asymptotic behaviour of Ψ^{eik} which reads [11]

$$\Psi^{\mathrm{eik}(m_0)}(\boldsymbol{R},\boldsymbol{r}) \underset{Z\to+\infty}{\longrightarrow} e^{iKZ} e^{i\chi_{cT}(\boldsymbol{b},\boldsymbol{s})+i\chi_{nT}(\boldsymbol{b},\boldsymbol{s})} \phi_{n_0 l_0 j_0 m_0}(\boldsymbol{r}), \tag{2.3.34}$$

where

$$\chi_{(c,n)T}(\boldsymbol{b},\boldsymbol{s}) = -\frac{1}{\hbar v}\int_{-\infty}^{+\infty} dZ\, V_{(c,n)T}(\boldsymbol{b}_{(\boldsymbol{c},\boldsymbol{n})\boldsymbol{T}}, Z) \tag{2.3.35}$$

are respectively the c-T and n-T eikonal phases. Note that the eikonal phases only depend on the transverse part of $\boldsymbol{R}$ and $\boldsymbol{r}$, respectively $\boldsymbol{b}$ and $\boldsymbol{s}$ (see Fig. 2.3.1). Compared to more elaborate models, e.g. CDCC and the DEA, the eikonal model exhibits an additional symmetry across the plane of the projectile's internal transverse coordinate $\boldsymbol{s}$, as briefly discussed in the Appendix of Ref. [111]. I study an impact of this additional symmetry in Chapter 4.

As in the two-body case (see Sec. 2.1.2), the eikonal solutions (2.3.33) can be interpreted semiclassically as the projectile following a straight-line trajectory at constant impact parameter b and accumulating a phase through its interaction with the target during the collision. This model is powerful because the eikonal phases have simple expressions, depending only on the optical potentials, and the cross sections are evaluated directly from these phases. Unfortunately, it is restricted to high energies, above $60A$ MeV where the P-T deflection is small and the adiabatic approximation holds. As mentioned above, I study in Chapter 3 the extension of this model to low energies through the use of corrections to the P-T Coulomb and nuclear deflections.

2.3.3.5 Coulomb-corrected eikonal approximation

The eikonal model has another drawback, it is incompatible with the infinite range of the Coulomb interaction, causing two divergences when this interaction becomes significant. The logarithmic divergence of the eikonal phase in the P-T elastic scattering has already been explained in Sec. 2.1.2. This can be solved by using the phase χ_{PT}^{C} (2.1.38) leading to the exact Coulomb scattering amplitude. The second divergence is due to the adiabatic treatment of the collision, which does not hold for long-range interactions as the collision time can then no longer be considered short. To explain this divergence, I write the eikonal phases (2.3.35) as a sum of Coulomb and nuclear contributions [112]

$$\chi_{cT}(\boldsymbol{b},\boldsymbol{s})+\chi_{nT}(\boldsymbol{b},\boldsymbol{s})=\chi_{PT}^{C}(b)+\chi^{C}(\boldsymbol{b},\boldsymbol{s})+\chi^{N}(\boldsymbol{b},\boldsymbol{s}), \tag{2.3.36}$$

where χ^N is the nuclear part of the eikonal phases. The phase χ^C corresponds to the Coulomb tidal force responsible for the Coulomb breakup, it depends on the difference between the c-T and P-T Coulomb interactions. It reads for a one-neutron halo nucleus [112]

$$\begin{aligned}\chi^{C}(\boldsymbol{b},\boldsymbol{s}) &= -\eta\int_{-\infty}^{+\infty}dZ\left(\frac{1}{R_{cT}}-\frac{1}{R}\right) &(2.3.37)\\ &= -\eta\ln\left(1-2\frac{m_n}{m_P}\frac{\hat{\boldsymbol{b}}\cdot\boldsymbol{s}}{b}+\frac{m_n^2}{m_P^2}\frac{s^2}{b^2}\right). &(2.3.38)\end{aligned}$$

The divergence occurs in the integration of the breakup matrix elements, which are computed from the operators (see Appendix A)

$$e^{i\chi_{PT}^{C}}e^{i\chi^{C}}e^{i\chi^{N}}=e^{i\chi_{PT}^{C}}\left[1+i\,\chi^{C}-\frac{1}{2}\left(\chi^{C}\right)^{2}+\cdots\right]e^{i\chi^{N}} \tag{2.3.39}$$

When integrated in b, the first-order term χ^C causes a divergence due to its slow decrease in b [112].

In Ref. [23], they propose to use of an upper cutoff $b_{\max}$, limiting the bs in the computation of the breakup cross sections. It is chosen as

$$b_{\max}=\frac{\hbar v}{2|E_{n_0l_0j_0}|}, \tag{2.3.40}$$

to ensure that the characteristic time of excitation $\hbar/|E_{n_0l_0j_0}|$ is shorter than the time of the collision b/v. The authors of Ref. [23] also introduce a factor 2. This cutoff method is artificial and does not account for the influence of the wave function at large bs, which play an important role for Coulomb-dominated collisions, viz. on heavy targets.

Alternatively to the cutoff method, the authors of Ref. [24] have proposed to replace within the breakup matrix element (2.3.39) the diverging Coulomb first-order term χ^C by the Coulomb first-order-perturbation approximation $\chi_{\rm FO}^{C}$ [24]

$$e^{i\chi_{PT}^{C}}e^{i\chi^{C}}e^{i\chi^{N}}\to e^{i\chi_{PT}^{C}}\left(e^{i\chi^{C}}-i\chi^{C}+i\chi_{\rm FO}^{C}\right)e^{i\chi^{N}}. \tag{2.3.41}$$

The first-order-perturbation theory solves perturbatively a time-dependent Schrödinger equation considering straight-line trajectories and a pure Coulomb interaction [98, 109]. Because this theory does not rely on the adiabatic approximation, the Coulomb first-order-perturbation approximation does not diverge. It reads

$$\chi^C_{\rm FO}(E,\boldsymbol{b},\boldsymbol{r}) = -\eta \int_{-\infty}^{+\infty} dZ\, e^{i\frac{\omega Z}{v}} \left(\frac{1}{R_{cT}} - \frac{1}{R}\right) \tag{2.3.42}$$

where $\omega = (E - E_{n_0 l_0 j_0})/\hbar$.

For one-neutron halo nuclei, the dipole term is dominant [113], and the first-order-perturbation Coulomb approximation can be approximated by its dipole contribution $\chi^{C,(\lambda=1)}_{\rm FO}$ (see its derivation in Appendix B), i.e., [112]

$$\begin{aligned} \chi^C_{\rm FO}(E,\boldsymbol{b},\boldsymbol{r}) &\approx \chi^{C,(\lambda=1)}_{\rm FO}(E,\boldsymbol{b},\boldsymbol{r}) & (2.3.43)\\ &= -2\eta\frac{\omega}{v}\frac{m_n}{m_P}\left[K_1\left(\frac{\omega}{v}b\right)\hat{\boldsymbol{b}}\cdot\boldsymbol{s} + iK_0\left(\frac{\omega}{v}b\right)z\right], & (2.3.44)\end{aligned}$$

where K_0 and K_1 are modified Bessel functions [92]. In Ref. [112], the authors show that this model is efficient to describe Coulomb-dominated breakup of one-neutron halo nuclei at energies around $70A$ MeV. In this thesis, I adopt for this model the name chosen in Ref. [112]: Coulomb-Corrected Eikonal approximation (CCE).

Note that the phase $\chi^C_{\rm FO}$ (2.3.42) can be computed exactly [25]. In Chapter 4, its exact expression is given and the influence of higher-order Coulomb terms is studied. Chapter 4 also presents an alternative model correcting for the eikonal Coulomb divergence.

2.3.4 Comparison of models and motivations

We have seen in this Chapter that in nuclear reaction theory, the collision of a one-neutron halo nucleus with a target is often modelled as a three-body collision. The three fragments, i.e. the core, the neutron and the target, involved in the collision, are assumed structureless. In this framework, the halo nucleus is described by a single-particle Hamiltonian with an effective potential, and its interaction with the target is modelled through optical potential. Different ways of solving this three-body problem have also been discussed.

The exact description of this three-body collision is solution to the Faddeev coupled equations. In this formalism, all transfer and breakup channels between the three fragments are accounted for. It has therefore a large numerical cost. Another drawback of this method is that it can only be applied to low-charged systems, in which the Coulomb interaction is not too important. Since it does not have any restriction on the nuclei charges and is fully quantal, CDCC is a powerful method. It provides accurate results for collisions involving halo nuclei [103]. Nevertheless, the discretization of the continuum is not straightforward and can induce some convergence issues at energies below $10A$ MeV [103].

Compared to CDCC, the eikonal approximation has a reduced computational time, and still keeps a quantal description of the collision. Unfortunately, this high-energy approximation is only valid at energies where the deflection of the projectile by the target is small, i.e., above $40A$ MeV for the DEA [107, 109] and $60A$ MeV for the usual eikonal model and the CCE [112]. Since facilities, such as HIE-ISOLDE at CERN and the future ReA12 at FRIB, reaccelerate their RIB at energy only up to $10A$ MeV, extending the validity of this model to these energies would be of great interest. In the first part of this thesis (Chapter 3), I analyse corrections aiming at improving the treatment of the

Coulomb and nuclear interactions, in order to extend the range of validity of the eikonal approximation down to $10A$ MeV.

As mentioned in Chapter 1, Coulomb-dominated breakup cross sections are enhanced for halo nuclei and are often used to study their structure [10, 35]. The usual eikonal model is not precise for such reaction because its adiabatic treatment is incompatible with the long-range Coulomb interaction. The CCE solves efficiently the problem, but it treats the Coulomb and nuclear interactions on different footings. Indeed, the nuclear part is treated with the usual eikonal model and the Coulomb interaction mixes the eikonal approach and the first-order perturbation theory. The authors in Refs. [66, 67, 68, 69, 72, 73, 74] have shown that the Coulomb and nuclear interferences impact greatly the accuracy of the information extracted from Coulomb-dominated breakup cross sections. For this reason, in collaboration with Daniel Baye, we have developed a simplification of the DEA, keeping the reduced numerical cost of the eikonal model, and removing elegantly the divergence due to the adiabatic approximation. This model is derived and studied in Chapter 4.

We have seen in Chapter 1 that knockout experiments have been widely used to probe the shell structure of halo nuclei. Because these reactions are measured at energies around $50A$-$100A$ MeV, they are often analysed with the eikonal model. As explained in Chapter 1, the agreement between theory and experiment worsens with the binding energy of the studied nucleus [27]. To understand why the agreement is good for loosely-bound nuclei and to determine what can be safely extracted from knockout reactions of one-neutron halo nuclei, I study the sensitivity of their observables to the nuclear structure of the projectile and to the choice of optical potentials in Chapter 5.

Chapter 3

Extension of the eikonal model to low energies

3.1 Introduction

In this Chapter, I study various corrections to the eikonal approximation aiming to extend the range of validity of the eikonal model down to $10A$ MeV, which is in the energy range of HIE-ISOLDE at CERN and the future ReA12 at FRIB. As mentioned previously, the eikonal solutions can be interpreted semiclassically as the projectile following a straight-line trajectory at constant impact parameter b along which it feels an external field that simulates its interaction with the target. In actual semiclassical models, the trajectory differs from a straight line because the projectile is deflected by its interaction with the target. At high enough energy, the difference is negligible, and straight-line trajectories make sense. However, at low energy, the deflection can no longer be neglected, and the eikonal model is not accurate. To extend the range of validity of the eikonal approximation down to lower energies, its modelisation of the deflection of the projectile has to be improved.

A first step in that direction has been made by Lenzi *et al.* [114] and Fukui *et al.* [115] for Coulomb-dominated collisions, viz. on heavy targets. Lenzi *et al.* have shown that the eikonal approximation combined with a semiclassical Coulomb correction [116] is accurate for the elastic scattering of one-body projectile on a heavy target at energies around $10A$ MeV. This correction improves the projectile-target Coulomb repulsion by replacing in the computation of the P-T interaction the impact parameter b of each straight-line trajectory by the distance of closest approach of the corresponding classical Coulomb trajectory b'_C, where $b'_C > b$. Fukui *et al.* [115] have studied this correction for three-body collisions, involving a one-neutron halo nucleus. They have demonstrated that this correction is accurate for Coulomb-dominated breakup at $20A$ MeV. Since the Coulomb deflection is already well accounted for by this semiclassical approach, this Chapter focuses on corrections to the nuclear deflection within the eikonal model, in order to extend its range of validity for nuclear-dominated reactions, viz. on light targets, down to $10A$ MeV.

The first correction I have studied is Wallace's correction [117, 118, 119], which is based on a perturbative expansion of the T-matrix (2.1.7). The perturbation accounts for the deviations of the wave vector from both the initial and final wave vectors experienced in the scattering [118]. However, as noted in Refs. [120, 121], this correction has convergence issues below a certain energy at which the perturbative approach is no longer valid. I address this problem and present a systematic method to ensure the convergence of the correction, which enables me to use it at $10A$ MeV. Since this correction induces an overestimation of the nuclear attraction, I couple it to the semiclassical Coulomb correction mentioned above. With this implementation, the deflection of the projectile by the target due to both the nuclear and Coulomb interactions are improved within the eikonal model. This study is presented in Sec. 3.3

As this combination of corrections does not provide a very consistent model, I have also studied the extension of the semiclassical correction to the nuclear interaction [114, 121]. The idea is to replace the impact parameter by the distance of closest approach computed considering both the Coulomb and nuclear interactions, to improve simultaneously the Coulomb and nuclear deflections within the eikonal model. The encouraging results obtained in Ref. [114, 121] for structureless nuclei suggest that it could be accurate for collisions involving more complex structures such as halo nuclei. In Sec. 3.4, I study this correction applied to two-body collisions and its generalization to three-body systems.

The exact continued S-matrix correction [122, 123, 124] is another way to improve the eikonal approximation. It is based on an exact correspondence between the partial-wave expansion (see Sec. 2.1.1) and the usual eikonal model (see Sec. 2.1.2). Wallace has demonstrated that the scattering amplitude of the partial-wave expansion (2.1.22) can be expressed exactly as a sum of integrals over the impact parameter [124], with the zeroth term corresponding to the eikonal scattering amplitude (2.1.39) where the eikonal phase is replaced by the exact phase shift. Brooke *et al.* have extended this correction to the elastic scattering of one-neutron halo nuclei; they have proven its accuracy in Ref. [122]. Its generalization to the breakup channel is presented in Sec. 3.5.

In the last part, I derive a Distorted-Wave Eikonal Approximation (DWEA) which uses a Coulomb distorted wave instead of a plane wave in the factorization of the eikonal wave function. The main advantage of this approach is that it naturally accounts for the Coulomb deflection of the projectile by the target, which is needed to reproduce elastic-scattering observables, as well as part of the transverse derivatives neglected by the eikonal approximation [see Eq. (2.1.29)]. Through the use of a change of coordinates, an equation similar to the eikonal one can be obtained. I emphasize in Sec. 3.6 the main practical difficulties of this model.

My methodology is to assess these corrections first in a simple case, the elastic scattering of structureless nuclei. If they are accurate, I generalise them to three-body collisions, involving a one-neutron halo nucleus. I take two nuclear-dominated collisions as test cases, first the elastic scattering of ^{10}Be with ^{12}C for the two-body collisions, then the elastic scattering and diffractive breakup of the one-neutron halo nucleus ^{11}Be with ^{12}C at $20A$ MeV and $10A$ MeV. As seen in Chapter 2, the description of such systems requires optical potentials to simulate the interaction between the colliding nuclei and an effective potential for the internal structure of the halo nucleus. Sec. 3.2 provides the two-body interactions used in the calculations of this Chapter.

Finally, in Sec. 3.7, I draw the conclusions from the analysis of these corrections.

	V_R [MeV]	R_R [fm]	a_R [fm]	W_I [MeV]	R_I [fm]	a_I [fm]	W_D [MeV]	R_D [fm]	a_D [fm]
^{10}Be-^{12}C	250.0	3.053	0.788	247.9	2.982	0.709	0	0	0
n-^{12}C	46.9395	2.5798	0.676	1.8256	2.5798	0.676	7.1585	2.9903	0.5426

Table 3.1: Parameters of the Woods-Saxon optical potential (2.2.2)–(2.2.3) used to simulate the nuclear ^{10}Be-^{12}C and n-^{12}C interactions. They are taken from Refs. [125, 126], respectively.

3.2 Two-body interactions and numerical details

The test case used in this study is the elastic scattering of ^{11}Be off ^{12}C at $20A$ MeV and $10A$ MeV. The halo nucleus ^{11}Be is described as an inert ^{10}Be core, assumed to be in its 0^+ ground state, to which a neutron is bound by 0.5 MeV. All particles, ^{10}Be, n and ^{12}C, are assumed structureless. I also neglect the spin of the neutron, in order to reduce the computational time of all the models considered in this Chapter. This simplification is mainly motivated by the heavy computational time of CDCC. This means that all the expressions derived in Sec. 2.3 and the cross sections in Appendix A simplify with $j = l$ and $m = m_l$.

The ^{11}Be nucleus is described within the single-particle model detailed in Sec. 2.3.1. As seen in Sec. 1.1.4, ^{11}Be has a $1/2^+$ ground state and is consistent with a $1s1/2$ single-particle state. However, because the spin of the neutron is neglected, the ground state of ^{11}Be is modelled $1s$ single-particle state in this Chapter. The ^{10}Be-n interaction is simulated by a purely real Woods-Saxon potential (2.2.2)–(2.2.3) similar to the one developed in Ref. [127]. I adjust the real depth $V_R = 62.98$ MeV to reproduce the energy of $1/2^+$ ground state in the $1s$ wave with the parameters $R_R = 2.585$ fm and $a_R = 0.6$ fm in the notations of Eqs. (2.2.2)–(2.2.3). The same potential is used in all partial waves but in the d wave, where I use $V_R = 69.15$ MeV to account for the known $5/2^+$ resonance in the ^{10}Be-n continuum (see Sec. 1.1.4). This potential produces a d resonance at energy $E_d = 1.27$ MeV and with a width $\Gamma_d = 160$ keV, which are close to the experimental values $E_{5/2^+} = 1.28$ MeV and $\Gamma_{5/2^+} = 100$ keV. The $1/2^-$ excited state of ^{11}Be is not described by this potential.

As explained in Sec. 2.2, the interactions of each fragments, ^{10}Be and n, with the target are modelled with optical potentials with a Woods-Saxon shape (2.2.2)–(2.2.3). The parameters of the ^{10}Be-^{12}C potential considered in this study are provided in the first line of Table 3.1. It has been chosen following Ref. [128]; it corresponds to the potential developed in Ref. [125] to reproduce ^{12}C-^{12}C elastic scattering at $25A$ MeV. The energy dependence of this potential is neglected. To account for the change in the projectile mass number, the radii are rescaled by $(10^{1/3} + 12^{1/3})/(12^{1/3} + 12^{1/3})$. The Coulomb interaction is described by the potential of a uniformly charged sphere (2.2.4) of radius $R_C = 5.777$ fm. The n-^{12}C interaction is also modelled with a Woods-Saxon shape (2.2.2)–(2.2.3). I use the Koning-Delaroche global nucleon-nucleus potential [126], whose parameters are functionals fit to reproduce interactions of neutrons and protons impinging on targets with number of mass $24 \leq A \leq 209$ at 1 keV up to 200 MeV. Its parameters are computed for a n-^{12}C collision at 20 MeV and are listed in the second line of Table 3.1. Since the goal of this work is to compare the eikonal model with its corrections, I use the same optical potentials in all calculations.

For the two-body collision, I compare the eikonal model and its correction to the exact solution, given by the partial-wave expansion (see Sec. 2.1.1). For the three-body reaction, I choose to use as benchmark the CDCC method [15, 17] (see Sec. 2.3.3.2), which provides accurate results at these energies and does not have any issue with the Coulomb interaction. To verify that my CDCC results are not sensitive to the discretization of the ^{10}Be-n continuum, I have made CDCC calculations with the program FRESCO [14] considering different discretizations. Converged results are obtained with the following model space: the ^{10}Be-n continuum is described up to the c-n orbital angular momentum $l_{\max} = 6$, the maximum c-n energy is set to be $E_{\max} = 10$ MeV, the number of bin states per partial wave is between 11 (for large l), 25 (at low l) and up to 49 (within the d wave to account for the presence of the resonance), and the total angular momentum is considered up to $J_{\max} = 20\,000$. The input file of the FRESCO program is given in Appendix C. The eikonal calculations in this Chapter are obtained using the following model space: the ^{10}Be-n continuum is described up to the c-n orbital angular momentum $l_{\max} = 10$ and a mesh in impact parameter up to 100 fm, with a step of 0.25 fm up to 30 fm and of 2 fm beyond. The dynamical eikonal approximation (DEA) uses the same numerical inputs as in Ref. [112].

3.3 Wallace's correction

3.3.1 T-matrix expansion

This correction results from an expansion of the T-matrix (2.1.7), developed in the PhD thesis of Wallace [117, 118, 119]. He has derived it for a two-body collision. The idea is to use a correction to the eikonal propagator which accounts for the deviations due to the nuclear interaction of the projectile-target wave vector from the initial and final wave vectors during the collision. Since this correction cancels for the Coulomb interaction, I present here the derivation of this correction for the neutral case, i.e, only considering the nuclear potential V_N.

As in Sec. 2.1, I consider a projectile P impinging on a target T with a initial wave vector $\boldsymbol{k} = k\hat{\boldsymbol{z}}$ (see Fig. 2.1.1), where the beam direction is chosen along the z-axis. For two-body collisions, the T-matrix element (2.1.7) can be written as a function of the exact propagator Γ, the final wave vector $\boldsymbol{k'} \equiv (k, \theta, \phi)$ and the initial plane wave [first term of Eq. (2.1.5)] [91]

$$T_{fi}(\theta) = \left\langle e^{i\boldsymbol{k'r}} \middle| V_N + V_N \Gamma V_N \middle| e^{ikz} \right\rangle \tag{3.3.1}$$

with θ the angle between the initial and final wave vectors and $\boldsymbol{r} \equiv (\boldsymbol{b}, z)$ the P-T coordinate (see Fig. 2.1.1). The inverse of Γ is defined as [91]

$$\Gamma^{-1} = \frac{1}{2\mu}\left(\hbar^2 k^2 - \boldsymbol{p^2}\right) - V_N + i\kappa, \tag{3.3.2}$$

where κ is a positive infinitesimal quantity, $\boldsymbol{p}$ and μ (2.1.2) are respectively the P-T relative momentum and reduced mass.

Different forms of the eikonal propagator exist, but I present here the form g used in Ref. [118]. It is obtained by neglecting the quadratic terms in the expansion of the momentum $\boldsymbol{p}$ about the average momentum $\hbar\left(\frac{\boldsymbol{k'}+\boldsymbol{k}}{2}\right)$

$$\begin{aligned}
\hbar^2\left(\frac{\boldsymbol{k'}+\boldsymbol{k}}{2}\right)^2-\boldsymbol{p}^2 &= \hbar^2\left(\frac{\boldsymbol{k'}+\boldsymbol{k}}{2}\right)^2-\left[\boldsymbol{p}-\hbar\left(\frac{\boldsymbol{k'}+\boldsymbol{k}}{2}\right)+\hbar\left(\frac{\boldsymbol{k'}+\boldsymbol{k}}{2}\right)\right]^2 \quad (3.3.3)\\
&= -\left[\boldsymbol{p}-\hbar\left(\frac{\boldsymbol{k'}+\boldsymbol{k}}{2}\right)\right]^2-2\hbar\left(\frac{\boldsymbol{k'}+\boldsymbol{k}}{2}\right)\cdot\left[\boldsymbol{p}-\hbar\left(\frac{\boldsymbol{k'}+\boldsymbol{k}}{2}\right)\right] \quad (3.3.4)\\
&\approx -2\hbar\left(\frac{\boldsymbol{k'}+\boldsymbol{k}}{2}\right)\cdot\left[\boldsymbol{p}-\hbar\left(\frac{\boldsymbol{k'}+\boldsymbol{k}}{2}\right)\right]. \quad (3.3.5)
\end{aligned}$$

With Eqs. (3.3.2) and (3.3.5), the inverse of the eikonal propagator reads [118]

$$g^{-1}=\frac{\hbar}{\mu}\left(\frac{\boldsymbol{k'}+\boldsymbol{k}}{2}\right)\left\{\hbar\left(\frac{\boldsymbol{k'}+\boldsymbol{k}}{2}\right)-\boldsymbol{p}\right\}-V_N+i\kappa. \quad (3.3.6)$$

By writing the eikonal wave function (2.1.31) with this propagator [91]

$$\left\langle\boldsymbol{r}\middle|\Psi^{\text{eik}}_{\boldsymbol{k}}\right\rangle = \left\langle\boldsymbol{r}\middle|1+gV_N\middle|e^{ikz}\right\rangle, \quad (3.3.7)$$

the eikonal T-matrix (3.3.1) reads [91, 118]

$$T^{\text{eik}}_{fi}(\theta)=\left\langle e^{i\boldsymbol{k'r}}\middle|V_N\middle|\Psi^{\text{eik}}_{\boldsymbol{k}}\right\rangle. \quad (3.3.8)$$

For central potentials, the correction terms N of the transition matrix are defined as [118]

$$\begin{aligned}
\Gamma &= g+gN\Gamma, \quad (3.3.9)\\
\text{where}\quad N &= \frac{1}{2\mu}(\boldsymbol{p}-\hbar\boldsymbol{k'})\cdot(\boldsymbol{p}-\hbar\boldsymbol{k}). \quad (3.3.10)
\end{aligned}$$

This correction accounts for the deviations of the wave vector from the initial and final wave vectors, due to the nuclear attraction between the nuclei during the reaction.

By solving iteratively Eq. (3.3.9), the exact propagator is given by a series of terms involving the eikonal propagator and the correction term N [118]

$$\Gamma=g+gNg+gNgNg+... \quad (3.3.11)$$

which leads to an expansion of the T-matrix (3.3.1)

$$\begin{aligned}
T_{fi}(\theta) &= \left\langle e^{i\boldsymbol{k'r}}\middle|(V_N+V_NgV_N)+V_NgNgV_N+V_NgNgNgV_N+...\middle|e^{ikz}\right\rangle \quad (3.3.12)\\
&= \mathsf{T}^{(0)}_{fi}(\theta)+\mathsf{T}^{(1)}_{fi}(\theta)+\mathsf{T}^{(2)}_{fi}(\theta)+\cdots \quad (3.3.13)
\end{aligned}$$

The first term of this expansion, in parenthesis in Eq. (3.3.12), corresponds to the eikonal T-matrix $\mathsf{T}^{(0)}_{fi}=T^{\text{eik}}_{fi}$ (3.3.8) and each additional term corrects for the nuclear deviations of the projectile by the target neglected in the eikonal model. The scattering amplitude at the order n can be expressed as [118]

$$\begin{aligned}
\mathcal{T}^{(n)}_{fi}(\theta) &= \sum_{j=0}^{n}\mathsf{T}^{(j)}_{fi}(\theta) \quad (3.3.14)\\
&= -i\hbar v\int_0^{+\infty} b\,db\,J_0(qb)t^{(n)}(b), \quad (3.3.15)
\end{aligned}$$

with

$$\begin{aligned} t^{(0)}(b) &= \left(e^{i\chi^N(b)} - 1\right), & (3.3.16)\\ t^{(1)}(b) &= \left(e^{i[\chi^N(b)+\tau_1^N(b)]} - 1\right), & (3.3.17)\\ \tau_1^N(b) &= -\frac{1}{\hbar v}\frac{\epsilon}{2}\int_{-\infty}^{+\infty} dz \left(\frac{1}{r}\frac{d}{dr}\right) r^2 V_N^2(r), & (3.3.18)\end{aligned}$$

$v = \hbar k/\mu$ the initial P-T relative velocity, χ^N the nuclear eikonal phase (2.1.33) and $\hbar q = \hbar|\boldsymbol{k}' - k\hat{\boldsymbol{z}}|$ the transferred momentum. The n^{th} corrective term is proportional to ϵ^n, with ϵ the expansion parameter [118]

$$\epsilon = \frac{1}{\hbar k v} = \frac{1}{2E} \qquad (3.3.19)$$

and $E = \hbar^2 k^2/(2\mu)$ the total kinetic energy. The first-order corrective phase τ_1^N can be interpreted as the classical energy density transfer between the incoming wave and the outgoing wave at the impact parameter b and divided by the velocity v [118].

When applied to the Coulomb potential between pointlike particles V_C (2.1.16), the correction (3.3.18) is identically zero. I have also verified numerically that this correction to the Coulomb interaction stays negligible when I consider the potential of a charged sphere (2.2.4). It is thus only significant for the nuclear interaction. The corrected amplitude at the n^{th} order is similar to the eikonal scattering amplitude (2.1.39), it reads [118]

$$f_{\boldsymbol{k}}(\theta) = f^C_{\boldsymbol{k}}(\theta) - ik\int_0^\infty b\,db\,J_0(qb)e^{i\chi^C_{PT}(b)}t^{(n)}(b), \qquad (3.3.20)$$

with χ^C_{PT} (2.1.38) the Coulomb eikonal phase and $f^C_{\boldsymbol{k}}$ (2.1.19) the Coulomb scattering amplitude. Because only the first order affects significantly the eikonal model [118], I do not present here the second and the third orders. Their analysis can be found in my Master's thesis [129].

3.3.2 Two-body collisions

As in Refs. [120, 121], I have observed that Wallace's correction has some convergence issues at low energy. These are due to the failure of the perturbation treatment: at low energies and small impact parameters bs, the expansion parameter ϵ (3.3.19) takes too large values to dampen the derivatives contained in the corrective phase τ_1 (3.3.18), which are thus no longer small compared to the standard eikonal phase χ^N (2.1.33). To illustrate the source of these problems, Fig. 3.3.1 displays the T-matrices $t^{(n)}$ (3.3.16)–(3.3.17) computed for a ^{10}Be projectile impinging on ^{12}C at 10A MeV as a function of the impact parameter b (upper scale) and the angular momentum l (bottom scale) with $l = kb$. The exact T-matrix is given by $S_l - 1$ (solid red line) with the S-matrix S_l (2.1.15). I compare this exact value to the eikonal T-matrix (3.3.16) (dashed green line) and the T-matrices obtained with Wallace's correction at the first order (3.3.17) (short-dashed blue line).

In Fig. 3.3.1, both real and imaginary parts of the T-matrix obtained with Wallace's correction diverge at small impact parameters ($b \leq 1.5$ fm). In that impact-parameter range, the collision is dominated by deep inelastic processes leading to strong absorption from the elastic channel. Accordingly, the T-matrix should be close to -1, as in the exact calculation and at the usual eikonal approximation. A close analysis of the problem [129] shows that it is due to a small or negative imaginary part of the corrected eikonal phase,

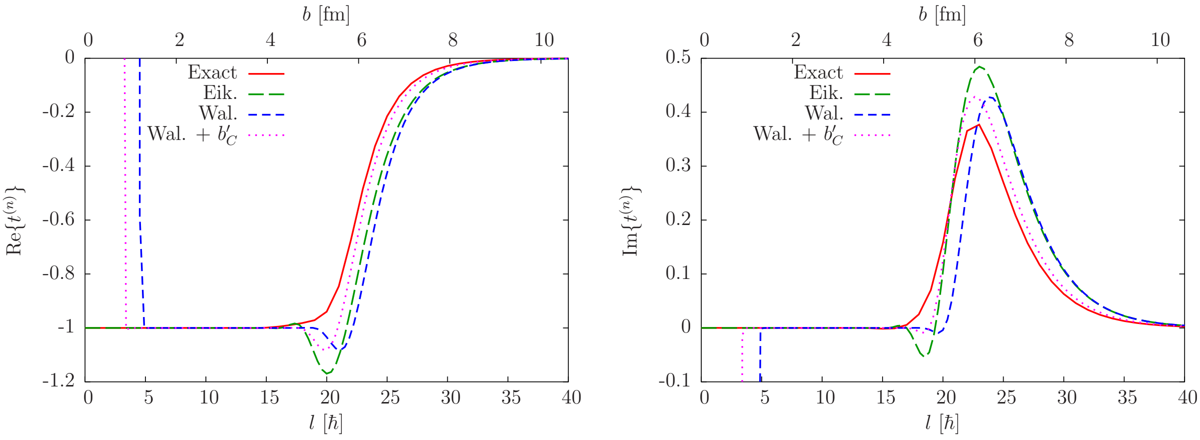

(a) (b)

Figure 3.3.1: Analysis of the convergence issue of Wallace's correction at low energies. The (a) real and (b) imaginary parts of the T-matrices for the elastic scattering of ^{10}Be off ^{12}C at $10A$ MeV as a function of the angular momentum and the impact parameter b. The solid red lines are obtained with the partial-wave expansion, the dashed green with the eikonal approximation, the small dashed blue with Wallace's correction and the dotted magenta with Wallace's correction combined with the semiclassical Coulomb correction.

i.e., $\mathrm{Im}\{\chi^N + \tau_1^N\} < 0$. Because this negative value appears in an imaginary exponential [see Eq. (3.3.17)], it causes a sudden increase of the modulus of the T-matrix instead of the strong damping expected. This erroneous behaviour happens due to the combination of two effects. First, the correction term to the eikonal phase τ_1 (3.3.18) involves the derivative of the nuclear potential. At places where the potential varies quickly, i.e., at short P-T distances, the integrand in Eq. (3.3.18) can become quite large. Second, at low energy, the expansion parameter ϵ (3.3.19) is not small enough to dampen these large variations of the integral.

To avoid the unrealistic values of the T-matrices in the small-b region, I introduce a cutoff in impact parameter from which I compute the corrections. Below this cutoff, the T-matrices are set equal to -1. I have also observed that replacing the corrected T-matrix by the usual eikonal one in that region, i.e., by setting $\tau_1 = 0$ below the cutoff, provides equally good results [129]. Detailed analyses of various optical potentials have shown that the results are not very sensitive to the choice of the cutoff and that a good rule of thumb is to take it slightly larger than the radius R_R of the real part of the optical potential (2.2.2) [129]. In the case studied here, $R_R = 3.053$ fm (see Table 3.1), and Fig. 3.3.1 shows that this cutoff can be taken between 1.7 and 4 fm, where the exact T-matrix is close to -1.

The elastic-scattering cross sections normalized to Rutherford for a ^{10}Be projectile impinging on ^{12}C at $20A$ MeV and $10A$ MeV are plotted in Fig. 3.3.2 as a function of the scattering angle θ. I compare each correction to the exact solution obtained with a partial-wave calculation (solid red lines). Since the eikonal approximation (long-dashed green lines) assumes that the deviation of the wave function from the initial plane wave are small (2.1.29) and relies on a small-angles approximation (2.1.35), it is more accurate at forward angles than at larger angles. It fails to reproduce the magnitude and the oscillatory pattern of the cross sections at larger angles: at the eikonal approximation,

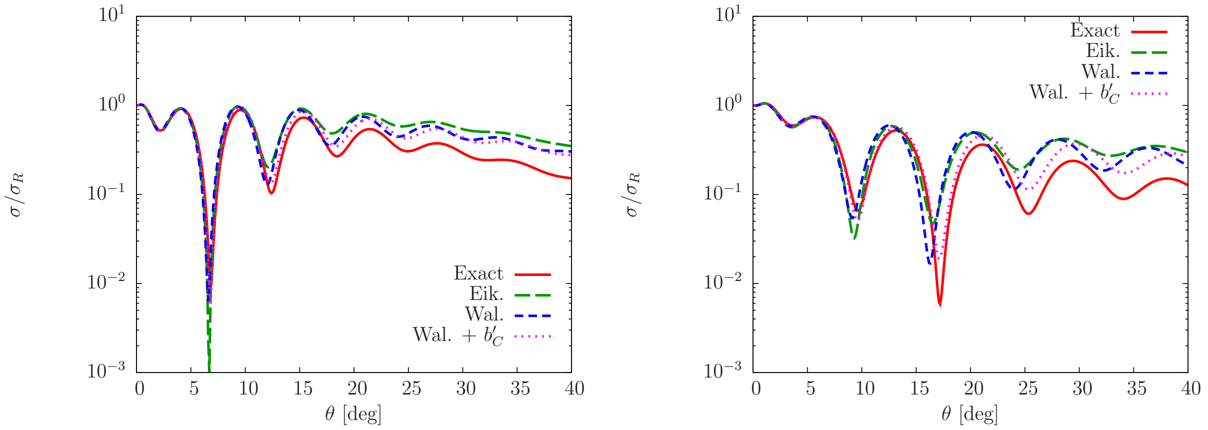

(a) (b)

Figure 3.3.2: Study of Wallace's correction for the elastic scattering of ^{10}Be off ^{12}C at (a) 20A MeV and (b) 10A MeV. The cross sections are normalized to Rutherford and plotted as a function of the scattering angle θ.

the cross sections are overestimated and the oscillations are damped and shifted towards forward angles. These differences with the exact cross section increase at lower energy, where the beam is deflected by the target to larger angles and the approximations (2.1.29) and (2.1.35) are worst.

Wallace's correction (short-dashed blue lines) slightly improves the eikonal calculations: it reduces the cross sections at large angles, which brings them a bit closer to their exact value, and it better reproduces the magnitude of the oscillations. However, the corrected cross sections still lie too high compared to the exact solutions, suggesting that this scheme does not properly account for the absorption from the elastic channel simulated by the optical potential. Physically, it can be interpreted as an underestimation of the inelastic channels of the collision. The results are also shifted to even more forward angles, leading to oscillations out of phase with the exact cross sections. Because Wallace's correction acts only on the nuclear interaction, I interpret this excessive shift by the fact that the correction tends to increase the attraction between the nuclei and, accordingly, to underestimate the scattering angle.

To counter this shift, the Coulomb repulsion has to be better accounted for. I therefore introduce the aforementioned semiclassical Coulomb correction [91, 114, 115, 116]. It consists in replacing in the eikonal nuclear phases χ^N and its correction τ_1^N the impact parameter b by the distance of closest approach b'_C of the corresponding Coulomb trajectory

$$\chi^N(b) \to \chi^N(b'_C) \qquad \tau_1^N(b) \to \tau_1^N(b'_C), \tag{3.3.21}$$

where the Coulomb distance of closest approach reads [91, 116]

$$b'_C = \frac{\eta + \sqrt{\eta^2 + b^2k^2}}{k} \tag{3.3.22}$$

and η is the Sommerfeld parameter (2.1.18). As b'_C is larger than the initial impact parameter of projectile, it simulates well the repulsion of the particles (see schematic view in Fig. 3.3.3). The influence of this correction is larger at lower energies [115].

I have also applied the shift of the impact parameter to the Coulomb distance b'_C within the computation of the Coulomb eikonal phase χ_{PT}^C (2.1.38) . My analysis shows that this

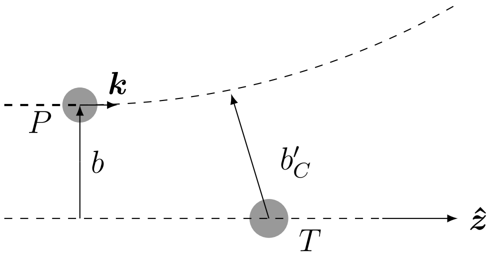

Figure 3.3.3: Schematic deflection of the projectile's trajectory due to the Coulomb repulsion.

shift does not significantly affect the calculations. Therefore, the Coulomb phase is not shifted and is evaluated in b, i.e., $\chi^C_{PT}(b)$.

We see in Fig. 3.3.1 that the sole action of the Coulomb correction (dotted magenta lines) in this nuclear-dominated reaction is to shift the S-matrix to smaller impact parameters closer to the exact S-matrix. Accordingly, Fig. 3.3.2 shows that the Coulomb correction shifts the cross sections to larger angles. This leads to oscillations in the cross sections that are in phase with the exact ones. Although the oscillations are better reproduced, the cross sections are still overestimated at large angles. Hence, the combination of Wallace's and the semiclassical Coulomb corrections provides only a minor improvement of the eikonal model at low energies.

3.3.3 Extension to three-body collisions

I have also applied Wallace's correction to collisions involving a one-neutron halo nucleus. As the neutron is assumed spinless, the elastic-scattering cross section derived with the eikonal model reads [$j = l$ and $m = m_l$ in Eq. (A.16)]

$$\frac{d\sigma_{el}}{d\Omega} = K^2 \frac{1}{2l_0+1} \sum_{m_{l_0} m'_{l_0}} \left| \int_0^{+\infty} b\, db\, J_{|m_{l_0}-m'_{l_0}|}(qb) S^{(m_{l_0})}_{0m'_{l_0}}(b) \right|^2 . \qquad (3.3.23)$$

where the elastic-scattering amplitude is defined as [see Eq. (A.17)]

$$S^{(m_{l_0})}_{0m'_{l_0}}(b) = \left\langle \phi_{n_0 l_0 m'_{l_0}} \middle| e^{i\chi_{cT}} e^{i\chi_{nT}} \middle| \phi_{n_0 l_0 m_{l_0}} \right\rangle - \delta_{m_{l_0} m'_{l_0}}, \qquad (3.3.24)$$

$\boldsymbol{R} \equiv (\boldsymbol{b}, Z)$ is the P-T relative coordinate (see Fig. 2.3.1), $\hbar \boldsymbol{q} = \hbar|\boldsymbol{K}' - K\hat{\boldsymbol{Z}}|$ is the transferred momentum defined from the final $\boldsymbol{K}' \equiv (K, \Omega)$ and initial $\boldsymbol{K} = K\hat{\boldsymbol{Z}}$ (2.3.12) P-T wave vectors, $\phi_{n_0 l_0 m_{l_0}}$ is the ground state of the projectile characterized by the quantum numbers $n_0 l_0 m_{l_0}$, $\chi_{(c,n)T}$ are respectively the c-T and n-T eikonal phases (2.3.35).

Wallace's correction is easily generalized to the elastic scattering of one-neutron halo nucleus: each c-T and n-T nuclear part of the eikonal phases, χ^N_{cT} and χ^N_{nT}, has to be corrected by a term τ^N_{1cT} and τ^N_{1nT} respectively. The elastic-scattering amplitude becomes

$$S^{(m_{l_0})}_{0m'_{l_0}}(b) = e^{i\chi^C_{PT}(b)} \left\langle \phi_{n_0 l_0 m'_{l_0}} \middle| e^{i\chi^C} e^{i\chi^N_{cT} + i\tau^N_{1cT} + i\chi^N_{nT} + i\tau^N_{1nT}} \middle| \phi_{n_0 l_0 m_{l_0}} \right\rangle - \delta_{m_{l_0} m'_{l_0}}, \qquad (3.3.25)$$

where χ^C_{PT} is the P-T Coulomb phase (2.1.38) and χ^C is the Coulomb tidal force (2.3.38). The corrective terms τ^N_{1cT} and τ^N_{1nT} are computed through Eq. (3.3.18) with the corresponding optical potentials V_{cT} and V_{nT}. As in the two-body case, this correction has

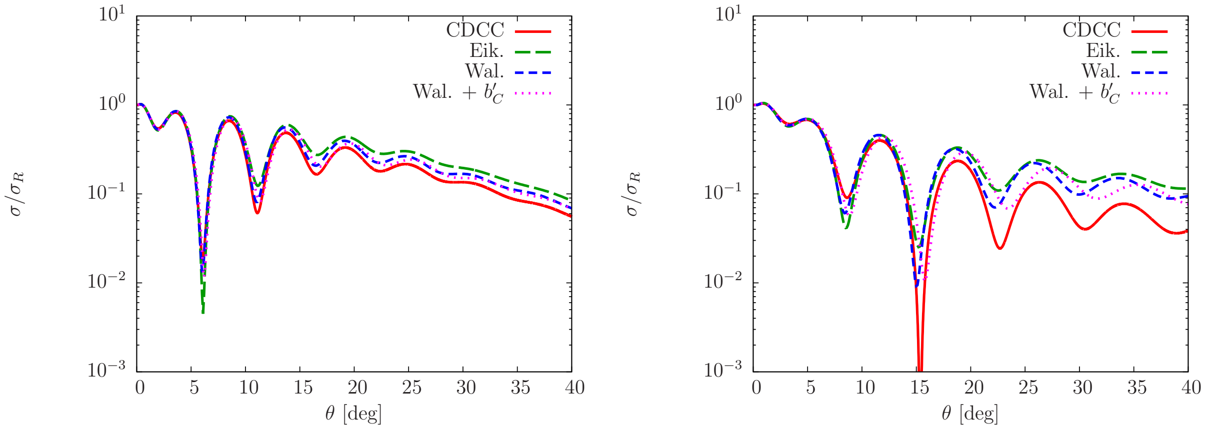

(a) (b)

Figure 3.3.4: Study of Wallace's correction for the elastic scattering of ^{11}Be off ^{12}C at (a) 20A MeV and (b) 10A MeV. The cross sections are normalized to Rutherford and plotted as a function of the scattering angle θ.

convergence issues at low energies and I solve them with a cutoff in impact parameters, taken slightly larger than the real radius of the potential.

The elastic-scattering cross sections of ^{11}Be off ^{12}C at 20A MeV and 10A MeV are plotted in Fig. 3.3.4. As mentioned in Sec. 3.2, I use CDCC calculations (solid red lines) as benchmark. Although the eikonal approximation (long-dashed green lines) includes the breakup channel, we still note that, as in the two-body calculations, it remains larger than the CDCC ones at large angles and that it fails to reproduce the oscillatory pattern (the oscillations are shifted towards forward angles and their magnitude is damped). The disagreement between the eikonal model and CDCC increases at low energy. As in the two-body case, Wallace's correction improves slightly the eikonal cross sections, bringing them closer to CDCC calculations and is more accurate at 20A MeV than at 10A MeV. Above 15°, it is still not sufficient and it overestimates CDCC at both 20A MeV and 10A MeV. Since it also induces a shift to forward angles at 10A MeV, leading to oscillations out of phase with the CDCC ones, I generalize the semiclassical Coulomb correction to the three-body case.

The generalization of the Coulomb semiclassical correction follows the idea of Ref. [115]. The impact parameter of the projectile b is shifted to the Coulomb distance of closest approach b'_C (3.3.22) within the computation of the eikonal phases. The nuclear eikonal phases and the corrective terms are thus computed with $\boldsymbol{b'_C} = b'_C\hat{\boldsymbol{b}}$ and the core-neutron transverse coordinate $\boldsymbol{s}$

$$\chi^N_{cT}(\boldsymbol{b},\boldsymbol{s}) \rightarrow \chi^N_{cT}(\boldsymbol{b'_C},\boldsymbol{s}) \qquad \tau^N_{1cT}(\boldsymbol{b},\boldsymbol{s}) \rightarrow \tau^N_{1cT}(\boldsymbol{b'_C},\boldsymbol{s}) \tag{3.3.26}$$

$$\chi^N_{nT}(\boldsymbol{b},\boldsymbol{s}) \rightarrow \chi^N_{nT}(\boldsymbol{b'_C},\boldsymbol{s}) \qquad \tau^N_{1nT}(\boldsymbol{b},\boldsymbol{s}) \rightarrow \tau^N_{1nT}(\boldsymbol{b'_C},\boldsymbol{s}) \tag{3.3.27}$$

As in the two-body collision, shifting the Coulomb phases χ^C_{PT} and χ^C does not impact significantly the results. Hence, I do not apply the semiclassical shift to these phases.

Fig. 3.3.4 shows that the combination of both Wallace's and Coulomb semiclassical corrections (dotted magenta lines) improves the oscillation pattern but still overestimates the cross sections at large angles. Moreover, the accuracy gain of this correction is insufficient at both energies. Further analyses have also shown that the correction to the neutron-target eikonal phase τ^N_{1nT} is negligible. I have also conducted a sensitivity analysis of Wallace's correction to the choice of the potential, in all cases, it lacks absorption at large angles. Because it is not accurate for elastic-scattering observable at $10A$ MeV, I have not studied the efficiency of this correction for breakup reactions. A summary of this analysis has been published in Refs. [20, 21].

3.4 Semiclassical correction

Similarly to the semiclassical Coulomb correction (3.3.21), an extension of this idea to the nuclear interaction is used in Refs. [114, 121]. They propose to replace the impact parameter by the distance of closest approach of the classical trajectory computed from both interactions. This correction aims at improving simultaneously the nuclear and Coulomb deflections of the projectile by the target within the eikonal model.

3.4.1 Real distance of closest approach

In a first attempt, I consider only the real part of the nuclear potential $\mathrm{Re}\{V_N\}$ and I study a two-body collision. As in Sec. 2.1.2, I consider that initially the projectile propagates towards the target along the z-axis with a wave vector $\boldsymbol{k} = k\hat{\boldsymbol{z}}$ and a velocity $v = \hbar k/\mu$. Because the potentials V_N (2.2.2) and V_C (2.2.4) are assumed central, both the energy E and angular momentum $\boldsymbol{L}$ are conserved. In classical mechanics, these equations of conservation expressed in spherical coordinates $\boldsymbol{r} \equiv (r, \theta, \phi)$ read [116]

$$\begin{cases} \dfrac{\mu v^2}{2} = & \dfrac{1}{2}\mu\left[\left(\dfrac{dr}{dt}\right)^2 + r^2\left(\dfrac{d\theta}{dt}\right)^2\right] + V_C(r) + \mathrm{Re}\{V_N(r)\} \\ \mu v b = & \mu r^2 \dfrac{d\theta}{dt} \end{cases} \tag{3.4.1}$$

where t is the time variable and b is the impact parameter, i.e., defined by the transverse coordinate $r\sin\theta$ at $t \to -\infty$. From this system, the radial velocity can be written as

$$\frac{dr}{dt} = \pm\sqrt{\frac{2}{\mu}\left[\frac{\mu v^2}{2} - V_C(r) - \mathrm{Re}\{V_N(r)\} - \frac{\mu v^2 b^2}{2r^2}\right]}, \tag{3.4.2}$$

where the + and − signs correspond respectively to the outgoing and incoming trajectories.

At the distance of closest approach b', i.e., the turning point, the radial velocity is null. This distance is therefore solution to

$$\frac{\mu v^2}{2} - V_C(b') - \mathrm{Re}\{V_N(b')\} = \frac{\mu v^2}{2}\left(\frac{b}{b'}\right)^2. \tag{3.4.3}$$

This distance of closest approach can also be approximated by a perturbation formula which reads [130, 131]

$$b' \quad\approx\quad b'_C + \frac{\mathrm{Re}[V_N(b'_C)]}{\frac{\mu v^2 b^2}{b'^3_C} - \left\{\dfrac{\partial}{\partial r}[\mathrm{Re}\{V_N(r)\} + V_C(r)]\right\}_{r=b'_C}}. \tag{3.4.4}$$

The elastic-scattering cross sections obtained with the semiclassical correction using the exact b'[1] and its approximated value (3.4.4) are similar for the optical potentials detailed in

---

[1] I have computed this distance exactly with two different methods: the calculation of the whole trajectory with a Newton-Raphson algorithm and a dichotomy method applied to Eq. (3.4.3).

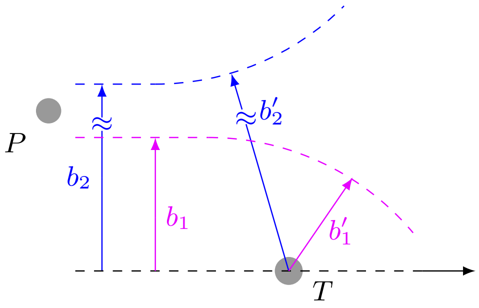

Figure 3.4.1: Schematic Coulomb-dominated (dashed blue line) and nuclear-dominated (dashed magenta line) trajectories.

Sec. 3.2. Because evaluating b' with the approximation (3.4.4) is more efficient numerically than computing its exact value, the results shown in this section are obtained with the approximation (3.4.4).

The distance of closest approach b' is larger than the actual impact parameter for a Coulomb-dominated trajectory and smaller for a nuclear-dominated trajectory (see Fig. 3.4.1). Therefore replacing the impact parameter by b' within the computation of the nuclear eikonal phase (2.1.33) might improve the deflection of the projectile by the target during the collision. As proposed in Ref. [121], a factor b'/b is also introduced to ensure the conservation of $\boldsymbol{L}$

$$\chi^N(b) \quad \rightarrow \quad \frac{b'}{b}\chi^N(b'). \tag{3.4.5}$$

This is equivalent to replacing the asymptotic velocity by the tangential velocity at the turning point. Similarly to the Coulomb semiclassical correction, shifting the Coulomb eikonal phase (2.1.38) does not affect the cross sections and I evaluate this phase at b, i.e., $\chi^C_{PT}(b)$.

The authors of Ref. [114] demonstrate the efficiency of this correction for a collision involving highly-charged nuclei, i.e., the elastic scattering of ^{16}O off ^{208}Pb at 12.5A MeV. They model the ^{16}O-^{208}Pb nuclear interaction by a Woods-Saxon optical potentials (2.2.2)–(2.2.3) with parameters taken from Ref. [132]: $V_R = -50$ MeV, $W_I = -42.2$ MeV, $R_R = R_I = 9.1458$ fm and $a_R = a_I = 0.755$ fm. The Coulomb interaction is simply simulated by the Coulomb potential between two pointlike particles (2.1.16). I reproduce their results in Fig. 3.4.2(a). Compared to the exact cross section (solid red line), which starts decreasing at 25°, the eikonal cross section (dashed green line) falls off at too small an angle, i.e., at 20°. The semiclassical correction (dotted black line) corrects this shift and leads to results close to the exact one. The trajectories for various impact parameters b are plotted in Fig. 3.4.2(b), where we can see that the Coulomb repulsion is dominant in this case.

Because this correction is very efficient for Coulomb-dominated systems, I analyse its accuracy in a nuclear-dominated case, the elastic scattering of ^{10}Be off ^{12}C at 10A MeV. The Rutherford-normalized cross sections, as well as the classical trajectories are displayed in Fig. 3.4.3[2]. Although there is a small improvement of the oscillation pattern of the cross

---

[2] For this figure, the optical potential used to simulate the ^{10}Be-^{12}C nuclear interaction reproduces the elastic scattering of ^{10}Be with ^{12}C at 59.4A MeV [133, 134] . It is parametrized as a Woods-Saxon potential (2.2.2)–(2.2.3) with $V_R = 123.0$ MeV, $W_I = 65.0$ MeV, $R_R = 3.33$ fm, $R_I = 3.47$ fm, $a_R = a_I = 0.80$ fm.

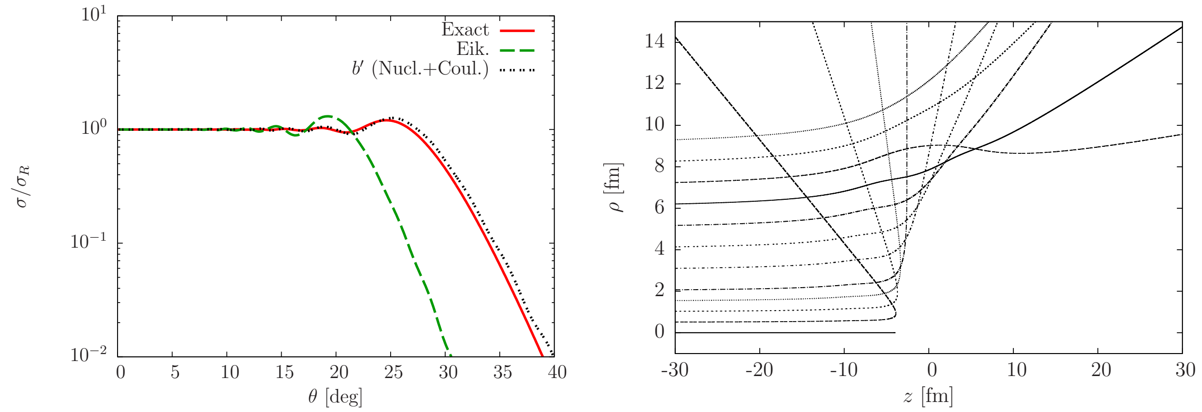

(a) (b)

Figure 3.4.2: Analysis of the real semiclassical correction for the elastic scattering of ^{16}O off ^{208}Pb at 12.5A MeV [114]. (a) The Rutherford-normalized cross section as a function of the scattering angle θ. (b) Set of real classical trajectories at different impact parameters, obtained for a Coulomb potential (2.1.16) and the real part of the nuclear interaction $\mathrm{Re}\{V_N\}$ (2.2.2).

section at forward angles (below 20°), this correction is still insufficient at large angles as it stays above the exact cross section. As previously, I interpret this by a lack of absorption from the elastic-scattering channel within the eikonal model. We see in the panel (b) that, as expected, the trajectories are mainly influenced by the nuclear interaction, and the distance of closest approach tends to be smaller than the impact parameter.

I have also evaluated the impact of the nuclear interaction onto b' within the semiclassical correction (3.4.5). My tests show that elastic-scattering cross sections obtained with the corrections using b' (3.4.5) and b'_C (3.3.21) have a similar magnitude. The only difference is that, when only the Coulomb interaction is corrected, the oscillations are shifted to larger angles, leading to an oscillatory pattern out of phase with the exact solution. This suggests that both interactions have to be corrected simultaneously.

This analysis indicates that the real semiclassical correction is valid for Coulomb-dominated system. Although, it improves the oscillatory pattern of the elastic-scattering cross sections for nuclear-dominated collisions, the magnitude of these observables are still overestimated at large angles, suggesting that the absorption from the elastic-scattering channel is still underpredicted. I have published this analysis in Ref. [20].

3.4.2 Complex distance of closest approach

To enhance the absorption from the elastic-scattering channel, I study the generalization of the semiclassical correction to complex distances b'', computed from the whole optical potentials, as proposed in Ref. [121]. In this way, the imaginary part of the potential would affect mostly small impact parameters, which would hopefully cause a reduction of the cross sections at large angles. This complex distance b'' is solution of an equation similar to Eq. (3.4.3), obtained from the conservation of energy and orbital angular momentum [116]

$$\frac{\mu v^2}{2} - V_C(b'') - V_N(b'') = \frac{\mu v^2}{2}\left(\frac{b}{b''}\right)^2 . \tag{3.4.6}$$

I have computed this distance exactly with a Newton-Raphson algorithm.

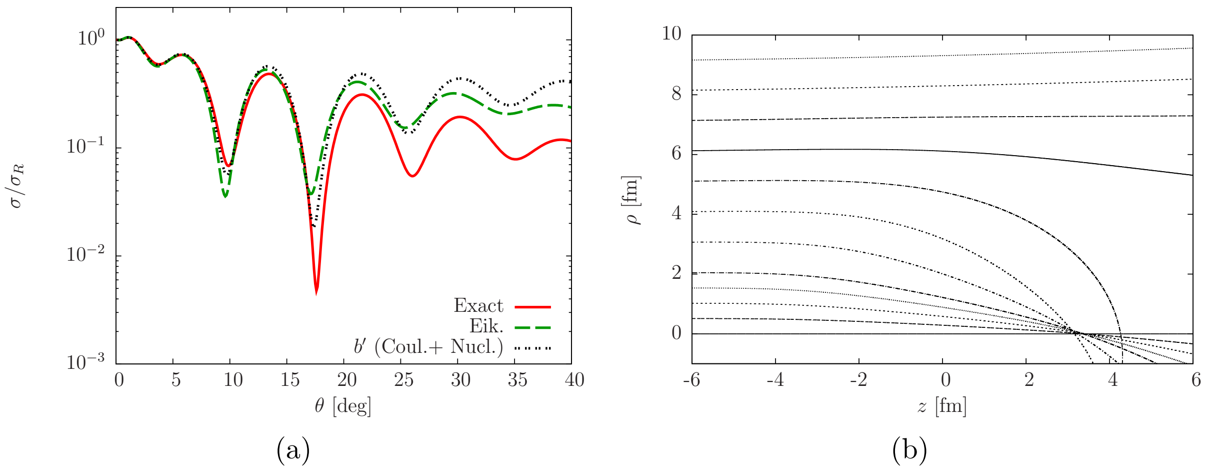

(a) (b)

Figure 3.4.3: Same as Fig. 3.4.2 but for the elastic scattering of ^{10}Be off ^{12}C at $10A$ MeV.

If the imaginary part of the potential and thus of b'' are small compared to their real part, the solution can be approximated by the first iteration of the Newton-Raphson method. In this perturbation view, the complex distance of closest approach b'' reads [135]

$$b'' \approx b' + i\,c \tag{3.4.7}$$

where b' is the real distance of closest approach that I compute with Eq. (3.4.4) and c is given by [130, 135]

$$c = \frac{\mathrm{Im}\{V_N(b')\}}{\frac{\mu v^2 b^2}{b'^3} - \left\{\frac{\partial}{\partial r}\left[\mathrm{Re}\{V_N(r)\} + V_C(r)\right]\right\}_{r=b'}}. \tag{3.4.8}$$

In the computation of the nuclear eikonal phase (2.1.33), the impact parameter b is thus replaced by the complex distance of closest approach

$$\chi^N(b) \quad \rightarrow \quad \chi^N(b''). \tag{3.4.9}$$

This implies that the nuclear potentials V_N (2.2.2) is computed from a complex distance

$$r'' = \sqrt{b''^2 + z^2}. \tag{3.4.10}$$

Computing the nuclear potential (2.2.2) with this complex distance r'' induces contributions from the real depth V_R (resp. imaginary depths W_I and W_D) of the potential to the imaginary part of the eikonal phase $\mathrm{Im}\{\chi^N\}$ (resp. real part of the eikonal phase $\mathrm{Re}\{\chi^N\}$). Therefore, the ratio of the real and imaginary parts of the eikonal phase $\mathrm{Re}\{\chi^N\}/\mathrm{Im}\{\chi^N\}$ changes, and the absorption from the elastic-scattering channel is modified. I did not shift the impact parameter to the complex distance b'' within the computation of the Coulomb eikonal phase (2.1.38) because the Coulomb interaction should not induce absorption and thus should stay real.

Because r'' is defined as the square root of a complex quantity, it has two possible values. As I interpret the overestimation of the cross sections at large angles by the eikonal model as a lack of absorption from the elastic-scattering channel, I would like to reduce the ratio $\mathrm{Re}\{\chi^N\}/\mathrm{Im}\{\chi^N\}$. This ratio diminishes when the imaginary part of r'' has the same sign as the imaginary part of b'', i.e., it is negative for optical potentials with $\mathrm{Im}\{V_N(b')\} < 0$ [see Eqs. (3.4.7)–(3.4.8)]. On the contrary, taking the square root which has a positive imaginary part causes an increase of the ratio $\mathrm{Re}\{\chi^N\}/\mathrm{Im}\{\chi^N\}$ and thus of the cross sections. To improve the absorption, I compute the nuclear potential appearing in the χ^N (2.1.33) with the negative root of r'', i.e., $V_N(r'')$.

I have compared the accuracy of the correction using the exact complex distance of closest approach, solution to Eq. (3.4.6), and its perturbative approximation (3.4.7)-(3.4.8). Both cross sections obtained for the elastic scattering of ^{10}Be with ^{12}C at 10A MeV lead to similar results up to $\theta \sim 30°$ and at larger angles, the approximation (3.4.7)-(3.4.8) leads to slightly better results. I have also verified that these observations are robust to changes in the beam energy as well as in the ratio of the imaginary and real depths of the optical potential. Similar tests made on the elastic scattering of ^{12}C off ^{16}O at 10A MeV (with the potential given in Ref. [121]) confirm these conclusions. Therefore, for numerical reasons, I have applied the correction (3.4.9) with the approximation (3.4.7)-(3.4.8).

Similarly to the real case (3.4.5), the conservation of the angular momentum can be ensured by adjusting the asymptotic velocity to the tangential velocity at the turning point of the classical trajectory, i.e, by multiplying the eikonal phase by b''/b. However, my results indicate that, in the cases considered here, it does not impact significantly the elastic-scattering cross sections at angles below 30° at 10A MeV. At larger angles, the cross sections are small and are usually not measured. I do not consider the ratio b''/b in the following.

The Rutherford-normalized elastic-scattering cross sections of ^{10}Be off ^{12}C at 20A MeV and 10A MeV are plotted in Fig. 3.4.4. The complex semiclassical correction (dash-dotted-dotted black lines) reduces the cross sections at large angles, which now lie close to the exact solution (solid red lines). Moreover, the oscillations are better reproduced at forward angles, even though, at larger angles, the oscillations have too large an amplitude. Using a complex distance of closest approach seems therefore the best way to simultaneously properly account for the absorption from the elastic channel and reproduce the correct oscillatory pattern. These findings are in full agreement with those of Ref. [121], where the ^{12}C-^{16}O and ^{16}O-^{208}Pb elastic scattering are studied. Because these results are so encouraging and robust to the choice of nuclei, I study in the next section the extension of the complex semiclassical correction to more complex reactions: the elastic scattering and the breakup of a one-neutron halo nucleus.

3.4.3 Extension to three-body collisions

To apply the complex semiclassical correction to the elastic scattering of one-neutron halo nuclei, it has to be generalized to three-body collisions (see the set of coordinates in Fig. 2.3.1). Similarly to the Coulomb semiclassical correction in Sec. 3.3, the complex semiclassical correction can be generalized by replacing the impact parameter b by the complex distance of closest approach b'' (3.4.7)–(3.4.8). The core-target and neutron-target nuclear eikonal phases (2.3.35)–(2.3.36) are then computed from $\boldsymbol{b}'' = b''\hat{\boldsymbol{b}}$ and $\boldsymbol{s}$

$$\chi^N_{(c,n)T}(\boldsymbol{b},\boldsymbol{s}) \to \chi^N_{(c,n)T}(\boldsymbol{b}'',\boldsymbol{s}) \tag{3.4.11}$$

This complex distance can be computed with different deflecting interactions. I consider two of them; the first uses V_{cT} and the second $V_{cT}+V_{nT}$, both evaluated at the distance R between the projectile center-of-mass and the target. These two methods lead to similar cross sections below 30° at 20A MeV and 50° at 10A MeV. Since the differences between

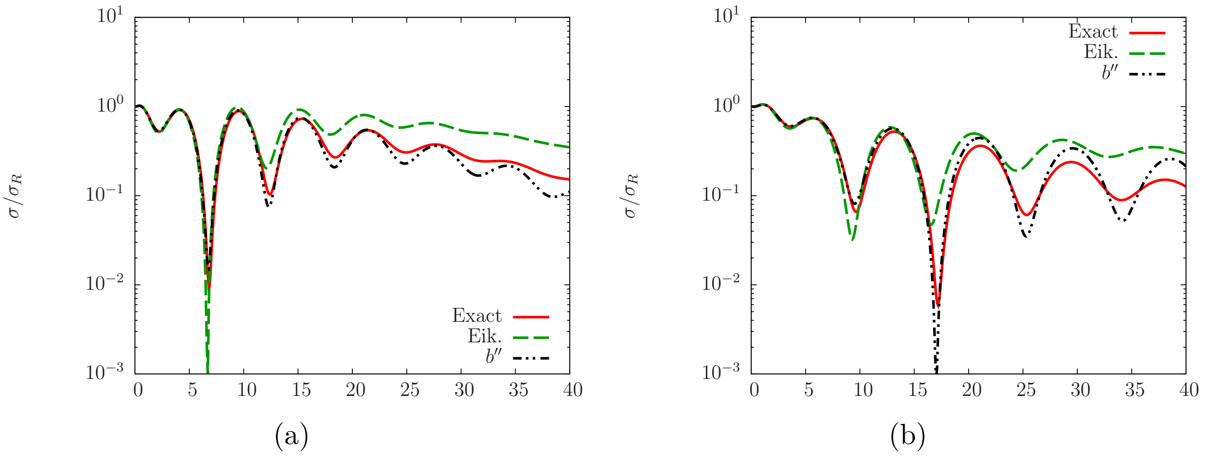

(a) (b)

Figure 3.4.4: Study of the complex semiclassical correction for the elastic scattering of ^{10}Be off ^{12}C at (a) 20A MeV and (b) 10A MeV. The cross sections are normalized to Rutherford and plotted as a function of the scattering angle θ.

these two calculations are small, only the results obtained with V_{cT} as deflecting interaction are presented here.

I have also tried a second generalization of the complex semiclassical interaction. I substitute within the nuclear eikonal phases (2.3.35)–(2.3.36), the c-T and n-T impact parameters b_{cT} and b_{nT} by their complex distances of closest approach b''_{cT} and b''_{nT} obtained from V_{cT} and V_{nT}, respectively, i.e.,

$$\chi^N_{cT}(\boldsymbol{b},\boldsymbol{s}) = \chi^N_{cT}(b_{cT}) \rightarrow \chi^N_{cT}(b''_{cT}) \tag{3.4.12}$$
$$\chi^N_{nT}(\boldsymbol{b},\boldsymbol{s}) = \chi^N_{nT}(b_{nT}) \rightarrow \chi^N_{nT}(b''_{nT}) \tag{3.4.13}$$

The drawback is that it affects the spatial extension of the projectile during the collision and thus violates the adiabatic approximation.

The elastic-scattering amplitude (3.3.24) at a certain b is thus computed with the phases (3.4.11) in the first implementation and with the phases (3.4.12) –(3.4.13) in the second one. As in the two-body case, the Coulomb interaction should not induce absorption and I do not shift the impact parameter within the Coulomb eikonal phases χ^C_{PT} (2.1.38) and χ^C (2.3.38) to the complex distance of closest approach. Moreover, shifting these phases to the real distance of closest approach b' does not impact significantly the results. Hence, I evaluate both Coulomb phases with $\boldsymbol{b}$ and $\boldsymbol{s}$.

At low energy, the adiabatic treatment of the collision becomes inadequate, since the collision time is not brief, and the dynamical effects start to play a role [136]. To test the influence of the sudden approximation at the energies considered here, I also extend the complex semiclassical correction to the DEA. As for the eikonal model, there are two possible generalizations. The first one shifts the projectile-target impact parameter b within the computation of the potentials in Eq. (2.3.31) to the complex distance of closest approach b'' [similarly to Eq. (3.4.11)]

$$\boldsymbol{R} \equiv (b,\theta,Z) \quad \rightarrow \quad \boldsymbol{R}'' \equiv (b'',\theta,Z) \tag{3.4.14}$$

where I compute b'' (3.4.7)–(3.4.8) with V_{cT} and $V_{cT}+V_{nT}$ as deflecting interaction. As in the eikonal model, both choices of deflecting interactions lead to similar cross sections below 30° at 20A MeV and 50° at 10A MeV. The second generalization replaces in Eq. (2.3.31) the transverse components of R_{cT} and R_{nT} by their corresponding complex distances of closest approach b''_{cT} and b''_{nT} obtained through Eq. (3.4.7)–(3.4.8)

$$\boldsymbol{R}_{cT} \equiv (b_{cT}, \theta, Z) \quad \rightarrow \quad \boldsymbol{R}''_{cT} \equiv (b''_{cT}, \theta, Z). \tag{3.4.15}$$

$$\boldsymbol{R}_{nT} \equiv (b_{nT}, \theta, Z) \quad \rightarrow \quad \boldsymbol{R}''_{nT} \equiv (b''_{nT}, \theta, Z). \tag{3.4.16}$$

In both implementations, shifting the Coulomb interactions induce a negligible modification of the results. To be consistent with the implementations of the semiclassical correction in the eikonal model, the results presented here are obtained without applying this shift to the Coulomb interaction.

The elastic-scattering cross sections of the one-neutron halo nucleus ^{11}Be impinging on a ^{12}C target at $20A$ MeV and $10A$ MeV are plotted in Fig. 3.4.5. I consider the CDCC method as the reference calculation (solid red lines). As already analysed in Sec. 3.3, the eikonal approximation (long-dashed green lines) overestimates CDCC cross sections at large angles and fails to reproduce the oscillatory pattern. Interestingly, the DEA cross sections (short-dashed magenta lines) lie close to the eikonal ones, indicating that the dynamics of the projectile has little effect on the elastic-scattering process at these energies.

At both energies, each implementation of the complex semiclassical correction seems to act similarly when applied to the eikonal model and the DEA. The first implementations in the eikonal model (3.4.11) (Eik. b'', dash-dotted-dotted black lines) and the DEA (3.4.14) (DEA b'', short-dashed gray lines) reproduce well CDCC cross sections at $20A$ MeV over the angular range considered here. At $10A$ MeV, the corrected DEA provides better results than the corrected eikonal, as it is closer to CDCC. Above 15°, it overestimates the magnitude of the oscillation, and induces a slight shift to larger angles. Nevertheless, the first implementation is accurate at both energies and improves significantly the accuracy of both the eikonal model and the DEA. The second implementations in the eikonal approximation (3.4.12)–(3.4.13) (Eik. b''_{cT} & b''_{nT}, dash-dotted blue lines) and the DEA (3.4.15)–(3.4.16) (DEA b''_{cT} & b''_{nT}, dotted orange lines) both produce a cross section in worst agreement with the reference CDCC calculation than the original eikonal and DEA calculations at $20A$ MeV, as the cross sections at angles above 15° fall below CDCC predictions. Surprisingly, it is not the same situation at $10A$ MeV, where they are as precise as CDCC up to 25°. At larger angles, the magnitude of the cross sections is well reproduced, even if the amplitudes of the oscillations are overcorrected. From this analysis, it seems that the first implementations in the eikonal model (3.4.11) and in the DEA (3.4.14) are more reliable than the second ones, respectively (3.4.12)–(3.4.13) and (3.4.15)–(3.4.16).

At $10A$ MeV, both implementations of the semiclassical correction improve greatly the eikonal description of the elastic scattering of halo nuclei at low energies, and, as such, properly correct the deflection of the projectile by the target. In particular, they simulate better the absorption from the elastic channel and reproduce the oscillatory pattern of the reference calculation. In addition, the major differences between these semiclassical corrections and the CDCC results are observed only at large angles, where measurements with exotic nuclei are usually difficult because of the low beam intensities achieved in RIB facilities. These encouraging results have driven me to extend this correction to breakup reactions.

Following the same idea, the complex semiclassical correction can be directly generalized to breakup reactions. To avoid the Coulomb divergence within the eikonal breakup matrix element, I use the CCE (see Secs. 2.3.3.4 and 2.3.3.5). In the CCE, the distribution of

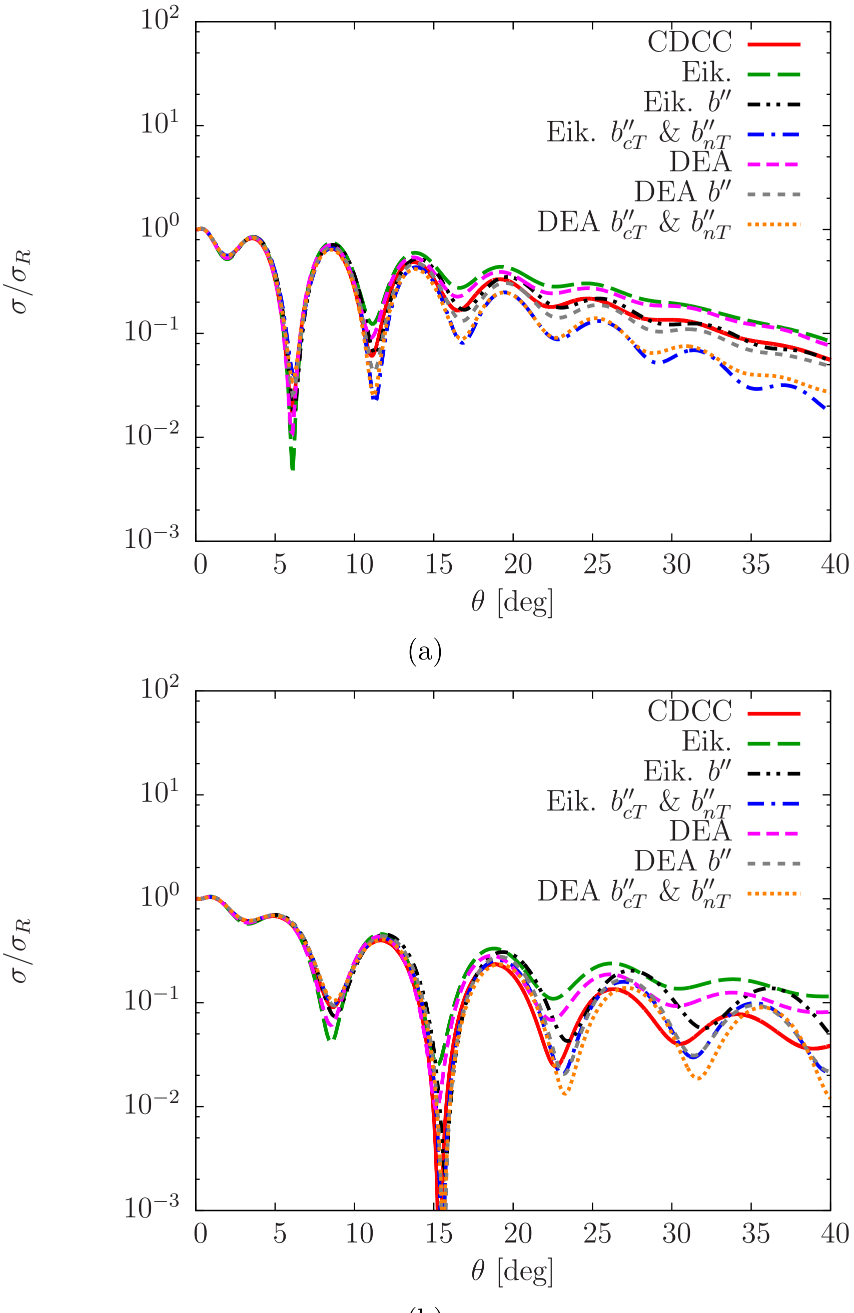

(a)

(b)

Figure 3.4.5: Analysis of the complex semiclassical correction for the elastic scattering of ^{11}Be off ^{12}C at (a) 20A MeV and (b) 10A MeV. I display the two different implementations of the corrections applied to both the eikonal approximation and the DEA: the one shifting the projectile impact parameter [see Eqs. (3.4.11) and (3.4.14), b''] and the other applied separately to each fragment's impact parameters [see Eqs. (3.4.12)–(3.4.13) and (3.4.15)–(3.4.16), b''_{cT} & b''_{nT}].

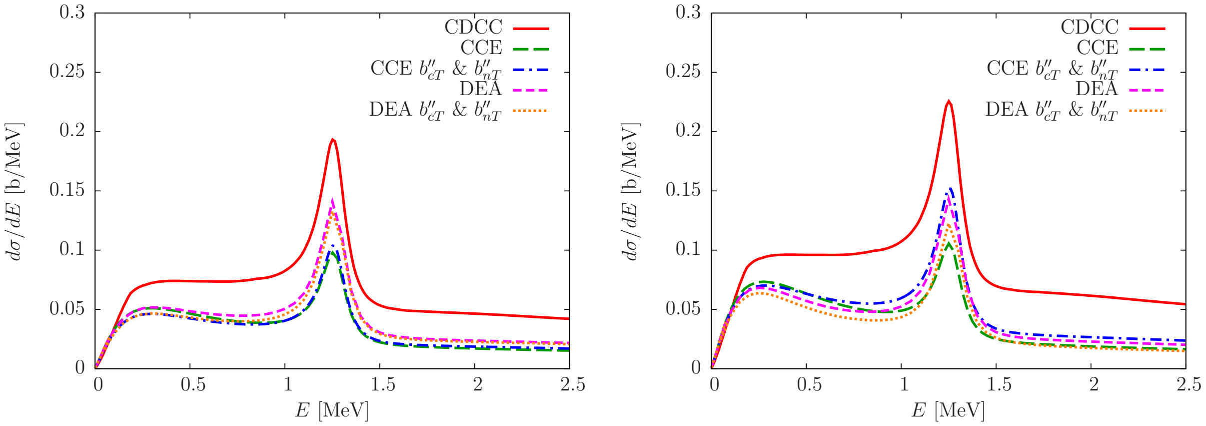

(a) (b)

Figure 3.4.6: Analysis of the complex semiclassical correction applied to the eikonal model and the DEA for the breakup cross sections of ^{11}Be off ^{12}C (a) at 20A MeV and (b) at 10A MeV. The breakup cross sections are plotted as a function of the ^{10}Be-n relative energy after dissociation E.

breakup as a function of the c-n relative energy after dissociation $E = \hbar^2 k^2/(2\mu_{cn})$ reads [$j = l$ and $m = m_l$ in Eq. (A.42)]

$$\frac{d\sigma_{bu}}{dE} = \frac{4\mu_{cn}}{\hbar^2 k}\frac{1}{2l_0+1}\sum_{m_{l_0}}\sum_{lm_l}\int_0^{+\infty} b\,db\,\left|S^{(m_{l_0})}_{klm_l}(b)\right|^2 \tag{3.4.17}$$

where the partial breakup amplitude is given by [$j = l$ and $m = m_l$ in Eq. (A.50)]

$$S^{(m_{l_0})}_{klm_l}(b) = e^{i[\delta_l(k)-l\pi/2]}e^{i\chi^C_{PT}(b)}\left\langle\phi_{klm_l}\right|\left[e^{i\chi^C} - i\chi^C + i\chi^{C,(\lambda=1)}_{\rm FO}\right]e^{i\chi^N}\left|\phi_{n_0l_0m_{l_0}}\right\rangle, \tag{3.4.18}$$

μ_{cn} is the c-n reduced mass and $\chi^{C,(\lambda=1)}_{\rm FO}$ is the dipole contribution of the first-order Coulomb approximation (2.3.44). I have applied both implementations (3.4.11) and (3.4.12)–(3.4.13) of the complex semiclassical correction to the nuclear phases appearing in the partial breakup amplitude (3.4.18).

The breakup cross section of ^{11}Be on ^{12}C at 20A MeV and at 10A MeV as a function of the ^{10}Be-n relative energy after dissociation E is plotted in Fig. 3.4.6. As explained in Chapter 1, these observables are sensitive to the continuum, in particular, the resonances cause peaks in the distribution [35]. In Fig. 3.4.6 , the peak is located at the energy of the d resonance in the ^{10}Be-n (see Sec. 3.2). Compared to CDCC (solid line), the CCE (dashed green line) reproduces the right shape of the distribution at both 20A MeV and 10A MeV, except in the range between 0.25 MeV and 1 MeV, where it predicts a local minimum. Unfortunately, it underestimates the cross sections by approximatively 30% at 20A MeV and 50% at 10A MeV, over the whole energy range. As in the elastic-scattering case, including the dynamics does not impact significantly the cross section: the DEA (short-dashed magenta lines) leads to a slightly larger cross section and improves the shape of the distribution between 0.25 MeV and 1 MeV, but this is far from enough to reach the CDCC accuracy.

Fig. 3.4.6 also shows that the second implementation of the semiclassical correction, shifting separately the c-T and n-T impact parameters, applied to the CCE (3.4.12)–(3.4.13) (dash-dotted blue lines) and to the DEA (3.4.15)–(3.4.16) (dotted orange lines) acts similarly on breakup observables at $20A$ MeV: it deteriorates the accuracy of these models, the cross sections are reduced below 1 MeV and there is no improvement at larger energy. However, at $10A$ MeV, the correction (3.4.12)–(3.4.13) applied to the CCE slightly improves the shape of the breakup distribution. Unfortunately, it still lies far from CDCC. The semiclassical correction (3.4.15)–(3.4.16) applied to the DEA reduces the magnitude of the cross sections and thus worsens the DEA calculations. Since the results obtained with the first implementation in the CCE (3.4.11) and in the DEA (3.4.14) lead to similar conclusions, I do not display the cross sections here. This suggests that using the complex distance of closest approach increases the absorption from all reaction channels and not just in the elastic-scattering one.

As shown in Appendix E, the complex semiclassical correction is sensitive to the choice of optical potentials. However, since in all cases it does not reproduce the breakup cross sections, I have not investigated more deeply the sensitivity to these interactions. The analysis made in this section is therefore specific to the potentials used in this Chapter. My conclusions are that this complex semiclassical correction is not a good approach, because it increases the absorption in all reaction channels and is sensitive to both the choice of optical potentials and beam energy. The analysis of this complex semiclassical correction has been published in Refs. [21, 22].

3.5 Exact continued S-matrix correction

3.5.1 Derivation of the exact continued S-matrix correction

Another way to correct the P-T relative motion is based on the exact correspondence between the partial-wave expansion and the eikonal model. Wallace has demonstrated it in the case of the elastic scattering of structureless nuclei, interacting through only the nuclear interaction [124]. I will account for the Coulomb interaction in a second step, as it is done in Ref. [123] .

First, I present Wallace's derivation for the neutral case. His main idea was to link the exact scattering amplitude (2.1.14) to the eikonal scattering amplitude (2.1.36). Eq. (2.1.14) can be written as

$$f_{\boldsymbol{k}}(\theta) \;=\; \sum_l A(l) P_l(\cos\theta). \tag{3.5.1}$$

If the potential varies smoothly, an analytic continuation $\mathcal{A}(\lambda)$ of $A(l)$ can be defined as [123, 124]

$$\begin{aligned} \mathcal{A}(\lambda) &= -i\frac{\lambda}{k}\left[S\left(\frac{\lambda}{k}\right)-1\right], & (3.5.2)\\ \text{with} \quad S\left(\frac{l+1/2}{k}\right) &= S_l(k), & (3.5.3)\end{aligned}$$

where S_l is the nuclear S-matrix (2.1.15) [124]. Regge demonstrated that physical values are realised for half-integer values of the λ with $\lambda = l + 1/2$ [137].

The sum in Eq. (3.5.1) is then converted into an integral using the Euler Summation Formula [92]. Wallace has demonstrated that, if the phase shifts at large l tend to zero and if their derivative is smaller than $\pi/2$ [124], we have

$$\sum_l A(l)P_l(\cos\theta) = \int_0^\infty d\lambda\, \mathcal{A}(\lambda)\, P_{\lambda-1/2}(\cos\theta) - R_1\left[\sin\left(\frac{\theta}{2}\right)\right], \tag{3.5.4}$$

where R_1 is a remainder, small at forward angles. He has then used the expansion of the Legendre function [124]

$$P_{\lambda-1/2}(\cos\theta)=\sum_{j=0}^{\infty}\frac{1}{(2j)!}\left(\frac{d}{d\lambda}\right)^{2j}b_j\left(\frac{d}{d\lambda}\left[\frac{\lambda}{2}\right]\right)J_0\left[2\lambda\sin\left(\frac{\theta}{2}\right)\right], \tag{3.5.5}$$

where the operators $b_j\,(x)=B_{2j}^{(2x)}(x)$ acts on the Bessel function J_0 and $B_{2j}^{(2x)}(x)$ are the generalized Bernoulli polynomials. The expressions of the first few orders j of these polynomials b_j are listed in Ref. [124]. With Eqs. (3.5.4) and (3.5.5), Wallace has shown that [124]

$$\begin{aligned}\sum_l A(l)P_l(\cos\theta) &= \int_0^{\infty}d\lambda\,J_0\left[2\lambda\sin\left(\frac{\theta}{2}\right)\right]\sum_{j=0}^{\infty}\frac{1}{(2j)!}b_j\left(-\frac{\lambda}{2}\frac{d}{d\lambda}\right)\left(\frac{d}{d\lambda}\right)^{2j}\mathcal{A}(\lambda)\\ &\quad\underbrace{+R_2\left[\sin\left(\frac{\theta}{2}\right)\right]-R_1\left[\sin\left(\frac{\theta}{2}\right)\right]}_{=0},\end{aligned} \tag{3.5.6}$$

where the remainder R_2 appears from the integration by part and cancels with R_1 [124].

In the impact parameter representation $b=\lambda/k$, Eq. (3.5.6) is the expansion of an exact Fourier-Bessel representation of the scattering amplitude [124]

$$f_{\boldsymbol{k}}(\theta)=-ik\int_0^{\infty}b\,db\,J_0(qb)[S^{\rm FB}(b)-1] \tag{3.5.7}$$

where $q=2k\sin(\theta/2)$. This scattering amplitude is similar to the eikonal one (2.1.36), where the eikonal S-matrix $S^{\rm eik}$ is replaced by the Fourier-Bessel S-matrix $S^{\rm FB}(b)$, which reads [124]

$$\begin{aligned}S^{\rm FB}(b) &= \frac{1}{b}\sum_{j=0}^{\infty}\frac{1}{(2j)!}b_j\left(-\frac{b}{2}\frac{d}{db}\right)\left(\frac{1}{k}\frac{d}{db}\right)^{2j}b\,S(b) && (3.5.8)\\ &= S(b)W[\delta] && (3.5.9)\\ \text{with } S(b) &= e^{2i\delta(b)} && (3.5.10)\\ W[\delta] &= \frac{1}{b}\sum_{j=0}^{\infty}\frac{1}{(2j)!}b_j\left(-ib\frac{d\delta}{db}(b)-\frac{1}{2}b\frac{d}{db}\right)\left(i\frac{2}{k}\frac{d\delta}{db}(b)+\frac{1}{k}\frac{d}{db}\right)^{2j}b, && (3.5.11)\end{aligned}$$

$\delta(b)$ the analytic continuation of the exact phase shift δ_l and $l=kb-1/2$. Since the expansion of the S-matrix $S^{\rm FB}$ is in k^{-2}, it will converge rapidly when k is large [124]. It is important to emphasize that no approximation is used to transform the partial-wave expansion sum (3.5.1) to this integral representation (3.5.7).

Brooke *et al.* proposed in Refs. [122, 123] to take only the first term of the expansion (3.5.8), i.e., to use $W[\delta]=1$ in Eq. (3.5.9). This corresponds to a small-angles approximation. The scattering amplitude is thus approximated by an eikonal amplitude (2.1.36), where the nuclear eikonal S-matrix $S^{\rm eik}$ (2.1.37) is replaced by the analytic continuation S (3.5.3) of the exact S-matrix S_l (2.1.15) [122, 123]

$$f_{\boldsymbol{k}}^{\rm EC}(\theta) = -ik\int_0^{\infty}b\,db\,J_0(qb)\left[S(b)-1\right], \tag{3.5.12}$$

where the impact parameter is linked to the angular momentum through $l=kb-1/2$. Brooke *et al.* have coined this approximation the *exact continued S-matrix correction* (EC) [122, 123].

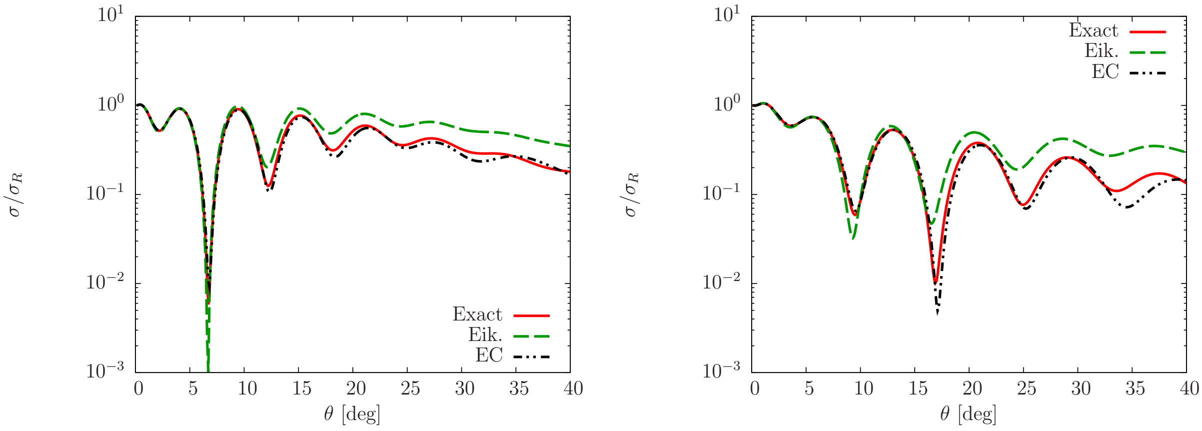

(a)

(b)

Figure 3.5.1: Analysis of the validity of the exact-continued S-matrix correction (EC) for the elastic scattering of ^{10}Be off ^{12}C at (a) $20A$ MeV and at (b) $10A$ MeV.

Since the P-T Coulomb phase χ^C_{PT} (2.1.38) leads to the exact Coulomb scattering amplitude, Brooke *et al.* have proposed in Refs. [122, 123] to account for the Coulomb interaction as in the eikonal model (2.1.39). The scattering amplitude computed with the exact continued S-matrix correction when both the nuclear and Coulomb interactions are considered reads [122, 123]

$$f^{\rm EC}_{\boldsymbol{k}}(\theta) = f^C_{\boldsymbol{k}}(\theta) - ik\int_0^\infty b\,db\,J_0(qb)e^{i\chi^C_{PT}(b)}\left[S(b)-1\right], \tag{3.5.13}$$

In my calculations, I thus simply replace the nuclear eikonal phase χ^N (2.1.33) by the exact phase shift $2\delta_l$ (2.1.12). I choose the angular momentum to be the closest integer l to the value obtained through $l = kb - 1/2$. I have checked that using this rough interpolation leads to similar results as more elaborate two- or four-points interpolation for noninteger l values.

First, I test the validity the exact continued S-matrix in a two-body collision. The Rutherford normalized elastic-scattering cross sections of ^{10}Be off ^{12}C at $20A$ MeV and $10A$ MeV are plotted in Fig. 3.5.1. We see that the exact continued S-matrix correction (EC, dash-dotted-dotted black lines) is very precise at both energies, its cross sections lie on top of the exact ones almost over the entire angular range considered here. They start to differ at $10A$ MeV only above 30°. The discrepancy appears at the lowest energy due to the convergence in k^{-2} of the expansion (3.5.8) and at large angles, because only the first term of Eq. (3.5.8) is considered. Nevertheless, this correction is accurate and hopefully is also efficient for three-body collisions.

3.5.2 Extension to three-body collisions

To extend the exact continued S-matrix correction to this three-body system, I follow Refs. [122, 123], where they approximate the elastic-scattering amplitude $S^{(m_{l_0})}_{0m'_{l_0}}(b)$ (3.3.24) by the matrix element of the product of the exact S-matrix of each constituent c, n

$$S^{(m_{l_0})}_{0m'_{l_0}}(b) = e^{i\chi^C_{PT}(b)}\left\langle \phi_{n_0l_0m'_{l_0}}\middle| e^{i\chi^C} S_{cT}S_{nT} \middle| \phi_{n_0l_0m_{l_0}}\right\rangle - \delta_{m_{l_0}m'_{l_0}}, \tag{3.5.14}$$

where S_{cT} and S_{nT} are the analytic continuations (3.5.3) of the exact nuclear S-matrix S_l (2.1.15) of the c-T and n-T collisions, respectively. As in the two body-case, I link

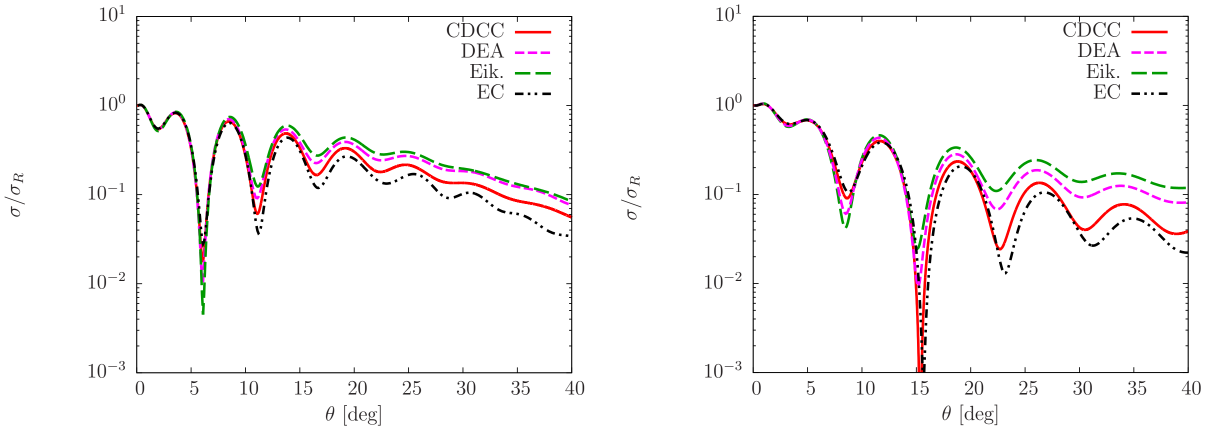

(a)

(b)

Figure 3.5.2: Analysis of the exact continued S-matrix for the elastic scattering of ^{11}Be off ^{12}C at (a) 20A MeV and (b) 10A MeV.

the angular momentum of each fragment to their impact parameter through $l_{(c,n)T} = K_{(c,n)}b_{(c,n)T} - 1/2$. This approximation makes sense in an adiabatic model, where the core and the neutron propagate at constant impact parameters, b_{cT} and b_{nT}, respectively.

To evaluate the accuracy of this correction for three-body collisions, the elastic scattering cross sections for ^{11}Be with ^{12}C at 20A MeV and at 10A MeV are plotted in Fig. 3.5.2. As for the other corrections, I use CDCC (solid red line) as benchmark. The exact continued S-matrix correction, displayed by the dash-dotted-dotted black line, reproduces well the magnitude of CDCC cross sections up to 15° at 20A MeV and up to 20° at 10A MeV. Contrary to the semiclassical correction, the accuracy of this correction does not depend significantly on the beam energy. At large angles, i.e. above 15° at 20A MeV and 20° at 10A MeV, it underestimates the CDCC predictions. In addition, the oscillatory pattern is precise but is slightly shifted to larger angles. My analysis indicates that this shift is due to the adiabatic assumption, still considered in this correction. The discrepancy with CDCC appears at large angles probably because the exact continued S-matrix truncates the series (3.5.8) at the zeroth order, which corresponds to a small-angles approximation.

Since it leads to interesting results for the elastic scattering, I apply this correction to the breakup of a one-neutron halo nucleus. To avoid the Coulomb divergence, I use the CCE (see Sec. 2.3.3.5) instead of the usual eikonal model. Similarly to the elastic-scattering, I replace within the computation of the partial-breakup amplitude (3.4.18) the nuclear eikonal S-matrix by the product of the exact S-matrix of each constituent c, n

$$S^{(m_{l_0})}_{klm_l}(b) = e^{i\chi^C_{PT}(b)} \langle \phi_{klm_l}| \left[e^{i\chi^C} - i\chi^C + i\chi^{C,(\lambda=1)}_{\rm FO}\right] S_{cT}S_{nT} \left|\phi_{n_0l_0m_{l_0}}\right\rangle . \tag{3.5.15}$$

The breakup cross sections for ^{11}Be with ^{12}C at 20A MeV and 10A MeV obtained with the generalization (3.5.15) are plotted in Fig. 3.5.3. Interestingly, the exact continued S-matrix correction gives results close to the DEA, although it still relies on the adiabatic approximation. This suggests that part of the projectile dynamics is restored through that correction. Unfortunately, even if this approach improves simultaneously both reaction channels, it is still not precise for breakup cross sections. From the short analysis presented in Appendix E, this conclusion seems to be independent of the choice of the optical potentials. This analysis has been published in Ref. [22].

Because the failure of the exact continued S-matrix correction might be due to too simplistic a generalization (3.5.15), I have tried to derive this correction properly from

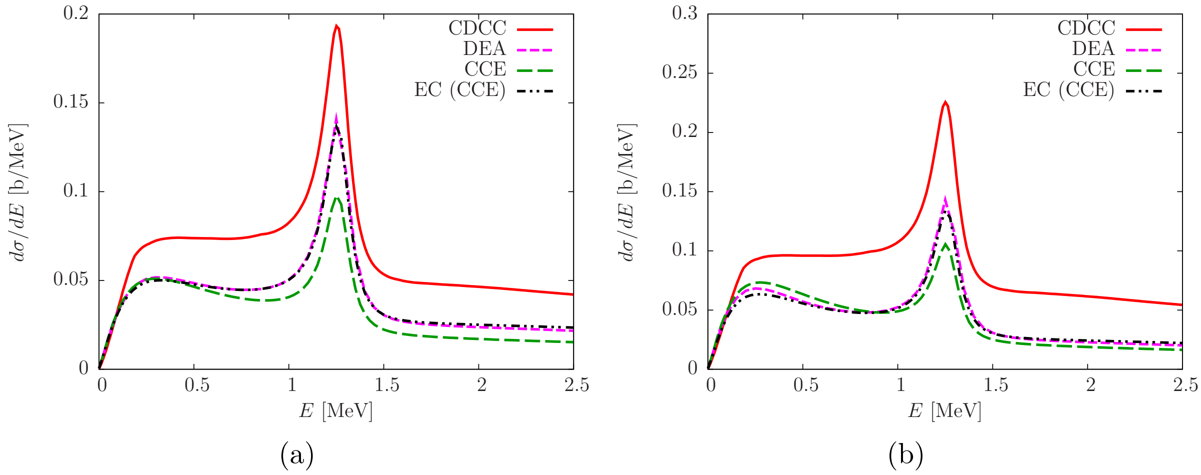

(a) (b)

Figure 3.5.3: Analysis of the exact continued S-matrix for the breakup of ^{11}Be off ^{12}C at (a) $20A$ MeV and (b) $10A$ MeV. The breakup distributions are plotted as a function of the relative c-n energy after dissociation E.

CDCC breakup amplitudes. As explained in Sec 2.3.3.2, the CDCC method relies on a discretization of the continuum states of the projectiles in bins. All projectile states are denoted p with $p = ilm_l$ for the bins in the continuum and $p = nlm_l$ for the bound states. The CDCC description of the three-body system is then solution to the partial-wave coupled equations for each $J_{\rm tot}$ (2.3.28), with $J_{\rm tot}$ resulting from the coupling of P-T and c-n angular momenta, respectively L and l. Each channel of the collision is thus characterized by the set of quantum numbers $\alpha = \{p, L\}$. The breakup amplitude for populating the bin state $p' = i'l'm_l'$ from the initial s ground state, i.e., $l_0 = m_{l_0} = 0$, with a P-T final wave vector $\boldsymbol{K'}_{p'} = (K'_{p'}, \Omega)$ reads [15]

$$\tilde{\mathcal{F}}_{m_l'0}(\boldsymbol{K'}_{p'}) = \frac{4\pi}{K}\sqrt{\frac{K'_{p'}}{K}} \sum_{LL'} (L' - m_l' l' m_l' | L0) \exp[i(\sigma_L + \sigma_{L'})] \frac{1}{2i} \mathbf{S}^L_{\alpha'\alpha_0}(p') Y_L^0\,(\Omega_0)\, Y_{L'}^{-m_l'}\,(\Omega) \tag{3.5.16}$$

where σ_L is the Coulomb phase shift (2.1.23), $\alpha_0 = \{n_0 l_0 m_{l_0}, L\}$ and $\alpha' = \{p', L'\}$ are respectively the initial and final channels and $\mathbf{S}^L_{\alpha'\alpha_0}(p')$ are the S-matrix elements (2.3.29) associated with an excitation of the projectile to the bin state p'. The differential cross section for the breakup of the projectile to a bin state p' as a function of the scattering angle of the center-of-mass of the projectile Ω is thus given by [15]

$$\frac{d\sigma(p')}{d\Omega} = \sum_{m_{l'}=-l'}^{+l'} \left|\tilde{\mathcal{F}}_{m_l'0}(\boldsymbol{K'}_{p'})\right|^2 . \tag{3.5.17}$$

I discuss here the difficulty that I have faced to relate the CDCC breakup cross sections to the eikonal one. The main challenge of this derivation is to transform the sums over the angular momenta into a continuous integral over the impact parameter, as in Eq (3.5.6). Because the P-T orbital angular momentum L is not conserved, the CDCC amplitude (3.5.16) contains two sums over the P-T angular momenta, generating couplings between the different states of the projectile. The analytic continuations of the angular momenta would therefore lead to two integrals over the impact parameters. I did not succeed to relate the CDCC breakup amplitude (3.5.16) to the eikonal one (A.32) because Eq. (A.32) contains only one integral over b. This is due to the fact that the derivatives over the transverse coordinate are neglected [see Eq. (2.1.29)]. This can be understood semiclassically as a lack of couplings between the different "trajectories" at neighbouring bs. It becomes more problematic at lower energies when the projectile spends more time around the target as its velocity is smaller. The projectile feels therefore more its interaction with the target, and more couplings between the angular momenta L arise.

The effects of these couplings between angular momenta onto reactions observables depend strongly on the transitions between the projectile states, triggered by its interaction with the target. For ^{11}Be, there are two main transitions from the ground state to the ^{10}Be-n continuum. First, the Coulomb tidal force induces a strong E1 transition from the s-wave ground state to the p-wave continuum. The strength of this E1 transition is larger for Coulomb-dominated breakup, viz. on heavy targets. Second, the nuclear interaction increases mainly the population of the d resonance, by allowing direct quadrupolar transitions from the s-wave ground state to this resonant state. Besides these two favoured ones, there are many other transitions within the ^{10}Be-n continuum and ^{11}Be bound states that occur during the collision.

To verify that the poor eikonal description of breakup at low energies is due to a lack of couplings between the angular momenta, I compare in Fig. 3.5.4 the contributions of dominating partial-waves to the energy distribution. Subfigures (a), (b) and (c) correspond respectively to the s, p and d contributions to the breakup of ^{11}Be with ^{12}C at 10A MeV obtained with CDCC (solid red lines), the DEA (short-dashed magenta lines), the CCE (dashed green lines) and the exact continued S-matrix (dash-dotted-dotted black lines). Compared to CDCC, all s-, p- and d-wave contributions are underestimated by the DEA, the CCE and the exact continued S-matrix correction. This suggests that the reaction mechanisms are not well described within these eikonal models and that the transitions that populate the continuum are underpredicted. In particular, the E1 transition which mainly populates the p wave below 1 MeV and the quadrupolar transition which excites the d resonance (see Appendix D) seem to be underestimated. Moreover, since the s-wave contribution is not well reproduced, it also suggests that the couplings within all the projectile states are not well simulated.

Finally, it is worth noting that the exact continued S-matrix changes the eikonal partial-wave cross section to a negligible extent except in the p wave, where it worsens the eikonal description. This correction does therefore not simulate well the transitions from the ground state to the continuum and within the continuum. My conclusions is that to improve these transitions and thus the description of breakup observables, the couplings between the different "trajectories" at different bs within the eikonal model have to be enhanced. This would hopefully improve the transitions between the states of the projectile.

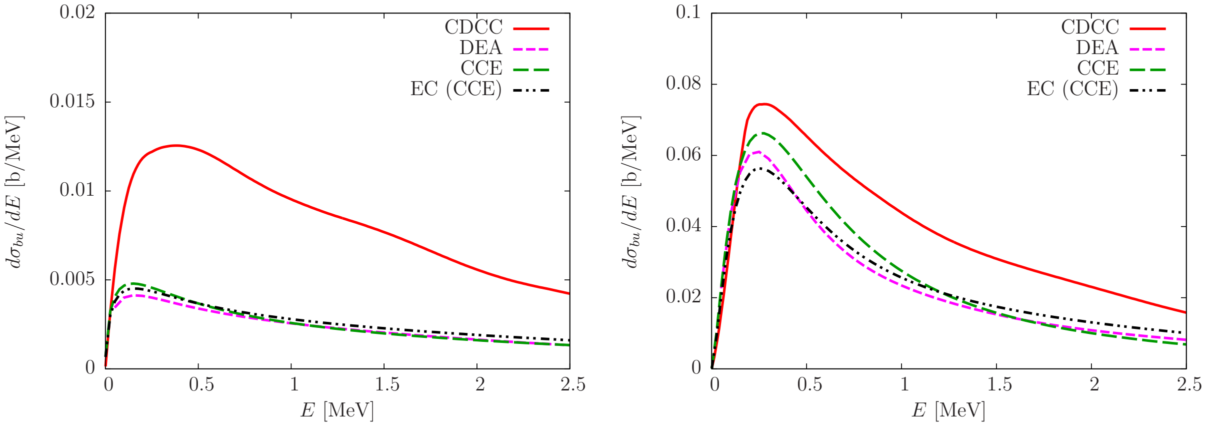

(a) s wave

(b) p wave

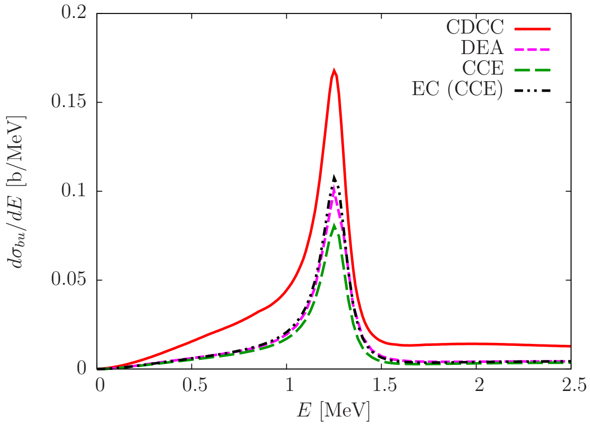

(c) d wave

Figure 3.5.4: Partial-wave analysis of the accuracy of the DEA, eikonal model and the exact continued S-matrix correction. Subfigures (a), (b) and (c) show respectively the s, p and d contributions to the ^{10}Be-n energy distribution after the breakup of ^{11}Be with ^{12}C at $10A$ MeV. The total breakup cross section is displayed in Fig. 3.5.3(b).

3.6 Distorted-Wave Eikonal Approximation

The main motivation of the DWEA is to simultaneously improve the deflection of the projectile by the target and restore some of the couplings between the different eikonal "trajectories". The idea is not to factorize a plane wave from the wave function but the asymptotic behaviour of a Coulomb wave function (2.1.17) and includes part of the second derivatives, which are neglected in the eikonal model (2.1.29). The P-T Coulomb deflection would therefore be included naturally. The numerical cost of the eikonal model can be recovered through a change of variables. This section presents the derivation of this model and emphasizes the main practical challenges.

3.6.1 Theoretical derivations

I derive this approximation in a simple case, the collision of two structureless and spinless nuclei, described by the Schrödinger equation (2.1.1). I consider both the nuclear and Coulomb potentials (2.1.16), i.e., $V = V_N + V_C$ in Eq (2.1.1). Similarly to the eikonal idea (2.1.27), I factorize the asymptotic behaviour of a Coulomb wave function (2.1.17) from the total wave function

$$\Psi(\boldsymbol{r}) = e^{i\varphi(\boldsymbol{r})}\,\tilde{\Psi}(\boldsymbol{r}). \tag{3.6.1}$$

with the Coulomb phase φ [90]

$$\varphi(\boldsymbol{r}) = kz + \eta\ln(kr - kz), \tag{3.6.2}$$

the P-T relative coordinate $\boldsymbol{r} \equiv (\rho, \phi, z)$, the initial P-T wave number k and the Sommerfeld parameter η (2.1.18).

In cylindrical coordinates, the Laplacian applied to this factorization reads

$$\Delta_{\boldsymbol{r}}\Psi(\boldsymbol{r}) \;=\; \left(\frac{\partial^2}{\partial\rho^2} + \frac{1}{\rho}\frac{\partial}{\partial\rho} + \frac{1}{\rho^2}\frac{\partial^2}{\partial\phi^2} + \frac{\partial^2}{\partial z^2}\right) e^{i\varphi(\boldsymbol{r})}\,\tilde{\Psi}(\boldsymbol{r}). \tag{3.6.3}$$

Using

$$\frac{\partial r}{\partial\rho} = \frac{\rho}{r} \tag{3.6.4}$$

$$\text{and}\quad \frac{\partial r}{\partial z} = \frac{z}{r} \tag{3.6.5}$$

the partial derivatives of φ can easily derived as

$$\frac{\partial\varphi}{\partial\rho}(\boldsymbol{r}) \;=\; \eta\frac{\rho}{r(r-z)}, \tag{3.6.6}$$

$$\frac{\partial^2\varphi}{\partial\rho^2}(\boldsymbol{r}) \;=\; -\eta\frac{r^3 - 2z^2 r + z^3}{r^3(r-z)^2}, \tag{3.6.7}$$

$$\frac{\partial\varphi}{\partial z}(\boldsymbol{r}) \;=\; k - \frac{\eta}{r}, \tag{3.6.8}$$

$$\frac{\partial\varphi}{\partial z^2}(\boldsymbol{r}) \;=\; \eta\frac{z}{r^3}, \tag{3.6.9}$$

and the following relation is respected

$$\Delta_{\boldsymbol{r}}\varphi(\boldsymbol{r}) = 0. \tag{3.6.10}$$

With the relations (3.6.6)–(3.6.10), Eq. (3.6.3) becomes

$$\begin{aligned}\Delta_{\boldsymbol{r}}\Psi(\boldsymbol{r}) &= -\left\{\left[\frac{\partial\varphi}{\partial\rho}(\boldsymbol{r})\right]^2+\left[\frac{\partial\varphi}{\partial z}(\boldsymbol{r})\right]^2\right\}e^{i\varphi(\boldsymbol{r})}\,\tilde{\Psi}(\boldsymbol{r})\\ &\quad +2ie^{i\varphi(\boldsymbol{r})}\left[\frac{\partial\varphi}{\partial\rho}(\boldsymbol{r})\frac{\partial\tilde{\Psi}}{\partial\rho}(\boldsymbol{r})+\frac{\partial\varphi}{\partial z}(\boldsymbol{r})\frac{\partial\tilde{\Psi}}{\partial z}(\boldsymbol{r})\right]+e^{i\varphi(\boldsymbol{r})}\Delta_{\boldsymbol{r}}\tilde{\Psi}(\boldsymbol{r}). \qquad (3.6.11)\end{aligned}$$

Following the idea of the eikonal model, I assume that the wave function does not differ much from this distorted wave and I neglect $\Delta_{\boldsymbol{r}}\tilde{\Psi}$ compared to its first-order derivatives. The P-T kinetic term of the Schrödinger equation (2.1.1) becomes

$$\begin{aligned}-\frac{\hbar^2}{2\mu}\Delta_{\boldsymbol{r}}\Psi(\boldsymbol{r}) &\approx \frac{\hbar^2}{2\mu}\left\{\left[\frac{\partial\varphi}{\partial\rho}(\boldsymbol{r})\right]^2+\left[\frac{\partial\varphi}{\partial z}(\boldsymbol{r})\right]^2\right\}e^{i\varphi(\boldsymbol{r})}\,\tilde{\Psi}(\boldsymbol{r})\\ &\quad -i\hbar\left[\frac{\hbar}{\mu}\frac{\partial\varphi}{\partial\rho}(\boldsymbol{r})\frac{\partial\tilde{\Psi}}{\partial\rho}(\boldsymbol{r})+\frac{\hbar}{\mu}\frac{\partial\varphi}{\partial z}(\boldsymbol{r})\frac{\partial\tilde{\Psi}}{\partial z}(\boldsymbol{r})\right]e^{i\varphi(\boldsymbol{r})}. \qquad (3.6.12)\end{aligned}$$

Considering the fact that the Sommerfeld parameter η (2.1.18) depends on k^{-1}, at high energies, i.e., large k, the first factor of the first term of Eq. (3.6.12) can be approximated by

$$\begin{aligned}\frac{\hbar^2}{2\mu}\left\{\left[\frac{\partial\varphi}{\partial\rho}(\boldsymbol{r})\right]^2+\left[\frac{\partial\varphi}{\partial z}(\boldsymbol{r})\right]^2\right\} &= \frac{\hbar^2}{2\mu}k^2-\frac{\hbar^2}{\mu}\frac{k\eta}{r}+\frac{\hbar^2}{\mu}\frac{\eta^2}{r(r-z)} \qquad (3.6.13)\\ &\approx \frac{\hbar^2}{2\mu}k^2-\frac{Z_PZ_Te^2}{4\pi\epsilon_0 r}. \qquad (3.6.14)\end{aligned}$$

The results (3.6.14) corresponds to the difference of the initial kinetic energy and the Coulomb potential (2.1.16).

In the second term of Eq. (3.6.12), the factors multiplying the derivatives of $\tilde{\Psi}$ have the dimensions of velocities, defined as

$$\begin{aligned}v_\rho(\boldsymbol{r}) &= \frac{\hbar}{\mu}\frac{\partial\varphi}{\partial\rho}(\boldsymbol{r})=\frac{\hbar\eta}{\mu}\frac{\rho}{r(r-z)} \qquad (3.6.15)\\ v_z(\boldsymbol{r}) &= \frac{\hbar}{\mu}\frac{\partial\varphi}{\partial z}(\boldsymbol{r})=\frac{\hbar k}{\mu}-\frac{\hbar\eta}{\mu r}. \qquad (3.6.16)\end{aligned}$$

These variables can be interpreted semiclassically as the transverse v_ρ and longitudinal v_z components of the velocity of a projectile which asymptotically is a straight line at an impact parameter b. The following relations are thus respected

$$\begin{aligned}\rho &\underset{z\to-\infty}{\longrightarrow} b \qquad (3.6.17)\\ v_\rho(\boldsymbol{r}) &\underset{z\to-\infty}{\longrightarrow} 0 \qquad (3.6.18)\\ v_z(\boldsymbol{r}) &\underset{z\to-\infty}{\longrightarrow} v, \qquad (3.6.19)\end{aligned}$$

where $v=\hbar k/\mu$ is the initial relative P-T velocity.

We can now define a new time variable τ as

$$v_\rho(\boldsymbol{r})=\frac{\partial\rho}{\partial\tau} \qquad (3.6.20)$$

$$v_z(\boldsymbol{r})=\frac{\partial z}{\partial\tau}. \qquad (3.6.21)$$

This new variable τ can be interpreted semiclassically as the intrinsic time of the trajectories following

$$\begin{aligned} z &= z_0 + \int_{-\infty}^{\tau} d\tau' \, v_z(\rho', z') & (3.6.22) \\ \rho &= b + \int_{-\infty}^{\tau} d\tau' \, v_\rho(\rho', z'), & (3.6.23) \end{aligned}$$

where z_0 is the initial value of z and (ρ', z') depend on (b, τ').

With the definitions of the velocities (3.6.15)–(3.6.16) and of τ (3.6.20)–(3.6.21), the second term of Eq. (3.6.12) becomes

$$\begin{aligned} -i\hbar\left[\frac{\hbar}{\mu}\frac{\partial\varphi}{\partial\rho}(\boldsymbol{r})\frac{\partial\tilde{\Psi}}{\partial\rho}(\boldsymbol{r}) + \frac{\hbar}{\mu}\frac{\partial\varphi}{\partial z}(\boldsymbol{r})\frac{\partial\tilde{\Psi}}{\partial z}(\boldsymbol{r})\right] &= -i\hbar\left[v_\rho(\boldsymbol{r})\frac{\partial\tilde{\Psi}}{\partial\rho}(\boldsymbol{r}) + v_z(\boldsymbol{r})\frac{\partial\tilde{\Psi}}{\partial z}(\boldsymbol{r})\right] & (3.6.24) \\ &= -i\hbar\frac{\partial\tilde{\Psi}}{\partial\tau}[\boldsymbol{r}(b,\tau)]. & (3.6.25) \end{aligned}$$

Using the DWEA approximation of the Laplacian (3.6.12), the approximation (3.6.14) and the new variable τ (3.6.25), the Schrödinger equation considering both the nuclear and Coulomb becomes, i.e., $V = V_N + V_C$ in Eq. (2.1.1), becomes

$$\begin{aligned} i\hbar\frac{\partial\tilde{\Psi}}{\partial\tau}[\boldsymbol{r}(b,\tau)] &= \left[V_C(r) + V_N(r) - \frac{Z_P Z_T e^2}{4\pi\epsilon_0 r}\right]\tilde{\Psi}[\boldsymbol{r}(b,\tau)] & (3.6.26) \\ &= V_N(r)\tilde{\Psi}[\boldsymbol{r}(b,\tau)]. & (3.6.27) \end{aligned}$$

Since the Coulomb deflection is already taken into account within the factorization (3.6.1), it does not appear in the DWEA equation (3.6.27). This equation describes a projectile following a trajectory defined by a velocity, whose components are given by Eqs. (3.6.15) and (3.6.16).

The DWEA scattering amplitude is derived by inserting the DWEA wave function (3.6.1) into Eq. (2.1.6)

$$f_{\boldsymbol{k}}(\theta) = \frac{1}{2\pi}\frac{\mu}{\hbar^2}\left\langle e^{i\boldsymbol{k}'\boldsymbol{r}}\middle| V_C + V_N \middle| e^{i\varphi(\boldsymbol{r})}\tilde{\Psi}\right\rangle, \qquad (3.6.28)$$

where $\boldsymbol{k}'$ is the final wave vector and $|\boldsymbol{k}'| = k$ because I am interested in the elastic-scattering channel. Using the Gellman-Golderger formula–also called the *two potential formula*–the scattering amplitude can be written as

$$f_{\boldsymbol{k}}(\theta) = \frac{1}{2\pi}\frac{\mu}{\hbar^2}\left\langle \psi_{\boldsymbol{k}'}^{C(-)}\middle| V_C \middle| e^{ikz}\right\rangle + \frac{1}{2\pi}\frac{\mu}{\hbar^2}\left\langle \psi_{\boldsymbol{k}'}^{C(-)}\middle| V_N \middle| e^{i\varphi(\boldsymbol{r})}\tilde{\Psi}\right\rangle \qquad (3.6.29)$$

where $\psi_{\boldsymbol{k}'}^{C(-)}$ is an incoming Coulomb function and is given by the exact solution of the Schrödinger equation considering only the Coulomb potential (2.1.16), i.e., $V = V_C$ in Eq. (2.1.1). The asymptotic behaviour of this function is given by the one of $\left(\psi_{-\boldsymbol{k}'}^{C}\right)^*$ (2.1.17).

I approximate the first term of Eq. (3.6.29) by its Born approximation

$$\begin{aligned}
\frac{1}{2\pi}\frac{\mu}{\hbar^2}\left\langle\psi_{\boldsymbol{k}'}^{C(-)}\middle|V_C\middle|e^{ikz}\right\rangle &\approx \frac{1}{2\pi}\frac{\mu}{\hbar^2}\left\langle e^{i\boldsymbol{k}'\boldsymbol{r}}\middle|V_C\middle|e^{ikz}\right\rangle && (3.6.30)\\
&= \frac{\mu}{\hbar^2}\int_0^{+\infty} dr\, r^2\int_0^{\pi}\sin\theta\, d\theta\, e^{-iqr\cos\theta}V_C(r) && (3.6.31)\\
&= \frac{\mu}{\hbar^2}\frac{2}{q}\int_0^{+\infty} dr\, r\sin(qr)V_C(r) && (3.6.32)\\
&= \frac{\mu}{\hbar^2}\frac{Z_TZ_Pe^2}{4\pi\epsilon_0}\frac{2}{q}\int_0^{+\infty} dr\,\sin(qr), && (3.6.33)
\end{aligned}$$

where $\hbar\boldsymbol{q} = \hbar(\boldsymbol{k}' - k\hat{\boldsymbol{z}})$ is the transferred momentum. By screening the integrand in Eq. (3.6.33)

$$\begin{aligned}
\int_0^{+\infty} dr\,\sin(qr) &= \lim_{\lambda\to 0}\int_0^{+\infty} dr\, e^{-\lambda r}\sin(qr) && (3.6.34)\\
&= \frac{1}{2i}\lim_{\lambda\to 0}\left[\int_0^{+\infty} dr\, e^{-\lambda r+iqr} - \int_0^{+\infty} dr\, e^{-\lambda r-iqr}\right] && (3.6.35)\\
&= \frac{1}{2i}\lim_{\lambda\to 0}\left[\frac{1}{\lambda - iq} - \frac{1}{\lambda + iq}\right] && (3.6.36)\\
&= \frac{1}{q}, && (3.6.37)
\end{aligned}$$

we can show that this scattering amplitude leads to the Rutherford cross section

$$\begin{aligned}
\frac{d\sigma_R}{d\theta} &= \left|\frac{1}{2\pi}\frac{\mu}{\hbar^2}\left\langle\psi_{\boldsymbol{k}'}^{C(-)}\middle|V_C\middle|e^{ikz}\right\rangle\right|^2 && (3.6.38)\\
&= \left(\frac{Z_TZ_Pe^2}{4\pi\epsilon_0}\right)^2\frac{\mu^2}{4\hbar^4k^4}\sin^{-4}\left(\frac{\theta}{2}\right). && (3.6.39)
\end{aligned}$$

Therefore, I approximate the first term of Eq. (3.6.29) by the exact Coulomb scattering amplitude $f_{\boldsymbol{k}}^C$ (2.1.19)

$$\frac{1}{2\pi}\frac{\mu}{\hbar^2}\left\langle\psi_{\boldsymbol{k}'}^{C(-)}\middle|V_C\middle|e^{ikz}\right\rangle \approx f_{\boldsymbol{k}}^C(\theta). \qquad (3.6.40)$$

Now I focus on the additional scattering amplitude given by the second term of Eq. (3.6.29), it reads

$$\begin{aligned}
f_{\boldsymbol{k}}^{\text{add}}(\theta) &= \frac{1}{2\pi}\frac{\mu}{\hbar^2}\int d\boldsymbol{r}\,\left[\psi_{\boldsymbol{k}'}^{C(-)}(\boldsymbol{r})\right]^* V_N(r)e^{i\varphi(\boldsymbol{r})}\widetilde{\Psi}(\boldsymbol{r}) && (3.6.41)\\
&= i\frac{1}{2\pi}\frac{\mu}{\hbar}\int d\boldsymbol{r}\,\left[\psi_{\boldsymbol{k}'}^{C(-)}(\boldsymbol{r})\right]^* e^{i\varphi(\boldsymbol{r})}\frac{\partial\widetilde{\Psi}}{\partial\tau}(\boldsymbol{r}). && (3.6.42)
\end{aligned}$$

Here I replace in Eq. (3.6.41) the right-hand side of Eq. (3.6.27) by its left-hand side. By changing the variable $(\rho,\phi,z)\to(b,\phi,\tau)$, this equation becomes

$$\begin{aligned}
f_{\boldsymbol{k}}^{\text{add}}(\theta) &= i\frac{1}{2\pi}\frac{\mu}{\hbar}\int_0^{2\pi} d\phi\int_0^{+\infty} b\, db\\
&\quad\times\int_{-\infty}^{\infty} d\tau\, J(b,\tau)\left\{\psi_{\boldsymbol{k}'}^{C(-)}[\boldsymbol{r}(b,\tau)]\right\}^* e^{i\varphi[\boldsymbol{r}(b,\tau)]}\frac{\partial\widetilde{\Psi}}{\partial\tau}[\boldsymbol{r}(b,\tau)], && (3.6.43)
\end{aligned}$$

where J is the Jacobian associated with the change of variable.

If I assume, as in the eikonal model that the transferred momentum is purely transverse, the product of the Coulomb wave function $\left(\psi_{\boldsymbol{k}'}^{C(-)}\right)^*$ and its asymptotic behaviour $e^{i\varphi}$ should be bound, i.e,

$$\left\{\psi_{\boldsymbol{k}'}^{C(-)}[\boldsymbol{r}(b,\tau)]\right\}^* e^{i\varphi[\boldsymbol{r}(b,\tau)]} \underset{\tau\to\pm\infty}{\longrightarrow} g^{\pm}(b), \tag{3.6.44}$$

where $g^{\pm}$ is the asymptotic value of this product for each b at $\tau \to \pm\infty$. As a first step, I could use this asymptotic value and approximate the scattering amplitude as

$$f_{\boldsymbol{k}}^{\text{add}}(\theta) \approx i\frac{1}{2\pi}\frac{\mu}{\hbar}\int_0^{2\pi} d\phi \int_0^{+\infty} b\,db\,g(b)\int_{-\infty}^{\infty} d\tau\, J(b,\tau)\frac{\partial\widetilde{\Psi}}{\partial\tau}[\boldsymbol{r}(b,\tau)]. \tag{3.6.45}$$

To recover the eikonal efficiency, J needs to be extracted from the integral on τ, and thus I need to find a good approximation of the Jacobian by a value independent on τ.

The Jacobian J is defined as

$$\begin{aligned} J(b,\tau) &= \begin{vmatrix} \frac{\partial\rho}{\partial b} & \frac{\partial\rho}{\partial\tau} \\ \frac{\partial z}{\partial b} & \frac{\partial z}{\partial\tau} \end{vmatrix} \\ &= \frac{\partial\rho}{\partial b}v_z - \frac{\partial z}{\partial b}v_\rho, \end{aligned} \tag{3.6.46}$$

where I use the definitions of the velocities v_ρ (3.6.20) and v_z (3.6.21). The partial derivatives appearing in the Jacobian (3.6.46) can be computed numerically along the trajectories defined by Eqs. (3.6.22)–(3.6.23).

By taking the limit $\tau \to -\infty$, I recover the Jacobian associated with straight-line "trajectories", i.e.,

$$J(b,\tau) \underset{\tau\to-\infty}{\longrightarrow} v. \tag{3.6.47}$$

After the collision at $\tau \to +\infty$, the Jacobian reads

$$J(b,\tau) \underset{\tau\to+\infty}{\to} \left[1 + \int_{-\infty}^{+\infty} d\tau\, \frac{\partial v_\rho(\rho,z)}{\partial b}\right] v - \int_{-\infty}^{+\infty} d\tau\, \frac{\partial v_z(\rho,z)}{\partial b} \lim_{\tau\to+\infty} v_\rho(\rho,z). \tag{3.6.48}$$

If the projectile stays far from the target, i.e., at large bs, the trajectories are close to straight lines, v_ρ tends to zero and the Jacobian is thus equal to the asymptotic velocity v. If the projectile passes close to the target, i.e., at small bs, the "trajectories" are distorted and the Jacobian takes values different from v.

3.6.2 Analysis of the DWEA trajectories and Jacobian

In this section, I present a numerical analysis of the DWEA trajectories defined by v_ρ (3.6.20) and v_z (3.6.21) and of the Jacobian (3.6.46). I use as a test case the elastic scattering of ^{10}Be off ^{208}Pb at $10A$ MeV.

Fig. 3.6.1 displays respectively (a) the classical Coulomb and (b) the DWEA trajectories for different impact parameters b. Interestingly, compared to classical Coulomb trajectories, these DWEA trajectories do not cross each other. This means that the variable change is bijective in all points of the (ρ, z) space, except for the ones behind the target that cannot be reached by these trajectories. This part of the space should not play an important physical role since it corresponds to the small-b region where the nuclear absorption is large.

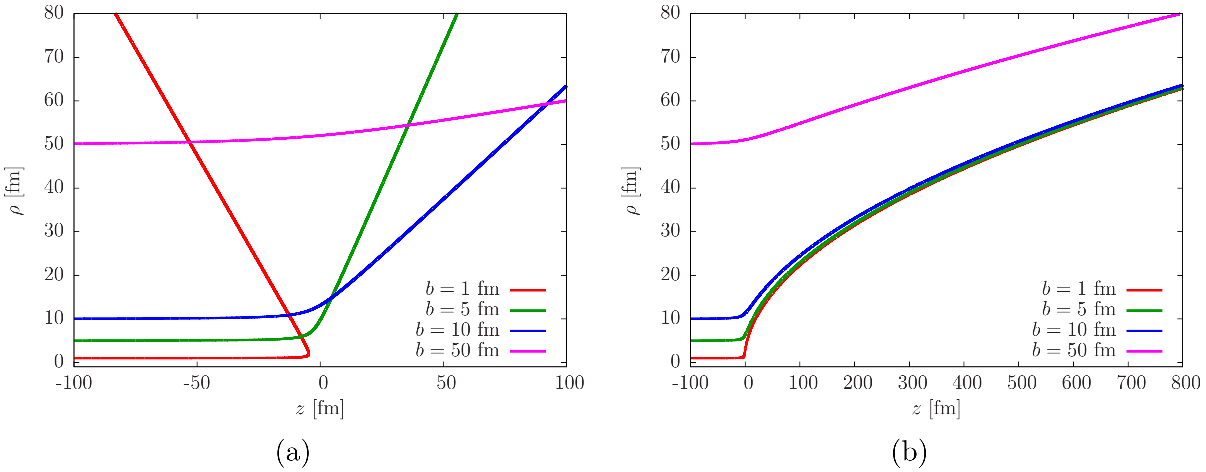

Figure 3.6.1: Comparison of (a) the classical Coulomb and (b) DWEA trajectories for the ^{10}Be impinging on ^{208}Pb at 10A MeV.

Compared to the eikonal approximation which assumes the velocity to be constant along the trajectory, the longitudinal velocity v_z varies during the collision. Fig. 3.6.2 shows the relative difference of the v_z (3.6.16) and the initial velocity v (3.6.19) for ^{10}Be impinging on ^{208}Pb at 10A MeV. We can see that the velocity decreases when the projectile approaches the target at $z = 0$ fm and increases again after the target. This is caused by the second term of Eq. (3.6.16), accounting for the P-T Coulomb repulsion. As expected, this change in longitudinal velocity is stronger for small impact parameters b.

In Fig. 3.6.3, I plot the Jacobian (3.6.46) normalized to the asymptotic velocity v calculated for ^{10}Be impinging on ^{208}Pb at 10A MeV. As predicted, for all impact parameters, the Jacobian is initially simply given by the asymptotic velocity v. At large impact parameter bs, the Jacobian does not deviate much from this value during the collision because the trajectory is close to a straight line. For smaller impact parameters, the Jacobian decreases when the projectile starts to interact with the target, around $z \sim 0$. This reduction is smoother and smaller for larger impact parameters, as their trajectories is less deflected. Because the Jacobian varies for most of the impact parameters which contribute to the cross section, approximating it by a value independent on τ would not be precise.

Because the Jacobian varies in τ, it cannot be extracted from the integral over τ in Eq. (3.6.45). Hence, I have not been able to recover the eikonal form and its numerical cost. In this form, the DWEA calculations would therefore be too heavy in practice. However, it would be interesting to conduct a numerical study the scattering amplitude (3.6.45) to evaluate if these variations in the Jacobian impact much the cross sections. This could be done by integrating by part over τ.

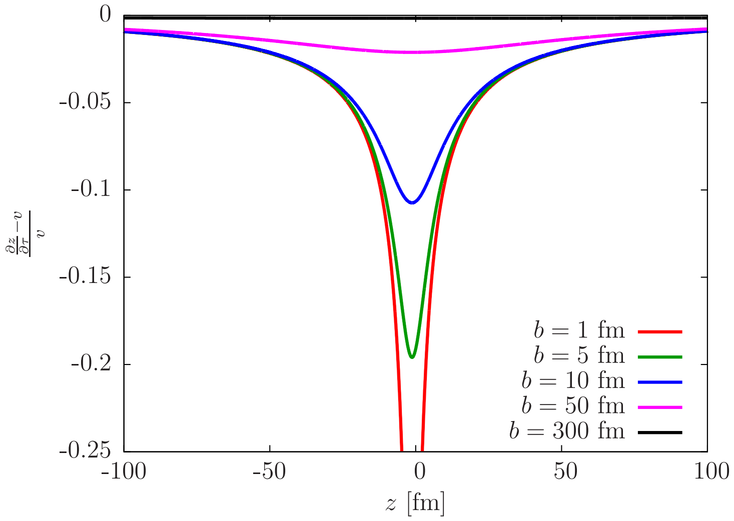

Figure 3.6.2: Analysis of the deviation of the longitudinal velocities v_z (3.6.16) from the initial velocity v for the ^{10}Be impinging on ^{208}Pb at 10A MeV.

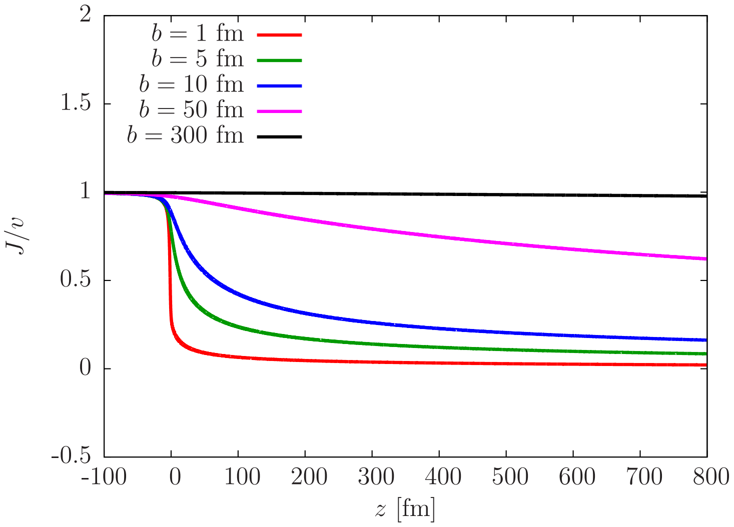

Figure 3.6.3: Normalized Jacobian of the coordinate change $(\rho, z) \rightarrow (b, \tau)$ as a function of the longitudinal coordinate z. This is calculated for ^{10}Be impinging on ^{208}Pb at 10A MeV.

3.7 Summary and prospects

The near-future facilities HIE-ISOLDE at CERN or ReA12 at FRIB will deliver RIBs at about 10A MeV. Around these energies, CDCC can have convergence issues [103] and is expensive computationally. This motivates the study of the extension of the eikonal model down to low energies. We have seen in this Chapter that for the elastic-scattering of structureless nuclei at low energies, the eikonal model overestimates the cross sections and dampens its oscillations at large angles. These two effects increase at lower energies, where the eikonal approximation is less accurate. The eikonal model behaves similarly in the case of the elastic scattering of one-neutron halo nucleus, as it also lacks absorption at large angles. The breakup channel is also not well described by the eikonal approximation, which underestimates CDCC calculations by approximatively 50% at 10A MeV and does not reproduce the right shape of the distribution.

In this Chapter, the extension of the eikonal model down to 10A MeV, in the energy range of HIE-ISOLDE at CERN or ReA12 at FRIB, is investigated through the study of corrections to the deflection of the projectile by the target. Because the authors of Refs. [114, 115] have already proven the efficiency of a Coulomb semiclassical correction, I have focused in this Chapter on corrections to the nuclear deflection within the eikonal model, in order to extend its range of validity for nuclear-dominated reactions down to 10A MeV.

Wallace's correction [117, 118, 119] relies on a T-matrix expansion, which accounts for the deflection of the projectile due to its nuclear interaction with the target. We have seen that, for one-body and two-body projectiles, this correction induces a shift of the oscillations of the cross sections to forward angles at low energy. I have interpreted this shift as a overestimation of the nuclear attraction between the colliding nuclei. To counter this shift, I have used the Coulomb semiclassical correction, which simulates the Coulomb repulsion between the nuclei. By combining both corrections, the oscillations are in phase with the exact ones. Unfortunately, the magnitude of the cross section is still overestimated at large angles. Since it is not accurate for the elastic scattering channel, I have not studied the extension of this correction to breakup reactions.

In order to have a correction that treats both interactions on the same footing, I have generalized the semiclassical correction to the nuclear attraction. As a first attempt, I have shifted the impact parameter to the real distance of closest approach computed from the sum of the Coulomb and real part of the nuclear potential. As observed in Ref. [114], this correction improves significantly the accuracy of two-body collisions dominated by the Coulomb repulsion where the nuclear interaction plays a small role. Unfortunately, I have shown here that it is not efficient for nuclear-dominated collisions [20].

On the contrary, the complex semiclassical correction [121] that uses a complex distance of closest approach is much more efficient, as it increases the absorption from the elastic-scattering channel within the eikonal model. Accordingly, it significantly reduces the elastic-scattering cross sections at large angles of both one- and two-body projectiles computed at the eikonal approximation, leading to values respectively close to the exact and CDCC calculations. Although its generalization to breakup reactions is straightforward, it tends to deteriorate the accuracy of the eikonal model as it reduces the breakup cross sections [21, 22]. This suggests that the semiclassical complex correction increases the absorption in all reaction channels. Moreover, this correction is not reliable since it is sensitive to both the choice of the optical potentials and the beam energy.

Another way to better simulate the deflection of the projectile by the target is to use the exact continued S-matrix correction [122, 123]. This correction, developed by Wallace for two-body collisions [124] consists on replacing the eikonal S-matrix by the exact S-matrix. Previous work [122] demonstrates its efficiency for the elastic scattering of both structureless nuclei and one-neutron halo nuclei with a target, I have generalized it here to breakup reactions. Unfortunately, this correction brings only a small accuracy gain in the description of nuclear-dominated breakup at the eikonal approximation [22].

All aforementioned corrections improves only the eikonal description of elastic scattering of one-neutron halo nuclei at energies reachable by HIE-ISOLDE and ReA12 but fail for breakup reactions. Because, they all focus on improving the nuclear deflection of the projectile by the target, I believe that to improve the eikonal description of breakup observables, another flaw of the model should be tackled. My analysis has emphasized that the dynamics of the projectile has little effects on both elastic-scattering and breakup observables at $10A$ MeV. By comparing the breakup matrix elements of CDCC and the eikonal model, I have noted that CDCC accounts for more couplings between the angular momenta. This lack of couplings between the eikonal "trajectories" is a consequence of the neglect of the transverse derivatives of the wave function, contained in the kinetic term. My analysis of the contribution of dominating partial-waves to the breakup cross sections indicates that transitions between the ground state and the continuum as well as within the continuum are not well reproduced by the eikonal model. I believe that to better account for these transitions, the couplings between the eikonal "trajectories" have to be enhanced.

This motivates the development of the DWEA, which aims at simultaneously improving the Coulomb deflection of the projectile by the target and including part of these transverse derivatives. Instead of the usual plane wave, the asymptotic form of a Coulomb function is factorized out of the projectile-target wave function. By reasoning similarly as in the eikonal model and with a change of variables, I have found an eikonal-like equation, depending on an intrinsic time τ and the impact parameter b. Unfortunately, the Jacobian associated to this change of variable varies with τ and cannot be extracted from the integral over τ in the scattering amplitude. Therefore, I have not been able to recover the eikonal efficiency. Further studies could be made to better understand the influence of this Jacobian on the cross sections.

Another avenue to address the lack of couplings between the angular momenta within the eikonal model would be to account for part of the second-order derivatives of the projectile-target wave function, neglected by the eikonal approximation. In order to keep the numerical cost small, I propose to treat only the first derivative along the transverse coordinate as a perturbation. This test would probably give an estimate of the significance of these couplings. I hope that it could simultaneously improve both the eikonal description of the elastic-scattering and breakup channels at $10A$ MeV. Nevertheless, one should keep in mind that the main advantage of the eikonal approximation is its numerical cost, it might not be worth to develop more elaborate corrections if they are expensive computationally.

Chapter 4

Simplification to the Dynamical Eikonal Approximation

4.1 Introduction

As mentioned in Chapter 1, Coulomb-dominated breakup reactions of halo nuclei can be used to infer the E1 strength functions from the ground state to the core-neutron continuum [10, 35, 64] and radiative-capture rates of astrophysical interest [70, 71]. Further works [66, 67, 68, 69, 72, 73, 74] emphasize that information inferred from Coulomb-dominated breakup reactions depend strongly on the interferences between the transitions due to both Coulomb and nuclear interactions. Because it relies on the adiabatic approximation and is thus incompatible with long-range interactions, the usual eikonal approximation diverges for Coulomb-dominated breakup (see Sec. 2.3.3.4). The dynamical eikonal approximation (DEA) does not have this issue, since it accounts for the dynamical effects. Moreover, its predictions are in good agreement with breakup data of one-neutron halo nuclei on light and heavy targets [107]. Unfortunately, the DEA is associated with a large numerical cost, since it is solved with an evolution calculation of the wave function [107, 108]. This motivates the development of approximations, which would be cheaper from a computational viewpoint.

The Coulomb-corrected eikonal approximation (CCE) solves efficiently the Coulomb divergence within the usual eikonal model. It simply replaces the diverging term by the first-order-perturbation Coulomb approximation (see Sec. 2.3.3.5). This model improves significantly the energy and parallel-momentum distributions for Coulomb-dominated breakup of one-neutron halo nuclei at 69 MeV [112]. Nonetheless, this correction mixes two reaction models and treats the nuclear and the Coulomb interactions on different footings.

In this Chapter, a simplification to the DEA (S-DEA), developed in collaboration with Daniel Baye, is presented. The S-DEA naturally removes the Coulomb divergence while treating both interactions within the same framework. This model is derived from an approximate solution of the DEA equation (2.3.31) and has the advantage of having a numerical cost similar to the usual eikonal model. After presenting the S-DEA in Sec. 4.2, its efficiency is studied in the cases of the nuclear- and Coulomb-dominated breakups of a one-neutron halo nucleus, viz. on light and heavy targets. I consider ^{11}Be impinging on ^{12}C and ^{208}Pb targets at 67A MeV and 69A MeV, respectively. Both of these reactions have been measured at RIKEN [35] and the experimental data are well reproduced by the DEA [107]. I compare the breakup observables computed with the S-DEA to the ones obtained with the full DEA and the CCE. I also present an analysis of the interferences between the transitions induced by both the Coulomb and nuclear interactions. Finally, the conclusions and some prospects for this model are given.

This work has been published in Phys. Rev. C [25].

4.2 Theoretical developments

As seen in Chapter 2, the reactions involving one-neutron halo nuclei are modelled as three-body collisions. I use in this Chapter the same three-body description and same system of coordinates (see Fig. 2.3.1) as the ones presented in Sec. 2.3. Within the DEA framework, the P-T relative motion is described by the solution $\Psi^{\rm DEA}$ of Eq. (2.3.31), rewritten here for convenience

$$i\hbar v\frac{\partial}{\partial Z}\widehat{\Psi}^{\rm DEA}(\boldsymbol{R},\boldsymbol{r}) =[h_{cn}-E_{n_0l_0j_0}+V_{cT}(R_{cT})+V_{nT}(R_{nT})]\widehat{\Psi}^{\rm DEA}(\boldsymbol{R},\boldsymbol{r}). \tag{4.2.1}$$

The S-DEA is based on a unitary transformation of the wave function $\widehat{\Psi}^{\rm DEA}$

$$\widehat{\Psi}^{\rm DEA}(\boldsymbol{R},\boldsymbol{r}) \;=\; e^{-i(h_{cn}-E_{n_0l_0j_0})\frac{Z}{\hbar v}}\,e^{-\frac{i}{\hbar v}\int_{-\infty}^{Z}dZ'\,V_C^{PT}(R')}\,\widetilde{\Psi}(\boldsymbol{R},\boldsymbol{r}) \tag{4.2.2}$$

where V_C^{PT} is a pure Coulomb potential (2.1.16) between the projectile and the target. With the initial condition on Ψ (2.3.12), this new wave function tends initially to the ground state of the projectile $\phi_{n_0l_0j_0m_0}$, i.e.,

$$\widetilde{\Psi}^{(m_0)}(\boldsymbol{R},\boldsymbol{r}) \xrightarrow[Z\to-\infty]{} \phi_{n_0l_0j_0m_0}(\boldsymbol{r}). \tag{4.2.3}$$

By inserting the unitary transformation (4.2.2) into the DEA equation (4.2.1), it becomes

$$i\hbar v\frac{\partial}{\partial Z}\widetilde{\Psi}(\boldsymbol{R},\boldsymbol{r}) = e^{i\frac{h_{cn}Z}{\hbar v}}[V_{cT}(R_{cT})+V_{nT}(R_{nT})-V_C^{PT}(R)]e^{-i\frac{h_{cn}Z}{\hbar v}}\widetilde{\Psi}(\boldsymbol{R},\boldsymbol{r}). \tag{4.2.4}$$

This equation is at the basis of all perturbation treatments [138]. We adopt here another strategy and we approximate the solution of (4.2.4) by the first term in the exponent of Magnus expansion [139] (equivalent to the first factor of the Fer expansion [140])

$$\begin{aligned}\widetilde{\Psi}(\boldsymbol{R},\boldsymbol{r}) \;\approx\; & \exp\left\{-\frac{i}{\hbar v}\int_{-\infty}^{Z}dZ'\,e^{i\frac{h_{cn}Z'}{\hbar v}}\left[V_{cT}(R'_{cT})+V_{nT}(R'_{nT})-V_C^{PT}(R')\right]e^{-i\frac{h_{cn}Z'}{\hbar v}}\right\}\\ \times\; & \phi_{n_0l_0j_0m_0}(\boldsymbol{r}).\end{aligned} \tag{4.2.5}$$

The breakup cross sections, obtained with these new wave functions (4.2.5), can be derived similarly to the ones of the DEA, the usual eikonal model and the CCE (see Appendix A). As for these three models, the S-DEA breakup distribution as a function of the c-n relative energy E after dissociation reads [see Eq. (A.42)]

$$\frac{d\sigma_{bu}}{dE} = \frac{4\mu_{cn}}{\hbar^2 k}\frac{1}{2j_0+1}\sum_{m_0}\sum_{ljm}|S_{kljm}^{(m_0)}(b)|^2. \tag{4.2.6}$$

where μ_{cn} is the c-n reduced mass and $k=\sqrt{2\mu_{cn}E/\hbar^2}$ is the final c-n wave number. The S-DEA partial breakup amplitudes are obtained by inserting the definition of the wave function (4.2.5) into Eqs. (A.10) and (A.31). They read

$$\begin{aligned} S^{(m_0)}_{kljm}(b) &= e^{i[\delta_{lj}(k)-l\pi/2]}e^{i\chi^C_{PT}(b)}\int d\boldsymbol{r}\;[\phi_{kljm}(\boldsymbol{r})]^* \\ &\quad\times\exp\left\{-\frac{i}{\hbar v}\int_{-\infty}^{+\infty}dZ\,e^{i\frac{h_{cn}Z}{\hbar v}}\Big[V_{cT}(R_{cT})+V_{nT}(R_{nT})-V_C^{PT}(R)\Big]e^{-i\frac{h_{cn}Z}{\hbar v}}\right\} \\ &\quad\times\quad\phi_{n_0l_0j_0m_0}(\boldsymbol{r}), \end{aligned}\tag{4.2.7}$$

where χ^C_{PT} is the P-T Coulomb phase (2.1.38), ϕ_{kljm} is a continuum state of the projectile associated with the phase shift δ_{lj} (2.3.8).

I make now an additional approximation of these amplitudes: the operators h_{cn} in the exponentials are evaluated by their eigenvalues corresponding to the closest wave functions, i.e., the final c-n energy E on the left-hand side and the energy $E_{n_0l_0j_0}$ on the right-hand side. I therefore obtain eikonal-like partial breakup amplitudes where the eikonal phases are replaced by their first-order-perturbation approximations χ_{FO}, i.e.,

$$S^{(m_0)}_{kljm}(b) \approx e^{i\chi^C_{PT}(b)}\,\langle\phi_{kljm}|\exp[i\chi_{\mathrm{FO}}]|\phi_{n_0l_0j_0m_0}\rangle \tag{4.2.8}$$

$$\text{with}\quad \chi_{\mathrm{FO}}(E,\boldsymbol{b},\boldsymbol{r}) = -\frac{1}{\hbar v}\int_{-\infty}^{+\infty}dZ\,e^{i\frac{\omega Z}{v}}\Big[V_{cT}(R_{cT})+V_{nT}(R_{nT})-V_C^{PT}(R)\Big] \tag{4.2.9}$$

and $\omega=(E-E_{n_0l_0j_0})/\hbar$. The Coulomb χ^C_{FO} and nuclear χ^N_{FO} parts of the first-order-perturbation approximation are evaluated separately

$$\chi_{\mathrm{FO}}(E,\boldsymbol{b},\boldsymbol{r}) = \chi^C_{\mathrm{FO}}(E,\boldsymbol{b},\boldsymbol{r})+\chi^N_{\mathrm{FO}}(E,\boldsymbol{b},\boldsymbol{r}). \tag{4.2.10}$$

Contrary to the CCE which approximates χ^C_{FO} by its dipole term (2.3.44), I evaluate it exactly. With the relations (9.6.13) and (9.6.21) of Ref. [92], it can be derived as

$$\chi^C_{\mathrm{FO}}(E,\boldsymbol{b},\boldsymbol{r}) = -\eta\int_{-\infty}^{+\infty}dZ\,e^{i\frac{\omega Z}{v}}\left(\frac{1}{R_{cT}}-\frac{1}{R}\right) \tag{4.2.11}$$

$$= -2\eta\left\{\exp\left[i\frac{\omega}{v}\frac{m_n}{m_P}z\right]K_0\left(\frac{\omega}{v}b_{cT}\right)-K_0\left(\frac{\omega}{v}b\right)\right\}, \tag{4.2.12}$$

where η is the Sommerfeld parameter (2.1.18). The nuclear first-order-perturbation approximation reads

$$\chi^N_{\mathrm{FO}}(E,\boldsymbol{b},\boldsymbol{r}) = -\frac{1}{\hbar v}\int_{-\infty}^{+\infty}dZ\,e^{i\frac{\omega Z}{v}}\left[V_{cT}(R_{cT})-\frac{\hbar v\eta}{R_{cT}}+V_{nT}(R_{nT})\right] \tag{4.2.13}$$

$$\begin{aligned} &= -\frac{1}{\hbar v}\int_{-\infty}^{+\infty}dZ\,e^{i\frac{\omega Z}{v}}\left\{e^{i\frac{\omega}{v}\frac{m_n}{m_P}z}\left[V_{cT}(\sqrt{b_{cT}^2+Z^2})-\frac{\hbar v\eta}{\sqrt{b_{cT}^2+Z^2}}\right]\right. \\ &\quad\left.+e^{-i\frac{\omega}{v}\frac{m_c}{m_P}z}V_{nT}(\sqrt{b_{nT}^2+Z^2})\right\} \end{aligned}\tag{4.2.14}$$

and is evaluated numerically. To improve the numerical efficiency of their evaluation, I compute the integrals of (4.2.14) for a uniform b-mesh. Then, I interpolate them for each b_{cT} and b_{nT} and multiply them by the exponentials accounting for the position of the fragments, i.e., the exponentials depending on z.

Additionally to its simple implementation, the S-DEA wave functions naturally tend to those obtained at the first-order-perturbation theory at large bs.

	V_R [MeV]	R_R [fm]	a_R [fm]	V_{LI} [MeV fm ^{2}]
Odd l	39.74	2.585	0.6	21
Even l	62.55	2.585	0.6	21

Table 4.1: Parameters of the real Woods-Saxon ^{10}Be-n potential (2.3.2) taken from Ref. [127]. It is given by the sum of a real Woods-Saxon potential (2.2.2)–(2.2.3) and a spin-orbit term (2.3.3).

	V_R [MeV]	R_R [fm]	a_R [fm]	W_I [MeV]	R_I [fm]	a_I [fm]	R_C [fm]
^{10}Be-^{12}C	123.0	3.33	0.8	65.0	3.47	0.9	5.33
n-^{12}C	34.54	2.68	0.75	13.4	2.88	0.58	
^{10}Be-^{208}Pb	70.0	7.43	1.04	58.9	7.19	1.0	5.92
n-^{208}Pb	29.46	6.93	0.75	13.4	7.47	0.58	

Table 4.2: Parameters of the optical potential (2.2.1)–(2.2.4) used to simulate the nuclear ^{10}Be-^{12}C, n-^{12}C, ^{10}Be-^{208}Pb and n-^{208}Pb interactions [133, 142, 143].

4.3 Nuclear- and Coulomb-dominated breakups

4.3.1 Two-body interactions

I now evaluate the accuracy of the S-DEA for the breakups of ^{11}Be with ^{12}C at 67A MeV and with ^{208}Pb at 69A MeV. For these two cases, the DEA reproduces well the experimental data [35, 107].

As it was done in the previous Chapters, ^{11}Be is described as a ^{10}Be core in its 0^+ ground state to which a neutron is bound by 0.504 MeV. Contrary to the Chapter 3 where I assume the neutron spinless, I consider here its spin. To simulate the ^{10}Be-n interaction, I follow Ref. [127], where they use the sum (2.3.2) of a central potential and a spin-orbit term, adjusted to the three first levels: $1/2^+$, $1/2^-$ and $5/2^+$, modelled respectively as a $1s1/2$ state, a $0p1/2$ state and a $d5/2$ resonance. The central part is parametrized as a purely real Woods-Saxon potential (2.2.2)–(2.2.3) and the spin-orbit potential as in Eq. (2.3.3). The parameters of these two potentials can be found in Tab. 4.1

The ^{10}Be-T and n-T interactions are modelled by optical potentials with Woods-Saxon shape (2.2.2)–(2.2.3). The same parameters as in Ref. [112], displayed in Tab. 4.2, are taken. The ^{10}Be-^{12}C potential reproduces the elastic scattering of ^{10}Be with ^{12}C at 59.4A MeV [133, 134]. To describe the ^{10}Be-^{208}Pb interaction, I follow Refs. [108, 141], I take the parametrisation of Bonin *et al.* which reproduces the elastic scattering of α on ^{208}Pb at 699 MeV [142]. In both cases, the Coulomb interaction is simulated by the potential of a uniformly charge sphere (2.2.4) of radius R_C. The global optical potential of Becchetti an Greenlees [143] is used for the n-T interactions.

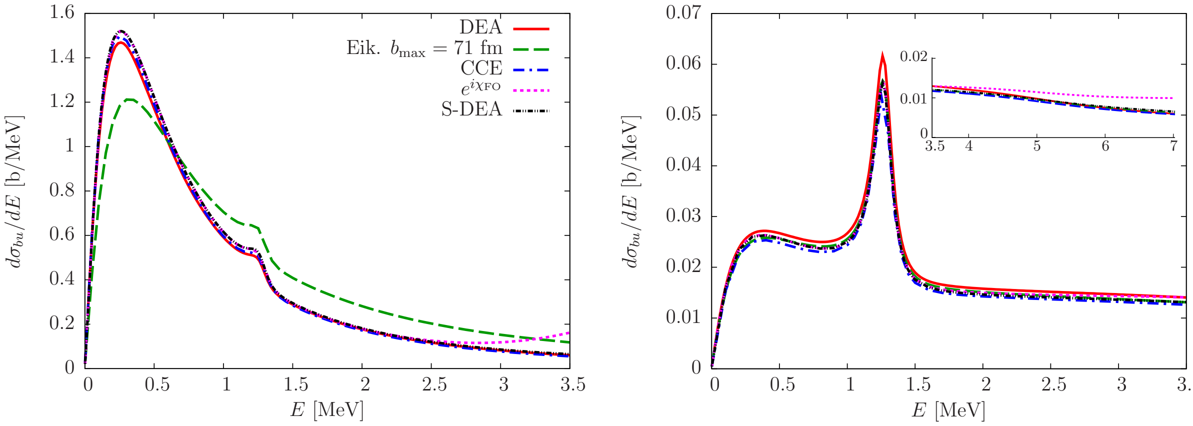

(a)

(b)

Figure 4.3.1: Analysis of the accuracy of the S-DEA for the energy distribution of the diffractive breakups of ^{11}Be with (a) ^{208}Pb at 69A MeV and (b) ^{12}C at 67A MeV. Panel (b) also displays an inset of the energy distributions between 3.5 MeV and 7 MeV.

4.3.2 Energy distributions

To evaluate the accuracy of the S-DEA, I first analyse the breakup cross section as a function of the relative ^{10}Be-n energy. Fig. 4.3.1 displays these distributions for the breakup of ^{11}Be on ^{208}Pb at 69A MeV and on ^{12}C at 67A MeV, respectively (a) and (b), obtained at the eikonal model, the CCE, the DEA and with the approximation (4.2.8). For these two reactions, the DEA (solid red line) reproduces well the experimental data [107] and is used as reference. As explained in Sec. 2.3.3.4, the eikonal model (dashed green lines) does not treat properly the Coulomb interaction and diverges at large bs. With the cutoff in impact parameter proposed in Ref. [23] (see Sec. 2.3.3.4), the usual eikonal model leads to results close to the DEA ones for the nuclear-dominated reaction but fails to describe the Coulomb-dominated breakup, due to the incompatibility of this long-range interaction with the adiabatic assumption.

Both panels (a) and (b) of Fig. 4.3.1 show that the CCE (dash-dotted blue lines) improves the eikonal treatment of the Coulomb interaction and gives accurate energy distributions for both reactions. For the Coulomb-dominated breakup distribution in Fig. 4.3.1(a), the approximation (4.2.8) (dotted magenta lines) is accurate at $E < 2.5$ MeV. Even if it slightly overestimates the peak of the distribution, it lies close to the DEA and the CCE. Moreover, this discrepancy in the peak is smaller than the experimental uncertainty [35]. The nuclear-dominated distribution in Fig. 4.3.1 (b) is also well reproduced by the approximation (4.2.8), which is on top of the CCE at $E < 2$ MeV. For both reactions, the approximation (4.2.8) starts to increase at higher energies and completely fails to reproduce the shape and the magnitude of the breakup cross section.

These unrealistic values at large E are caused by a negative imaginary part of the first-order-approximations $\mathrm{Im}\{\chi_{\rm FO}\} < 0$ (4.2.10), which leads to a strong increase in the breakup matrix elements (4.2.8) as they depend on $\exp[i\chi_{\rm FO}]$. Since the potentials are multiplied by imaginary exponentials [see Eqs. (4.2.12)–(4.2.14)], both the imaginary and real parts of the potentials contribute to $\mathrm{Im}\{\chi_{\rm FO}\}$. As explained in Chapter 2, the imaginary parts of the optical potentials are negative and simulate the absorption into channels other than the elastic one in the core or the neutron interactions with the target.

Unfortunately, the complex exponentials in Eq. (4.2.14) reduce the contribution of the imaginary part of the c-T (resp. n-T) potential by a factor $\cos\left[\frac{\omega}{v}\left(Z'+\frac{m_n}{m_P}z\right)\right]$ (resp. $\cos\left[\frac{\omega}{v}\left(Z'-\frac{m_c}{m_P}z\right)\right]$). The absorption is hence diminished. Moreover, if the cosines are negative, the imaginary part of the potential contribute negatively to $\mathrm{Im}\{\chi_{\mathrm{FO}}\}$ and lead to unrealistic cross sections. Furthermore, the contributions of the real parts of the optical potentials to the imaginary parts of the first-order-perturbation phases can also be negative. This is the case for the imaginary part of the Coulomb first-order-perturbation phase when $z<0$ [see Eq. (4.2.12)]. For the nuclear interaction [see Eq. (4.2.14)], the real part of the c-T (resp. n-T) nuclear potential $\mathrm{Re}\{V_{cT}\}<0$ (resp. $\mathrm{Re}\{V_{nT}\}<0$), has a negative contribution to $\mathrm{Im}\{\chi^N_{\mathrm{FO}}\}$, when $\sin\left(Z'+\frac{m_n}{m_P}z\right)>0$ [resp. $\sin\left(Z'-\frac{m_c}{m_P}z\right)<0$]. All these negative contributions to $\mathrm{Im}\{\chi_{\mathrm{FO}}\}$ lead to unrealistic values of the cross sections.

To cure partly this problem, I treat separately the absorptive part of the potentials with the usual eikonal approximation. This ensures that the imaginary parts of the optical potentials suppress the unphysical contributions of the real potentials. The S-DEA partial-breakup amplitude is thus defined by

$$S^{(m_0)}_{kljm}(b) \;=\; e^{i\chi^C_{PT}(b)}\,\langle\phi_{kljm}|e^{i\chi^C_{\mathrm{FO}}}e^{i\chi^N_{\text{S-DEA}}}|\phi_{n_0l_0j_0m_0}\rangle \tag{4.3.1}$$

with

$$\begin{aligned}\chi^N_{\text{S-DEA}}(E,\boldsymbol{b},\boldsymbol{r}) \;=\;& \mathrm{Im}\left\{\chi^N(\boldsymbol{b},\boldsymbol{s})\right\}\\ &-\frac{1}{\hbar v}\int_{-\infty}^{+\infty}dZ\,e^{i\frac{\omega Z}{v}}\left(e^{i\frac{\omega}{v}\frac{m_n}{m_P}z}\left[\mathrm{Re}\left\{V_{cT}(\sqrt{b_{cT}^2+Z^2})\right\}-\frac{\hbar v\eta}{\sqrt{b_{cT}^2+Z^2}}\right]\right.\\ &\left.+e^{-i\frac{\omega}{v}\frac{m_c}{m_P}z}\mathrm{Re}\left\{V_{nT}(\sqrt{b_{nT}^2+Z^2})\right\}\right)\end{aligned} \tag{4.3.2}$$

where χ^N is the nuclear eikonal phase (2.3.36).

The distributions obtained with the S-DEA (4.3.1) are plotted in Fig. 4.3.1 by the dash-dotted-dotted black lines. For both collisions with lead and carbon targets, the S-DEA is accurate over the whole considered energy range. Note that, the distribution of the Coulomb-dominated breakup still exhibits an unphysical increase at $E=12$ MeV. However, at these energies, the breakup cross section is negligible.

4.3.3 Parallel-momentum distributions

Since the S-DEA is accurate for energy distributions on both light and heavy targets, I study it for parallel-momentum distributions. As mentioned in Chapter 1, these observables are interesting because they are measured in inclusive processes, such as knockout (see Chapter 5). Their expression is similar to the ones (A.48) of the DEA, CCE and the eikonal model, presented in Appendix A. It reads [97, 107, 112]

$$\frac{d\sigma_{bu}}{dk_\parallel}=\frac{8\pi}{2j_0+1}\sum_{m_0}\int_0^\infty bdb\int_{|k_\parallel|}^\infty\frac{dk}{k}\sum_{\nu m}\left|\sum_{lj}(lIm-\nu\nu|jm)Y_l^{m-\nu}(\theta_k,0)S^{(m_0)}_{kljm}(b)\right|^2, \tag{4.3.3}$$

where $\theta_k=\arccos\left(k_\parallel/k\right)$ is the colatitude of the c-n relative wave vector $\boldsymbol{k}$ after breakup and ν is the spin projection. Interestingly, this observable sums coherently the partial

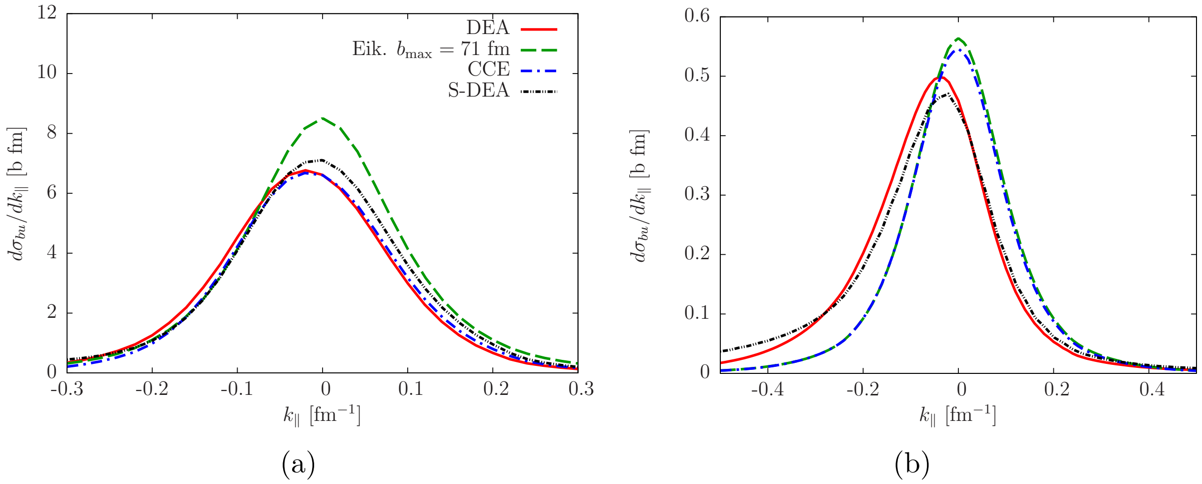

Figure 4.3.2: Analysis of the accuracy of the S-DEA for the parallel-momentum distribution of breakup cross sections of ^{11}Be with (a) ^{208}Pb at 69A MeV and (b) ^{12}C at 67A MeV.

breakup amplitudes and is therefore sensitive to their interferences. This observable is thus a particularly severe test for reaction models.

Fig. 4.3.2 displays the breakup distribution as a function of the relative ^{10}Be-n parallel momentum, after the breakup of ^{11}Be (a) on ^{208}Pb at 69A MeV and (b) on ^{12}C at 67A MeV[1]. For the lead and carbon targets, the integrations over k in Eq. (4.3.3) are limited to respectively $k_{\max} = 0.7$ fm^{-1} and $k_{\max} = 1.4$ fm^{-1}, which correspond to energies in the continuum of $E_{\max} = 11.3$ MeV and $E_{\max} = 45$ MeV. These values are enough to reach the convergence. In both cases, the DEA (solid red lines) lead to an asymmetric distribution centered in $k_\parallel = -0.02$ fm^{-1} and $k_\parallel = -0.04$ fm^{-1} for the lead and carbon targets, respectively. This asymmetry and the fact that it is not centered in $k_\parallel = 0$ are also seen in the experimental data of knockout reactions [76]. They are caused by interferences between higher-order transitions from the bound states to the continuum and within the continuum during the reaction.

The usual eikonal model (dashed green lines) overestimates the magnitude of the cross section and does not reproduce the asymmetry of the distribution. Indeed, the eikonal distribution is perfectly symmetric around $k_\parallel = 0$. This can be understood with the analytical expression of the eikonal cross section, obtained from Eq. (4.3.3) and the partial-breakup amplitude (A.49)

$$S^{(m_0)}_{kljm}(b) = e^{i[\delta_{lj}(k)-l\pi/2]} \left\langle \phi_{kljm} | e^{i\chi_{cT}} e^{i\chi_{nT}} | \phi_{n_0 l_0 j_0 m_0} \right\rangle , \tag{4.3.4}$$

where $\chi_{(c,n)T}$ are the c-T and n-T eikonal phases (2.3.35)

To understand the symmetries of these partial breakup amplitude, I expand the eikonal phases onto the spherical harmonics in the vectorial space defined by $\boldsymbol{r}$

$$\begin{aligned} \exp\left[i\chi_{cT}(\boldsymbol{b},\boldsymbol{s}) + i\chi_{nT}(\boldsymbol{b},\boldsymbol{s})\right] &= \sum_{\lambda\mu} F_{\lambda\mu}(b,r) Y^\mu_\lambda(\Omega_r), & (4.3.5)\\ \text{with} \quad F_{\lambda\mu}(b,r) &= \int d\Omega_r\, Y^{\mu *}_\lambda(\Omega_r) \exp[i\chi_{cT}(\boldsymbol{b},\boldsymbol{s}) + i\chi_{nT}(\boldsymbol{b},\boldsymbol{s})]. & (4.3.6) \end{aligned}$$

---

[1] We have noted that the magnitudes of the parallel-momentum distributions in Figs. 4, 5, 8 and 9 of Ref. [112] are underestimated by a factor 2.

The property of the spherical harmonics imposes

$$Y_\lambda^\mu(\theta_r,\phi_r) = (-1)^{\lambda+\mu} Y_\lambda^\mu(\pi-\theta_r,\phi_r). \tag{4.3.7}$$

Since the eikonal phases $\chi_{(c,n)T}$ (2.3.35) are symmetric across the plane defined by $\boldsymbol{s}$, i.e., $\theta_r \to \pi-\theta_r$, only even $\lambda+\mu$ multipoles contribute in the eikonal model.

By using the expansion (4.3.5) and the expressions of the eigenstates of the projectile (2.3.5)–(2.3.6), the partial breakup amplitude (4.3.4) becomes

$$\begin{aligned}
S_{kljm}^{(m_0)}(b) &= \sum_{m_l\nu}\sum_{m_{l_0}\nu_0}\sum_{\lambda\mu}(lIm_l\nu|jm)(l_0Im_{l_0}\nu_0|j_0m_0)e^{i[\delta_{lj}(k)-l\pi/2]} \\
&\quad \int dr\, u_{klj}(r)F_{\lambda\mu}(b,s)u_{n_0l_0j_0}(r) \\
&\quad \int d\Omega_r\, Y_l^{m_l*}(\Omega_r)Y_\lambda^\mu(\Omega_r)Y_{l_0}^{m_{l_0}}(\Omega_r)\underbrace{\langle I\nu|I\nu_0\rangle}_{=\delta_{\nu\nu_0}} && (4.3.8)\\
&= \sum_{m_lm_{l_0}\nu}\sum_{\lambda\mu}(lIm_l\nu|jm)(l_0Im_{l_0}\nu|j_0m_0)e^{i[\delta_{lj}(k)-l\pi/2]} \\
&\quad \int dr\, u_{klj}(r)F_{\lambda\mu}(b,s)u_{n_0l_0j_0}(r) \\
&\quad (-1)^m\sqrt{\frac{(2l_0+1)(2\lambda+1)}{4\pi(2l+1)}}(l_0\lambda 00|l0)(l_0\lambda m_{l_0}\mu|lm_l), && (4.3.9)
\end{aligned}$$

where $u_{n_0l_0j_0}$ (2.3.7) and u_{klj} (2.3.8) are the radial wave functions of the ground and scattering states, respectively. The Clebsch-Gordan coefficients in this expression impose several conditions onto the quantum numbers: $m_l = m-\nu$, $m_{l_0} = m_0-\nu$, $\mu = m_l - m_{l_0} = m - m_0$ and $l_0+\lambda+l$ has to be even. With these conditions, one can deduce that even $\lambda+\mu$ correspond to even $l_0+l+m-m_0$. Therefore, only the amplitudes $S_{kljm}^{(m_0)}$ with even $l_0+l+m-m_0$ contribute in the eikonal model.

In the case studied here, the ground state of the projectile is in the s wave, i.e., $l_0 = m_{l_0} = 0$ and $m_0 = \nu$. Therefore, only $S_{kljm}^{(\nu)}$ with even $l+m-\nu$ are significant at the usual eikonal approximation. The symmetry of the spherical harmonics (4.3.7) combined with this condition on the quantum number implies that the parallel-momentum distribution (4.3.3) are symmetric in $\theta_k \to \pi-\theta_k$, and thus in $k_\parallel \to -k_\parallel$.

On the contrary, the CCE cross sections (dash-dotted blue lines), plotted in Fig. 4.3.2, are not perfectly symmetric. Mathematically, it is due to the fact that the imaginary part of dipole contribution of the Coulomb first-order-perturbation approximations $\mathrm{Im}\{\chi_{\mathrm{FO}}^{C,(\lambda=1)}\}$ (2.3.44) is asymmetric in $\theta_r \to \pi-\theta_r$ and $S_{kljm}^{(\nu)}$ with odd $l+m-\nu$ contribute. Physically, it means that the CCE includes part of dynamics of the reaction. For the Coulomb-dominated breakup, the CCE lies close to the DEA results and is precise, as already observed in Ref. [112]. However, the CCE fails to reproduce the breakup on the carbon target, its distribution is nearly symmetric and lies close to the eikonal result. This can be explained by the fact that its Coulomb correction (2.3.41) and thus $\mathrm{Im}\{\chi_{\mathrm{FO}}^{C,(\lambda=1)}\}$ are small for such nuclear-dominated reactions [112].

Since the S-DEA (dash-dotted-dotted black lines) also includes dynamical effect, it also leads to asymmetric parallel-momentum distributions in Fig. 4.3.2. Mathematically, it is also explained by the asymmetric terms in $\theta_r \to \pi-\theta_r$ in both Coulomb and nuclear first-order-perturbation approximations (4.2.12)–(4.2.14). However, it leads to too symmetrical a distribution compared to the DEA for the Coulomb-dominated breakup. The peak

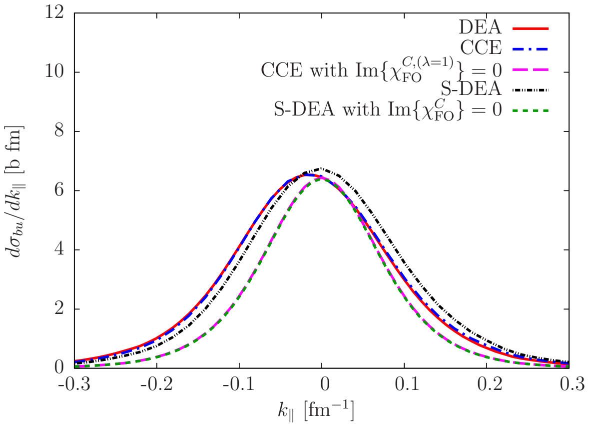

Figure 4.4.1: Analysis of the asymmetry of parallel-momentum distributions for the pure Coulomb breakup of ^{11}Be with ^{208}Pb at 69A MeV obtained with the CCE and the S-DEA. These calculations are performed with a cutoff in impact parameter $b_{\mathrm{min}} = 10$ fm.

of the distribution is also overestimated. On the contrary, the shape and magnitude of the parallel-momentum distributions obtained with the S-DEA for the carbon target are improved compared to the usual eikonal approximation, and the cross section lies closer to the DEA one. This suggests that a first-order simplification of the DEA already improves significantly the parallel-momentum distributions. Similarly to the energy distribution on the carbon target, the S-DEA underestimates the DEA magnitude.

4.4 Asymmetry of parallel-momentum distributions obtained with the CCE and S-DEA

As mentioned in the previous section, the asymmetry of parallel-momentum distributions is caused by dynamical effects in higher-order transitions between the states of the projectile. In this section, I study the asymmetry of both CCE and S-DEA parallel-momentum distributions to understand how well these transitions are accounted for by these two models. In particular, I analyse the influence of electric transitions for the breakup on the lead target, as it is dominated by the Coulomb interaction. Then, I make a similar analysis of the transitions in nuclear-dominated breakup on the carbon target.

I first study purely Coulombic calculations by switching off the nuclear interaction. Fig 4.4.1 illustrates the results of these calculations for the parallel-momentum distribution of ^{11}Be with ^{208}Pb at 69A MeV. The nuclear absorption, is simulated with a cutoff in impact parameter $b_{\mathrm{min}} = 10$ fm. On one hand, the CCE (dash-dotted blue line) reproduces exactly the DEA Coulomb contribution (solid red line). This indicates that the CCE includes correctly the dynamical effects due to the Coulomb interaction and that the small discrepancy with the DEA observed in Fig. 4.3.2(a) is caused by the adiabatic treatment of the nuclear interaction. On the other hand, the S-DEA distribution (dashed-dotted-dotted black line) lacks asymmetry and slightly overestimates the DEA results. In the pure Coulomb breakup, the asymmetry of distributions are caused by the imaginary parts of either the dipole term of the Coulomb first-order-perturbation approximation $\mathrm{Im}\{\chi_{\mathrm{FO}}^{C,(\lambda=1)}\}$ (2.3.44) in the CCE or that of the full Coulomb phase $\mathrm{Im}\{\chi_{\mathrm{FO}}^{C}\}$ (4.2.12) in the S-DEA. To illustrate this, I put $\mathrm{Im}\{\chi_{\mathrm{FO}}^{C,(\lambda=1)}\} = 0$ within the CCE (2.3.41) (dashed

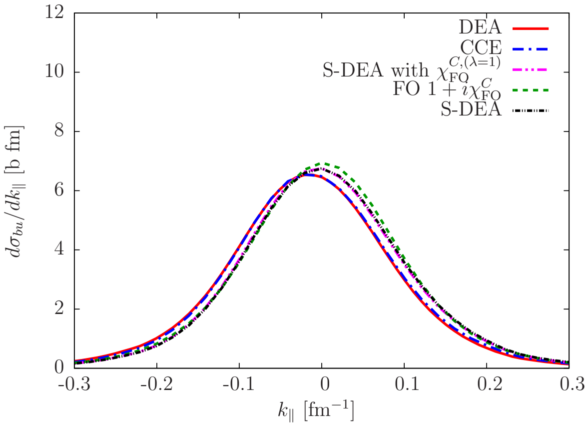

Figure 4.4.2: Analysis of the influence of higher-order terms of $\chi^C_{\rm FO}$ on the S-DEA parallel-momentum distributions for the pure Coulomb breakup of ^{11}Be with ^{208}Pb at 69A MeV. These calculations are performed with a cutoff in impact parameter $b_{\rm min} = 10$ fm.

magenta line) and $\mathrm{Im}\{\chi^C_{\rm FO}\} = 0$ within the S-DEA (4.3.2) (dotted green line) in Fig. 4.4.1. Interestingly, both distributions are symmetric and perfectly superimposed, suggesting that the real part of the Coulomb first-order-perturbation is treated similarly in both models.

There are two main differences between the CCE and the S-DEA in the treatment of the Coulomb interaction. First, the CCE depends linearly on the Coulomb first-order-perturbation approximation $\chi^C_{\rm FO}$ [see Eq. (2.3.41)]. In this thesis, $\chi^C_{\rm FO}$ is approximated by its dipole contribution $\chi_{\rm FO}^{C,(\lambda=1)}$ within the CCE, which is dominant for the Coulomb breakup of one-neutron halo nuclei [113]. Second, the S-DEA includes dynamical effects in all electric transitions at all orders since its treatment of the Coulomb tidal force reads $\exp\left[i\chi^C_{\rm FO}\right]$ (4.2.12).

I first verify that the $\chi^C_{\rm FO} \approx \chi_{\rm FO}^{C,(\lambda=1)}$ is a good approximation, and that higher-order multipoles of the Coulomb interaction, e.g., E2 transitions, can be safely neglected. To do so, I plot in Fig. 4.4.2 the Coulomb contribution to the parallel-momentum distributions for the breakup of ^{11}Be on ^{208}Pb at 69A MeV obtained with the S-DEA approximating $\exp\left[i\chi^C_{\rm FO}\right] \approx \exp\left[i\chi_{\rm FO}^{C,(\lambda=1)}\right]$ (dash-dotted-dotted magenta line). I compare this calculation to the one obtained with the DEA (solid red line), the CCE (dash-dotted blue line) and the S-DEA considering the full Coulomb phase (dash-dotted-dotted black line). As previously, I use a cutoff $b_{\rm min} = 10$ fm to simulate the nuclear absorption. We can see that the S-DEA approximating $\exp\left[i\chi^C_{\rm FO}\right] \approx \exp\left[i\chi_{\rm FO}^{C,(\lambda=1)}\right]$ is on top of the standard S-DEA, and therefore the dipole approximation is valid here. Using the sum of the dipole and quadrupole (B.11) terms of the Coulomb interaction in the S-DEA, i.e., $\exp\left[i\chi^C_{\rm FO}\right] \approx \exp\left[i\chi_{\rm FO}^{C,(\lambda=1)} + i\chi_{\rm FO}^{C,(\lambda=2)}\right]$, leads to the same conclusion. This confirms that the E1 transitions are dominant for this collision.

Then, I investigate if approximating the S-DEA operator by its first order, i.e., $\exp\left[i\chi^C_{\rm FO}\right] \approx 1 + i\chi^C_{\rm FO}$, and therefore neglecting higher-order transitions would lead to a distribution close to the CCE one. This approach corresponds to the first-order-perturbation theory (FO) and leads to the distribution plotted in dotted green in Fig. 4.4.2. As already seen in Ref. [112], the resulting distribution is almost perfectly symmetric. Moreover, it is a bit more symmetric than the S-DEA, suggesting that the S-DEA grasps more dynamical effects.

The operator of the CCE appearing in the $S^{(m_0)}_{kljm}$ depends linearly on $\chi^{C,(\lambda=1)}_{\rm FO}$ [see Eq. (A.50)]. To understand how electric transitions are modelled, I expand this operator onto the spherical harmonics in the vectorial space defined by $\boldsymbol{r}$

$$e^{i\chi^C_{PT}(b)}\left[e^{i\chi^C(\boldsymbol{b},\boldsymbol{s})} - i\chi^C(\boldsymbol{b},\boldsymbol{s}) + i\chi^{C,(\lambda=1)}_{\rm FO}(E,\boldsymbol{b},\boldsymbol{r})\right] = \sum_{\lambda\mu} F_{\lambda\mu}(E,b,r)Y^{\mu}_{\lambda}(\Omega_r), \quad (4.4.1)$$

where

$$F_{\lambda\mu}(E,b,r) = e^{i\chi^C_{PT}(b)}\int d\Omega_r\, Y^{\mu *}_{\lambda}(\Omega_r)\left[e^{i\chi^C(\boldsymbol{b},\boldsymbol{s})} - i\chi^C(\boldsymbol{b},\boldsymbol{s}) + i\chi^{C,(\lambda=1)}_{\rm FO}(E,\boldsymbol{b},\boldsymbol{r})\right]. \quad (4.4.2)$$

As explained previously, the property (4.3.7) imposes that the asymmetric terms in $\theta_r \to \pi-\theta_r$ are contained in the multipoles with odd $\lambda+\mu$. Therefore, the asymmetric term $\mathrm{Im}\{\chi^{C,(\lambda=1)}_{\rm FO}\}$ contributes to only the dipole term $\lambda = 1$ and $\mu = 0$ of the operator (4.4.1). Since the ground state of the projectile is in the s wave, this implies that the dynamical effects affects only the p waves in the core-neutron continuum.

On the contrary, the operator appearing in the S-DEA $S^{(m_0)}_{kljm}$ (4.3.1) depends exponentially on the term $\chi^C_{\rm FO}$. Its expansion onto the spherical harmonics in the vectorial space defined by $\boldsymbol{r}$ reads

$$e^{i\chi^C_{PT}(b)}e^{i\chi^C_{\rm FO}(E,\boldsymbol{b},\boldsymbol{r})} = \sum_{\lambda\mu} F_{\lambda\mu}(E,b,r)Y^{\mu}_{\lambda}(\Omega_r), \quad (4.4.3)$$

with

$$F_{\lambda\mu}(E,b,r) = e^{i\chi^C_{PT}(b)}\int d\Omega_r\, Y^{\mu *}_{\lambda}(\Omega_r)e^{i\chi^C_{\rm FO}(E,\boldsymbol{b},\boldsymbol{r})}. \quad (4.4.4)$$

The asymmetric terms are contained in $\exp\left[-\mathrm{Im}\{\chi^C_{\rm FO}\}\right]$. These terms as well as dynamical effects are included in all electric transitions at all orders. They therefore contribute to all multipoles with odd $\lambda+\mu$ and affect all partial waves in the core-neutron continuum.

To understand how this influences the shape of the parallel-momentum distributions, I plot in Fig. 4.4.3 the Coulomb contribution for the breakup of ^{11}Be with ^{208}Pb obtained with different maximum values $l_{\max}$ in the sum over l in Eq. (4.3.3). In the results shown here, I take the order of the higher multipoles $\lambda_{\max}$ of the operators (4.4.1) and (4.4.3) equal to $l_{\max}$, i.e., $\lambda_{\max} = l_{\max}$. As expected, the distributions at $l_{\max} = 0$ (green lines) are symmetric for both the CCE (dash-dotted lines) and S-DEA (dash-dotted-dotted lines). Indeed, because the sum $l+m-\nu = 0$ when $l = 0$, this contribution is always symmetric due to the property of the spherical harmonics (4.3.7). For both models, the asymmetry first arises when $l_{\max} = 1$ (blue lines) from the interferences of the monopole $\lambda = 0$ and dipole $\lambda = 1$ terms of the CCE operator (4.4.1) and S-DEA operator (4.4.3). The asymmetry of the CCE distribution is more pronounced, indicating that the interferences between $e^{i\chi^C} - i\chi^C$ and $\chi^{C,(\lambda=1)}_{\rm FO}$ in Eq. (4.4.2) push the distribution to negative $k_{\|}$. Note that the magnitude of both distributions increases drastically at $l_{\max} = 1$, because this reaction is dominated by direct E1 transitions.

The main difference between the two models appears at $l_{\max} = 2$ and is due to the influence of the quadrupole term $\lambda = 2$ of the CCE operator (4.4.1) and S-DEA operator (4.4.3). As we have seen that higher-order multipoles of the Coulomb interaction can be safely neglected, the quadrupole terms $\lambda = 2$ of the CCE and S-DEA operators describe mainly higher-order E1 transitions, such as two successive E1 transitions. In

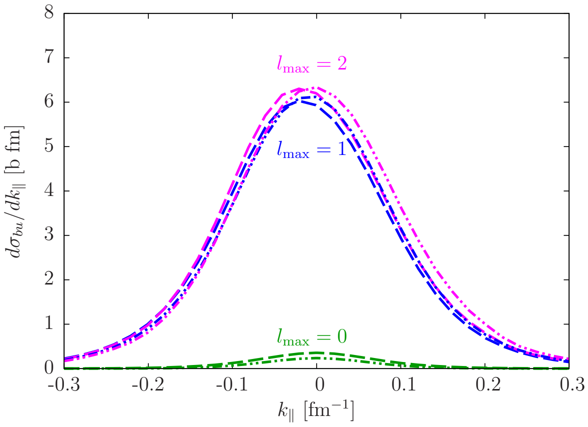

Figure 4.4.3: Coulomb contribution to the parallel-momentum distributions for ^{11}Be with ^{208}Pb at 69 MeV/nucleon obtained with the CCE (dash-dotted lines) and the S-DEA (dash-dotted-dotted lines). They are computed with $l_{\rm max} = 0$ in the sum over l in Eq. (4.3.3) (green lines), $l_{\rm max} = 1$ (blue lines) and $l_{\rm max} = 2$ (magenta lines). These calculations are performed with a cutoff in impact parameter $b_{\rm min} = 10$ fm.

the CCE, this term is treated adiabatically, as it depends on $\exp\left[i\chi^C\right] - i\chi^C$ which is symmetric, and thus barely influences the shape of the distribution. In the S-DEA, the quadrupole term $\lambda = 2$ of the S-DEA operator (4.4.3) includes dynamical effects and depends on powers of $\chi^C_{\rm FO}$, which all contain an asymmetric component. Due to the property of the spherical harmonics (4.3.7), each partial-wave contribution to the parallel-momentum distribution (4.3.3) differs by a phase $(-1)^l$ for two opposite $k_\parallel$. Because the ground state of the projectile is in the s wave, $l = \lambda$. Therefore, the quadrupole term $\lambda = 2$ operator (4.4.3) contributes in an opposite way to its dipole term $\lambda = 1$, i.e., more to positive $k_\parallel$ values. It thus tends to diminish the asymmetry of the distribution. Therefore, all electric transitions at all orders influence the shape of the parallel-momentum distribution in the S-DEA and the total effect is a reduction of the asymmetry due to direct E1 transitions.

I now perform a similar analysis for the nuclear interaction, performing purely nuclear calculations, i.e., assuming the charge of the target to be nil. Fig. 4.4.4(a) displays the results of these calculations in the case of the breakup of ^{11}Be on ^{12}C at 67A MeV. The DEA distribution exhibits a similar asymmetry as in Fig. 4.3.2(b) where the Coulomb interaction is accounted for. This means that for this nuclear-dominated reactions, the asymmetry of the distribution is mainly due to the nuclear interaction. Since the Coulomb interaction is not considered here, the CCE (dash-dotted blue line) is reduced to the usual eikonal approximation and leads to perfectly symmetric distributions. On the contrary, the S-DEA distribution (dash-dotted-dotted black lines) is asymmetric, illustrating the interest of the S-DEA that includes dynamical effects due to the nuclear interaction.

I proceed as in the analysis of the pure Coulomb case and I plot in Fig. 4.4.4(b) the nuclear contribution for the breakup of ^{11}Be with ^{12}C obtained with different maximum values $l_{\rm max}$ in the sum over l in Eq. (4.3.3). As previously, I take $\lambda_{\rm max} = l_{\rm max}$. As expected, the CCE (dash-dotted lines) distributions obtained with various $l_{\rm max}$ are perfectly symmetric. In the S-DEA, the asymmetry starts to be visible when $l_{\rm max} = 2$. Contrary to the Coulomb first-order-perturbation approximation, the nuclear S-DEA phase $\chi^N_{\rm S\text{-}DEA}$ (4.3.2) has two imaginary exponentials, one depending on z, and another one on $-z$. The asym-

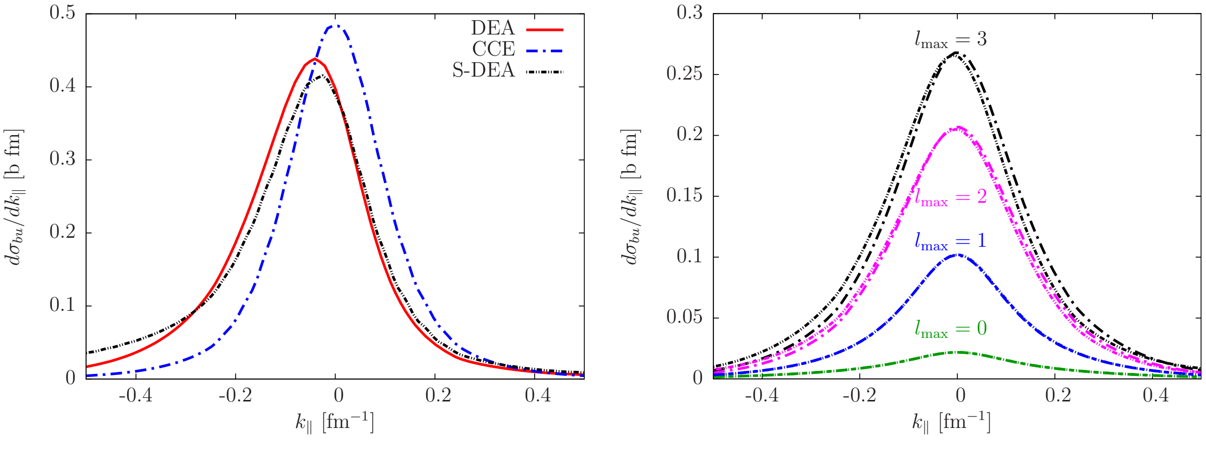

(a) (b)

Figure 4.4.4: Analysis of the asymmetry of parallel-momentum distributions for the pure nuclear breakup of ^{11}Be with ^{12}C at 67A MeV obtained with the DEA (solid lines), the CCE (dash-dotted lines) and the S-DEA (dash-dotted-dotted lines). (a) Fully converged distributions and (b) distributions computed with $l_{\max} = 0$ in the sum over l in Eq. (4.3.3) (green lines), $l_{\max} = 1$ (blue lines), $l_{\max} = 2$ (magenta lines) and $l_{\max} = 3$ (black lines).

metric part of $\mathrm{Im}\{\chi^N_{\text{S-DEA}}\}$ is thus given by the sum of two terms of opposite signs and depending on z, b_{cT} and b_{nT}. This complex dependence implies that partial waves with odd and even l do not necessarily have opposite contributions to the asymmetry of the parallel-momentum distribution. In this case, we observe in Fig. 4.4.4(b) that both odd and even partial-waves contribute to the asymmetry of the S-DEA (dash-dotted-dotted lines), i.e., push the distribution to negative $k_\parallel$. Contrary to the Coulomb-dominated reaction, the asymmetry of the total distribution in Fig. 4.4.4(b) is overestimated compared to the DEA. This analysis suggests that the S-DEA improves the descriptions of electric and nuclear transitions compared to the usual eikonal approximation but still misses part of the dynamics of the reaction.

4.5 Summary and prospects

In collaboration with Daniel Baye, we have developed a simplification to the DEA, which has a similar numerical cost as the usual eikonal approximation. This model relies on two approximations: the first is made on the solutions of the DEA wave functions (4.2.5) and the second on the breakup matrix element (4.2.8). This leads to an eikonal-like model, where the eikonal phases are replaced by the expression of the breakup transition obtained at first-order perturbation theory. Compared to the eikonal approximation, this model does not diverge for the Coulomb breakup and its wave functions have the correct behaviour at large bs, i.e., it tends to the first-order-perturbation theory.

I have studied this model for both nuclear- and Coulomb-dominated breakups of ^{11}Be. The energy distributions are well reproduced at low energies, i.e., $E \leq 2$ MeV, but take unphysical values at larger energies. This is due to negative values of the imaginary part of the first-order-perturbation approximation, which arise at small bs. We have shown that precise energy distributions can be obtained when the approximation is applied to only the real part of the potentials, treating the imaginary part at the usual eikonal model.

This ensures that the unphysical contributions are suppressed.

Compared to the usual eikonal approximation, the S-DEA improves the parallel-momentum distribution of both breakup reactions since it lies closer to the DEA results. For nuclear-dominated breakup, the S-DEA improves both the shape and the magnitude of the distribution, confirming that the asymmetry is due to dynamical effects during the collision. It is therefore an excellent model to describe both energy and parallel-momentum distributions of breakup with light targets. The S-DEA does however not reproduce fully the asymmetry of the parallel-momentum distribution of Coulomb-dominated reactions. This underestimation of the asymmetry is caused by interferences between higher-order E1 transitions, that decrease the effect of the dominant direct E1 transitions.

Since the S-DEA elegantly solves the Coulomb divergence within the eikonal model and significantly enhances its accuracy while keeping a small numerical cost, it would be interesting to study its extension to three-body projectiles, such as two-neutron halo nuclei. An extension of the CCE to such projectiles has already been studied for ^{6}He and ^{11}Li in Refs. [111, 144]. Computing breakup observables of three-body projectiles with the S-DEA would require both the calculations of the breakup states and the generalisation of the S-DEA to four-body reactions. This could be done using the hyperspherical harmonics [34].

As there are still some differences with the DEA, higher-order approximations could be studied. A first step could be to improve the crude approximation of the breakup matrix elements (4.2.8). This could be done by expanding the wave function onto a basis of eigenstates of the c-n internal Hamiltonian, composed of bound states and pseudostates for the c-n continuum (as in CDCC, see Sec. 2.3.3.2). The matrix elements could then be obtained through a diagonalization method [145] and an interpolation between the energies of the pseudostates. Besides the more complex implementation of this model, two additional issues might arise. First, the diagonalization of the matrix might be heavy from a computational viewpoint since the first-order-perturbation approximations (4.2.12)–(4.2.14) are complex. Second, the lack of absorption that we have observed with Eq. (4.2.8) might also appear in this matrix through eigenvalues with an negative imaginary part. Despite these two difficulties, this modification of the S-DEA might improve the shape of its parallel-momentum distribution, since it will include more dynamical effects.

Chapter 5

Sensitivity of knockout observables to the halo structure

5.1 Introduction

As seen in Chapter 1, one-neutron knockout reactions correspond to the removal of one neutron from the projectile. They are inclusive processes, meaning that only the core is detected after the dissociation. These reactions are of great interest for halo nuclei, because their cross sections are large thanks to the low binding energy of the halo neutron to the core [9]. Moreover, knockout observables exhibit a much higher statistics than exclusive measurements, in which both the core and the neutron are detected in coincidence. Hence, they are often favoured for the low intensities available at radioactive-ion beam facilities. Because these reactions are measured at intermediate to high energies, i.e between $50A$ to $100A$ MeV, they are usually studied with the eikonal approximation [9]. As mentioned in Chapter 1, the agreement between the theoretical predictions and experiment worsens when the knocked out nucleon is more bound [26, 27]. In this Chapter, I try to understand why theory and experiment agree so well for loosely-bound nuclei and to determine what nuclear-structure information can be safely inferred from these reactions. To do so, I conduct a thorough sensitivity analysis of the knockout cross sections for one-neutron halo nuclei to the projectile structure and to the optical potentials simulating its interaction with the target.

Theoretical models for inclusive breakup reactions of two-body projectiles have been developed in the eighties in Refs. [100, 146, 147, 148]. The corresponding observables are obtained through the sum of the diffractive breakup, where both the halo neutron and the core survive the collision, and the stripping cross sections, where the neutron is absorbed by the target. The cross sections are usually expressed as a function of the momentum of the detected core along the beam axis, also referred as the parallel-momentum of the core. Sec. 5.2 presents the eikonal derivation of knockout cross sections. In particular, the diffractive breakup cross section is expressed as a function of the momentum of the remaining core. Then, the stripping cross section is derived following the formalism of Hussein and McVoy [100], relying on the spectator core model.

This analysis is conducted on the one-neutron knockout of ^{11}Be with ^{9}Be at $60A$ MeV, which was measured at National Superconducting Cyclotron Laboratory [76, 77]. To study in detail the sensitivity of knockout observables to the nuclear structure of the projectile, ^{11}Be is described within halo effective field theory (Halo-EFT [149, 150, 151]). This model exploits the clear separation of scales observed in halo nuclei, viz. the large size of the halo R_{halo} compared to the compact size of the core R_{core}, to expand the projectile Hamiltonian upon the small parameter $R_{\text{halo}}/R_{\text{core}} < 1$. This very systematic expansion facilitates the identification of the nuclear-structure observables which affect most the reaction process. Following Refs. [66, 152], I apply this method up to next-to-leading order (NLO) to simulate the ^{10}Be-n interaction. Sec. 5.3 summarizes the Halo-EFT description of ^{11}Be used in this Chapter.

After providing the numerical details and the optical potentials considered in this study in Sec. 5.4.1, I investigate, in Sec. 5.4.2 the sensitivity of the parallel-momentum distribution of the remaining ^{10}Be core to the ^{11}Be ground-state wave function. For this purpose, various Halo-EFT potentials, generating different ground-state wave functions, are considered. Secs. 5.4.3 and 5.4.4 present sensitivity studies of knockout observables to other features of the projectile description, namely the presence of an excited subthreshold bound state and the description of the ^{10}Be-n continuum. A similar analysis on the hypothetical one-neutron knockout of ^{11}Be with ^{12}C at 68A MeV has been published in Refs. [30, 31].

After pinning down what is the relevant information of the projectile description for knockout reactions, I assess how the choice of optical potentials affects the shape and the magnitude of the parallel-momentum distributions in Sec. 5.5. To do so, I compare the eikonal predictions obtained with different sets of optical potentials to experimental data. The significance of the dynamical effects, which are neglected in the eikonal model, are also discussed.

Finally, I draw conclusions from these two sensitivity analyses and give some prospects of this work in Sec. 5.6.

5.2 Knockout cross sections

As explained in Chapter 1, one-neutron knockout reactions correspond to the one-neutron removal of the projectile by a target. Knockout cross sections are inclusive and are often given as a function of the parallel-momentum of the core after the neutron has been knocked out [76, 77, 78, 82]. There are two possible processes that contribute to this reaction: the diffractive breakup, where the neutron survives the collision, and the stripping, where the neutron is absorbed by the target. One-neutron knockout cross sections are thus obtained through the sum of the diffractive and the stripping cross sections. In particular, its distribution as a function of the parallel momentum of the remaining core in the projectile restframe $k_{c\|}$ reads [153, 154]

$$\frac{d\sigma_{ko}}{dk_{c\|}} = \frac{d\sigma_{bu}}{dk_{c\|}} + \frac{d\sigma_{str}}{dk_{c\|}}. \tag{5.2.1}$$

where σ_{ko}, σ_{bu} and σ_{str} are respectively the knockout, the diffractive-breakup and the stripping cross sections. As mentioned before, these reactions occur at energies where the eikonal model is valid, and are thus often analysed with this model. This section presents the derivation of these cross sections within the eikonal framework [100, 153].

As in Chapter 4, the spin of the neutron I is considered and the optical potentials, V_{cT} and V_{nT}, simulating respectively the c-T and n-T interactions are assumed central. The diffractive-breakup cross section as a function of the c-n parallel-momentum $k_{\|}$ after the dissociation is given by Eq. (A.48). To compute the knockout cross section (5.2.1), this distribution has to be expressed as a function of the parallel-momentum of the core $k_{c\|}$ in the projectile restframe. In the non-relativistic regime, the impulsion of each fragment $x = c$ or n in the projectile restframe is defined as [44]

$$\boldsymbol{p_x} = m_x \boldsymbol{u_x}, \tag{5.2.2}$$

where m_x and $\boldsymbol{u_x}$ are respectively the mass and the velocity of the fragment x. The conservation of impulsion in the projectile center-of-mass imposes [97]

$$m_c \boldsymbol{u_c} + m_n \boldsymbol{u_n} = 0 \tag{5.2.3}$$

Combining this equation with the definition of the relative velocity $\boldsymbol{u}$ between the core and the fragment

$$\boldsymbol{u} = \boldsymbol{u_n} - \boldsymbol{u_c}, \tag{5.2.4}$$

we obtain

$$\boldsymbol{u_c} \quad = \quad -\frac{m_n}{m_P}\boldsymbol{u}. \tag{5.2.5}$$

These velocities are linked to the momenta through $\boldsymbol{u_c} = \hbar\boldsymbol{k}_c/m_c$ and $\boldsymbol{u} = \hbar\boldsymbol{k}/\mu_{cn}$ with $\mu_{cn} = m_c m_n/m_P$ the c-n reduced mass and $m_P = m_c + m_n$ the projectile mass. These momenta are thus simply related through

$$\boldsymbol{k_c} \quad = \quad -\boldsymbol{k}. \tag{5.2.6}$$

The diffractive breakup cross section as a function of the parallel-momentum of the core is thus just obtained by changing the sign of $k_\|$ in Eq. (A.48)

$$\frac{d\sigma_{bu}}{dk_{c\|}}(k_{c\|}) = \frac{d\sigma_{bu}}{dk_\|}(-k_\|). \tag{5.2.7}$$

To compute the stripping cross section, I use the formalism of Hussein and McVoy [100]. As mentioned in Chapter 2, it assumes that the core acts only as a spectator during the collision, i.e., it can only scatter elastically with the target. The stripping distribution as a function of the deflection angle of the core Ω_{cT} and its final energy E_{cT} is obtained through Eqs. (2.3.18)–(2.3.19). These equations depend on the three-body wave function $\Psi^{(m_0)}$, solution of Eq. (2.3.9) with Eq. (2.3.12) as initial condition. At the usual eikonal approximation, this wave function reads (2.3.33)

$$\Psi^{\mathrm{eik}(m_0)}(\boldsymbol{R},\boldsymbol{r}) \quad = \quad e^{iKZ} e^{-\frac{i}{\hbar v}\int_{-\infty}^{Z} dZ'\, V_{cT}(R'_{cT}) + V_{nT}(R'_{nT})} \phi_{n_0 l_0 j_0 m_0}(\boldsymbol{r}) \tag{5.2.8}$$

where $\hbar\boldsymbol{K} = \hbar K\hat{\boldsymbol{Z}}$ and $v = \hbar K/\mu$ are respectively the initial relative P-T momentum and velocity, μ (2.1.2) is the P-T reduced mass, $\phi_{n_0 l_0 j_0 m_0}$ is the projectile ground-state wave function, $\boldsymbol{R_{cT}} \equiv (\boldsymbol{b_{cT}}, Z_{cT})$, $\boldsymbol{R_{nT}} \equiv (\boldsymbol{b_{nT}}, Z_{nT})$ and $\boldsymbol{r} \equiv (\boldsymbol{s}, z)$ are respectively the c-T, n-T and c-n coordinates (see Fig. 2.3.1).

To derive the cross section, I write this three-body wave function (5.2.8) as a function of $(\boldsymbol{R_{cT}}, \boldsymbol{R_{nT}})$. Using the definitions of the coordinates (2.3.10)–(2.3.11), the eikonal three-body wave function (5.2.8) reads

$$\begin{aligned} \Psi^{\mathrm{eik}(m_0)}(\boldsymbol{R_{cT}},\boldsymbol{R_{nT}}) \quad &= \quad e^{iK\frac{m_c}{m_P}Z_{cT}} e^{iK\frac{m_n}{m_P}Z_{nT}} e^{-\frac{i}{\hbar v}\int_{-\infty}^{Z_{cT}} dZ'_{cT}\, V_{cT}(R'_{cT})} e^{-\frac{i}{\hbar v}\int_{-\infty}^{Z_{nT}} dZ'_{nT}\, V_{nT}(R'_{nT})} \\ &\times \quad \phi_{n_0 l_0 j_0 m_0}(\boldsymbol{R_{nT}} - \boldsymbol{R_{cT}}). \end{aligned} \tag{5.2.9}$$

Initially, the c-T and n-T relative velocities, respectively v_{cT} and v_{nT}, are equal to the relative P-T velocity v. The initial momenta of the core and the neutron are thus given by

$$\boldsymbol{K_{xT}} = \frac{\mu_{xT}}{\mu}\boldsymbol{K} \tag{5.2.10}$$

with $x = (c, n)$ and $\mu_{xT} = m_x m_T/(m_x + m_T)$ the x-T reduced masses. In Ref. [100], Hussein and McVoy approximate these momenta by

$$\boldsymbol{K_{xT}} \approx \frac{m_x}{m_P}\boldsymbol{K}. \tag{5.2.11}$$

This approximation holds if $m_T \gg m_P$. The three-body wave function modifies accordingly into [100]

$$\begin{aligned}\Psi^{\text{eik}(m_0)}(\boldsymbol{R_{cT}}, \boldsymbol{R_{nT}}) &= e^{iK_{cT}Z_{cT}} e^{iK_{nT}Z_{nT}} e^{-\frac{i}{\hbar v}\int_{-\infty}^{Z_{cT}} dZ'_{cT}\, V_{cT}(R'_{cT})} e^{-\frac{i}{\hbar v}\int_{-\infty}^{Z_{nT}} dZ'_{nT}\, V_{nT}(R'_{nT})} \\ &\times \quad \phi_{n_0l_0j_0m_0}(\boldsymbol{R_{nT}} - \boldsymbol{R_{cT}}).\end{aligned} \tag{5.2.12}$$

The stripping distributions also depend on the final c-T distorted wave function $\zeta^{\text{eik}}_{\boldsymbol{K'_{cT}}}$ characterized by the relative c-T wave vector $\boldsymbol{K'_{cT}} \equiv (K'_{cT}, \Omega_{cT})$ with $K'_{cT} = \sqrt{2\mu_{cT}E_{cT}/\hbar^2}$. As the spectator approximation assumes that the core can only scatter elastically with the target, the initial and final wave numbers of the core are equal by energy conservation, i.e., $K'_{cT} = K_{cT}$. Similarly to the diffractive breakup derivation (see Appendix A), the transferred momentum $\hbar\boldsymbol{q} = \hbar(\boldsymbol{K'_{cT}} - \boldsymbol{K_{cT}})$ is assumed to be purely transverse, i.e, $q_Z \approx 0$ and $\boldsymbol{K'_{cT}} \cdot \hat{\boldsymbol{Z}} \approx \boldsymbol{K_{cT}} \cdot \hat{\boldsymbol{Z}}$. With this approximation, the final distorted wave function $\zeta^{\text{eik}}_{\boldsymbol{K'_{cT}}}$ can be written as [see Eq. (2.1.31)] [100]

$$\zeta^{(-)\text{eik}}_{\boldsymbol{K'_{cT}}}(\boldsymbol{R_{cT}}) = e^{i\boldsymbol{K'_{cT}}\boldsymbol{R_{cT}}} e^{\frac{i}{\hbar v}\int_{Z_{cT}}^{+\infty} dZ'_{cT}\, V^*_{cT}(R'_{cT})}. \tag{5.2.13}$$

By using the definitions of the eikonal wave functions (5.2.12) and (5.2.13), Eq. (2.3.19) becomes [100]

$$\begin{aligned}\rho_n^{(+)}(\boldsymbol{R_{nT}}) &= e^{iK_{nT}Z_{nT}} e^{-\frac{i}{\hbar v}\int_{-\infty}^{Z_{nT}} dZ'\, V_{nT}(R'_{nT})} \\ &\times \int d\boldsymbol{R_{cT}}\, e^{-i\boldsymbol{q}\boldsymbol{R_{cT}}} e^{i\chi_{cT}(b_{cT})} \phi_{n_0l_0j_0m_0}(\boldsymbol{R_{nT}} - \boldsymbol{R_{cT}}),\end{aligned} \tag{5.2.14}$$

where χ_{cT} is the c-T eikonal phase (2.3.35).

As experimentally the beam is not polarized, different initial projections m_0 of the ground state are possible. The cross section is just averaged over the values m_0. By inserting the expression (5.2.14) into Eq. (2.3.18), the differential stripping cross section reads [100]

$$\begin{aligned}\frac{d\sigma_{str}}{d\Omega_{cT}dE_{cT}} &= \frac{\mu_{cT}K_{cT}}{(2\pi)^3\hbar^2}\frac{1}{2j_0+1}\sum_{m_0}\int d\boldsymbol{b_{nT}} \\ &\times \int_{-\infty}^{+\infty} dZ_{nT}\, \frac{2}{\hbar v}\text{Im}\{-V_{nT}(R'_{nT})\} e^{-\frac{2}{\hbar v}\int_{-\infty}^{Z_{nT}} dZ'\, \text{Im}\{V_{nT}(R_{nT})\}} \\ &\times \left|\int d\boldsymbol{R_{cT}}\, e^{-i\boldsymbol{q}\boldsymbol{R_{cT}}} e^{i\chi_{cT}(b_{cT})} \phi_{n_0l_0j_0m_0}(\boldsymbol{R_{nT}} - \boldsymbol{R_{cT}})\right|^2 \end{aligned} \tag{5.2.15}$$

$$\begin{aligned} &= \frac{\mu_{cT}K_{cT}}{(2\pi)^3\hbar^2}\frac{1}{2j_0+1}\sum_{m_0}\int d\boldsymbol{b_{nT}} \left(1 - \left|e^{i\chi_{nT}(b_{nT})}\right|^2\right) \\ &\times \left|\int d\boldsymbol{R_{cT}}\, e^{-i\boldsymbol{q}\boldsymbol{R_{cT}}} e^{i\chi_{cT}(b_{cT})} \phi_{n_0l_0j_0m_0}(\boldsymbol{R_{nT}} - \boldsymbol{R_{cT}})\right|^2, \end{aligned} \tag{5.2.16}$$

where χ_{nT} is the n-T eikonal phase (2.3.35). In the spectator model, the transferred momentum is equal to the relative c-n momentum after the reaction, i.e., $\boldsymbol{q} = \boldsymbol{k}$. With Eq. (5.2.6), the transferred momentum is linked to $\boldsymbol{k_c}$ through

$$\boldsymbol{q} = -\boldsymbol{k_c}. \tag{5.2.17}$$

With this relation and a change of variable $\boldsymbol{R_{cT}}$ and $\boldsymbol{R_{nT}}$ to $\boldsymbol{r}$ (2.3.11), the cross section becomes

$$\begin{aligned}\frac{d\sigma_{str}}{d\Omega_{cT}dE_{cT}} &= \frac{\mu_{cT}K_{cT}}{(2\pi)^3\hbar^2}\frac{1}{2j_0+1}\sum_{m_0}\int d\boldsymbol{b_{nT}}\left(1-\left|e^{i\chi_{nT}(b_{nT})}\right|^2\right)\\ &\times\left|\int d\boldsymbol{r}\, e^{-i\boldsymbol{k_c r}}e^{i\chi_{cT}(\boldsymbol{b_{nT}},\boldsymbol{s})}\phi_{n_0l_0j_0m_0}(\boldsymbol{r})\right|^2.\end{aligned} \tag{5.2.18}$$

It can also be expressed as a function of the final c-T relative momentum

$$\begin{aligned}\frac{d\sigma_{str}}{d\boldsymbol{K'_{cT}}} &= \frac{1}{(2\pi)^3}\frac{1}{2j_0+1}\sum_{m_0}\int d\boldsymbol{b_{nT}}\left(1-\left|e^{i\chi_{nT}(b_{nT})}\right|^2\right)\\ &\times\left|\int d\boldsymbol{r}\, e^{-i\boldsymbol{k_c r}}e^{i\chi_{cT}(\boldsymbol{b_{nT}},\boldsymbol{s})}\phi_{n_0l_0j_0m_0}(\boldsymbol{r})\right|^2.\end{aligned} \tag{5.2.19}$$

or as a function of the final momentum of the core in the projectile restframe [100, 153, 154]

$$\begin{aligned}\frac{d\sigma_{str}}{d\boldsymbol{k_c}} &= \frac{1}{(2\pi)^3}\frac{1}{2j_0+1}\sum_{m_0}\int d\boldsymbol{b_{nT}}\left(1-|e^{i\chi_{nT}(b_{nT})}|^2\right)\\ &\times\left|\int d\boldsymbol{r}\, e^{-i\boldsymbol{k_c r}}e^{i\chi_{cT}(\boldsymbol{b_{nT}},\boldsymbol{s})}\phi_{n_0l_0j_0m_0}(\boldsymbol{r})\right|^2.\end{aligned} \tag{5.2.20}$$

The cross section as a function of the parallel-momentum is obtained by integrating along the transverse momentum $\boldsymbol{k_{c\perp}}$. By using the property [154]

$$\int d\boldsymbol{k_{c\perp}}\, e^{i\boldsymbol{k_c}(\boldsymbol{s}-\boldsymbol{s'})} = (2\pi)^2\delta(\boldsymbol{s}-\boldsymbol{s'}), \tag{5.2.21}$$

the parallel-momentum distribution reads

$$\begin{aligned}\frac{d\sigma_{str}}{dk_{c\parallel}} &= \frac{1}{2\pi}\frac{1}{2j_0+1}\sum_{m_0}\int d\boldsymbol{b_{nT}}\left(1-|e^{i\chi_{nT}(b_{nT})}|^2\right)\int d\boldsymbol{s}\left|e^{i\chi_{cT}(\boldsymbol{b_{nT}},\boldsymbol{s})}\right|^2\\ &\times\left|\int_{-\infty}^{\infty} dz\, e^{-ik_{c\parallel}z}\phi_{n_0l_0j_0m_0}(\boldsymbol{r})\right|^2.\end{aligned} \tag{5.2.22}$$

The distribution of the one-neutron knockout as a function of the parallel-momentum of the core after the collision is thus obtained through the sum (5.2.1) of the diffractive (5.2.7) and the stripping (5.2.22) cross sections.

5.3 Halo-EFT description of the projectile

To understand which structure information is probed by knockout reactions, I study the one-neutron knockout of ^{11}Be on a ^{9}Be target at 60A MeV. This knockout reaction was measured at the National Superconducting Cyclotron Laboratory [76, 77]. As in Chapters 3 and 4, we model ^{11}Be within the single-particle model (see Sec. 1.1.3). The halo nucleus ^{11}Be is seen as an inert ^{10}Be core, assumed to be in its 0^+ ground state, to which a neutron is bound by 0.504 MeV. The ground $1/2^+$ and excited $1/2^-$ states of ^{11}Be are described by the single-particle states $1s1/2$ and $0p1/2$, respectively, with unit spectroscopic factors (1.1.9)–(1.1.10), i.e., $S^{1/2^+0^+}_{s1/2} = S^{1/2^-0^+}_{p1/2} = 1$. Contrary to the previous Chapters, the effective internal Hamiltonian of the projectile (2.3.1) is constructed within Halo-EFT (see Ref. [151] for a recent review). This model expands the projectile Hamiltonian upon the small parameter $R_{\text{core}}/R_{\text{halo}} \approx 0.4$ [152]. The core and the halo neutron are considered structureless and thus constitute the degrees of freedom of the Halo-EFT and the breakdown scale of the EFT is set by the size of the core. Similarly, this expansion can be done with the ratio of momenta associated with the neutron separation energy $S_n = 0.504$ MeV and with the energy of the first excited state 2^+ of the ^{10}Be core of energy $E_{2^+} = 3.4$ MeV, i.e., with $\sqrt{S_n/E_{2^+}} \approx 0.4$ [152].

Halo-EFT is expressed through Lagrangians, in which the operators are expanded up to a given order. Since Halo-EFT can be described as an extension of pionless-EFT, the interactions involved in the Lagrangians are contact interactions [151]. The coefficients of these interactions are called the low-energy constants and have to be constrained. Usually they are adjusted to reproduce experimental data or outputs of structure calculations [151]. The Halo-EFT description of ^{11}Be at leading order (LO) involves one low-energy constant in the $s1/2$ channel. At NLO, one additional parameter in the $s1/2$ and two in the $p1/2$ channels need to be constrained[1] [151, 152].

Following Refs. [66, 152], I use a description of ^{11}Be at NLO. The effective c-n potential V_{cn} in Eq. (2.3.1) is parametrized as contact interactions and their derivatives, which are regulated by Gaussians to obtain numerically tractable potentials. The potential in the partial wave lj reads [152]

$$V^{lj}_{cn}(r) = -V^{lj}_0 e^{-\frac{r^2}{2r_0^2}} - V^{lj}_2 r^2 e^{-\frac{r^2}{2r_0^2}}, \tag{5.3.1}$$

where V^{lj}_0 and V^{lj}_2 are adjustable parameters, which can be fit to reproduce experimental data or predictions from microscopic models in that partial wave. The range of the Gaussians r_0 is an unfit parameter, which can be varied to estimate the sensitivity of the calculations to the short-range physics of the projectile. Since in this parametrization, there is no spin-orbit term and the effective potential does not depend explicitly on the spin of the neutron, the first derivative of the potential is not considered. Indeed, the part of the nuclear potential independent on the spin has to be scalar and thus can only depend on powers of r^2 [155].

As mentioned before, at NLO, the potential (5.3.1) has to be constrained in the $s1/2$ and $p1/2$ partial waves. It is fit to reproduce the experimental binding energies of the $1/2^+$

---

[1] If there were no bound state in the p wave, the interactions would scale "naturally" and the p-wave interaction would only appear at next-to-next-to-next-to-leading order (N3LO). However, as the $1/2^-$ state is modelled as a $0p1/2$ state, the interaction needs to be enhanced in the $p1/2$ wave. Therefore, a $p1/2$-wave interaction arises at LO [151, 152], which is NLO for the whole nucleus, because the expansion has a different counting in each partial wave.

	r_0 [fm]	V_0^{lj} [MeV]	V_2^{lj} [MeV]	E_{nlj} [MeV]	b_{nlj} [fm$^{-1/2}$]
$1s_{1/2}$	1.2	50.375	45	-0.504	0.786
	2	80.54	-2.97	-0.504	0.786
	1.2	-86.03	108.62	-0.504	0.829
$0p_{1/2}$	1.2	96.956	0	-0.184	0.129

Table 5.1: Depths of the Halo-EFT potential (5.3.1) at NLO used to simulate the ^{10}Be-n interaction in the $s1/2$ and $p1/2$ partial waves. The depths are fit to the experimental binding energy and the ANC predicted by Calci *et al.* [51].

($E_{1/2^+} = -0.504$ MeV) and $1/2^-$ ($E_{1/2^-} = -0.184$ MeV) bound states of ^{11}Be. Halo-EFT potentials are also adjusted to the ANC of these states [see Eqs. (1.1.11) and (2.3.7)] predicted by the *ab initio* no-core shell model with continuum (NCSMC) calculations of Calci *et al.* [51]: $b_{1s1/2} = \mathcal{C}_{s1/2} = 0.786$ fm$^{-1/2}$ and $b_{0p1/2} = \mathcal{C}_{p1/2} = 0.129$ fm$^{-1/2}$.

To test the influence of the $1s1/2$ ground state on the reaction calculations, I generate various $s1/2$ Halo-EFT potentials. First, I consider two Gaussian ranges $r_0 = 1.2$ fm and 2 fm. Then, since the *ab initio* calculations predict a spectroscopic factor $S^{1/2^+0^+}_{s1/2} = 0.9$ for the $0^+ \otimes s1/2$ configuration [51] (see Sec. 1.1.4), I also fit the potentials to reproduce a wave function with the same ANC when its norm is reduced to $\sqrt{0.9}$, i.e., $b_{1s1/2} = 0.829$ fm$^{-1/2}$[$=0.786/\sqrt{0.9}$ fm$^{-1/2}$, see Eq. (1.1.11)]. The parameters $V_0^{s1/2}$ and $V_2^{s1/2}$ obtained from these different fits are displayed in Table 5.1 alongside the resulting eigenenergies and SPANCs. The $1s1/2$ wave functions generated from these potentials are plotted in Fig. 5.4.1(a).

Similarly, in the $p1/2$ partial wave, I have initially considered two Gaussian ranges $r_0 = 1.2$ and 2 fm. and I have fit the potential depths to reproduce the binding energy and ANC of the excited state $1/2^-$. However, since the cross sections obtained with these two potentials are similar, only the results obtained with the potential fit with $r_0 = 1.2$ fm in the $p1/2$ are displayed in this thesis. The potential depths in the $p1/2$ are listed in the last line of Table 5.1.

5.4 Sensitivity to the projectile's structure

5.4.1 Optical potentials and numerical details

The test case of this sensitivity analysis is the one-neutron knockout of ^{11}Be with ^{9}Be target at 60A MeV. As seen in Chapter 2, the P-T interactions are simulated through optical potentials. The potentials chosen for both c-T and n-T interactions have a Woods-Saxon shape (2.2.2)–(2.2.3). For the ^{10}Be-^{9}Be interaction, I use the parameters of Ref. [133], which reproduce the ^{10}Be-^{12}C elastic scattering at 59.4A MeV [134]. To account for the different sizes of ^{9}Be and ^{12}C targets, I rescale the radii of the potential by $(10^{1/3} + 9^{1/3})/(10^{1/3} + 12^{1/3})$. The parameters of this optical potential is listed in the first line of Table 5.2. The Coulomb interaction is simulated by a potential generated by a uniformly charged sphere (2.2.4) of radius $R_C = 1.2\,(10^{1/3} + 9^{1/3})$ fm. The n-^{9}Be interaction is modelled by the potential developed in Ref. [156], fit to elastic scattering data of a nucleon off a nucleus with $A \leq 13$ at energies between 65 MeV and 75 MeV. The parameters of this potential at the beam energy considered here are listed in the third

	V_R [MeV]	R_R [fm]	a_R [fm]	W_I [MeV]	R_I [fm]	a_I [fm]	W_D [MeV]	R_D [fm]	a_D [fm]	
^{10}Be-^{9}Be	123.0	3.17	0.8	65.0	3.31	0.8	0	0	0	PRC55
	127.0	3.39	0.78	13.9	5.29	0.7	0	0	0	PRC87
n-^{9}Be	33.08	2.38	0.65	4.15	2.38	0.65	9.175	2.83	0.178	JPG45
	22.6	2.85	0.295	5.3	2.7	0.3	15.25	2.7	0.3	PRC89

Table 5.2: Parameters of the Woods-Saxon optical potentials (2.2.2)–(2.2.3) used to simulate the ^{10}Be-^{9}Be and n-^{9}Be interactions for the one-neutron knockout of ^{11}Be on ^{9}Be at 60A MeV [133, 156, 157, 158].

line of Table 5.2[2]. For both potentials, the energy dependence is neglected in the reaction model.

All the computations use the following model space: the ^{10}Be-n continuum is described up to the c-n orbital angular momentum $l_{\max} = 10$ and a mesh in impact parameter is considered up to 100 fm, with a step of 0.25 fm up to 30 fm and of 2 fm beyond. In this Chapter, all parallel-momentum distributions for the diffractive breakup (5.2.7) are obtained with the CCE. The stripping cross section (5.2.22) is obtained by integrating b_{nT} up to 10 fm, which is enough to reach convergence. Both contributions (A.48) and (5.2.22) are integrated up to $k_{\max} = 1.5$ fm^{-1}, which corresponds to $E_{\max} = 51.3$ MeV. Note that at these large continuum energies, other reaction channels than the elastic scattering of ^{10}Be-n are open. These large energies contributions might therefore be better modelled by an optical potential than the Halo-EFT interaction considered here. In this thesis, I do not study the impact of these other channels and I use the Halo-EFT potential to describe the ^{10}Be-n continuum.

In the following, the parallel-momentum distributions are expressed in the projectile restframe. The total diffractive-breakup and stripping cross sections mentioned in the text are obtained by integrating respectively the diffractive-breakup energy distribution (A.42) up to 100 MeV in the continuum and the stripping parallel-momentum distribution (5.2.22) up to $k_{\max} = 2.1$ fm^{-1}, which corresponds to $E_{\max} = 100$ MeV. These two values ensure the convergence of the total cross sections.

5.4.2 Ground-state wave function

As detailed in Sec. 5.3, I have generated different ^{10}Be-n potentials leading to various $1s1/2$ ground-state wave functions. The corresponding ground-state wave functions are plotted in Fig. 5.4.1(a). By construction, the two wave functions obtained with different ranges ($r_0 = 1.2$ fm in red line and $r_0 = 2$ fm in green line) exhibit identical asymptotics and differ at short distance, i.e., below 6 fm. The ground-state wave function reproducing a larger SPANC (2.3.7) (blue lines) has larger asymptotics and a very different short-range behaviour. To determine if the breakup process is sensitive only to the asymptotics, I normalize this third wave function to the spectroscopic factor 0.9 predicted by Calci *et al.* [51]. By construction, this normalized wave function (brown lines) exhibits the same asymptotics as the previous ones while being very different below $r \approx 4$ fm.

The corresponding parallel-momentum distributions of ^{10}Be for the diffractive breakup (dashed lines) and stripping (dotted lines) of ^{11}Be on ^{9}Be at 60A MeV are plotted in

---

[2] The second and fourth lines of Table 5.2 are discussed further in this Chapter, in Sec. 5.5.

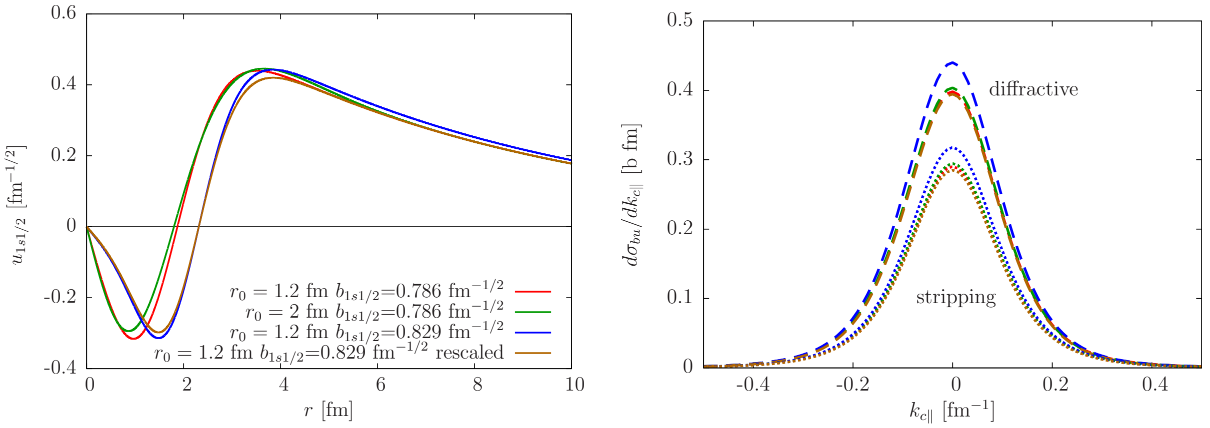

(a) (b)

Figure 5.4.1: Influence of the ground-state wave function onto the parallel-momentum distribution of ^{10}Be resulting from the diffractive breakup (dashed lines) and the stripping (dotted lines) of ^{11}Be on ^{9}Be at 60A MeV. Panel (a) shows the radial wave functions of the 1s1/2 ground state of ^{11}Be, obtained with the potentials detailed in Sec. 5.3. Panel (b) displays the parallel-momentum distribution obtained with these ground-state wave functions.

Fig. 5.4.1(b). The two cross sections obtained with the potentials fit with $r_0 = 1.2$ fm and $r_0 = 2$ fm (red and green lines, respectively) are almost superimposed to one another for both the stripping and the diffractive processes. This confirms the results of Refs. [159, 160, 161] which show that these observables are not sensitive to changes in the ground-state wave function at small distance r. When the reaction is computed with the ground-state wave function fit to the larger SPANC (blue lines), we observe an increase of about 10% in both cross sections. After scaling that initial wave function to the 0.9 spectroscopic factor predicted by Calci *et al.* [51], the cross sections are nearly identical to the previous ones (brown lines).

The total diffractive-breakup $\sigma_{bu}^{\rm total}$, stripping σ_{str} and knockout σ_{ko} cross sections obtained with different ground-state wave functions reproducing the ANC of Calci *et al.* are displayed in Table 5.3. We can see that all these cross sections are similar, the deviations from the case obtained with $b_{1s1/2} = 0.786$ fm$^{-1/2}$ and a unit spectroscopic factor are maximum 2.5%. Therefore, similarly to the exclusive breakup [161], the inclusive breakup of one-neutron halo nuclei is purely peripheral, in the sense that it is sensitive only to the tail of the initial ground-state wave function. This confirms the result obtained by Hansen using a simple geometric model, where the stripping cross sections are shown to be proportional to the square of the SPANC [159], and to the confirmation of this result within an eikonal framework [160]. The tiny difference observed in both the diffractive and stripping part comes from contributions at high ^{10}Be-n relative energies, where the process starts to be slightly more sensitive to the projectile radial wave function at small distances, viz. $r < 4$ fm. An analysis of the diffractive breakup distribution as a function of the relative ^{10}Be-n energy shows that this cross section scales perfectly with the square of the ANC at $E < 40$ MeV.

This analysis confirms that the one-neutron knockout of one-neutron halo nuclei is a peripheral reaction. Therefore, information about the internal part of the wave function cannot be reliably inferred from such measurements. This is in particular true for the spectroscopic factor. Since calculations performed with two wave functions that exhibit

r_0 [fm]	$b_{1s1/2}$ [fm$^{-1/2}$]	$S_{s1/2}^{1/2^+0^+}$	$\sigma_{bu}^{\text{total}} \times S_{s1/2}^{1/2^+0^+}$ [mb]	$\sigma_{str} \times S_{s1/2}^{1/2^+0^+}$ [mb]	$\sigma_{ko} \times S_{s1/2}^{1/2^+0^+}$ [mb]
1.2	0.786	1	107.8	83.4	201.1
2	0.786	1	108.2	84.6	202.8
1.2	0.829	0.9	106.5	81.4	197.9

Table 5.3: Influence of the asymptotics of the ground-state wave function onto the total diffractive-breakup, stripping and knockout cross sections for the collision ^{11}Be with ^{9}Be at 60A MeV. They are obtained with the different ground-state wave functions plotted in Fig. 5.4.1.

different norms but the same ANC provide nearly identical results, it is not clear how accurate the spectroscopic factors extracted from knockout measurements are. However, what is clear from this analysis, is that the parallel-momentum distributions for both diffractive breakup and stripping, are sensitive to the asymptotics of the ground-state wave function. It suggests that these observables would be good candidates to extract accurately the ANC of the wave function of halo nuclei, as done in Refs. [162, 163, 164, 165]. To confirm this, I analyse in the next sections the sensitivity of these observables to other features of the projectile description, viz. the presence of an excited subthreshold bound state and the description of the projectile continuum.

5.4.3 Excited states

This section investigates how the presence of the $1/2^-$ excited state in the ^{11}Be description affects knockout observables. Due to the form of the stripping cross section (5.2.22), which depends only on the ground state wave function, this study is restricted to the sole diffractive breakup. As explained previously, this $1/2^-$ bound state is described as a $0p1/2$ single-particle state, using the Halo-EFT ^{10}Be-n potential (5.3.1) with the parameters listed in the last line of Table 5.1.

The presence of that subthreshold state significantly changes the low-energy continuum in the $p1/2$ partial wave [152, 166, 167], which itself affects the calculation of breakup cross sections at low energy [152, 166]. We therefore expect to see some influence of that state in the diffractive component of the parallel-momentum distribution of the ^{10}Be following the breakup of ^{11}Be. To investigate this in detail, I consider first two ^{10}Be-n interactions in that partial wave. In addition to the $V_{cn}^{p1/2}$ potential described in Sec. 5.3, I consider no interaction at all, hence without considering the $1/2^-$ excited state of ^{11}Be and describing the ^{10}Be-n motion in the $p1/2$ continuum by mere plane waves. Fig. 5.4.2 shows the $p1/2$ waves in the continuum at (a) $E = 0.3$ MeV and (b) $E = 2$ MeV, obtained with the Halo-EFT potential (dashed green lines) and a nil potential, i.e., plane waves (solid magenta lines). One can see that the presence of the $1/2^-$ bound state induces a node at distances $r \sim 6.5$ fm at $E = 0.3$ MeV and $r \sim 4.5$ fm at $E = 2$ MeV. In addition to this node, the distorted wave differs from the plane wave in the asymptotic region due to the phase shift (2.3.8).

The panels (c) and (d) of Fig. 5.4.2 display the cross sections for the diffractive breakup of ^{11}Be on ^{9}Be at 60A MeV as a function of (c) the ^{10}Be-n relative energy and (d) the parallel-momentum of the remaining ^{10}Be. Fig. 5.4.2(c) also includes the contribution of the $p1/2$ partial wave separately. We see that the presence of the $1/2^-$ bound state

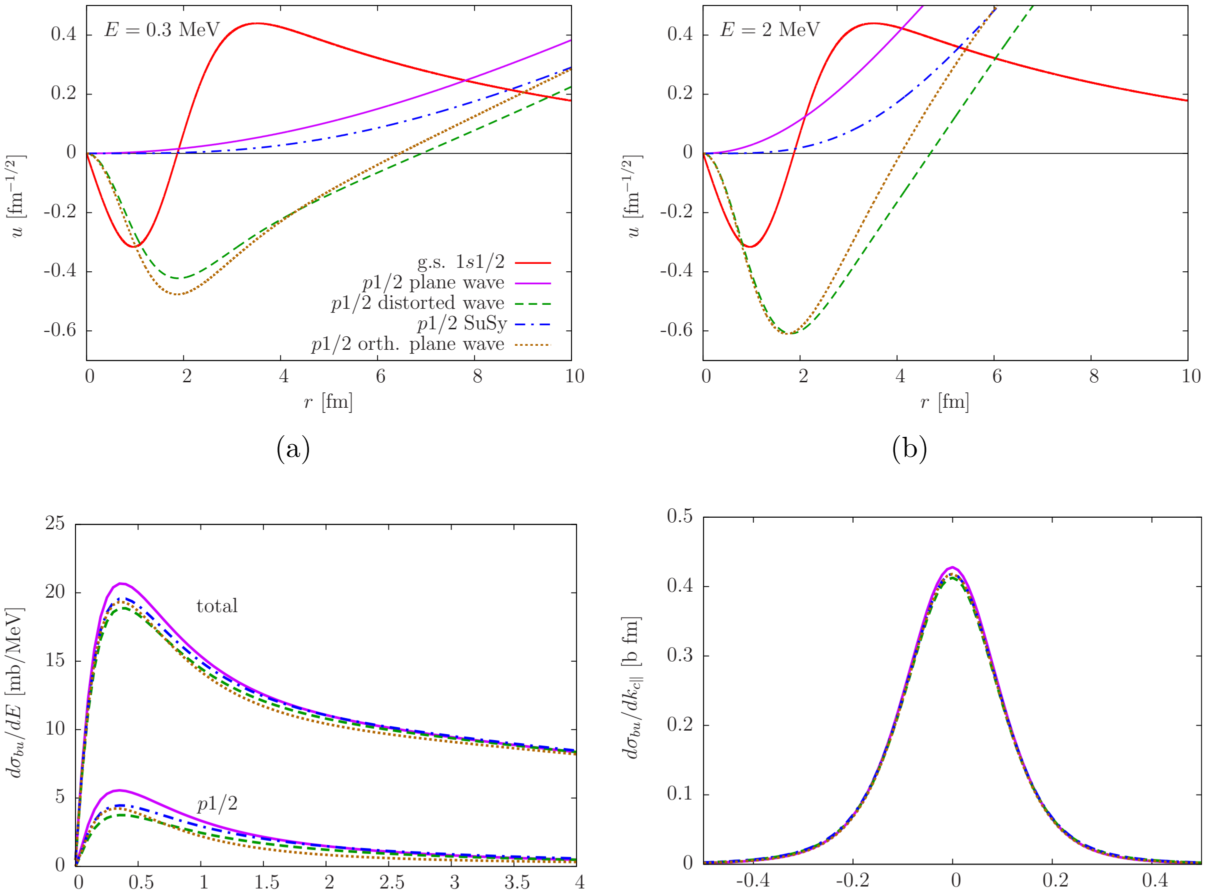

(a) (b)

(c) (d)

Figure 5.4.2: Influence of the presence of a subthreshold bound state in the projectile spectrum on breakup observables for ^{11}Be on ^{9}Be at 60A MeV. Radial wave functions for different c-n interactions in the $p1/2$ waves at (a) $E = 0.3$ MeV and (b) $E = 2$ MeV in the ^{10}Be-n continuum and of the $1s1/2$ ground-state. Diffractive-breakup cross section as a function of (c) the ^{10}Be-n relative energy (total and $p1/2$ contribution) and (d) the parallel-momentum of ^{10}Be.

	$1s1/2$ + $0p1/2$	$1s1/2$ + $p1/2$ pw	$1s1/2$ + SuSy $p1/2$	$1s1/2$ + $p1/2$ opw
$\sigma_{bu}^{\text{total}}$ [mb]	107.8	109.3	109.3	107.4
$\sigma_{bu}^{p1/2}$ [mb]	7.9	9.4	9.4	7.6
σ_{inel} [mb]	2.1	0	0	2.1
$\sigma_{bu}^{\text{total}} + \sigma_{inel}$ [mb]	109.9	109.3	109.3	109.5

Table 5.4: Influence of the presence of a subthreshold bound state on the total breakup and inelastic cross sections for the collision ^{11}Be with ^{9}Be at $60A$ MeV. They are obtained from computations considering both the $1/2^+$ ground-state and the $1/2^-$ excited state ($1s1/2 + 0p1/2$), when the $1/2^-$ excited state is not included ($1s1/2$ + $p1/2$ pw), when this $1/2^-$ state is removed by supersymmetry [168, 169, 170] ($1s1/2$ + SuSy $p1/2$) and when the $1/2$ continuum is described by plane waves orthogonalized to the $0p1/2$ wave function ($1s1/2$ + $p1/2$ opw).

in the description of the projectile reduces the $p1/2$ diffractive breakup, mostly at low energies in the continuum (compare the dashed green line to the solid magenta one). This is reflected in the parallel-momentum distribution by the drop of the amplitude of the peak by approximatively 2.1%. Note that the presence of the $1/2^-$ state enhances the energy distribution above 25 MeV but the cross sections are very small at such high energies. Table 5.4 displays the diffractive-breakup cross sections $\sigma_{bu}^{\text{total}}$, its $p1/2$ breakup contribution $\sigma_{bu}^{p1/2}$ and the inelastic-scattering cross section σ_{inel}. It shows that the presence of the $1/2^-$ bound state reduces the diffractive-breakup cross sections $\sigma_{bu}^{\text{total}}$ by 1.5 mb, which corresponds to a relative diminution of 1.4%. Only the $p1/2$ breakup contribution $\sigma_{bu}^{p1/2}$ is affected by the presence of the $1/2^-$ state.

Adding the $1/2^-$ bound state also opens another reaction channel, the inelastic excitation of ^{11}Be from the ground state $1/2^+$ to the excited state $1/2^-$. I evaluate the inelastic cross sections from a ground state $n_0 l_0 j_0$ to an excited state nlj with the usual eikonal model. The corresponding cross section reads (see Appendix A)

$$\sigma_{inel}^{nlj} = \frac{2\pi}{2j_0+1} \sum_{m_0 m} \int_0^{+\infty} b\,db\, \left| \langle \phi_{nljm} | e^{i\chi^C} e^{i\chi^N} | \phi_{n_0 l_0 j_0 m_0} \rangle \right|^2 , \qquad (5.4.1)$$

where $\chi^{C,N}$ are the eikonal phases (2.3.36). The total inelastic-scattering cross section is listed in Table 5.4. Interestingly, the flux of probability lost in the $p1/2$ breakup seems to be transferred to the inelastic cross section σ_{inel}. This suggests that, for such reactions at intermediate energies where the dynamical effects are small, a conservation of the probability flux within a partial wave is approximately respected.

This decrease in the cross section can be qualitatively explained by studying the overlap of $p1/2$ radial wave function in the continuum with the one of the $1s1/2$ ground state, appearing in the CCE partial breakup amplitude (A.50). At both energies in the continuum in Fig. 5.4.2, the node of the distorted $p1/2$ wave is located in a range where the $1s1/2$ wave function (solid red lines) is significant. Moreover, the phase shifts induced by the $p1/2$ interaction can also play a role [166]. To discriminate the impact of the node from the phase shifts on the breakup cross sections, I follow two different approaches. The first is to remove the $1/2^-$ state with phase-equivalent transformations of the potential through supersymmetry [168, 169, 170]. These transformations conserve the phase shifts while eliminating the bound state, hence the node at small r in the $p1/2$ wave function as seen in Fig. 5.4.2 (dash-dotted blue lines).

The construction of a phase-equivalent potential where the nlj bound state is removed, can be done by applying two subsequent transformations [168, 169]: the first removes the bound state nlj leaving the rest of the bound spectrum unchanged but modifies the phase shift in the lj partial wave; the second restores the initial lj phase shift. After these two transformations, the new potential in the lj partial wave reads [169]

$$V_{cn}^{lj(2)}(r) = V_{cn}^{lj}(r) - \frac{\hbar^2}{\mu_{cn}}\frac{d^2}{dr^2}\ln\int_0^r dr'\,[u_{nlj}(r')]^2, \tag{5.4.2}$$

where u_{nlj} is the radial wave function of the removed bound state obtained with the initial potential V_{cn}^{lj}. These transformations affect the new lj scattering wave functions at short distances, their radial parts read [169]

$$u_{klj}^{(2)}(r) \;=\; u_{klj}(r) - u_{nlj}(r)\frac{\int_0^r dr'\,u_{nlj}(r')u_{klj}(r')}{\int_0^r dr'\,[u_{nlj}(r')]^2} \tag{5.4.3}$$

where u_{klj} and $u_{klj}^{(2)}$ are the radial part of the scattering wave functions before and after the supersymmetric transformations, respectively.

The corresponding energy distribution (dash-dotted blue line), displayed in Fig. 5.4.2(c), lies between the plane-wave and the distorted-wave cases below 1 MeV whereas, at larger energies, it tends to the plane-wave computations and overestimates it above 4 MeV. The discrepancy between the distorted-wave case and the supersymmetric case can be explained by the fact that the transformations are applied to a loosely-bound state and thus affect the asymptotics of the $p1/2$ waves, i.e., above 5 fm [see Eq. (5.4.3)]. Similarly to the energy distribution, the parallel-momentum cross sections in Fig. 5.4.2(d) show that the supersymmetric case lies between the plane-wave and the distorted-wave cases.

The second approach is to keep the zero at short distances in the $p1/2$ wave function, and thus the $1/2^-$ state, but have a nil $p1/2$ phase shift. To do so, I use plane waves to describe the $p1/2$ continuum, and orthogonalize them to the $0p1/2$ wave function. The orthogonalization of continuum wave functions in the lj wave to a nlj bound state read

$$u_{klj}^{\text{opw}}(r) \;=\; krj_l(kr) - u_{nlj}(r)\int_0^{+\infty} dr'\,u_{nlj}(r')kr'j_l(kr') \tag{5.4.4}$$

where "opw" stands for orthogonalized-plane waves, $krj_l(kr)$ is the radial wave function of a plane wave [$\delta_{lj} = 0$ in Eq. (2.3.8)] and j_l is a spherical Bessel function of the first kind [92]. Fig. 5.4.2 shows that these orthogonalized plane waves (dotted brown lines) exhibit a node in the $p1/2$ wave around 6.5 fm at $E = 0.3$ MeV and 4 fm at $E = 2$ MeV while keeping a nil phase shift. These nodes are located in the asymptotics of the $p1/2$ waves because the $0p1/2$ state is loosely-bound and the $p1/2$ waves are modified at large r [see Eq. (5.4.4)].

The energy distribution computed with the orthogonalized plane-waves (dotted brown line) plotted in Fig. 5.4.2(c) is closer at the peak to the $p1/2$ distorted-wave case than the supersymmetric case. This can be explained by the fact that the orthogonalized plane waves are closer to the distorted waves at both energies than to the plane waves. The orthogonalized plane-wave computation overestimates the distorted-wave calculation below 0.7 MeV while it underestimates it at larger energies. Since these two contributions tend to compensate each other when they are integrated, the parallel-momentum distribution seems to be on top of the supersymmetric case at the peak and lies between the plane-wave and the distorted-wave cases.

Even if the parallel-momentum distributions obtained with the two additional descriptions of the continuum, i.e. the $p1/2$ waves obtained with the supersymmetric transformations and the $p1/2$ orthogonalized plane waves, are similar at the peak, their total cross sections differ noticeably. In Table 5.4, the diffractive breakup cross sections obtained with the supersymmetric transformations is similar to the plane-wave case. This is due to the compensation of the high-energy, i.e. above 4 MeV, and low-energy contributions. However, the total diffractive breakup cross section obtained with the orthogonalized-plane waves is reduced by 1.9 mb compared to the plane-wave case, which corresponds to a relative diminution of 1.7%. This reduction is similar to the one observed in the distorted-wave case and seems also to be transferred to the inelastic scattering observable, which is 2.1 mb. Because both distorted waves and the orthogonalized planes include the $1/2^-$ bound state, this analysis is therefore consistent with the hypothesis of conservation of the probability flux within one partial-wave.

The same study performed within the DEA, where the adiabatic approximation is not considered (see Sec. 2.3.3.3), leads to identical results. Moreover, this conclusion remains unchanged when the excited bound state is in the d wave, as would be the case for a ^{15}C projectile, another well known one-neutron halo nucleus. Therefore, such reactions at intermediate energies, where the dynamical effects are small, seems to conserve the probability flux within a partial wave, simply shifting that flux from the inelastic to the breakup channels. This effect has already been observed by Moro *et al.* in their theoretical analysis of the Coulomb-breakup measurement of ^{11}Be performed at RIKEN [35]. Including the $1/2^-$ bound excited state in the description of ^{11}Be reduces the E1 strength to the continuum by an amount that is almost equal to the E1 strength for the Coulomb excitation from the $1/2^+$ ground state to the $1/2^-$ excited state [171].

Theoretically, this transfer from the breakup to the inelastic channel is a consequence of the Hermicity of the ^{10}Be-n Hamiltonian and the adiabatic treatment of the reaction. Since the wave functions of the bound states ϕ_{nljm} and of the continuum ϕ_{kljm} form an orthogonal basis in the subvectorial space defined by the partial wave ljm, the following closure relation holds

$$\sum_n |\phi_{nljm}\rangle\langle\phi_{nljm}| + \frac{2}{\pi}\frac{\mu_{cn}}{\hbar^2 k}\int dE\, |\phi_{kljm}\rangle\langle\phi_{kljm}| = \mathbb{1}_{ljm}, \tag{5.4.5}$$

where the sum runs over all the bound states in the partial wave ljm. At the usual eikonal approximation, i.e., relying on the adiabatic approximation, the contribution to the diffractive-breakup cross section of each partial wave σ_{bu}^{lj} is simply obtained by integrating the corresponding contribution to the energy distribution. It reads [see Eqs. (A.42) and (A.49)]

$$\sigma_{bu}^{lj} = \frac{4\mu_{cn}}{\hbar^2 k}\frac{1}{2j_0+1}\sum_{m_0 m}\int dE \int b\, db \left| \langle\phi_{kljm}|e^{i\chi^N}e^{i\chi^C}|\phi_{n_0 l_0 j_0 m_0}\rangle\right|^2. \tag{5.4.6}$$

By using the closure relation (5.4.5) into the breakup cross section per partial-wave (5.4.6), we can write for any partial wave that does not include the ground state, i.e., $lj \neq l_0 j_0$,

$$\sigma_{bu}^{lj} = \frac{2\pi}{2j_0+1}\sum_{m_0 m}\int b\, db \int dr \left|\lim_{Z\to+\infty}\psi_{ljm}^{(m_0)}(b,0,Z,r)\right|^2 - \sum_n \sigma_{inel}^{nlj}, \tag{5.4.7}$$

where $\psi_{ljm}^{(m_0)}$ (A.10) is the radial ljm contribution of the three-body wave function $\Psi^{\mathrm{eik}(m_0)}$ and σ_{inel}^{nlj} (5.4.1) is the contribution of the bound state nlj to the inelastic scattering cross sections.

The first term of (5.4.7) does not depend on the description of the continuum, nor on the presence of excited states, the sum

$$\sigma^{lj}_{\text{sum}} = \sigma^{lj}_{bu} + \sum_n \sigma^{nlj}_{inel} \tag{5.4.8}$$

is therefore sensitive only to the ground-state wave function and the optical potentials. This relation explains the transfer within each partial-wave of the flux from the breakup to the inelastic-scattering channel when an additional bound state is included. Accordingly, the sum of the total breakup and inelastic cross sections should be independent from the choice of $V^{p1/2}_{cn}$ (see the last line of Table 5.4). The small differences are due to the fact that the calculations have been performed with the CCE, which accounts for part of the dynamics (see Sec. 2.3.3.5). The conservation of the sum of the inelastic-scattering and diffractive-breakup flux cannot therefore be demonstrated because the operators within the partial breakup amplitudes (A.50) depend on $\chi^{C,(\lambda=1)}_{\text{FO}}$ (2.3.44) and thus on E. However, as mentioned above, the dynamical effects are small for this reaction, and thus the conservation of the flux within a given partial wave is almost respected.

In conclusion, the presence of a loosely-bound excited state changes non-negligibly the shape and magnitude of the c-n relative energy distribution for the diffractive breakup. The parallel-momentum distributions of the remaining core are affected in a smaller extent, i.e., less than 3% reduction at the peak. This reduction of the cross section is caused by both the node at short distance in the continuum wave functions and the non-zero phase shift introduced by the c-n interaction. The amplitude loss in the diffractive breakup goes to the inelastic-scattering channel, as already seen in Coulomb-breakup calculations by Moro *et al.* [171]. I have shown that this feature can be explained at the adiabatic approximation by the conservation of probability flux shared between the inelastic and breakup channels.

5.4.4 Resonances

I now investigate the influence of the resonant ^{10}Be-n continuum on the breakup distributions. As in the previous section, only the diffractive breakup is studied because at the usual eikonal approximation the stripping cross section (5.2.22) does not depend on the description of the continuum of the projectile. To do so, a resonance in the $d5/2$ partial-wave is included at $E_{d5/2} = 1.27$ MeV with a width of $\Gamma_{d5/2} = 98$ keV, close to the experimental values of the $5/2^+$ resonance $E^{\text{exp}}_{5/2^+} = 1.28$ MeV and $\Gamma^{\text{exp}}_{5/2^+} = 100$ keV. This approach goes beyond the NLO of the Halo-EFT expansion, since there is an interaction in the d partial-wave [152]. To fully study the impact of the continuum, resonances at the same energy with other widths are considered, i.e. $\Gamma_{d5/2} = 51$ keV and $\Gamma_{d5/2} = 162$ keV, and at a higher energy $E_{d5/2} = 3$ MeV with various widths $\Gamma_{d5/2} = 451$ keV, $\Gamma_{d5/2} = 876$ keV and $\Gamma_{d5/2} = 1487$ keV. To model these resonances, I vary the depths of the Gaussian potential (5.3.1) in that sole $d5/2$ partial wave. The parameters of these potentials are listed in Table 5.5.

Fig. 5.4.3(a) displays the $d5/2$ contribution to the diffractive-breakup cross section for ^{11}Be on ^{9}Be at 60A MeV as a function of the ^{10}Be-n relative energy. These energy distributions are obtained with no interaction in the $d5/2$ (solid magenta line), with a resonance at $E_{d5/2} = 1.27$ MeV (dashed lines) and at $E_{d5/2} = 3$ MeV (dotted lines) characterized with different widths $\Gamma_{d5/2}$ (green, blue and brown lines). We can see that the presence of a resonance causes a peak in the energy distribution at energy $E_{d5/2}$ with

$E_{d5/2}$ [MeV]	$\Gamma_{d5/2}$ [keV]	r_0 [fm]	$V_0^{d5/2}$ [MeV]	$V_2^{d5/2}$ [MeV]
1.27	51	1.2	330	-50
	98	1.2	106.6	30
	162	1.2	-231.8	100
3	451	1.2	199.35	0
	876	1.2	4.7	50
	1487	1.2	-19.9	150

Table 5.5: Depths of the Halo-EFT potential (5.3.1) used to simulate the ^{10}Be-n interaction in the $d5/2$ partial-wave. The depths are fit to the to reproduce various $d5/2$ resonances at a energy $E_{d5/2}$ with a width $\Gamma_{d5/2}$.

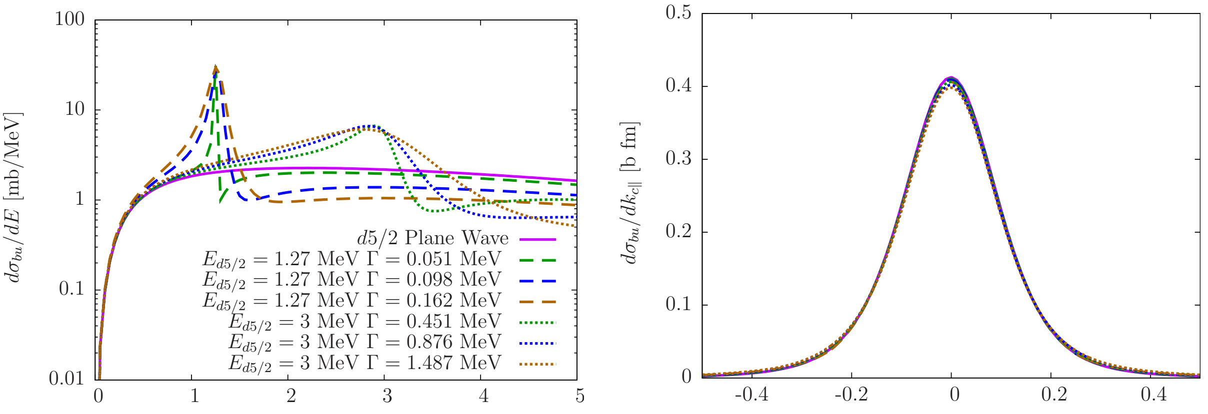

(a)

(b)

Figure 5.4.3: Influence of a $d5/2$ resonance on breakup observables for ^{11}Be on ^{9}Be at 60A MeV. Panel (a) displays the $d5/2$ contribution to the energy distribution and panel (b) the parallel-momentum of the remaining ^{10}Be.

a width of the order of the resonance width $\Gamma_{d5/2}$, as seen in Refs. [35, 127] and explained in Chapter 1. Moreover, these peaks are all followed by a depletion area resulting from destructive interferences caused by the phase shift going over $\pi/2$. The width of this area is proportional to the peak width: sharper resonances have a steeper drop and tends more rapidly to the plane-wave computation after the resonance. When this distribution is integrated, these two effects tend to compensate. The integrated breakup cross sections, listed in Table 5.6, are similar for the different descriptions of the $d5/2$ continuum, even within a partial-wave. This confirms the hypothesis of a conservation of the probability flux within the $d5/2$ partial wave. The discrepancies are explained as before, the conservation of the flux is not perfectly respected for the CCE, since this model includes part of the projectile dynamics. The corresponding parallel-momentum distributions shown in Fig. 5.4.3(b) are similar. This implies that the knockout observable is quite insensitive to the description of the continuum: the presence (or absence) of a resonance does not influence the parallel-momentum distribution for the diffractive breakup and therefore the knockout cross sections.

In conclusion, the description of the continuum has a negligible influence on the inclusive breakup observables. Contrary to the energy distributions, where the resonance has a significant impact, a precise description of the continuum is not necessary in the

	$d5/2$ pw	Res. $E_{d5/2} = 1.27$ MeV			Res. $E_{d5/2} = 3$ MeV		
$\Gamma_{d5/2}$ [keV]		51	98	162	451	876	1487
$\sigma_{bu}^{\text{total}}$ [mb]	107.8	107.6	107.8	107.8	107.8	107.8	107.8
$\sigma_{bu}^{d5/2}$ [mb]	16.9	16.8	16.9	16.9	17.0	17.0	17.0

Table 5.6: Influence of a $d5/2$ resonance on the total and the $d5/2$ contribution to breakup cross sections of ^{11}Be with ^{9}Be at 60A MeV. Both the $1/2^+$ ground state and the $1/2^-$ excited state are considered, with either plane waves (pw) in $d5/2$ or resonances at $E_{d5/2} = 1.27$ MeV and $E_{d5/2} = 3$ MeV with different widths $\Gamma_{d5/2}$.

computation of the parallel-momentum distributions and total cross sections. Putting simply plane waves to describe the continuum is therefore sufficient. Note that this conclusion is not specific for one partial-wave, similar features are observed for p and f resonances at different energies with various widths. I have also conducted the same analysis with the DEA, which includes the dynamics of the projectile, and the conclusions were identical. This independence on the description of the continuum suggests that this observable can be used to extract other precise information pertaining to the initial ground-state, such as its ANC (see Sec. 5.4.2).

5.5 Sensitivity to the optical potential

To extract reliable information from knockout observables, the sensitivity of the cross sections to the choice of optical potentials needs to be assessed. To do so, I compare the eikonal predictions to the experimental data of the one-neutron knockout of ^{11}Be with ^{9}Be at 60A MeV, which was measured at National Superconducting Cyclotron Laboratory [76, 77]. The experimental setup relies on two detectors: a spectrograph and a Gamma-ray scintillator. The spectrograph detects ^{10}Be residues after the reaction. As some of these residues are in an excited state, the scintillator collects the Gamma-rays emitted through their deexcitation. Combining these two measurements, the cross sections of the one-neutron knockout of the projectile populating a given final state of the residue can be extracted. The errors associated with the experimental procedure is evaluated to be about 12% of the total knockout cross section [77]. They account for the uncertainties in target thickness, incident particle rate, particle identification, and the spectrograph acceptance. The experimental setup is presented in more details in Ref. [82]. I study here only the one-neutron knockout reaction of ^{11}Be where the ^{10}Be residue is in its ground state 0^+.

The momentum distributions are shown in the laboratory system and thus are expressed as a function of the parallel-momentum of the core in this frame $p_{cT\|} = \hbar K'_{cT\|}$ (5.2.19). The distributions are centered around the initial momentum of the core $p^i_{cT\|}$, which is computed in the relativistic regime through [44]

$$p^i_{cT\|} = m_c v \gamma, \tag{5.5.1}$$

where v is the initial P-T velocity, $\gamma = 1/(1 - v^2/c^2)$ is the relativistic factor with c the speed of light in vacuum. For one-neutron knockout of ^{11}Be with ^{9}Be at 60A MeV, $p^i_{cT\|} = 3.397$ GeV/c. However, the experimental distribution is centered at 3.33 GeV/c. This shift in momentum is due to the fact that the core slows down in the target. To

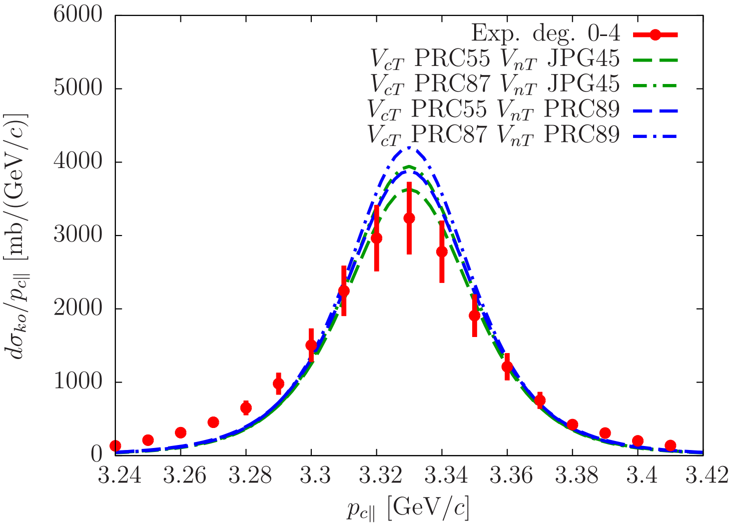

Figure 5.5.1: Influence of the choice of optical potentials on the parallel-momentum distribution of ^{10}Be after the one-neutron knockout of ^{11}Be with ^{9}Be at 60A MeV. The experimental data are the red points [76, 77].

compare with experimental data, the theoretical predictions are centered at 3.33 GeV/c. The deflection of the remaining core after the knockout is small, only the angles up to 4° in the laboratory frame contribute significantly to the cross sections [76, 77]. The data are thus measured up to 4°. Moreover, because the deflection angle is small, the relativistic effects can be accounted for by simply broadening the distributions by the relativistic factor $\gamma = 1.064$ [77].

I use the Halo-EFT description of ^{11}Be at NLO presented in Sec. 5.3. To analyse the impact of the choice of optical potentials, two new optical potentials are considered. Additionally to the ^{10}Be-^{9}Be interaction presented in Sec. 5.5, I consider the potential developed in Ref. [157]. This potential has a Woods-Saxon shape (2.2.2)–(2.2.3) and is adjusted to reproduce the elastic scattering of ^{9}Be off ^{13}C at 40 MeV. I rescale the radii of the potential with the numbers of mass, i.e., with $(9^{1/3}+10^{1/3})(9^{1/3}+13^{1/3})$ (second line of Table 5.2). The Coulomb interaction is simulated by a potential generated by a uniformly charged sphere of radius $R_C = 4.23$ fm. Obviously, the energy range of this potential is not well adapted for this collision, but it is the second most realistic potential that I have found. I also consider an additional n-^{9}Be interaction, which has been developed in Ref. [158] and is fit to reproduce the total, the elastic, and the reaction cross sections of a neutron with ^{9}Be at energies between 1 and 100 MeV. It is also parametrized with a Woods-Saxon shape (2.2.2)–(2.2.3). Its parameters at the beam energy considered here are displayed in the fourth line of Table 5.2.

Fig. 5.5.1 shows how the choice of the optical potentials impacts the parallel-momentum distribution of ^{10}Be after the one-neutron knockout of ^{11}Be with ^{9}Be at 60A MeV. The distribution (V_{cT} PRC55 V_{nT} JPG45, dashed green line) obtained with the set of potentials that I have used initially in this Chapter (see first and third lines of Table. 5.2) has a peak within the hypothetical[3] error bars of the experimental cross section (red points). The other ^{10}Be-^{9}Be interaction, denoted PRC87 (dash-dotted green and blue lines, second line of Table 5.2), leads to cross sections with a higher peak and overestimates the experimental

---

[3] As I could not get access to the data, I have scanned the values of Ref. [77]. I have assumed that the relative errors are constant and I have estimated them with the experimental error on the total cross section which is about 15.27% [76, 77].

	V_{cT}	PRC55	PRC87	PRC55	PRC87	Exp.
	V_{nT}	JPG45	JPG45	PRC89	PRC89	
σ_{ko} [mb]		192	203	204	215	203± 31

Table 5.7: Total one-neutron knockout cross section of ^{11}Be with ^{9}Be at 60A MeV. The theoretical predictions obtained with different choices of projectile-target optical potentials are compared to the experimental value [77].

peak. This indicates that the potential PRC55 is more absorptive than the one denoted PRC87. This is not surprising since the imaginary depth of PRC55 is approximately five times larger than the one of PRC87 (compare the two first lines of Table 5.2). Using another n-^{9}Be potential also influences the parallel-momentum distribution. We can see that using the potential PRC89 (fourth line of Table 5.2) instead of the one denoted JPG45 leads to a distribution with a larger peak (the blue lines compared to the green lines). This can be explained by the fact that the radius of the imaginary surface term of the potential JPG45 is larger than the one of the potential PRC89 (compare the two last lines of Table 5.2). Therefore, the predictions obtained with all four sets of potentials tend to overestimate the peak of the experimental distribution.

The experimental and eikonal knockout cross sections are displayed in Table 5.7. These cross sections are obtained by integrating the parallel-momentum distribution between $p_{cT\|} = 3.24$ to 3.41 GeV/c. As expected, less absorptive potentials such as PRC87 and PRC89 lead to larger knockout cross sections. We can also note that the agreement between the theoretical predictions with the experimental data is good. Since these cross sections are mostly sensitive to the ANC, the knockout data seems to agree well with the ANC predicted with Calci *et al.* [51].

We can also see in Fig. 5.5.1 that none of the predictions reproduce the asymmetry and the width of the experimental distribution. As explained in the Chapter 4, the shape of the distribution is due to dynamical effects, which are not included at the usual eikonal approximation. For the diffractive breakup contribution, dynamical models, such as CDCC, the DEA and the S-DEA, predict an asymmetric parallel-momentum distribution. In Ref. [77], the authors analyse how the shape of the CDCC distribution evolves with the deflection angle of ^{14}C after the diffractive breakup of ^{15}C with ^{9}Be at 54A MeV. Fig. 5.5.2 displays the Fig. 5 of Ref. [77]. This figure shows that the laboratory angles larger than 4° do not contribute significantly to the cross sections. Moreover, at forward angles, i.e., below 0.5°, the CDCC (lines) and eikonal (solid circles) predictions are superimposed, and both lead to a symmetric distribution with the same width. This is expected since the eikonal approximation relies on a small-angles approximation (A.27). At larger angles, the distribution becomes more asymmetric indicating that the dynamical effects play an important role [77, 172]. The forward angles can thus be analysed by the usual eikonal approximation while the larger angles should be compared with models including dynamical effects in both the diffractive and stripping contributions.

In conclusion, my comparison of eikonal predictions obtained with different sets of optical potentials to experimental data shows that the shape of the parallel-momentum distributions is insensitive to the choice of the potentials. However, the magnitude of the knockout observables are sensitive to both the c-T and n-T optical potentials, which have thus to be chosen carefully. We have also seen that the eikonal model lacks asymmetry due to its adiabatic approach. Since this asymmetry and thus the dynamical effects are small at forward angles, the eikonal model might be more accurate if applied only at

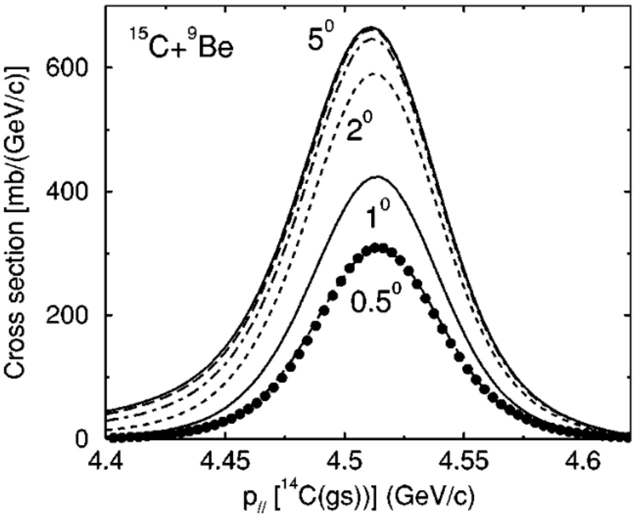

Figure 5.5.2: Evolution of the asymmetry of parallel-momentum distribution for the diffractive breakup of ^{15}C with ^{9}Be at 54A MeV, as a function of the maximum angle of detection of the ^{14}C residue in the laboratory frame. The lines are obtained with CDCC and the solid circles with the eikonal model at $\theta \leq 0.5°$. This figure is taken from Ref. [77].

these angles. Finally, for all these calculations, the parallel-momentum distributions are integrated up to 51.3 MeV in the ^{10}Be-n continuum (see Sec. 5.5), where other channels than the elastic scattering one are open. Since the Halo-EFT description of ^{10}Be-n is only suited to describe the low-energy part of ^{10}Be-n spectrum, the large energies in the ^{10}Be-n continuum might therefore be better modelled by including an imaginary part that simulates missing channels in the description of ^{11}Be at these high continuum energies.

5.6 Summary and prospects

Knockout reactions are often used to probe experimentally the structure of halo nuclei. These inclusive reactions are of particular interest since they have much higher statistics than exclusive measurements. To reliably extract structure information, one needs to know precisely the sensitivity of the reaction observables to the projectile description and the choice of nuclear interactions. This study enables to pin down what nuclear-structure information can be safely inferred from knockout data and it also provides an idea of the uncertainties due to the choice of optical potentials. In the first part of this Chapter, I have investigated how the ground-state wave function, the presence of subthreshold excited states and resonances in the core-neutron continuum influence the parallel-momentum distribution of the remaining core after the collision. I have also studied the influence of these structure features on the relative core-neutron energy distribution after the diffractive breakup of one-neutron halo nuclei. This analysis is performed for the one-neutron knockout of ^{11}Be with ^{9}Be at 60A MeV.

By using a Halo-EFT description of ^{11}Be at NLO [66, 152], I have generated ground-state wave functions with very different inner parts but similar large-distance behaviour. I have shown that the parallel-momentum distributions of both the diffractive breakup and stripping, are sensitive only to the asymptotics of the ground-state wave function. This confirms the conclusions of Refs. [159, 160] for knockout and of Ref. [161] for diffractive breakup: the inclusive breakup observables of one-neutron halo nuclei cannot be used to probe the ground-state wave function below 4 fm. In particular, the spectroscopic factor of such loosely-bound nuclei cannot be determined reliably from these observables. However, information about the tail of the wave function, viz. the ANC, can be safely extracted. This suggests that the good agreement between theory and experiments observed for loosely-bound nuclei [26, 27] is rather due to a fair reproduction of the ANC in the single-particle model of the projectile than a precise prediction of the spectroscopic factor.

The presence of an excited subthreshold state, such as the $1/2^-$ excited state in ^{11}Be, reduces the breakup cross section. I have demonstrated that at the adiabatic approximation, this reduction in the breakup amplitude is transferred to the inelastic channel, viz. to the excitation of the projectile towards that subthreshold state. I have also shown that the presence of a resonance in the continuum has a negligible impact on the parallel-momentum distribution and the total cross section for one-neutron knockout reactions. Therefore, in the theoretical analyses of these distributions, an accurate description of the core-neutron resonant continuum is not needed. This strongly reduces the uncertainty related to the projectile model in the study of such reactions. Knockout observables of loosely-bound nuclei are therefore ideal to extract structure information pertaining to the asymptotics of the ground-state wave function, such as the ANC. Similar conclusions are also obtained for the one-neutron knockout ^{15}C on ^{9}Be at $54A$ MeV. This sensitivity analysis to the projectile's structure has been published in Refs. [30, 31].

Because optical potentials are needed to simulate the projectile-target interactions, I have also estimated the sensitivity of knockout cross sections to the choice of optical potentials. To do so, I have compared the eikonal predictions obtained with different sets of optical potentials to experimental data [76, 77]. The magnitude of the knockout observables are sensitive to the optical potentials, suggesting that the uncertainty introduced by their choice should be assessed in theoretical analyses. This uncertainty quantification could be done following a Bayesian approach, as it has been done for transfer reactions in Refs. [173, 174]. Since knockout observables are integrated up to high energy in the continuum, e.g. up to 51.3 MeV in the ^{10}Be-n continuum, the absorption channels in the c-n system might also influence the magnitude of the cross section. It would therefore be also interesting to evaluate the impact of the absorption channels in the c-n system, through the use of phenomenological optical potential to describe the scattering states.

The eikonal model misses the asymmetry of the experimental data, due to its adiabatic approach. However, since this asymmetry and thus the dynamical effects are small at forward angles [77, 172], the eikonal model might be accurate at these angles. A direct prospect of this work would be to compare the eikonal cross sections calculated only for these forward angles to the corresponding experimental data. For larger laboratory angles, dynamical effects play a non-negligible role, and should be included within the reaction model. It would therefore be also interesting to study a generalization of the DEA and S-DEA to knockout reactions.

After quantifying the uncertainty due to the choice of interaction potentials, I could extract an ANC for ^{11}Be from the knockout cross section at forward angles and compare it to the *ab initio* predictions of Calci *et al.* [51]. A similar comparison of the ANC extracted from knockout data [76, 77] with the *ab initio* predictions could also be performed for ^{15}C. Hopefully, this would confirm similar analyses performed recently for diffractive breakup [66, 152] and transfer [175, 176]. In the future, a sensitivity analysis combining

Halo-EFT and the eikonal reaction model could also be applied to the one- and two-neutrons knockout of two-neutron halo nuclei, using the eikonal framework for three-body projectiles [111, 144, 177, 178]

Conclusions

In this thesis, I have focused on the improvement of the eikonal approximation for reactions involving one-neutron halo nuclei. Because they are very short-lived, these nuclei are often studied through reactions. The accuracy of the nuclear-structure information inferred from reaction measurements depends strongly on the validity of the reaction model and the quality of the description of the nucleus involved in the reaction. Improving the eikonal approximation is motivated by its small numerical cost compared to the exact solution provided by the Faddeev formalism or other state-of-the-art methods such as CDCC. Thanks to its relatively low numerical cost, the eikonal approximation could be extended to more complex descriptions of the nucleus while keeping a reasonable computational time. However, since it assumes that the deflection of the projectile by the target is small and relies on the adiabatic approximation, the eikonal model is restricted to beam energy above $60A$ MeV. At lower energy, the eikonal approximation tends to overestimate the elastic-scattering cross section at large angles and underestimate the breakup observables.

In the first part of this thesis, I have studied the extension of the eikonal model down to $10A$ MeV, which is in the energy range of HIE-ISOLDE at CERN and ReA12 at the upcoming FRIB. Because its extension has already been achieved by a semiclassical correction for Coulomb dominated reactions [114, 115], I have studied nuclear corrections to the eikonal model in order to enhance its accuracy for reactions on light targets. I have analysed three different corrections to the eikonal approximation, i.e., Wallace's [118, 119], the semiclassical [121] and exact continued S-matrix [122, 123, 124] corrections, which follow different approaches but all aim at improving the projectile-target nuclear deflection. I have studied them systematically by first assessing their accuracy for simpler two-body problems and then generalizing them to three-body collisions involving one-neutron halo nuclei. My research has shown that all these corrections lead to elastic-scattering cross sections closer to the reference calculations for two- and three-body collisions [20, 21, 22]. However, only the semiclassical and exact continued S-matrix corrections improve significantly the description of the elastic-scattering channel.

I have also extended the two corrections which reproduce accurately the elastic-scattering observables to breakup reactions. I have shown that in the best case, the eikonal description of the breakup channel is only slightly improved [22]. Their failure to reproduce breakup cross sections has surprised me and pushed me to understand better what lacks in the eikonal description of breakup reactions on light targets at low energies. By comparing the predictions of the dynamical eikonal approximation (DEA) to the ones of the usual eikonal model, I have noted that the dynamical effects play a small role at these energies and can explain only a small part of the discrepancy between CDCC and the eikonal cross sections. The adiabatic treatment therefore does not seem to be the most significant issue of the eikonal model at low energies. Then, I have analysed the breakup matrix elements of both CDCC and the eikonal approximation. CDCC accounts for more couplings between the projectile-target angular momenta, and therefore models more transitions during the collision than the eikonal approximation. This is reflected in the breakup observables computed by the eikonal model through too low a total cross section and an incorrect distribution of the breakup strength between the core-neutron partial waves. This suggests that the eikonal model lacks couplings between its “trajectories” at different impact parameters.

From this observation, I have studied an alternative model, the Distorted-Wave Eikonal Approximation (DWEA), which factorizes the asymptotic behaviour of a Coulomb wave function instead of the usual plane wave. This model would simultaneously improve the projectile-target Coulomb deflection and account for part of the couplings neglected in the usual eikonal model. My hopes were that the DWEA would enhance both the accuracy of the eikonal description of the elastic-scattering channel and the couplings between the eikonal “trajectories” needed to reproduce the breakup cross sections. This model relies on a change of variable within the calculation of the T-matrix. Unfortunately, the Jacobian associated with this transformation varies along these new coordinates, and the eikonal form and its numerical cost cannot be recovered in these variables. However, another choice of coordinates or an efficient approximation of the T-matrix might exist. Further studies could be performed to better understand the influence of this Jacobian on the cross sections.

Despite the fact that I did not succeed to improve simultaneously the accuracy of the eikonal approximation for both elastic-scattering and breakup observables at $10A$ MeV, this work has pointed out what are the main flaws of the eikonal approximation at these energies. The projectile-target deflection during the collision has to be improved in order to ameliorate the eikonal description of the elastic-scattering channel and it seems that the couplings between different eikonal “trajectories” should be better accounted for, in order to reproduce the breakup channel. It would be interesting to quantify the effects of these couplings on breakup observables. Nevertheless, one should keep in mind that the main advantage of the eikonal approximation is its numerical cost, and an efficient correction should preserve this strong point.

The second goal of this thesis is to include dynamical effects within the usual eikonal approximation, while keeping its numerical efficiency. This is motivated by the incompatibility of the adiabatic approximation with the Coulomb interaction, which causes a Coulomb divergence in the eikonal calculations [23, 24, 112]. Since it does not rely on an adiabatic approach, the DEA does not have this issue but is computationally expensive. We have developed with Daniel Baye a simplification to the DEA at first order (S-DEA), which has a numerical cost comparable to the usual eikonal approximation. This model leads to accurate energy distributions for both nuclear- and Coulomb-dominated breakup of halo nuclei. These encouraging results have pushed us to study the accuracy of the S-DEA for parallel-momentum distributions after the dissociation.

We have compared the accuracy of the S-DEA with the Coulomb-corrected eikonal approximation [24, 112] (CCE) for both observables. They lead to similar energy distributions but different parallel-momentum cross sections. Compared to the usual eikonal approximation which misses the asymmetry of the data, the S-DEA improves it for both nuclear- and Coulomb-dominated breakups while the CCE only enhances it for Coulomb-dominated reactions. This can easily be explained by the fact that the S-DEA includes dynamical effects in all transitions due to both nuclear and Coulomb interactions, while the CCE treats dynamically only direct E1 transitions. Unfortunately, the asymmetry caused by direct E1 transition, dominant for one-neutron halo nuclei, is correctly reproduced by the CCE but underestimated by the S-DEA. Our analysis has shown that this underestimation is due to interferences between higher-order E1 transitions, which all include dynamical effects at first order [25].

Because the S-DEA accounts for part of the dynamical effects while keeping the small numerical cost of the eikonal approximation, it would be interesting to extend it to three-body projectiles. Such a model could be used to study the Coulomb breakup of two-neutron halo nuclei such as ^{6}He, ^{11}Li and ^{22}C. This study would require to calculate the three-body breakup states of the projectile as well as extending the S-DEA to four-body reactions. Then, since there are still discrepancies with the DEA, especially in the shape of the parallel-momentum distributions, it would also be interesting to study the next-order approximations of the DEA.

My third and last goal in this thesis is to understand what nuclear-structure information are probed within knockout reactions of one-neutron halo nuclei. The motivation of this study is twofold. The first is to understand why the theoretical predictions and the experimental data agree so well for the one-neutron removal of one-neutron halo nuclei [26, 27]. The second is to pin down what can safely be extracted from knockout cross sections of halo nuclei. With different Halo-EFT descriptions of the projectile, I have determined that knockout cross sections of one-neutron halo nuclei scale with the square of the ANC of the ground-state wave function [30, 31]. Moreover, they are insensitive to its inner part, especially to its norm. It is therefore unclear how accurate the spectroscopic factors extracted from knockout measurements of loosely-bound nuclei are. The good agreement between the theoretical predictions and the experimental data for these nuclei observed by Gade and collaborators [26, 27] seems to be explained by a fair reproduction of the ANC in the single-particle model of the projectile rather than by a precise prediction of the spectroscopic factors.

I have also demonstrated that, in an adiabatic model, the flux is conserved within each core-neutron partial wave: the presence of a subthreshold excited state induces a drop of the diffractive-breakup cross section, which is exactly transferred to the inelastic-scattering channel. On the contrary, the presence of a resonance in the projectile continuum does not influence significantly knockout cross sections. This independence to the description of the continuum suggests that precise estimates of the ground-state ANC could be inferred from such observables [30, 31]. The direct prospect of this work would be to extract ANCs for loosely-bound nuclei, such as ^{11}Be and ^{15}C, for which experimental data are available [76, 77]. Because the optical potentials simulating the projectile-target interactions impact the cross sections, it would be useful to quantify the uncertainty associated with these potentials, as it has been done for transfer reactions in Refs. [173, 174]. Moreover, the ANC should be inferred from only forward-angles data, in order to minimize the errors caused by the lack of dynamics within the usual eikonal approximation [77, 172]. The extracted ANCs of ^{11}Be and ^{15}C could then be compared to the *ab initio* predictions of Calci *et al.* [51] and recent analyses performed for diffractive breakup [66, 152] and transfer [175, 176].

Finally, it would be interesting to conduct a similar sensitivity analysis of one-neutron removal of more proton-rich nuclei. My hopes are that such a study might help understanding why the agreement between knockout data and theoretical predictions worsens when the binding energy increases. It could also indicate what can be safely extracted from such experimental data. For the knockout of more-bound nucleon, dynamical effects might play an even bigger role, it would hence also be interesting to study a generalization of the DEA and S-DEA to knockout reactions. This might improve the analysis of the data at large laboratory angles. As a long-term prospect, a sensitivity analysis could be conducted for both two-neutrons and one-proton knockout, which are also often used to probe exotic nuclei.

In conclusion, different improvements of the eikonal model have been studied in this thesis. My analysis suggests that the flaws of the eikonal model at $10A$ MeV cannot be tackled by a simple correction of the deflection of the projectile by the target [20, 21, 22]. More elaborate corrections might extend the validity of the eikonal approximation down to $10A$ MeV. However, because the main advantage of the eikonal model is its small numerical cost, it might not be worth to develop them if they are expensive from a computational viewpoint. I have also shown that dynamical effects can be included at first order, without loosing much of the numerical efficiency of the eikonal approximation [25]. This study constitutes only a first step, since the main goal would be to apply this model to collisions involving more complex projectiles, that other state-of-the-art method cannot describe. Finally, as many nuclear scientists before me, I have used the eikonal model to analyse knockout reactions [30, 31]. This work has emphasized what information can be safely probed from knockout reactions of one-neutron halo nuclei and also what are the limits of the reaction model in these analyses. In particular, uncertainties arise from the choice of the optical potentials and the adiabatic treatment of the eikonal model. In my opinion, these two issues should be investigated more deeply in the future.

Appendix A

Derivation of the DEA, eikonal and CCE cross sections

I present here the derivation of the cross sections for elastic scattering, diffractive breakup and inelastic scattering within the DEA. From these expressions, the forms of the eikonal and CCE cross sections are deduced. This appendix summarizes the results developed in the PhD thesis of Goldstein [97].

As in Chapter 2, all three fragments, i.e. the core, the neutron and the target, are considered structureless and only the spin of the neutron is considered. In this Appendix, I drop the superscript DEA of the wave function in this section, i.e., $\widehat{\Psi}^{\rm DEA}$ is denoted $\widehat{\Psi}$.

A.1 Elastic-scattering cross sections

The elastic-scattering T-matrix for the elastic scattering of one-neutron halo nucleus in the direction $\boldsymbol{K'} \equiv (K,\Omega)$ is given by Eq. (2.3.14), which reads [97]

$$T_{fi}(\Omega) = \left\langle e^{i\boldsymbol{K'R}}\phi_{n_0l_0j_0m_0'}\middle|V_{cT}+V_{nT}\middle|\Psi^{(m_0)}\right\rangle. \tag{A.1}$$

By inserting the eikonal factorization (2.3.30) and using the fact that $\phi_{n_0l_0j_0m_0'}$ is a eigenstate of the internal Hamiltonian (2.3.1), this matrix element becomes [97]

$$T_{fi}(\Omega) = \left\langle e^{i\boldsymbol{K'R}}\phi_{n_0l_0j_0m_0'}\middle|e^{iKZ}\left(h_{cn}-E_{n_0l_0j_0}+V_{cT}+V_{nT}\right)\middle|\widehat{\Psi}^{(m_0)}\right\rangle, \tag{A.2}$$

where we recognize the right-hand side of the DEA equation (2.3.31), from which we can deduce [97]

$$T_{fi}(\Omega) = \left\langle e^{i\boldsymbol{K'R}}\phi_{n_0l_0j_0m_0'}\middle|e^{iKZ}\frac{\partial}{\partial Z}\middle|\widehat{\Psi}^{(m_0)}\right\rangle. \tag{A.3}$$

The T-matrix element can be written in terms of transferred momentum $\hbar\boldsymbol{q} = \hbar(\boldsymbol{K'} - K\hat{\boldsymbol{Z}})$ as [97]

$$T_{fi}(\Omega) \;=\; \int d\boldsymbol{b}\, e^{-i\boldsymbol{q}_\perp \boldsymbol{b}}\int_{-\infty}^{+\infty} dZ\, e^{-iq_Z Z}\frac{\partial}{\partial Z}\left\langle\phi_{n_0l_0j_0m_0'}\middle|\widehat{\Psi}^{(m_0)}\right\rangle \tag{A.4}$$

where $\boldsymbol{q}_\perp$ and q_Z are respectively the transverse and longitudinal components of $\boldsymbol{q}$. The energy conservation imposes $|\boldsymbol{K'}| = K$ and thus $q = 2K\sin(\theta/2)$.

As in the usual eikonal approximation (see Sec. 2.1.2), the transferred momentum is assumed purely transverse $\boldsymbol{q} \approx \boldsymbol{q}_\perp$ and the phase $e^{-iq_Z Z}$ is neglected. This approximation holds if this phase oscillates slowly in the range ΔZ where the $\frac{\partial}{\partial Z}\left\langle \phi_{n_0 l_0 j_0 m_0'} \middle| \widehat{\Psi}^{(m_0)} \right\rangle$ takes significant values, i.e., if

$$\frac{2\pi}{|q_Z|} > \Delta Z. \tag{A.5}$$

This is the case if θ is small enough

$$\theta < \sqrt{\frac{4\pi}{K\Delta Z}}, \tag{A.6}$$

where the small-angles approximation $q_Z = 2K \sin^2(\theta/2) \approx K\theta^2/2$ is used.

When $e^{-iq_Z Z}$ is neglected, the T-matrix element becomes [97]

$$\begin{aligned} T_{fi}(\Omega) &\approx \int d\boldsymbol{R}\, e^{-i\boldsymbol{qb}} \frac{\partial}{\partial Z} \left\langle \phi_{n_0 l_0 j_0 m_0'} \middle| \widehat{\Psi}^{(m_0)} \right\rangle & \text{(A.7)} \\ &= \int d\boldsymbol{b}\, e^{-i\boldsymbol{qb}} \left[\left\langle \phi_{n_0 l_0 j_0 m_0'} \middle| \widehat{\Psi}^{(m_0)} \right\rangle \right]_{Z\to-\infty}^{Z\to+\infty}. & \text{(A.8)} \end{aligned}$$

In Ref. [97], Goldstein defines the elastic-scattering amplitude as

$$S_{0m_0'}^{(m_0)}(\boldsymbol{b}) = \left[\left\langle \phi_{n_0 l_0 j_0 m_0'} \middle| \widehat{\Psi}^{(m_0)} \right\rangle \right]_{Z\to-\infty}^{Z\to+\infty}. \tag{A.9}$$

By defining the radial ljm contribution of the DEA wave function as

$$\psi_{ljm}^{(m_0)}(b,\phi,Z,r) = r \sum_\nu (lIm-\nu\nu|jm) \int d\Omega_r\, Y_l^{m-\nu *}(\Omega_r) \left\langle I\nu \middle| \widehat{\Psi}^{(m_0)}(b,\phi,Z,\boldsymbol{r}) \right\rangle \tag{A.10}$$

and using the symmetry along the z-axis of the DEA solution, Goldstein shows that the elastic-scattering amplitude can be written as [97]

$$\begin{aligned} S_{0m_0'}^{(m_0)}(\boldsymbol{b}) &= e^{i(m_0-m_0')\phi} S_{0m_0'}^{(m_0)}(b) & \text{(A.11)} \\ \text{where} \quad S_{0m_0'}^{(m_0)}(b) &= \lim_{Z\to+\infty} \int_0^{+\infty} dr\, u_{n_0 l_0 j_0}(r) \psi_{l_0 j_0 m_0'}^{(m_0)}(b,0,Z,r) - \delta_{m_0 m_0'}, & \text{(A.12)} \end{aligned}$$

where $u_{n_0 l_0 j_0}$ is the radial wave function of the ground state (2.3.7).

With these notations Eq. (A.8) reads [97]

$$T_{fi}(\Omega) = \int d\boldsymbol{b}\, e^{-i\boldsymbol{qb}} e^{i(m_0-m_0')\phi} S_{0m_0'}^{(m_0)}(b) \tag{A.13}$$

where $\boldsymbol{qb} = qb\cos(\phi-\varphi)$ and φ is the azimuthal angle of $\boldsymbol{q} \equiv (q_\perp, \varphi, q_Z)$. After integrating over the azimuthal angle {using Eq. (9.1.21) of Ref. [92]}, the matrix element becomes [97]

$$T_{fi}(\Omega) = 2\pi i\hbar v \frac{e^{i(m_0-m_0')\varphi}}{i^{|m_0-m_0'|}} \int_0^{+\infty} b\, db\, J_{|m_0-m_0'|}(qb) S_{0m_0'}^{(m_0)}(b), \tag{A.14}$$

where J_n is a Bessel function of order n [92].

The elastic-scattering cross sections has to account for the initial and final projections of the orbital angular momentum m_0 and m_0'. Since the beam is usually not polarized, the cross section is just averaged over m_0 and sums over all possible final projections m_0'. Using Eq. (2.1.7), the elastic-scattering cross section of one-neutron halo nucleus reads [97]

$$\begin{aligned}\frac{d\sigma_{el}}{d\Omega} &= \frac{1}{(2\pi)^2}\left(\frac{\mu}{\hbar^2}\right)^2 \frac{1}{2j_0+1}\sum_{m_0 m_0'} |T_{fi}(\Omega)|^2 &\text{(A.15)}\\ &= K^2 \frac{1}{2j_0+1}\sum_{m_0 m_0'}\left|\int_0^{+\infty} b\, db\, J_{|m_0-m_0'|}(qb) S^{(m_0)}_{0m_0'}(b)\right|^2 . &\text{(A.16)}\end{aligned}$$

As mentioned in Sec. 2.3.3.3, contrary to a semiclassical model the DEA accounts for part of the interferences between neighbouring bs.

In the usual eikonal model, the cross sections have the same form. Since the asymptotic form of the eikonal solution is known (2.3.34), the elastic-scattering amplitude at the eikonal model reads [97, 107]

$$S^{(m_0)}_{0m_0'}(b) = \left\langle \phi_{n_0l_0j_0m_0'} \middle| e^{i\chi_{cT}} e^{i\chi_{nT}} \middle| \phi_{n_0l_0j_0m_0} \right\rangle - \delta_{m_0m_0'}. \qquad \text{(A.17)}$$

In the case of the elastic scattering, the CCE cross section is exactly the eikonal one since the Coulomb correction is zero for this channel.

A.2 Diffractive-breakup cross sections

The T-matrix element for the diffractive breakup is given by Eq. (2.3.15), that I rewrite here for convenience [97]

$$T_{fi}(\boldsymbol{K'},\boldsymbol{k}) = \left\langle e^{i\boldsymbol{K'R}} \phi^{(-)}_{\boldsymbol{k}\nu} \middle| V_{cT} + V_{nT} \middle| \Psi^{(m_0)} \right\rangle , \qquad \text{(A.18)}$$

where $\boldsymbol{K'} \equiv (K', \Omega)$ is the final wave vector between the target and center-of-mass of P, $\phi^{(-)}_{\boldsymbol{k}\nu}$ (2.3.16) is a c-n incoming stationary scattering state characterized by wave vector $\boldsymbol{k}$ and the spin projection ν. Using the eikonal factorization (2.3.30) and the fact that this scattering state is an eigenstate of the internal Hamiltonian with an eigenvalue E, the T-matrix can be written as [97]

$$\begin{aligned}T_{fi}(\boldsymbol{K'},\boldsymbol{k}) &= \left\langle e^{i\boldsymbol{K'R}} \phi^{(-)}_{\boldsymbol{k}\nu} \middle| e^{iKZ} \left(h_{cn} - E + V_{cT} + V_{nT}\right) \middle| \widehat{\Psi}^{(m_0)} \right\rangle &\text{(A.19)}\\ &= \left\langle e^{i\boldsymbol{K'R}} \phi^{(-)}_{\boldsymbol{k}\nu} \middle| e^{iKZ} \left(E_{n_0l_0j_0} - E + h_{cn} - E_{n_0l_0j_0} + V_{cT} + V_{nT}\right) \middle| \widehat{\Psi}^{(m_0)} \right\rangle &\text{(A.20)}\end{aligned}$$

where we recognize the right-hand side of the DEA equation (2.3.31). By inserting the DEA equation, the matrix element becomes [97]

$$\begin{aligned}T_{fi}(\boldsymbol{K'},\boldsymbol{k}) &= i\hbar v \left\langle e^{i\boldsymbol{K'R}} \phi^{(-)}_{\boldsymbol{k}\nu} \middle| e^{iKZ} \left(\frac{\partial}{\partial Z} + i\frac{E - E_{n_0l_0j_0}}{\hbar v}\right) \middle| \widehat{\Psi}^{(m_0)} \right\rangle &\text{(A.21)}\\ &= i\hbar v \int d\boldsymbol{R}\, e^{-i\boldsymbol{qR}} e^{-i\frac{E-E_{n_0l_0j_0}}{\hbar v}Z} \frac{\partial}{\partial Z}\left(e^{i\frac{E-E_{n_0l_0j_0}}{\hbar v}Z} \left\langle \phi^{(-)}_{\boldsymbol{k}\nu} \middle| \widehat{\Psi}^{(m_0)} \right\rangle \right), &\text{(A.22)}\end{aligned}$$

where $\hbar\boldsymbol{q} = \hbar(\boldsymbol{K'} - K\boldsymbol{\hat{Z}})$ is the transferred momentum.

The energy conservation imposes

$$\frac{\hbar^2 K^2}{2\mu} + E_{n_0l_0j_0} = \frac{\hbar^2 K'^2}{2\mu} + E \qquad \text{(A.23)}$$

and

$$\frac{q^2}{2K} + \frac{E - E_{n_0 l_0 j_0}}{\hbar v} + q_Z = 0. \tag{A.24}$$

With this relation, the breakup matrix element reads [97]

$$T_{fi}(\boldsymbol{K'}, \boldsymbol{k}) \;=\; i\hbar v \int d\boldsymbol{R}\, e^{-i\boldsymbol{q}_\perp \boldsymbol{b}} e^{i\frac{q^2 Z}{2K}} \frac{\partial}{\partial Z}\left(e^{i\frac{E-E_{n_0 l_0 j_0}}{\hbar v} Z} \left\langle \phi^{(-)}_{\boldsymbol{k}\nu} \middle| \widehat{\Psi}^{(m_0)} \right\rangle \right), \tag{A.25}$$

where $q_\perp$ is the transverse component of $\boldsymbol{q}$.

Assuming that the transfer of energy is small, i.e., $K' \approx K$, the norm of the transferred momentum can be approximated by [97]

$$q \approx 2K \sin\left(\frac{\theta}{2}\right). \tag{A.26}$$

Moreover, as in the elastic scattering, the small-angles approximation (A.6) is made. Hence, the transferred momentum is assumed to be purely transverse $\boldsymbol{q} \approx \boldsymbol{q}_\perp$ and the factor $e^{i\frac{q^2 Z}{2K}}$ is neglected. This simplifies the breakup matrix element into [97]

$$T_{fi}(\boldsymbol{K'}, \boldsymbol{k}) \;\approx\; i\hbar v \int d\boldsymbol{R}\, e^{-i\boldsymbol{q}\boldsymbol{b}} \frac{\partial}{\partial Z}\left(e^{i\frac{E-E_{n_0 l_0 j_0}}{\hbar v} Z} \left\langle \phi^{(-)}_{\boldsymbol{k}\nu} \middle| \widehat{\Psi}^{(m_0)} \right\rangle \right). \tag{A.27}$$

Since the projectile is initially in its ground state, which is orthogonal to the scattering states, the matrix element becomes [97]

$$T_{fi}(\boldsymbol{K'}, \boldsymbol{k}) \;=\; i\hbar v \lim_{Z\to+\infty} e^{i\frac{E-E_{n_0 l_0 j_0}}{\hbar v} Z} \int d\boldsymbol{b}\, e^{-i\boldsymbol{q}\boldsymbol{b}} \left\langle \phi^{(-)}_{\boldsymbol{k}\nu} \middle| \widehat{\Psi}^{(m_0)} \right\rangle. \tag{A.28}$$

The phase $(E - E_{n_0 l_0 j_0})Z/\hbar v$ is dropped because it has no physical meaning and does not influence the cross sections.

In Ref. [97], Goldstein defines the breakup amplitude as

$$S^{(m_0)}_{\boldsymbol{k}\nu}(\boldsymbol{b}) = \left[\left\langle \phi^{(-)}_{\boldsymbol{k}\nu} \middle| \widehat{\Psi}^{(m_0)} \right\rangle \right]_{Z\to+\infty}. \tag{A.29}$$

With the definition of the scattering state (2.3.16) and using the symmetry of the DEA wave function (A.11), it reads [97]

$$S^{(m_0)}_{\boldsymbol{k}\nu}(\boldsymbol{b}) = \frac{4\pi}{k} \sum_{ljm} (lIm-\nu\nu|jm) Y_l^{m-\nu}(\Omega_k) e^{i(m_0-m)\phi} S^{(m_0)}_{kljm}(b) \tag{A.30}$$

where the partial breakup amplitude is given by [97]

$$S^{(m_0)}_{kljm}(b) \;=\; \lim_{Z\to+\infty} e^{i[\delta_{lj}(k) - l\pi/2]} \int_0^{+\infty} dr\, u_{klj}(r) \psi^{(m_0)}_{ljm}(b, 0, Z, r), \tag{A.31}$$

u_{klj} is the radial wave function of the scattering state (2.3.2) and $\psi^{(m_0)}_{ljm}$ is defined in Eq. (A.10). With these definitions and after integrating over the azimuthal angle {using Eq. (9.1.21) of Ref [92]}, the breakup matrix element (A.28) reads [97]

$$T_{fi}(\boldsymbol{K'}, \boldsymbol{k}) = i8\pi^2 \frac{\hbar v}{k} \sum_{ljm} (lIm-\nu\nu|jm) Y_l^{m-\nu}(\Omega_k) \frac{e^{i(m_0-m)\varphi}}{i^{|m-m_0|}} \int_0^{+\infty} b\, db\, J_{|m-m_0|}(qb) S^{(m_0)}_{kljm}(b). \tag{A.32}$$

Because experimentally, the beam is usually not polarized, the diffractive breakup cross section is averaged on m_0 and sums over all possible final spin projections of the neutron ν. The cross section as a function of the deflection angle Ω of the center-of-mass of P and the c-n final wave vector $\boldsymbol{k}$ (2.3.17) thus reads [97]

$$\begin{aligned}
\frac{d\sigma_{bu}}{d\boldsymbol{k}d\Omega} &= \frac{1}{(2\pi)^5}\frac{\mu K'}{\hbar^3 v}\frac{1}{2j_0+1}\sum_{m_0\nu}|T_{fi}(\boldsymbol{K'},\boldsymbol{k})|^2 &\text{(A.33)}\\
&= \frac{2}{\pi}\frac{K'K}{k^2}\frac{1}{2j_0+1}\sum_{m_0\nu}\Bigg|\sum_{ljm}(lIm-\nu\nu|jm)Y_l^{m-\nu}(\Omega_k)\frac{e^{-im\varphi}}{i^{|m-m_0|}}\\
&\qquad\times\int_0^{+\infty} b\,db\,J_{|m-m_0|}(qb)S^{(m_0)}_{kljm}(b)\Bigg|^2. &\text{(A.34)}
\end{aligned}$$

In this thesis, I analyse the energy and parallel-momentum distributions of the diffractive breakup of one-neutron halo nucleus.

The energy distribution can be obtained by integrating the cross section (A.34) over Ω and Ω_k [97]

$$\begin{aligned}
\frac{d\sigma_{bu}}{dE} &= \frac{\mu_{cn}k}{\hbar^2}\int d\Omega\int d\Omega_k\frac{d\sigma_{bu}}{d\boldsymbol{k}d\Omega} &\text{(A.35)}\\
&= \frac{2}{\pi}\frac{\mu_{cn}}{\hbar^2 k}K'K\frac{1}{2j_0+1}\sum_{m_0\nu}\sum_{ljm}\sum_{l'j'm'}(lIm-\nu\nu|jm)(l'Im'-\nu\nu|j'm')\frac{e^{-im\varphi}}{i^{|m-m_0|}}\frac{e^{im'\varphi}}{(-i)^{|m'-m_0|}}\\
&\quad\times\int d\Omega\int_0^{+\infty} b\,db\,J_{|m-m_0|}(qb)S^{(m_0)}_{kljm}(b)\int_0^{+\infty} b'\,db'\,J_{|m'-m_0|}(qb')S^{(m_0)*}_{kl'j'm'}(b')\\
&\quad\times\underbrace{\int d\Omega_k Y_l^{m-\nu}(\Omega_k)Y_{l'}^{m'-\nu*}(\Omega_k)}_{=\delta_{ll'}\delta_{mm'}} &\text{(A.36)}\\
&= \frac{2}{\pi}\frac{\mu_{cn}}{\hbar^2 k}K'K\frac{1}{2j_0+1}\sum_{m_0}\sum_{ljm}\sum_{j'}\int_0^{+\infty} b\,db\,S^{(m_0)}_{kljm}(b)\int_0^{+\infty} b'\,db'\,S^{(m_0)*}_{klj'm}(b')\\
&\quad\times\int d\Omega\,J_{|m-m_0|}(qb)J_{|m-m_0|}(qb')\underbrace{\sum_\nu(lIm-\nu\nu|jm)(lIm-\nu\nu|j'm)}_{=\delta_{jj'}} &\text{(A.37)}\\
&= \frac{2}{\pi}\frac{\mu_{cn}}{\hbar^2 k}K'K\frac{1}{2j_0+1}\sum_{m_0}\sum_{ljm}\int_0^{+\infty} b\,db\,S^{(m_0)}_{kljm}(b)\int_0^{+\infty} b'\,db'\,S^{(m_0)*}_{kljm}(b')\\
&\quad\times\int d\Omega\,J_{|m-m_0|}(qb)J_{|m-m_0|}(qb'). &\text{(A.38)}
\end{aligned}$$

Here, the orthogonality relations of the spherical harmonics and of Clebsch-Gordan are used [44].

Using the approximation of q (A.26), the integration over θ becomes [97]

$$\begin{aligned}
\int d\Omega &= \int_0^{2\pi} d\phi\int_0^{\pi}\sin\theta\,d\theta &\text{(A.39)}\\
&\approx \frac{1}{K^2}\int_0^{2\pi} d\phi\int_0^{2K} q\,dq. &\text{(A.40)}
\end{aligned}$$

For most of the values of b, we have $K \gg 1/b$ and the maximal value of the integration $2K$ can approximated by $+\infty$. In the DEA, this approximation is made for all bs, which enables us to use the property [179]

$$\int_0^{+\infty} q\, dq\, J_m(qb) J_m(qb') = \frac{1}{b}\delta(b - b'). \tag{A.41}$$

After integrating over Ω, the energy distribution of breakup reads [97]

$$\frac{d\sigma_{bu}}{dE} = \frac{4\mu_{cn}}{\hbar^2 k}\frac{1}{2j_0+1}\sum_{m_0}\sum_{ljm}\int_0^{+\infty} b\, db \left|S^{(m_0)}_{kljm}(b)\right|^2. \tag{A.42}$$

The parallel-momentum distribution is obtained by integrating Eq. (A.34) over $\boldsymbol{k}_\perp$ and Ω

$$\begin{aligned}
\frac{d\sigma_{bu}}{dk_\parallel} &= \int d\boldsymbol{k}_\perp \int d\Omega \frac{d\sigma_{bu}}{d\boldsymbol{k} d\Omega} && \text{(A.43)}\\
&= \frac{2K'K}{\pi k^2}\frac{1}{2j_0+1}\sum_{m_0\nu}\sum_{ljm}\sum_{l'j'm'}(lIm-\nu\nu|jm)(l'Im'-\nu\nu|j'm')\frac{e^{-im\varphi}}{i^{|m-m_0|}}\frac{e^{im'\varphi}}{(-i)^{|m'-m_0|}}\\
&\times \int d\boldsymbol{k}_\perp Y_l^{m-\nu}(\Omega_k) Y_{l'}^{m'-\nu *}(\Omega_k)\int_0^{+\infty} b\, db\, S^{(m_0)}_{kljm}(b)\int_0^{+\infty} b'\, db'\, S^{(m_0)*}_{kl'j'm'}(b')\\
&\times \int d\Omega\, J_{|m-m_0|}(qb) J_{|m'-m_0|}(qb'). && \text{(A.44)}
\end{aligned}$$

With the relation $d\boldsymbol{k}_\perp = k_\perp dk_\perp d\phi_k$ and the property [179]

$$\int_0^{2\pi} d\phi_k\, Y_l^{m-\nu}(\Omega_k) Y_{l'}^{m'-\nu *}(\Omega_k) = 2\pi\delta_{mm'} Y_l^{m-\nu}(\theta_k, 0) Y_{l'}^{m-\nu *}(\theta_k, 0), \tag{A.45}$$

Eq. (A.44) becomes [97]

$$\begin{aligned}
\frac{d\sigma_{bu}}{dk_\parallel} &= \frac{4K'K}{k^2}\frac{1}{2j_0+1}\sum_{mm_0\nu}\sum_{lj}\sum_{l'j'}(lIm-\nu\nu|jm)(l'Im-\nu\nu|j'm)\\
&\times \int_0^{+\infty} k_\perp\, dk_\perp\, Y_l^{m-\nu}(\theta_k, 0) Y_{l'}^{m-\nu *}(\theta_k, 0)\int_0^{+\infty} b\, db\, S^{(m_0)}_{kljm}(b)\int_0^{+\infty} b'\, db'\, S^{(m_0)*}_{kl'j'm}(b')\\
&\times \int d\Omega\, J_{|m-m_0|}(qb) J_{|m-m_0|}(qb'). && \text{(A.46)}
\end{aligned}$$

By approximating the integration in Ω with Eq. (A.40) and using the property (A.41), the parallel-momentum cross section reads [97]

$$\frac{d\sigma_{bu}}{dk_\parallel} = \frac{8\pi}{k^2}\frac{1}{2j_0+1}\sum_{mm_0\nu}\int_0^{+\infty} b\, db \int_0^{+\infty} k_\perp\, dk_\perp \left|\sum_{lj}(lIm-\nu\nu|jm) Y_l^{m-\nu}(\theta_k, 0) S^{(m_0)}_{kljm}(b)\right|^2, \tag{A.47}$$

where $\tan\theta_k = k_\perp/k_\parallel$.

Since the momentum k is related to $k_\perp$ through $k^2 = k_\perp^2 + k_\parallel^2$, the cross section can be written as [97]

$$\frac{d\sigma_{bu}}{dk_\parallel} = \frac{8\pi}{k^2}\frac{1}{2j_0+1}\sum_{mm_0\nu}\int_0^{+\infty} b\, db \int_{|k_\parallel|}^{+\infty} \frac{dk}{k} \left|\sum_{lj}(lIm-\nu\nu|jm) Y_l^{m-\nu}(\theta_k, 0) S^{(m_0)}_{kljm}(b)\right|^2. \tag{A.48}$$

This observable sums coherently the contributions of each partial-wave and is thus sensitive to their interferences.

At the usual eikonal model and the CCE, the cross sections have a similar form. By using the asymptotic behaviour of the eikonal wave function (2.3.34) into Eq. (A.31), the eikonal partial-wave breakup amplitude $S^{(m_0)}_{kljm}$ reads [107, 112]

$$S^{(m_0)}_{kljm}(b) = e^{i[\delta_{lj}(k)-l\pi/2]}\,\langle\phi_{kljm}|e^{i\chi_{cT}}e^{i\chi_{nT}}|\phi_{n_0l_0j_0m_0}\rangle\,. \tag{A.49}$$

The CCE amplitude can be derived similarly except that it inserts the correction (2.3.41). Its partial-breakup amplitude reads [112]

$$S^{(m_0)}_{kljm}(b) = e^{i[\delta_{lj}(k)-l\pi/2]}e^{i\chi^C_{PT}(b)}\,\langle\phi_{kljm}|\left[e^{i\chi^C} - i\chi^C + i\chi^{C,(\lambda=1)}_{\rm FO}\right]e^{i\chi^N}\,|\phi_{n_0l_0j_0m_0}\rangle\,. \tag{A.50}$$

A.3 Inelastic-scattering cross section

The inelastic scattering corresponds to the excitation of the projectile to a bound state nlj of energy E_{nlj}, and is deflected by the target in a direction $\boldsymbol{K'} \equiv (K', \Omega)$. The energy conservation imposes that [97]

$$\frac{\hbar^2K^2}{2\mu} + E_{n_0l_0j_0} = \frac{\hbar^2K'^2}{2\mu} + E_{nlj}. \tag{A.51}$$

I do not present here the derivation of the inelastic observables, as its derivation is similar to the elastic-scattering cross section [97]. The cross section for the inelastic scattering of the projectile excited to a bound state nlj and deflected by the target to Ω reads [97]

$$\frac{\mathrm{d}\sigma^{nlj}_{inel}}{\mathrm{d}\Omega} = KK'\frac{1}{2j_0+1}\sum_{m_0m}\left|\int_0^{+\infty} b\,db\,J_{|m-m_0|}(qb)S^{(m_0)}_{nljm}(b)\right|^2. \tag{A.52}$$

where the inelastic-scattering amplitude is given by [97]

$$S^{(m_0)}_{nljm}(b) \;=\; \lim_{Z\to+\infty}\int_0^{+\infty} dr\,u_{nlj}(r)\psi^{(m_0)}_{ljm}(b,0,Z,r), \tag{A.53}$$

u_{nlj} is the radial wave function of the bound state nlj (2.3.7) and $\psi^{(m_0)}_{ljm}$ (A.10) is the radial ljm partial-wave contribution to the DEA wave function $\widehat{\Psi}^{(m_0)}$.

To compute the inelastic-scattering cross section of an excited state nlj, Eq. (A.52) is integrated over the solid angle Ω

$$\begin{aligned}\sigma^{nlj}_{inel} \;&=\; KK'\frac{1}{2j_0+1}\sum_{m_0m}\int_0^{+\infty} b\,db\,S^{(m_0)}_{nljm}(b)\int_0^{+\infty} b'\,db'\,S^{(m_0)*}_{nljm}(b') \\ &\quad\int d\Omega\,J_{|m_0-m|}(qb)J_{|m_0-m|}(qb') \qquad\qquad (\mathrm{A.54}) \\ &\approx\; \frac{2\pi}{2j_0+1}\sum_{m_0m}\int_0^{+\infty} b\,db\,\left|S^{(m_0)}_{nljm}(b)\right|^2. \qquad\qquad (\mathrm{A.55})\end{aligned}$$

Here the approximations (A.26) and (A.40) and the orthogonality of the Bessel function (A.41) are used.

The total inelastic-scattering cross section sums over the inelastic-scattering channels

$$\sigma_{inel} \;=\; \sum_{nlj}\sigma^{nlj}_{inel}. \tag{A.56}$$

The eikonal cross sections are calculated similarly except for the inelastic-scattering amplitude $S_{nljm}^{(m_0)}$ (A.53). As for the elastic scattering, the asymptotic form of the eikonal solution (2.3.34) is known. Therefore, the inelastic-scattering amplitude at the eikonal model reads

$$S_{nljm}^{(m_0)}(b) \;=\; \langle \phi_{nljm} | e^{i\chi_{cT}} e^{i\chi_{nT}} | \phi_{n_0 l_0 j_0 m_0} \rangle \,. \tag{A.57}$$

The CCE amplitude is similar except that it inserts the correction (2.3.41). Its inelastic-scattering amplitude reads [112]

$$S_{nljm}^{(m_0)}(b) \;=\; e^{i\chi_{PT}^{C}(b)} \langle \phi_{nljm} | \left[e^{i\chi^{C}} - i\chi^{C} + i\chi_{\mathrm{FO}}^{C,(\lambda=1)} \right] e^{i\chi^{N}} | \phi_{n_0 l_0 j_0 m_0} \rangle \,. \tag{A.58}$$

Appendix B

Coulomb first-order-perturbation approximation

To derive the dipole and quadrupole contributions to the Coulomb first-order-perturbation approximation, the difference of Coulomb potentials appearing in Eq. (2.3.42) is expanded onto the spherical harmonics in the vectorial space defined by $\boldsymbol{r}$ (see Complement $\mathrm{E_X}$ of Ref. [44])

$$\begin{aligned}
\frac{Z_T Z_P e^2}{4\pi\epsilon_0}\left(\frac{1}{R_{cT}}-\frac{1}{R}\right) &= \frac{Z_T Z_P e^2}{4\pi\epsilon_0}\left(\frac{1}{\left|\boldsymbol{R}-\frac{m_n}{m_P}\boldsymbol{r}\right|}-\frac{1}{R}\right) && \text{(B.1)}\\
&= \frac{Z_P Z_T e^2}{4\pi\epsilon_0}\sum_{\lambda=0}^{+\infty}\frac{4\pi}{2\lambda+1}\frac{\min\left(R,\frac{m_n}{m_P}r\right)^{\lambda}}{\max\left(R,\frac{m_n}{m_P}r\right)^{\lambda+1}}\sum_{\mu=-\lambda}^{+\lambda}Y_\lambda^{\mu *}(\Omega_r)Y_\lambda^{\mu}(\Omega)\\
&\quad -\frac{Z_P Z_T e^2}{4\pi\epsilon_0 R} && \text{(B.2)}
\end{aligned}$$

where $Z_P = Z_c$ for neutron halo nuclei. Here I use the relations (2.3.10)–(2.3.11) between the coordinates $\boldsymbol{R}_{cT}$, $\boldsymbol{R} \equiv (R,\Omega)$ and $\boldsymbol{r} \equiv (r,\Omega_r)$.

We now use the far field approximation, which holds if the projectile-target relative distance is larger than the core-fragment distance. The expansion (B.2) can be approximated as [44]

$$\frac{Z_T Z_P e^2}{4\pi\epsilon_0}\left(\frac{1}{R_{cT}}-\frac{1}{R}\right) \approx \sum_{\lambda=1}^{\infty}(-1)^{\lambda}\frac{Z_T Z_{eff}^{(\lambda)} e^2}{4\pi\epsilon_0}\frac{4\pi}{2\lambda+1}\sum_{\mu=-\lambda}^{\lambda} r^{\lambda} Y_\lambda^{\mu *}(\Omega_r)\frac{Y_\lambda^{\mu}(\Omega)}{R^{\lambda+1}} \qquad \text{(B.3)}$$

with the effective charge defined as

$$Z_{eff}^{(\lambda)} = \left(-\frac{m_n}{m_P}\right)^{\lambda} Z_c. \qquad \text{(B.4)}$$

The dipole contribution to the first-order Coulomb term can be obtained by inserting the expansion (B.3) into Eq. (2.3.42) and taking $\lambda = 1$

$$\chi_{\mathrm{FO}}^{C,(\lambda=1)}(E,\boldsymbol{b},\boldsymbol{r}) = \frac{1}{\hbar v}\int_{-\infty}^{+\infty} dZ\, e^{i\frac{\omega Z}{v}}\frac{Z_T Z_{eff}^{(1)} e^2}{4\pi\epsilon_0}\frac{4\pi}{3}\sum_{\mu=-1}^{1} r Y_1^{\mu *}(\Omega_r)\frac{Y_1^{\mu}(\Omega)}{R^2}. \qquad \text{(B.5)}$$

Since the first-order perturbation theory considers straight-line trajectories, this integral can be computed analytically with Eq. (15) of Ref. [180]

$$\int_{-\infty}^{+\infty} dZ\, e^{i\frac{\omega Z}{v}} \frac{Y_\lambda^\mu(\Omega)}{R^{\lambda+1}} = \sqrt{\frac{2\lambda+1}{4\pi}}\, 2 \frac{i^{\lambda+\mu}}{\sqrt{(\lambda+\mu)!(\lambda-\mu)!}} \left(\frac{\omega}{v}\right)^\lambda K_{|\mu|}\left(\frac{\omega b}{v}\right), \tag{B.6}$$

where $K_{|\mu|}$ are modified Bessel functions [92].

We thus find

$$\begin{aligned} \chi_{\mathrm{FO}}^{C,(\lambda=1)}(E,\boldsymbol{b},\boldsymbol{r}) &= -2\eta\frac{\omega}{v}\frac{m_n}{m_P} r \left\{ \sin(\theta_r)\cos(\phi_r) K_1\left(\frac{\omega}{v}b\right) \right. \\ . \quad & \quad \left. + iK_0\left(\frac{\omega}{v}b\right)\cos(\theta_r) \right\} \qquad \text{(B.7)} \\ &= -2\eta\frac{\omega}{v}\frac{m_n}{m_P}\left[K_1\left(\frac{\omega}{v}b\right)x + iK_0\left(\frac{\omega}{v}b\right)z\right], \qquad \text{(B.8)} \end{aligned}$$

where (x, y, z) are the Cartesian coordinates of $\boldsymbol{r}$.

The quadrupole contribution to the first-order Coulomb term can be obtained similarly with $\lambda = 2$

$$\begin{aligned} \chi_{\mathrm{FO}}^{C,(\lambda=2)}(E,\boldsymbol{b},\boldsymbol{r}) &= -\frac{1}{\hbar v}\int_{-\infty}^{+\infty} dZ\, e^{i\frac{\omega Z}{v}} \frac{Z_T Z_{eff}^{(2)} e^2}{4\pi\epsilon_0}\frac{4\pi}{5}\sum_{\mu=-2}^{2} r^2 Y_2^{\mu*}(\Omega_r)\frac{Y_2^\mu(\Omega)}{R^3} \qquad \text{(B.9)} \\ &= -\frac{1}{\hbar v}\frac{Z_T Z_{eff}^{(2)} e^2}{4\pi\epsilon_0}\left(\frac{\omega}{v}\right)^2 r^2 \left\{ \frac{1}{2}\sin^2(\theta_r)\cos(2\phi_r) K_2\left[\frac{\omega b}{v}\right] \right. \\ & \quad + 2i\cos(\phi_r)\sin(\theta_r)\cos(\theta_r) K_1\left[\frac{\omega b}{v}\right] \\ & \quad \left. - \frac{1}{2}\left[3\cos^2(\theta_r) - 1\right] K_0\left[\frac{\omega b}{v}\right] \right\} \qquad \text{(B.10)} \\ &= -\frac{1}{\hbar v}\frac{Z_T Z_{eff}^{(2)} e^2}{4\pi\epsilon_0}\left(\frac{\omega}{v}\right)^2 \left\{ \frac{1}{2}(x^2 - y^2) K_2\left[\frac{\omega b}{v}\right] + 2ixz K_1\left[\frac{\omega b}{v}\right] \right. \\ & \quad \left. - \frac{1}{2}\left[3z^2 - 1\right] K_0\left[\frac{\omega b}{v}\right] \right\}. \qquad \text{(B.11)} \end{aligned}$$

Appendix C

CDCC input for ^{11}Be-^{12}C collision at 10A MeV

I give here the input file of FRESCO [14], I have used to obtain fully converged CDCC results for the breakup and elastic scattering of ^{11}Be with ^{12}C at 10A MeV, presented in Chapter 3. This program developed by Ian Thompson solves the coupled-channel equations (2.3.28). The program as well as its user guide can be found on the website www.fresco.org.uk. I also briefly explain how this input is structured.

The first part of the input &CDCC gives the numerical details: the parameters used by the Numerov algorithm (hcm, rmatch, rasym, accrcy, absend, cutr), the energy of the collision (elab), the parameters of the total angular momentum mesh (jbord and jump), the parameters of the angular mesh (thmax and thinc), the desired output files (smats and xstabl), the interactions (ncoul), the couplings considered (reor) and the order of the highest multipole of the nuclear and Coulomb interactions (q).

The second part of the input &NUCLEUS provides the description of the nuclei: their charge, mass, spin, parity, binding energy (be), the number of node (n), the orbital (l) and total (j) angular quantum numbers of the ground-state radial wave function.

The third part &BIN details the discretization of the continuum into bins. Each bin is characterized by the total spin and parity of the state, the orbital (l) and total (j) angular momenta, its energy which is defined by intervals taken between the minimum energy (start) and maximum energy with a certain step which has an equal size in energy (energy=T) or in momentum (energy=F).

The fourth part, called &POTENTIAL, corresponds to the optical potentials of both fragments with the target and the effective potential used to describe the projectile structure. The variable a1 specifies the number mass with which the radii have to be scaled with, and the other variables the parameters of the interaction, given in Sec. 3.2.

```
user
CDCC 11Be+12C 10MeV/nucleon ; N+C

&CDCC
hcm=0.01 rmatch= -60 rasym=1000 accrcy=0.001 absend=-50
elab=110
jbord= 0 200 500 20000
jump= 1 10 50
thmax=180 thinc=0.01 cutr=-20
smats=4 xstabl=1
```

```
ncoul=0 reor=0 q=6/

&NUCLEUS part='Proj' name='11Be' charge=4 mass=11 spin=0 parity=+1
         be=0.50323 n=2 l=0 j=0/
&NUCLEUS part='Core' name='10Be' charge=4 mass=10 /
&NUCLEUS part='Valence' name='neutron' charge=0 mass=1 spin=0 /
&NUCLEUS part='Target' name='12C' charge=6 mass=12 spin=0 /

&BIN  spin=0 parity=+1 start=0.001 step=0.15 end=0.15 energy=T l=0 j=0 /
&BIN  spin=0 parity=+1 start=0.15 step=0.15 end=2.5 energy=F l=0 j=0 /
&BIN  spin=0 parity=+1 start=2.5 step=3 end=10 energy=F l=0 j=0 /
&BIN  spin=1 parity=-1 start=0.001 step=0.15 end=0.15 energy=T l=1 j=1 /
&BIN  spin=1 parity=-1 start=0.15 step=0.2 end=4 energy=F l=1 j=1 /
&BIN  spin=1 parity=-1 start=4 step=3 end=10 energy=F l=1 j=1 /
&BIN  spin=2 parity=+1 start=0.001 step=0.15 end=0.15 energy=F l=2 j=2 /
&BIN  spin=2 parity=+1 start=0.15 step=0.2 end=1 energy=F l=2 j=2 /
&BIN  spin=2 parity=+1 start=1 step=0.02 end=1.5 energy=F l=2 j=2 /
&BIN  spin=2 parity=+1 start=1.5 step=0.2 end=4.5 energy=F l=2 j=2 /
&BIN  spin=2 parity=+1 start=4.5 step=3 end=10 energy=F l=2 j=2 /
&BIN  spin=3 parity=-1 start=0.001 step=0.15 end=0.15 energy=T l=3 j=3 /
&BIN  spin=3 parity=-1 start=0.15 step=0.4 end=5 energy=F l=3 j=3 /
&BIN  spin=3 parity=-1 start=5 step=3 end=10 energy=F l=3 j=3 /
&BIN  spin=4 parity=+1 start=0.001 step=0.15 end=0.15 energy=T l=4 j=4 /
&BIN  spin=4 parity=+1 start=0.15 step=0.4 end=4 energy=F l=4 j=4 /
&BIN  spin=4 parity=+1 start=3 step=3 end=10 energy=F l=4 j=4 /
&BIN  spin=5 parity=-1 start=0.001 step=0.15 end=0.15 energy=T l=5 j=5 /
&BIN  spin=5 parity=-1 start=0.15 step=0.4 end=4 energy=F l=5 j=5 /
&BIN  spin=5 parity=-1 start=4 step=3 end=10 energy=F l=5 j=5 /
&BIN  spin=6 parity=+1 start=0.001 step=0.15 end=0.15 energy=T l=6 j=6 /
&BIN  spin=6 parity=+1 start=0.15 step=0.5 end=5 energy=F l=6 j=6 /
&BIN  spin=6 parity=+1 start=5 step=4 end=10 energy=F l=6 j=6 /
&BIN  /

&POTENTIAL part='Proj' /
&POTENTIAL part='Core' a1=1 rc=5.777 v=250 vr0=3.053 a=0.788
           w=247.9 wr0=2.982 aw=0.709 /
&POTENTIAL part='Valence' a1=1 v=46.9395 vr0=2.5798 a=0.676
           w=1.8256 wr0=2.5798 aw=0.676 wd=7.158 wdr0=2.9903 awd=0.5426 /
&POTENTIAL part='Gs' a1=1 v=62.98 vr0=2.585 a=0.6 /
&POTENTIAL part='Bi' l=2 a1=1 v=69.15 vr0=2.585 a=0.6 /
```

Appendix D

Coulomb and nuclear contributions to the diffractive breakup of ^{11}Be on ^{12}C at $10A$ MeV

In this appendix, I analyse separately the nuclear and Coulomb contribution to the diffractive breakup of ^{11}Be on ^{12}C at $10A$ MeV with the potentials presented in Sec. 3.2. To do so, I compare in Fig. D.1 CDCC calculations considering both Coulomb and nuclear potentials (solid red line) and separately the nuclear and the Coulomb interactions. Compared to the full calculation, the pure nuclear breakup (dashed green line) underestimates the energy distribution below 1 MeV, suggesting that the Coulomb interaction influences strongly these energies. This is confirmed by the pure Coulomb contribution (dash-dotted blue line), which reproduces well the full calculation below 0.2 MeV and underestimates it at larger energy. Moreover, the pure Coulomb breakup is dominated by E1 transitions and therefore does not populate the d resonance, as explained in Chapter 1.

To understand better the reaction mechanisms which are at stake here, we can now look at the contributions of the dominating partial waves in Fig. D.2. The panels (a), (b) and (c) correspond respectively to the breakup distribution in s, p and d wave. The pure nuclear contribution (dashed green lines) lies close to the full calculation (solid red lines) in the s and d wave, suggesting that the breakup in these partial-waves are due mainly to nuclear-induced transitions. However, the p wave is underestimated at energies below 1 MeV. This is expected since at low energies, this partial-wave is populated mostly by E1 transitions from the ground state. On the contrary, the pure Coulomb calculation (dash-dotted blue lines) does not have significant s and d wave contributions, because these partial waves cannot be reached directly by E1 transitions. This figure also shows that the p-wave contribution due to the pure Coulomb interaction is larger than the one due to the pure nuclear interaction up to 1 MeV. At larger energies, the nuclear contribution to the p wave dominates.

Finally, these figures illustrate also the interferences between the Coulomb and nuclear interactions. We can see that the full calculations is not simply given by the sum of the cross sections obtained with each interaction. This justifies the need to have a reaction model that treats both interactions simultaneously.

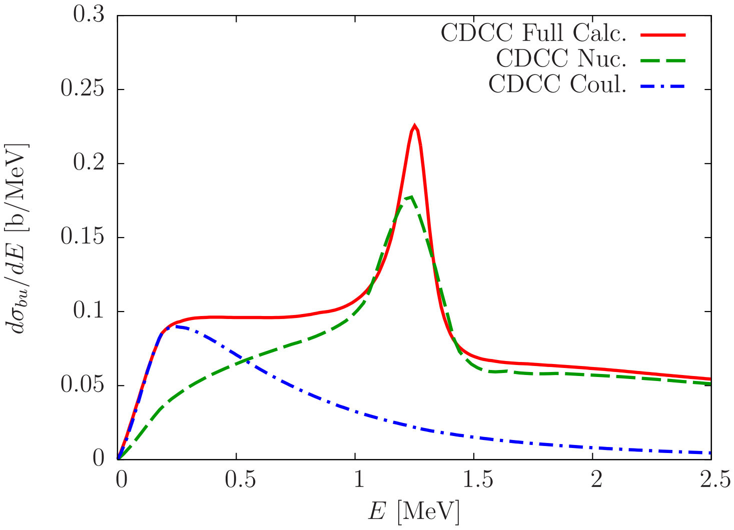

Figure D.1: Comparison of the full calculations of the diffractive breakup of ^{11}Be on ^{12}C at 10A MeV with its pure nuclear and Coulomb contributions.

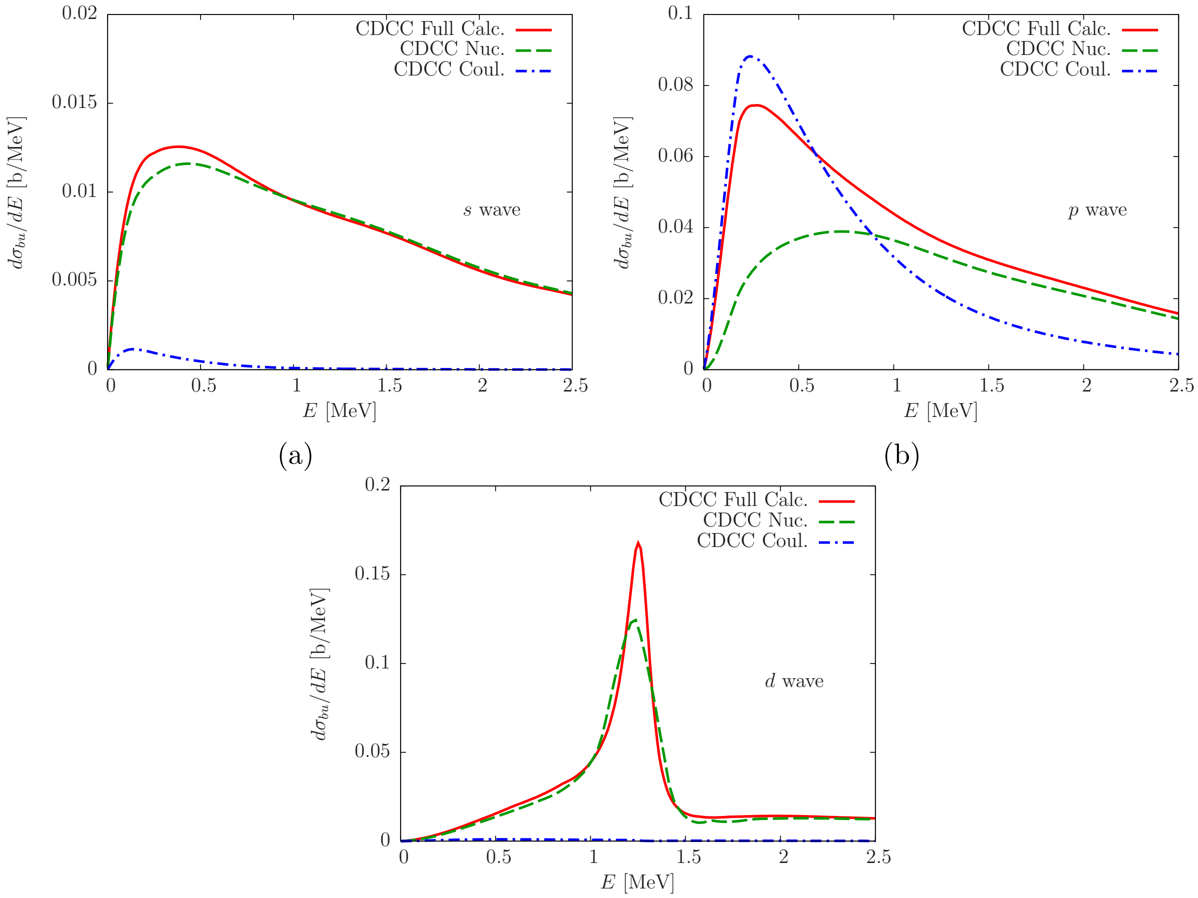

(a) (b)

(c)

Figure D.2: (a) s-, (b) p- and (c) d-wave contributions to the full calculations, the pure nuclear and Coulomb contributions to diffractive breakup of ^{11}Be on ^{12}C at 10A MeV.

Appendix E

Sensitivity of the corrections to the optical potentials

In this appendix, I evaluate the sensitivity of the exact continued S-matrix and the complex semiclassical corrections to the choice of the optical potentials. As in Chapter 3, this study is made considering a ^{11}Be impinging on ^{12}C at 20A MeV and 10A MeV. To assess the sensitivity of the corrections to the projectile-target interactions, I consider two sets of optical potentials: the one presented in Sec. 3.2 and the one used in Ref. [122], in which the authors study the exact continued S-matrix correction.

The interaction potentials chosen in Ref. [122] are detailed here. The ^{10}Be-^{12}C interaction is simulated by a Wood-Saxon potential (2.2.2)–(2.2.3) with parameters which are consistent with data for the ^{10}Be-^{12}C elastic scattering at 59.4A MeV [133, 134]. These parameters are listed in the two first lines of Table E.1. The Coulomb interaction is simulated by a potential generated by a uniformly charged sphere (2.2.4) of radius $R_C = 5.333$ fm. The n-^{12}C interaction is modelled by the Wood-Saxon potential (2.2.2)–(2.2.3) developed by Becchetti and Greenlees in Ref. [143]. This global potential is fit to elastic-scattering data of a nucleon off a nucleus with $A > 40$ at an energy $E < 50$ MeV. As in Ref. [122, 181], I take the parameters consistent with 58 MeV, which are displayed in the two last lines of Table E.1. For both potentials, I neglect any energy dependence.

^{10}Be-^{12}C	$V_R = -123$ MeV	$R_R = 3.33$ fm	$a_R = 0.8$ fm	[133]
	$W_I = -65$ MeV	$R_I = 3.47$ fm	$a_I = 0.8$ fm	
n-^{12}C	$V_R = -37.4$ MeV	$R_R = 2.7473$ fm	$a_R = 0.75$ fm	[143, 181]
	$W_I = -10$ MeV	$R_I = 2.9762$ fm	$a_I = 0.6$ fm	

Table E.1: Optical potentials used to simulate the projectile-target interaction for the elastic scattering of ^{11}Be off ^{12}C at 20AMeV and 10A MeV. These potentials have a Wood-Saxon form (2.2.2)–(2.2.3) and are the same as the ones used in Ref. [122].

Fig. E.1 shows the elastic-scattering cross sections of ^{11}Be off ^{12}C at [(a) and (b)] 20A MeV and [(c) and (d)] 10A MeV, obtained with (a) and (c) the set of optical potentials listed in Table 3.1 and with (b) and (d) the potentials listed in Table E.1. As in Chapter 3, I take CDCC calculations (solid red lines) as reference. At both energies, CDCC predictions are similar for both choices of optical potentials. The eikonal approximation (dashed green lines) behave similarly for both sets of potentials: it overestimates the cross sections at large angles, dampens the magnitude oscillations and is less accurate at 10A MeV than

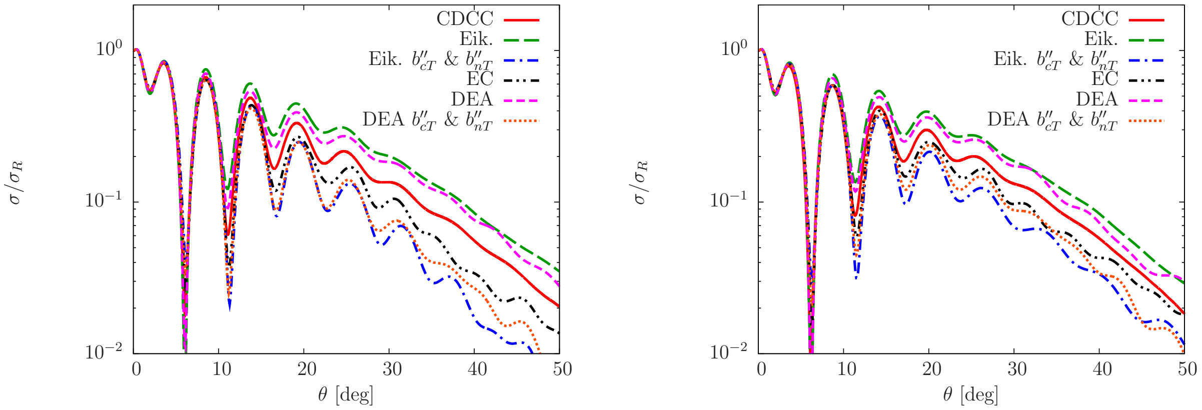

(a) $20A$ MeV (b) $20A$ MeV

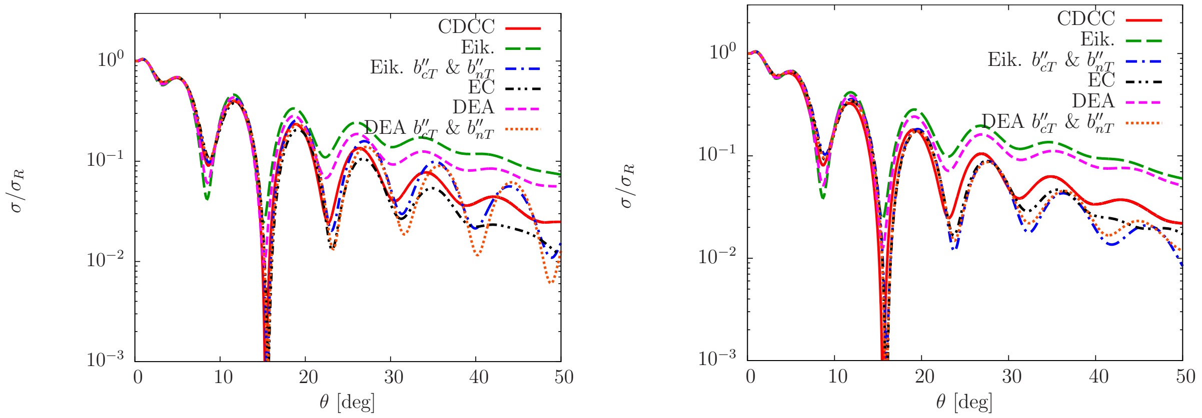

(c) $10A$ MeV (d) $10A$ MeV

Figure E.1: Influence of the choice of optical potentials on the complex semiclassical and the exact continued S-matrix corrections. Rutherford-normalized cross sections for the elastic scattering of ^{11}Be off ^{12}C at [(a) and (b)] $20A$ MeV and [(c) and (d)] $10A$ MeV as a function of the scattering angle θ. The panels (a) and (c) are obtained with the optical potentials listed in Table 3.1 and the panels (b) and (d) with the ones listed in Table E.1.

at $20A$ MeV. This figure also shows that DEA (small dashed magenta lines) stays close to the eikonal approximation, confirming that the dynamical effects are small at these energies and are not much influenced by the choice of interactions.

Fig. E.1 also displays the elastic-scattering cross sections obtained with the exact continued S-matrix correction (EC, dash-dotted-dotted black lines) for the two sets of potentials. We can see that in all cases this correction improves the accuracy of the eikonal approximation, as it lies closer to CDCC predictions. Moreover, it behaves similarly for both sets of optical potentials; it improves the oscillation pattern but underestimates CDCC at large angles. This correction seems therefore to be insensitive to the choice of the projectile-target interactions. Since this correction does not reproduce breakup cross sections, I have not investigated more deeply the sensitivity of this correction to the optical potentials.

As already observed in Sec. 3.4, the complex semiclassical corrections applied to the eikonal approximation (3.4.12)–(3.4.13) (dash-dotted blue lines) and to the DEA (3.4.15)–(3.4.16) (dotted orange lines) give similar results at both energies in Fig. E.1. This

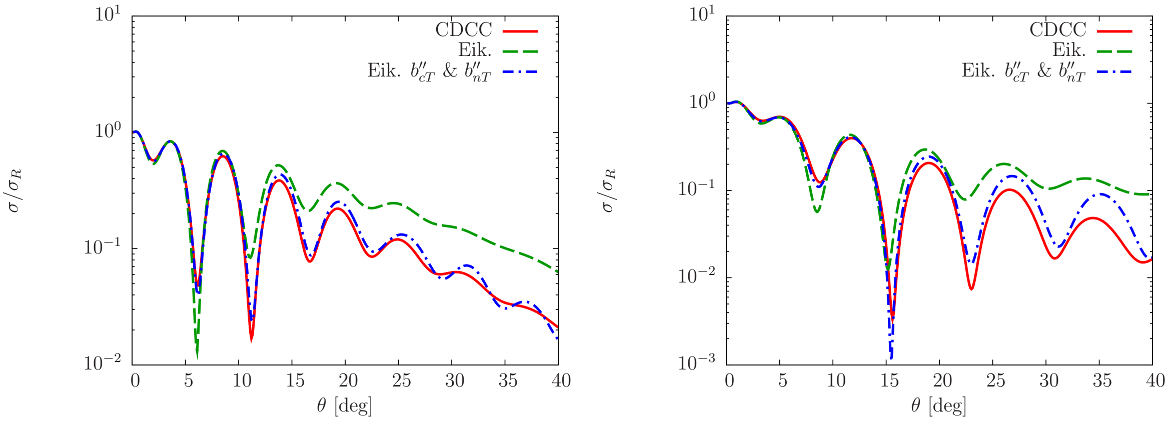

(a) (b)

Figure E.2: Rutherford-normalized cross sections for the elastic scattering of ^{11}Be off ^{12}C (a) at 20A MeV and (b) at 10A MeV as a function of the scattering angle θ, obtained with the potentials presented in Sec. 3.2 except that the n-^{12}C potential has a surface imaginary depth four times larger. These results are published in Ref. [21].

observation is robust to the choice of interactions. At both energies, they underestimate CDCC cross sections at large angles, but they are more accurate at 10A MeV, as already seen in Sec. 3.4. However, the elastic-scattering cross sections analysed in Ref. [21] obtained with an unrealistic n-^{12}C interaction does not lead to the same conclusions. In that article, I have used the same potentials as in Sec. 3.2 except that the n-^{12}C interaction has a imaginary surface depth four times larger. I have made this error by accounting twice the factor 4 in the surface term (2.2.2). This potential simulates therefore more absorption from the n-^{12}C elastic channel. The elastic-scattering cross sections of ^{11}Be off ^{12}C at (a) 20A MeV and (b) 10A MeV, obtained with this unrealistic potential, are displayed in Fig. E.2. As expected, the cross sections have a smaller magnitude than in the previous case, since the n-^{12}C potential is more absorptive. The discrepancies between the eikonal and CDCC results are similar for the two previous optical potentials. Nonetheless, the complex semiclassical correction behaves differently in this case: it overestimates CDCC cross sections and is more accurate at 20A MeV than at 10A MeV. This analysis emphasizes that the semiclassical correction is sensitive to the choice of optical potentials. However, because for all interactions discussed in this appendix, this correction fails to reproduce the breakup cross sections, I have also not studied more deeply this sensitivity.

List of publications

- C. Hebborn and D. Baye. *Simplified dynamical eikonal approximation.* Phys. Rev. C **101**, 054609 (2020).

- C. Hebborn and P. Capel. *Sensitivity of one-neutron knockout of halo nuclei to the their nuclear structure.* Proc. of the 27th International Nuclear Physics Conference (INPC2019), to appear in J. Phys. Conf. Ser., Glasgow, 2019.

- C. Hebborn and P. Capel. *Sensitivity of one-neutron knockout to the nuclear structure of halo nuclei.* Phys. Rev. C **100**, 054607 (2019).

- C. Hebborn and P. Capel. *Low-energy corrections to the eikonal description of elastic scattering and breakup of one-neutron halo nuclei in nuclear-dominated reactions.* Phys. Rev. C **98**, 044610 (2018).

- C. Hebborn, D. Baye and P. Capel. *Adiabatic correction to the eikonal approximation.* Proc. of the International Summer School on Nuclear Physics, in Basic Concepts in Nuclear Physics: Theory, Experiments and Applications, volume 225, edited by J. E. García-Ramos, M. Andrés, J. Valera, A. Moro, and F. Pérez-Bernal, Springer, La Rábida, 2019.

- C. Hebborn and P. Capel. *Analysis of corrections to the eikonal approximation.* Phys. Rev. C **96**, 054607 (2017).

- C. Hebborn and P. Capel. *Study of corrections to the eikonal approximation.* Proc. of the 55th International Winter Meeting on Nuclear Physics, edited by C. Sfienti, L. Fabbietti, and W. Kühn, in PoS(BORMIO2017)056, Bormio, 2017.

List of contributions to conferences, workshops and seminars

List of contributions to conferences and workshops

- July 2019: Oral communication at the 27th International Nuclear Physics Conference (INPC 2019), Glasgow (UK). Title: *Sensitivity of one-neutron knockout of halo nuclei to the their nuclear structure.*

- January 2019: Poster contribution at the 57th International Winter Meeting on Nuclear Physics, Bormio (Italy). Title: *Peripherality in inclusive nuclear breakup of halo nuclei.*

- June 2018: Oral communication at the International Summer School on Nuclear Physics, La Rábida (Spain). Title: *Adiabatic correction to the eikonal approximation.*

- June 2018: Oral communication at the Direct Reactions with Exotic Beams (DREB 2018), Matsue (Japan). Title: *Corrections to the eikonal description of elastic scattering and breakup of halo nuclei.*

- March 2018: Oral communication at the Recent advances and challenges in the description of nuclear reactions at the limit of stability (ECT* workshop), Trento (Italy). Title: *Low-energy corrections to the eikonal description of elastic scattering and breakup of halo nuclei.*

- February 2017: Oral communication at the Unraveling the complexity of nuclear systems: single-particle and collective aspects through the looking glass (ECT* workshop), Trento (Italy). Title: *Extension of the eikonal approximation to low energies.*

- January 2017: Poster contribution at the 55th International Winter Meeting on Nuclear Physics, Bormio (Italy). Title: *Study of corrections to the eikonal approximation.*

External seminars

- December 2019: Seminar of National Superconducting Cyclotron Laboratory, Michigan State University (USA). Title: *Study of the eikonal approximation to model exotic reactions.*
- November 2019: Seminar of Nuclear Data & Theory Group, Lawrence Livermore National Laboratory (USA). Title: *Study of the eikonal approximation to model exotic reactions.*
- May 2019: Seminar of the Institut für Kernphysik, Johannes Gutenberg-Universität Mainz (Germany). Title: *What nuclear-structure information can be inferred from inclusive measurements of breakup of halo nuclei?.*

Bibliography

[1] C. E. Rolfs and W. S. Rodney. *Cauldrons in the cosmos : nuclear astrophysics.* University of Chicago Press, Chicago, 1988.

[2] M. Arnould, S. Goriely, and K. Takahashi. *The r-process of stellar nucleosynthesis: Astrophysics and nuclear physics achievements and mysteries.* Phys. Rep. **450**, 97 (2007).

[3] H. Geissel, G. Munzenberg, and K. Riisager. *Secondary exotic nuclear beams.* Ann. Rev. Nucl. Part. Sc. **45**, 163 (1995).

[4] Y. Blumenfeld. *Review of accelerators for radioactive beams.* Proc. of the 11th European Particle Accelerator Conference (EPAC2008), in Conf. Proc. C 0806233 (2008) MOZAM01, Genoa, 2008.

[5] J. C. Cornell. *Radioactive ion beam facilities in Europe: current status and future development.* Proc. of the 17th International Conference on Cyclotrons and their Applications (CYCLOTRONS04), Tokyo, 2004.

[6] M. Freer. *Clusters in nuclei.* Scholarpedia **5**, 9652 (2010).

[7] P. G. Hansen and B. Jonson. *The neutron halo of extremely neutron-rich nuclei.* Europhys. Lett. **4**, 409 (1987).

[8] I. Tanihata. *Neutron halo nuclei.* J. Phys. G **22**, 157 (1996).

[9] P. G. Hansen and J. A. Tostevin. *Direct reactions with exotic nuclei.* Ann. Rev. Nucl. Part. Sc. **53**, 219 (2003).

[10] T. Aumann and T. Nakamura. *The electric dipole response of exotic nuclei.* Phys. Script. **T152**, 014012 (2013).

[11] D. Baye and P. Capel. *Breakup reaction models for two- and three-cluster projectiles.* In Clusters in Nuclei, Vol. 2, edited by C. Beck, Lecture Notes in Physics Vol. 848, Springer, Heidelberg, 2012.

[12] L. D. Faddeev. *Scattering theory for a three-particle system.* Sov. Phys. JETP **12**, 1014 (1961).

[13] R. Lazauskas and J. Carbonell. *The Faddeev–Yakubovsky Symphony.* Few-Body Systems **60**, 62 (2019).

[14] I. J. Thompson. *Coupled reaction channels calculations in nuclear physics.* Comp. Phys. Rep. **7**, 167 (1988).

[15] I. J. Thompson and F. M. Nunes. *Nuclear reactions for astrophysics : Principles, calculation and applications of low-energy reactions.* Cambridge University Press, Cambridge, 2009.

[16] N. Austern, Y. Iseri, M. Kamimura, M. Kawai, G. Rawitscher, and M. Yahiro. *Continuum-discretized coupled-channels calculations for three-body models of deuteron-nucleus reactions.* Phys. Rep. **154**, 125 (1987).

[17] M. Kamimura, M. Yahiro, Y. Iseri, H. Kameyama, Y. Sakuragi, and M. Kawai. *Coupled-channels theory of breakup processes in nuclear reactions.* Prog. Theor. Phys. Suppl. **89**, 1 (1986).

[18] R. J. Glauber. *High energy collision theory.* In Lecture in Theoretical Physics, Vol. 1, edited by W. E. Brittin and L. G. Dunham, Interscience, New York, 1959.

[19] K. V. Shajesh *Eikonal Approximation.* University of Oklahoma, Norman, 2004.

[20] C. Hebborn and P. Capel. *Study of corrections to the eikonal approximation.* Proc. of the 55th International Winter Meeting on Nuclear Physics, edited by C. Sfienti, L. Fabbietti, and W. Kühn, in PoS(BORMIO2017)056, Bormio, 2017.

[21] C. Hebborn and P. Capel. *Analysis of corrections to the eikonal approximation.* Phys. Rev. C **96**, 054607 (2017).

[22] C. Hebborn and P. Capel. *Low-energy corrections to the eikonal description of the elastic scattering and breakup of one-neutron halo nuclei in nuclear-dominated reactions.* Phys. Rev. C **98**, 044610 (2018).

[23] B. Abu-Ibrahim and Y. Suzuki. *Scatterings of complex nuclei in the Glauber model calculations.* Phys. Rev. C **62**, 034608 (2000).

[24] J. Margueron, A. Bonaccorso, and D. M. Brink. *A non-perturbative approach to halo breakup.* Nucl. Phys. A **720**, 337 (2003).

[25] C. Hebborn and D. Baye. *Simplified dynamical eikonal approximation.* Phys. Rev. C **101**, 054609 (2020).

[26] J. A. Tostevin and A. Gade. *Systematics of intermediate-energy single-nucleon removal cross sections.* Phys. Rev. C **90**, 057602 (2014).

[27] A. Gade, P. Adrich, D. Bazin, M. D. Bowen, B. A. Brown, C. M. Campbell, J. M. Cook, T. Glasmacher, P. G. Hansen, K. Hosier, S. McDaniel, D. McGlinchery, A. Obertelli, K. Siwek, L. A. Riley, J. A. Tostevin, and D. Weisshaar. *Reduction of spectroscopic strength: Weakly-bound and strongly-bound single-particle states studied using one-nucleon knockout reactions.* Phys. Rev. C **77**, 044306 (2008).

[28] M. B. Tsang, Jenny Lee, S. C. Su, J. Y. Dai, M. Horoi, H. Liu, W. G. Lynch, and S. Warren. *Survey of excited state neutron spectroscopic factors for* $Z = 8$–28 *nuclei.* Phys. Rev. Lett. **102**, 062501 (2009).

[29] J. Lee, J. A. Tostevin, B. A. Brown, F. Delaunay, W. G. Lynch, M. J. Saelim, and M. B. Tsang. *Reduced neutron spectroscopic factors when using potential geometries constrained by Hartree-Fock calculations.* Phys. Rev. C **73**, 044608 (2006).

[30] C. Hebborn and P. Capel. *Sensitivity of one-neutron knockout to the nuclear structure of halo nuclei.* Phys. Rev. C **100**, 054607 (2019).

[31] C. Hebborn and P. Capel. *Sensitivity of one-neutron knockout of halo nuclei to their nuclear structure.* Proc. of 27th International Nuclear Physics Conference (INPC 2019) to appear in J. Phys. Conf. Ser., arXiv:1911.01489 [nucl-th], Glasgow, 2019.

[32] I. Tanihata, H. Hamagaki, O. Hashimoto, Y. Shida, N. Yoshikawa, K. Sugimoto, O. Yamakawa, T. Kobayashi, and N. Takahashi. *Measurements of interaction cross sections and nuclear radii in the light p-shell region.* Phys. Rev. Lett. **55**, 2676 (1985).

[33] I. Tanihata, H. Hamagaki, O. Hashimoto, S. Nagamiya, Y. Shida, N. Yoshikawa, O. Yamakawa, K. Sugimoto, T. Kobayashi, D. E. Greiner, N. Takahashi, and Y. Nojiri. *Measurements of interaction cross sections and radii of* He *isotopes.* Phys. Lett. B **160**, 380 (1985).

[34] M. V. Zhukov, B. V. Danilin, D. V. Fedorov, J. M. Bang, I. J. Thompson, and J. S. Vaagen. *Bound state properties of Borromean halo nuclei:* ^{6}He *and* ^{11}Li. Phys. Rep. **231**, 151 (1993).

[35] N. Fukuda, T. Nakamura, N. Aoi, N. Imai, M. Ishihara, T. Kobayashi, H. Iwasaki, T. Kubo, A. Mengoni, M. Notani, H. Otsu, H. Sakurai, S. Shimoura, T. Teranishi, Y. X. Watanabe, and K. Yoneda. *Coulomb and nuclear breakup of a halo nucleus* ^{11}Be. Phys. Rev. C **70**, 054606 (2004).

[36] L. Zu-Hua. *Halo nature of* ^{14,15}C. Chin. Phys. Lett. **19**, 8 (2002).

[37] F. M. Marqués, M. Labiche, N. A. Orr, J. C. Angélique, L. Axelsson, B. Benoit, U. C. Bergmann, M. J. G. Borge, W. N. Catford, S. P. G. Chappell, N. M. Clarke, G. Costa, N. Curtis, A. D'Arrigo, F. de Oliveira Santos, E. de Góes Brennand, O. Dorvaux, M. Freer, B. R. Fulton, G. Giardina, C. Gregori, S. Grévy, D. Guillemaud-Mueller, F. Hanappe, B. Heusch, B. Jonson, C. Le Brun, S. Leenhardt, M. Lewitowicz, M. J. López, K. Markenroth, M. Motta, A. C. Mueller, T. Nilsson, A. Ninane, G. Nyman, I. Piqueras, K. Riisager, M. G. Saint Laurent, F. Sarazin, S. M. Singer, O. Sorlin, and L. Stuttgé. *Two-neutron interferometry as a probe of the nuclear halo.* Phys. Lett. B **476**, 219 (2000).

[38] Y. Suzuki, R. G. Lovas, K. Yabana, and K. Varga. *Structure and reactions of light exotic nuclei.* Taylor & Francis, London, 2003.

[39] A. S. Jensen and K. Riisager. *Towards necessary and sufficient conditions for halo occurrence.* Phys. Lett. B **480**, 39 (2000).

[40] J. H. Kelley, E. Kwan, J. E. Purcell, C. G. Sheu, and H. R. Weller. *Energy levels of light nuclei A=11.* Nucl. Phys. A **880**, 88 (2012).

[41] F. Ajzenberg-Selove. *Energy levels of light nuclei A=13–15.* Nucl. Phys. A **523**, 1 (1991).

[42] D. R. Tilley, C. M. Cheves, J. L. Godwin, G. M. Hale, H. M. Hofmann, J. H. Kelley, C. G. Sheu, and H. R. Weller. *Energy levels of light nuclei A=5, 6, 7.* Nucl. Phys. A **708**, 3 (2002).

[43] A. S. Jensen and M. V. Zhukov. *Few-body effects in nuclear halos.* Nucl. Phys. A **693**, 411 (2001).

[44] C. Cohen-Tannoudji, B. Diu, and F. Laloë. *Mécanique quantique.* Herman, Paris, 1973.

[45] D. V. Fedorov, A. S. Jensen, and K. Riisager. *General properties of halos.* Phys. Lett. B **312**, 1 (1993).

[46] K. Riisager, D. V. Fedorov, and A. S. Jensen. *Quantum halos.* Europhys. Lett. **49**, 547 (2000).

[47] A. Poves. *Shell model and spectroscopic factors.* In Lecture at "Physics at the femtometer scale" 30th Ecole Joliot-Curie, La Colle Sur Loup, 2011.

[48] N. K. Timofeyuk. *Overlap functions for reaction theories: challenges and open problems.* J. Phys. G: Nucl. Part. Phys. **41**, 094008 (2014).

[49] P. Capel. *Introduction to nuclear-reaction theory.* In Basic Concepts in Nuclear Physics: Theory, Experiments and Applications, volume 225, edited by J. E. García-Ramos, M. Andrés, J. Valera, A. Moro, and F. Pérez-Bernal, Springer, La Rábida, 2019.

[50] T. Duguet, H. Hergert, J. D. Holt, and V. Somà. *Nonobservable nature of the nuclear shell structure: Meaning, illustrations, and consequences.* Phys. Rev. C **92**, 034313 (2015).

[51] A. Calci, P. Navrátil, R. Roth, J. Dohet-Eraly, S. Quaglioni, and G. Hupin. *Can ab initio theory explain the phenomenon of parity inversion in* $^{11}\mathrm{Be}$*?* Phys. Rev. Lett. **117**, 242501 (2016).

[52] S. Quaglioni and P. Navrátil. *Ab initio many-body calculations of* n-$^{3}\mathrm{H}$*,* n-$^{4}\mathrm{He}$*,* p-$^{3,4}\mathrm{He}$*, and* n-$^{10}\mathrm{Be}$ *scattering.* Phys. Rev. Lett. **101**, 092501 (2008).

[53] D. J. Morrissey and B. M. Sherrill. *In-flight separation of projectile fragments.* In The Euroschool Lectures on Physics with Exotic Beams, Vol. 1, volume 641, edited by J. Al-Khalili and E. Roeckl, Springer, Heidelberg, 2004.

[54] Z. Meisel. *From dripline to dripline: Nuclear astrophysics in the laboratory.* Proc. of FAIRNESS 2016, Garmisch-Partenkirchen, J. Phys. Conf. Ser. **742**, 012019 (2016).

[55] P. Van Duppen. *Isotope separation on line and post acceleration.* In The Euroschool Lectures on Physics with Exotic Beams, Vol. 2, volume 700, edited by J. Al-Khalili and E. Roeckl, Springer, Heidelberg, 2006.

[56] I. Tanihata, T. Kobayashi, O. Yamakawa, S. Shimoura, K. Ekuni, K. Sugimoto, N. Takahashi, T. Shimoda, and H. Sato. *Measurement of interaction cross sections using isotope beams of* Be *and* B *and isospin dependence of the nuclear radii.* Phys. Lett. B **206**, 592 (1988).

[57] K. S. Krane. *Introductory nuclear physics.* Wiley, New York, 1988.

[58] E. Arnold, J. Bonn, R. Gegenwart, W. Neu, R. Neugart, E.-W. Otten, G. Ulm, and K. Wendt. *Nuclear spin and magnetic moment of* ^{11}Li. Phys. Lett. B **197**, 311 (1987).

[59] E. Arnold, J. Bonn, R. Neugart W. Neu, E. W. Orten, and The Isolde Collaboration. *Quadrupole interaction of* ^{8}Li *and* ^{9}Li *in LiNbO*$_3$ *and the quadrupole moment of* ^{9}Li. Z. Phys. A **331**, 295 (1988).

[60] E. Arnold, J. Bonn, A. Klein, R. Neugart, M. Neuroth, E. W. Otten, P. Lievens, H. Reich, and W. Widdra. *Quadrupole moment of* ^{11}Li. Phys. Lett. B **281**, 16 (1992).

[61] A. Di Pietro, G. Randisi, V. Scuderi, L. Acosta, F. Amorini, M. J. G. Borge, P. Figuera, M. Fisichella, L. M. Fraile, J. Gomez-Camacho, H. Jeppesen, M. Lattuada, I. Martel, M. Milin, A. Musumarra, M. Papa, M. G. Pellegriti, F. Perez-Bernal, R. Raabe, F. Rizzo, D. Santonocito, G. Scalia, O. Tengblad, D. Torresi, A. Maira Vidal, D. Voulot, F. Wenander, and M. Zadro. *Elastic scattering and reaction mechanisms of the halo nucleus* ^{11}Be *around the Coulomb barrier.* Phys. Rev. Lett. **105**, 022701 (2010).

[62] A. Di Pietro, V. Scuderi, A. M. Moro, L. Acosta, F. Amorini, M. J. G. Borge, P. Figuera, M. Fisichella, L. M. Fraile, J. Gomez-Camacho, H. Jeppesen, M. Lattuada, I. Martel, M. Milin, A. Musumarra, M. Papa, M. G. Pellegriti, F. Perez-Bernal, R. Raabe, G. Randisi, F. Rizzo, G. Scalia, O. Tengblad, D. Torresi, A. Maira Vidal, D. Voulot, F. Wenander, and M. Zadro. *Experimental study of the collision* ^{11}Be *+* ^{64}Zn *around the Coulomb barrier.* Phys. Rev. C **85**, 054607 (2012).

[63] T. Nakamura, T. Motobayashi, Y. Ando, A. Mengoni, T. Nishio, H. Sakurai, S. Shimoura, T. Teranishi, Y. Yanagisawa, and M. Ishihara. *Coulomb excitation of* ^{11}Be. Phys. Lett. B **394**, 11 (1997).

[64] R. Palit, P. Adrich, T. Aumann, K. Boretzky, B. V. Carlson, D. Cortina, U. Datta Pramanik, T. W. Elze, H. Emling, H. Geissel, M. Hellström, K. L. Jones, J. V. Kratz, R. Kulessa, Y. Leifels, A. Leistenschneider, G. Münzenberg, C. Nociforo, P. Reiter, H. Simon, K. Sümmerer, and W. Walus. *Exclusive measurement of breakup reactions with the one-neutron halo nucleus* ^{11}Be. Phys. Rev. C **68**, 034318 (2003).

[65] T. Nakamura, S. Shimoura, T. Kobayashi, T. Teranishi, K. Abe, N. Aoi, Y. Doki, M. Fujimaki, N. Inabe, N. Iwasa, K. Katori, T. Kubo, H. Okuno, T. Suzuki, I. Tanihata, Y. Watanabe, A. Yoshida, and M. Ishihara. *Coulomb dissociation of a halo nucleus* ^{11}Be *at 72A MeV.* Phys. Lett. B **331**, 296 (1994).

[66] L. Moschini and P. Capel. *Reliable extraction of the dB(E1)/dE for* ^{11}Be *from its breakup at 520 MeV/nucleon.* Phys. Lett. B **790**, 367 (2019).

[67] A. M. Moro, J. A. Lay, and J. Gómez-Camacho. *Determining B(E1) distributions of weakly bound nuclei from breakup cross sections using Continuum Discretized Coupled Channels calculations. Application to* ^{11}Be. arXiv:2004.14612 [nucl-th], 2020.

[68] P. Capel and Y. Nollet. *Reconciling Coulomb breakup and neutron radiative capture.* Phys. Rev. C **96**, 015801 (2017); Erratum: Phys. Rev. C **98**, 019906 (2018).

[69] J. Singh, T. Matsumoto, and K. Ogata. *Systematic study on the role of various higher-order processes in the breakup of weakly-bound projectiles.* arXiv:2005.05605 [nucl-th], 2020.

[70] G. Baur, C. A. Bertulani, and H. Rebel. *Coulomb dissociation as a source of information on radiative capture processes of astrophysical interest.* Nucl. Phys. A **458**, 188 (1986).

[71] G. Baur, K. Hencken, and D. Trautmann. *Electromagnetic dissociation as a tool for nuclear structure and astrophysics.* Prog. Part. Nucl. Phys. **51**, 487 (2003).

[72] N. C. Summers and F. M. Nunes. *Extracting (n, γ) direct capture cross sections from Coulomb dissociation: Application to* ^{14}C$(n, \gamma)^{15}$C. Phys. Rev. C **78**, 011601 (2008); Erratum: Phys. Rev. C **78**, 069908 (2008).

[73] H. Esbensen. *Coulomb dissociation of* ^{15}C *and radiative neutron capture on* ^{14}C. Phys. Rev. C **80**, 024608 (2009); Erratum: H. Esbensen and R. Reifarth. Phys. Rev. C **80**, 059904 (2009).

[74] J. Margueron, A. Bonaccorso, and D. M. Brink. *Coulomb-nuclear coupling and interference effects in the breakup of halo nuclei.* Nucl. Phys. A **703**, 105 (2002).

[75] E. Sauvan, F. Carstoiu, N. A. Orr, J. C. Angélique, W. N. Catford, N.M. Clarke, M. Mac Cormick, N. Curtis, M. Freer, S. Grévy, C. Le Brun, M. Lewitowicz, E. Liégard, F. M. Marqués, P. Roussel-Chomaz, M. G. Saint Laurent, M. Shawcross, and J. S. Winfield. *One-neutron removal reactions on neutron-rich psd-shell nuclei.* Phys. Lett. B **491**, 1 (2000).

[76] T. Aumann, A. Navin, D. P. Balamuth, D. Bazin, B. Blank, B. A. Brown, J. E. Bush, J. A. Caggiano, B. Davids, T. Glasmacher, V. Guimarães, P. G. Hansen, R. W. Ibbotson, D. Karnes, J. J. Kolata, V. Maddalena, B. Pritychenko, H. Scheit, B. M. Sherrill, and J. A. Tostevin. *One-neutron knockout from individual single-particle states of* ^{11}Be. Phys. Rev. Lett. **84**, 35 (2000).

[77] J. A. Tostevin, D. Bazin, B. A. Brown, T. Glasmacher, P. G. Hansen, V. Maddalena, A. Navin, and B. M. Sherrill. *Single-neutron removal reactions from* ^{15}C *and* ^{11}Be*: Deviations from the eikonal approximation.* Phys. Rev. C **66**, 02460 (2002).

[78] E. Sauvan, F. Carstoiu, N. A. Orr, J. S. Winfield, M. Freer, J. C. Angélique, W. N. Catford, N. M. Clarke, N. Curtis, S. Grévy, C. Le Brun, M. Lewitowicz, E. Liégard, F. M. Marqués, M. Mac Cormick, P. Roussel-Chomaz, M.-G. Saint Laurent, and M. Shawcross. *One-neutron removal reactions on light neutron-rich nuclei.* Phys. Rev. C **69**, 044603 (2004).

[79] N. A. Orr. *Fragment momentum distributions and the halo.* Nucl. Phys. A **616**, 155 (1997).

[80] T. Kobayashi, O. Yamakawa, K. Omata, K. Sugimoto, T. Shimoda, N. Takahashi, and I. Tanihata. *Projectile Fragmentation of the Extremely Neutron-Rich Nucleus* ^{11}Li *at 0.79 GeV/nucleon.* Phys. Rev. Lett. **60**, 2599 (1988).

[81] C. A. Bertulani and K. W. McVoy. *Momentum distributions in reactions with radioactive beams.* Phys. Rev. C **46**, 2638 (1992).

[82] V. Maddalena, T. Aumann, D. Bazin, B. A. Brown, J. A. Caggiano, B. Davids, T. Glasmacher, P. G. Hansen, R. W. Ibbotson, A. Navin, B. V. Pritychenko, H. Scheit, B. M. Sherrill, M. Steiner, J. A. Tostevin, and J. Yurkon. *Single-neutron knockout reactions: Application to the spectroscopy of* ^{16,17,19}C*.* Phys. Rev. C **63**, 024613 (2001).

[83] J. S. Al-Khalili. *Validity of spectator core model in neutron knock-out reactions.* Proc. of European Few-Body Problems in Physics, Evora, Nucl. Phys. A **689**, 551c (2001).

[84] L. Lapikás. *Quasi-elastic electron scattering off nuclei.* Nucl. Phys. A **553**, 297 (1993).

[85] G. J. Kramer, H. P. Blok, and L. Lapikás. *A consistent analysis of* $(e, e'p)$ *and* $(d,\, ^3\mathrm{He})$ *experiments.* Nucl. Phys. A **679**, 267 (2001).

[86] M. Gómez-Ramos and A. M. Moro. *Binding-energy independence of reduced spectroscopic strengths derived from* $(p, 2p)$ *and* (p, pn) *reactions with nitrogen and oxygen isotopes.* Phys. Lett. B **785**, 511 (2018).

[87] F. Flavigny, A. Gillibert, L. Nalpas, A. Obertelli, N. Keeley, C. Barbieri, D. Beaumel, S. Boissinot, G. Burgunder, A. Cipollone, A. Corsi, J. Gibelin, S. Giron, J. Guillot, F. Hammache, V. Lapoux, A. Matta, E. C. Pollacco, R. Raabe, M. Rejmund, N. de Séreville, A. Shrivastava, A. Signoracci, and Y. Utsuno. *Limited asymmetry dependence of correlations from single nucleon transfer.* Phys. Rev. Lett. **110**, 122503 (2013).

[88] Ø. Jensen, G. Hagen, M. Hjorth-Jensen, B. A. Brown, and A. Gade. *Quenching of spectroscopic factors for proton removal in oxygen isotopes.* Phys. Rev. Lett. **107**, 032501 (2011).

[89] F. Flavigny, A. Obertelli, A. Bonaccorso, G. F. Grinyer, C. Louchart, L. Nalpas, and A. Signoracci. *Nonsudden limits of heavy-ion induced knockout reactions.* Phys. Rev. Lett. **108**, 252501 (2012).

[90] D. Baye. *Mécanique quantique : Notions de base.* Presses Universitaires de Bruxelles, Brussels, 2012.

[91] C. A. Bertulani and P. Danielewicz. *Introduction to nuclear reactions.* Institute of Physics Publishing, Bristol, 2004.

[92] M. Abramowitz and I. A. Stegun. *Handbook of Mathematical Functions with Formulas, Graphs, and Mathematical Tables.* Dover, New York, 1964.

[93] P. Descouvemont and D. Baye. *The R-matrix theory.* Rep. Prog. Phys. **73**, 036301 (2010).

[94] H. Feshbach. *Unified theory of nuclear reactions.* Ann. Phys. **5**, 357 (1958).

[95] L. J. Titus, F. M. Nunes, and G. Potel. *Explicit inclusion of nonlocality in* (d, p) *transfer reactions.* Phys. Rev. C **93**, 014604 (2016).

[96] X. Li, G. Potel, and F. M. Nunes. *Nonlocal interactions in the (d,p) surrogate method for (n,γ) reactions.* Phys. Rev. C **98**, 044621 (2018).

[97] G. Goldstein. *Description de la dissociation de noyaux à halo par l'approximation eikonale dynamique.* PhD thesis, Université libre de Bruxelles, Brussels, 2007.

[98] P. Capel. *Coulomb breakup of halo nuclei by a time-dependent method.* PhD thesis, Université libre de Bruxelles, Brussels, 2004.

[99] N. Austern. *Direct reaction theories.* Wiley, New-York, 1970.

[100] M. S. Hussein and K. W. McVoy. *Inclusive projectile fragmentation in the spectator model.* Nucl. Phys. A **445**, 124 (1985).

[101] R. Lazauskas. *Solution of the n-^{4}He elastic scattering problem using the Faddeev-Yakubovsky equations.* Phys. Rev. C **97**, 044002 (2018).

[102] F. M. Nunes. *Continuum-discretized coupled channels methods.* Scholarpedia **6**, 10497 (2011).

[103] N. J. Upadhyay, A. Deltuva, and F. M. Nunes. *Testing the continuum-discretized coupled channels method for deuteron-induced reactions.* Phys. Rev. C **85**, 054621 (2012).

[104] A. Deltuva, A. M. Moro, E. Cravo, F. M. Nunes, and A. C. Fonseca. *Three-body description of direct nuclear reactions: Comparison with the continuum discretized coupled channels method.* Phys. Rev. C **76**, 064602 (2007).

[105] A. M. Moro. *Models for nuclear reactions with weakly bound systems.* Proc. of the International School of Physics Enrico Fermi, volume 201, edited by F. Gramegna, P. Van Duppen, A. Vitturi, and S. Pirrone, IOS Press, Varenna, 2018.

[106] D. Baye, P. Capel, and G. Goldstein. *Collisions of halo nuclei within a dynamical eikonal approximation.* Phys. Rev. Lett. **95**, 082502 (2005).

[107] G. Goldstein, D. Baye, and P. Capel. *Dynamical eikonal approximation in breakup reactions of* ^{11}Be. Phys. Rev. C **73**, 024602 (2006).

[108] P. Capel, D. Baye, and V. S. Melezhik. *Time-dependent analysis of the breakup of halo nuclei.* Phys. Rev. C **68**, 014612 (2003).

[109] G. Goldstein, P. Capel, and D. Baye. *Analysis of Coulomb breakup experiments of* ^{8}B *with a dynamical eikonal approximation.* Phys. Rev. C **76**, 024608 (2007).

[110] P. Capel, H. Esbensen, and F. M. Nunes. *Comparing nonperturbative models of the breakup of neutron-halo nuclei.* Phys. Rev. C **85**, 044604 (2012).

[111] D. Baye, P. Capel, P. Descouvemont, and Y. Suzuki. *Four-body calculation of* ^{6}He *breakup with the Coulomb-corrected eikonal method.* Phys. Rev. C **79**, 024607 (2009).

[112] P. Capel, D. Baye, and Y. Suzuki. *Coulomb-corrected eikonal description of the breakup of halo nuclei.* Phys. Rev. C **78**, 054602 (2008).

[113] P. Capel and D. Baye. *Coupling-in-the-continuum effects in Coulomb dissociation of halo nuclei.* Phys. Rev. C **71**, 044609 (2005).

[114] S. M. Lenzi, A. Vitturi, and F. Zardi. *Range of validity of the eikonal approximation within the coupled-channel description of heavy-ion scattering processes.* Z. Phys. A **352**, 303 (1995).

[115] T. Fukui, K. Ogata, and P. Capel. *Analysis of a low-energy correction to the eikonal approximation.* Phys. Rev. C **90**, 034617 (2014).

[116] R. A. Broglia and A. Winther. *Heavy Ion Reactions, Lectures Notes, Vol. 1: Elastic and Inelastic Reactions.* Benjamin-Cummings, Reading, 1981.

[117] S. J. Wallace. *Eikonal expansion in atomic and nuclear scattering.* PhD thesis, University of Washington, Seattle, 1971.

[118] S. J. Wallace. *Eikonal expansion.* Ann. Phys. **78**, 190 (1973).

[119] S. J. Wallace. *Eikonal expansion.* Phys. Rev. Lett. **27**, 622 (1971).

[120] M. Buuck and G. A. Miller. *Corrections to the eikonal approximation for nuclear scattering at medium energies.* Phys. Rev. C **90**, 024606 (2014).

[121] C. E. Aguiar, F. Zardi, and A. Vitturi. *Low-energy extensions of the eikonal approximation to heavy-ion scattering.* Phys. Rev. C **56**, 1511 (1997).

[122] J. M. Brooke, J. S. Al-Khalili, and J. A. Tostevin. *Noneikonal calculations for few-body projectiles.* Phys. Rev. C **59**, 1560 (1999).

[123] J. M. Brooke. *Noneikonal corrections to nuclear few-body scattering models.* PhD thesis, University of Surrey, Surrey, 1999.

[124] S. J. Wallace. *High-energy expansions of scattering amplitudes.* Phys. Rev. D **8**, 1846 (1973).

[125] C. C. Sahm, T. Murakami, J. G. Cramer, A. J. Lazzarini, D. D. Leach, D. R. Tieger, R. A. Loveman, W. G. Lynch, M. B. Tsang, and J. Van der Plicht. *Total reaction cross section for* ^{12}C *on* ^{12}C, ^{40}Ca, ^{90}Zr, *and* ^{208}Pb *between* 10 *and* 35 *MeV/nucleon.* Phys. Rev. C **34**, 2165 (1986).

[126] A. J. Koning and J. P. Delaroche. *Local and global nucleon optical models from 1 keV to 200 MeV.* Nucl. Phys. A **713**, 231 2003.

[127] P. Capel, G. Goldstein, and D. Baye. *Time-dependent analysis of the breakup of* ^{11}Be *on* ^{12}C *at 67 MeV/nucleon.* Phys. Rev. C **70**, 064605 (2004).

[128] F. Colomer, P. Capel, F. M. Nunes, and R. C. Johnson. *Extension of the ratio method to low energy.* Phys. Rev. C **93**, 054621 (2016).

[129] C. Hebborn. *Study of corrections to the eikonal approximations.* Master's thesis, Université libre de Bruxelles, Brussels, 2016.

[130] D. M. Brink and G. R. Satchler. *The role of the attractive nuclear potential in determining reaction cross sections.* J. Phys. G: Nucl. Phys. **7**, 43 (1981).

[131] M. H. Cha. *Modified Glauber model II description for heavy-ion elastic scattering.* Phys. Rev. C **46**, 1026 (1992).

[132] M. C. Mermaz, B. Berthier, J. Barrette, J. Gastebois, A. Gillibert, R. Lucas, J. Matuszek, A. Miczaika, E. Van Renterghem, T. Suomijärvi, A. Boucenna, D. Disdier, P. Gorodetzky, L. Kraus, I. Linck, B. Lott, V. Rauch, R. Rebmeister, F. Scheibling, N. Schulz, J. C. Sens, C. Grunberg, and W. Mittig. *One-nucleon stripping reactions to discrete levels induced by a 793 MeV* ^{16}O *beam on a* ^{208}Pb *target.* Z. Phys. A **326**, 353 (1987).

[133] J. S. Al-Khalili, J. A. Tostevin, and J. M. Brooke. *Beyond the eikonal model for few-body systems.* Phys. Rev. C **55**, 1018(R) (1997).

[134] M. D. Cortina-Gil. *Étude de la diffusion élastique et de la réaction d'échange de charge* (p,n) *avec des faisceaux exotiques légers riches en neutrons.* PhD thesis, Université de Caen, Caen, 1996.

[135] D. M. Brink. *Semi-classical methods in nucleus-nucleus scattering.* Cambridge University Press, Cambridge, 1985.

[136] N. C. Summers, J. S. Al-Khalili, and R. C. Johnson. *Nonadiabatic corrections to elastic scattering of halo nuclei.* Phys. Rev. C **66**, 014614 (2002).

[137] T. Regge. *Introduction to complex orbital momenta.* Nuovo Cim. **14**, 951 (1959).

[138] C. J. Joachain. *Quantum Collision Theory.* Benjamin-Cummings, Amsterdam, 1975.

[139] W. Magnus. *On the exponential solution of differential equations for a linear operator.* Comm. Pure Appl. Math. **7**, 649 (1954).

[140] F. Fer. *Résolution de l'équation matricielle* $du/dt = pu$ *par produit infini d'exponentielles matricielles.* Bull. Cl. Sc. Acad. Roy. Belg. **44**, 818 (1958).

[141] S. Typel and R. Shyam. *Dynamical description of the breakup of one-neutron halo nuclei* ^{11}Be *and* ^{19}C. Phys. Rev. C **64**, 024605 (2001).

[142] B. Bonin, N. Alamanos, B. Berthier, G. Bruge, H. Faraggi, J.C. Lugol, W. Mittig, L. Papineau, A.I. Yavin, J. Arvieux, L. Farvacque, M. Buenerd, and W. Bauhoff. *Alpha-nucleus elastic scattering at intermediate energies.* Nucl. Phys. A **445**, 381 (1985).

[143] F. D. Becchetti and G. W. Greenlees. *Nucleon-nucleus optical-model parameters,* $A > 40$*,* $E < 50$ *MeV.* Phys. Rev. **182**, 1190 (1969).

[144] E. C. Pinilla, P. Descouvemont, and D. Baye. *Three-body breakup of* ^{11}Li *with the eikonal method.* Phys. Rev. C **85**, 054610 (2012).

[145] D. Baye and P.-H. Heenen. *A theoretical study of fast proton-atomic hydrogen scattering.* J. Phys. B **6**, 105 (1973).

[146] M. Ichimura, N. Austern, and C. M. Vincent. *Equivalence of post and prior sum rules for inclusive breakup reactions.* Phys. Rev. C **32**, 431 (1985).

[147] M. S. Hussein, T. Frederico, and R. C. Mastroleo. *Faddeev and DWBA description of inclusive break-up and incomplete fusion reactions.* Nucl. Phys. A **511**, 269 (1990).

[148] M. Ichimura. *Relation among theories of inclusive breakup reactions.* Phys. Rev. C **41**, 834 (1990).

[149] C. A. Bertulani, H.-W. Hammer, and U. van Kolck. *Effective field theory for halo nuclei: shallow p-wave states.* Nucl. Phys. A **712**, 37 (2002).

[150] P. F. Bedaque, H.-W. Hammer, and U. van Kolck. *Narrow resonances in effective field theory.* Phys. Lett. B **569**, 159 (2003).

[151] H.-W. Hammer, C. Ji, and D. R. Phillips. *Effective field theory description of halo nuclei.* J. Phys. G: Nucl. Part. Phys. **44**, 103002 (2017).

[152] P. Capel, D. R. Phillips, and H.-W. Hammer. *Dissecting reaction calculations using halo effective field theory and ab initio input.* Phys. Rev. C **98**, 034610 (2018).

[153] K. Hencken, G. Bertsch, and H. Esbensen. *Breakup reactions of the halo nuclei* ^{11}Be *and* ^{8}B. Phys. Rev. C **54**, 3043 (1996).

[154] C. A. Bertulani and A. Gade. *MOMDIS: a Glauber model computer code for knockout reactions.* Comp. Phys. Comm. **175**, 372 (2006).

[155] C. Elster. *Physics 755 Nuclear Theory : The nucleon-nucleon system.* Ohio University, Athens, 2020.

[156] S. P. Weppner. *A nucleon–nucleus optical model for A $\leq$ 13 nuclei at 65–75 MeV projectile energy.* J. Phys. G: Nucl. Part. Phys. **45**, 095102 (2018).

[157] Z. H. Li, Y. J. Li, J. Su, B. Guo, E. T. Li, K. J. Dong, X. X. Bai, Z. C. Li, J. C. Liu, S. Q. Yan, Y. B. Wang, S. Zeng, G. Lian, B. X. Wang, S. J. Jin, X. Liu, W. J. Zhang, W. Z. Huang, Q. W. Fan, L. Gan, Z. D. Wu, and W. P. Liu. *New determination of the proton spectroscopic factor in ^{9}Be from the ^{13}C(^{9}Be,^{8}Li)^{14}N angular distribution.* Phys. Rev. C **87**, 017601 (2013).

[158] A. Bonaccorso and R. J. Charity. *Optical potential for the n-^{9}Be reaction.* Phys. Rev. C **89**, 024619 (2014).

[159] P. G. Hansen. *Momentum content of single-nucleon halos.* Phys. Rev. Lett. **77**, 1016 (1996).

[160] C. A. Bertulani and P. G. Hansen. *Momentum distributions in stripping reactions of radioactive projectiles at intermediate energies.* Phys. Rev. C **70**, 034609 (2004).

[161] P. Capel and F. M. Nunes. *Peripherality of breakup reactions.* Phys. Rev. C **75**, 054609 (2007).

[162] L. Trache, A. Azhari, F. Carstoiu, C. A. Gagliardi, A. M.Mukhamedzhanov, X. D. Tang, R. E. Tribble, and S. Zhou, Tex. A & M Cyclotron Prog. Rep. I:16, 2002.

[163] L. Trache, F. Carstoiu, C. A. Gagliardi, and R. E. Tribble. *Asymptotic Normalization Coefficient of* ^{8}B *from Breakup Reactions and the S_{17} Astrophysical Factor.* Phys. Rev. Lett. **87**, 271102 (2001).

[164] L. Trache, F. Carstoiu, M. Mukhamedzhanov, and R. E. Tribble. *Determination of the S_{18} astrophysical factor for* $^{8}\mathrm{B}(p,\gamma)\,^{9}\mathrm{C}$ *from the breakup of* $^{9}\mathrm{C}$ *at intermediate energies.* Phys. Rev. C **66**, 035801 (2002).

[165] J. Enders, T. Baumann, B. A. Brown, N. H. Frank, P. G. Hansen, P. R. Heckman, B. M. Sherrill, A. Stolz, M. Thoennessen, J. A. Tostevin, E. J. Tryggestad, S. Typel, and M. S. Wallace. *Spectroscopic factors measured in inclusive proton-knockout reactions on* $^{8}\mathrm{B}$ *and* $^{9}\mathrm{C}$ *at intermediate energies.* Phys. Rev. C **67**, 064301 (2003).

[166] P. Capel and F. M. Nunes. *Influence of the projectile description on breakup calculations.* Phys. Rev. C **73**, 014615 (2006).

[167] J.-M. Sparenberg, P. Capel, and D. Baye. *Influence of low-energy scattering on loosely bound states.* Phys. Rev. C **81**, 011601(R) (2010).

[168] D. Baye. *Supersymmetry between deep and shallow nucleus-nucleus potentials.* Phys. Rev. Lett. **58**, 2738 (1987).

[169] D. Baye. *Phase-equivalent potentials from supersymmetry.* J. Phys. A: Math. Gen. **20**, 5529 (1987).

[170] C. V. Sukumar. *Supersymmetry, factorisation of the Schrödinger equation and a Hamiltonian hierarchy.* J. Phys. A: Math. Gen. **18**, L57 (1985).

[171] A. Moro. private communication, 2019.

[172] J. A. Tostevin. *Single-nucleon knockout reactions at fragmentation beam energies.* Nucl. Phys. A **682**, 320 (2001).

[173] A. E. Lovell, F. M. Nunes, J. Sarich, and S. M. Wild. *Uncertainty quantification for optical model parameters.* Phys. Rev. C **95**, 024611 (2017).

[174] A. E. Lovell and F. M. Nunes. *Constraining transfer cross sections using Bayes' theorem.* Phys. Rev. C **97**, 064612 (2018).

[175] J. Yang and P. Capel. *Systematic analysis of the peripherality of the* $^{10}\mathrm{Be}(d,p)^{11}\mathrm{Be}$ *transfer reaction and extraction of the asymptotic normalization coefficient of* $^{11}\mathrm{Be}$ *bound states.* Phys. Rev. C **98**, 054602 (2018).

[176] L. Moschini, J. Yang, and P. Capel. $^{15}\mathrm{C}$*: From halo effective field theory structure to the study of transfer, breakup, and radiative-capture reactions.* Phys. Rev. C **100**, 044615 (2019).

[177] B. V. Carlson, T. Frederico, and M. S. Hussein. *Inclusive breakup of three-fragment weakly bound nuclei.* Phys. Lett. B **767**, 53 (2017).

[178] L. A. Souza, E. V. Chimanski, T. Frederico, B. V. Carlson, and M. S. Hussein. *Four-body eikonal approach to three-body halo nuclei scattering.* arXiv:1806.06278 [nucl-th], 2018.

[179] D. A. Varshalovich, A. N. Moskalev, and V. K. Khersonskii. *Quantum Theory of Angular Momentum.* World Scientific, Singapore, 1988.

[180] H. Esbensen and C. A. Bertulani. *Multipole expansion for relativistic Coulomb excitation.* Phys. Rev. C **65**, 024605 (2002).

[181] J. S. Al-Khalili, I. J. Thompson, and J. A. Tostevin. *Evaluation of an eikonal model for* ^{11}Li-*nucleus elastic scattering.* Nucl. Phys. A **581**, 331 (1995).